

**Multiscale Quantitative Imaging of Human Femoral Heads Using X-ray
Microtomography**

Farhat Ahmed
BSc (Eng)

A thesis submitted in fulfilment of the requirements for the degree of Doctor of
Philosophy in the Faculty of Science, University of London

Department of Materials, School of Engineering and Materials Science, Queen Mary
University of London

Declaration

I declare that the material in this thesis is entirely my own work and that I have attributed any brief quotations, both at the appropriate point in the text and in the bibliography at the end of this piece of work, to their authors.

I also declare, that I have not used extensive quotations or close paraphrasing and that I have neither copied work from another person, nor used the ideas of another person without proper acknowledgement.

Name:

Farhat Ahmed

Title of Work Submitted:

**Multiscale Quantitative Imaging of Human Femoral Heads Using X-ray
Microtomography**

Signature

Date

Abstract

Clinical diagnostic tools provide limited information on the underlying structural and mechanical properties of bone-tissue affected by degenerative and bone metabolic diseases. *In-vivo* bone failure studies provide limited information due to constraints such as X-ray dosage, cost and various other practicalities. *In-vitro* studies are thus required to enhance understanding of this phenomenon. The aims of this study were to use quantitative high-definition X-ray Micro-Tomography (XMT) to assess factors contributing to pathological and non-pathological bone failure and repair in relation to the mechanics of whole human femoral heads.

XMT images of one normal and six pathological femoral heads were collected at 26 – 8.8 μm voxel resolution and evaluated to determine structural features; bone mineral concentration (BMC); and using image analysis, identify microcallus formations. In addition, *in-vitro* compression tests were carried out on specimens taken from regions with different anatomical loading. Bone quality was then related to the anatomical loading and BMC.

Results from non-pathological tissue were used to establish a baseline for measurements of structural features. Microcallus formations were identified and used as markers to map the occurrence of bone damage. In osteoarthritic (OA) heads, the damage was found to be concentrated in localised clusters. Conversely, in the osteoporotic head damage was distributed homogeneously throughout the entire specimen. No significant difference in the BMC was observed, however there was a

significant difference in the bone quality values between the non-pathological and pathological heads, and also between the pathologies. *In-vitro* mechanical testing revealed a difference in the mechanical properties of OA trabecular bone in relation to bone quality measurements but the samples exhibited no significant correlation to anatomical loading.

X-ray Ultra Microscopy (XuM) at 200nm and 775nm voxel resolution was used to investigate the nano-morphology of individual trabeculae. The XuM images showed differences in bone structure and fewer osteocyte lacunae present close to fracture site. XuM also identified micro-cracks within trabeculae that were encased by microcallus formations.

The application of novel quantitative high definition X-ray imaging to clinically relevant tissue at multiple length scales has provided new metrological data on the distribution of damage within pathological tissue. Insight into the vulnerability of diseased tissue to damage could ultimately lead to improved diagnosis from clinical radiographs.

*Dedicated to the most inspiring people in my life,
My Mother, Yasmin and My beloved Husband, Umar
This is your achievement*

Acknowledgements

Firstly I would like to thank Allah for enabling me to achieve my goal in completing this thesis. I would also like to thank Professor Liz Tanner for encouraging me into this area of research and always supporting me in my academic and personal life. I would never have been able to reach this stage without the active support and care of my supervisors Dr. Graham Davis and Dr. Andy Bushby. I would also like to thank Prof. Jim Elliott for taking me under his wing during the course of my time here.

I would like to say a big heartfelt thanks to Steve for all our little chats. Thank you Steve, you are a star! A huge thanks to Rory for all his help and continuous support in guiding me in my work.

A huge thank you to Mediah and Francesca, for all the amazing lunches and helping me in keeping my sanity throughout my PhD. I would like to thank Prof. Alan Boyde in all his guidance and Mo, for always putting a smile on my face. Thank you to Mr. Gareth Scott in providing the tissue and his valuable time for this project.

A big thank you to all of my friends and family who have supported me, and helped me in their own unique ways. This journey would never have completed without some very special friends. Thank you for all your prayers.

Without my parents this would never have been possible, Ami, Daddy, Mum and Dad, thank you all for taking such good care of me and supporting me in realising my dream. I am sincerely grateful to my mother Sajda, for supporting me through all the difficult times and for encouraging me to never give up. Thank you to my little sisters, Sonia, Sadia and Sabah, for putting up with big sister syndrome, you are my strength, thank you. This achievement will always belong to my ami. Thank you ami, for always believing in my ability to succeed. You are the most cherished person in my life. Also, a huge thank you to my father and dad, for keeping me grounded throughout this journey.

This achievement would never have been possible without the prayers of all my loved ones, especially my grandmother (nani ama) and Ami Jee (may her soul rest in peace).

Last but not least, my wonderful husband Umar, sorry for all the painstaking moments you have had to endure throughout my studies and thank you for your patience, support and love in helping me achieve this. Without you, this holds no value.

Contents

Declaration	i
Abstract	ii
Dedication.....	iv
Acknowledgements.....	v
List of Figures	xiv
List of Tables.....	xxv
List of Abbreviations.....	xxvi
Part I Literature Survey	1
Chapter 1 Bone	3
1.1 Bone Tissue	3
1.2 Bone Composition	3
1.3 Organisation of Bone	4
1.3.2 Micro-Structure	5
1.3.3 Nano-structure.....	7
1.3.4 Bone Mineral.....	8
1.3.5 Bone Cells	8
1.4 Bone Physiology.....	11
1.4.1 Bone remodelling.....	11
1.4.2 Bone Turnover	13
1.4.3 Trabecular Bone Architecture	14
1.5 Bone Quality.....	17
1.6 Mechanical Properties of Trabecular Bone	18
1.6.1 Stress-strain Behaviour	18
1.6.2 Shear Strength	19
1.6.3 Compressive Strength	20
1.6.4 Trabecular Bone Density	20
1.6.5 Effect of Age	21
1.6.6 Principles of Hip Mechanics	22

1.7 Bone Fracture and Repair Mechanisms	25
1.7.1 Microdamage	26
1.7.2 Detection of microcracks	26
1.7.3 Microcallus Formations	27
1.8 Bone Pathology.....	29
1.8.1 Osteoarthritis	29
1.8.2 Osteoporosis.....	33
1.9 Clinical Diagnostic Techniques	33
1.9.1 Radiographs	33
1.9.2 DXA.....	35
1.9.3 Quantitative Ultrasound	36
1.9.4 CT Imaging	36
Chapter 2 X-ray Microscopy.....	38
2.1 Introduction.....	38
2.1.1 EM Spectrum	38
2.2 X-ray production.....	39
2.2.1 Bremsstrahlung radiation	39
2.2.2 Characteristic (k-shell) X-rays	40
2.2.3 Impact sources.....	41
2.3 Synchrotron Radiation	43
2.4 X-ray interactions with matter	44
2.4.1 Attenuation mechanisms	44
2.5 Beer's Law.....	45
2.5.1 Attenuation Coefficients	46
2.6 Beam Attenuation	48
2.7 X-ray Microtomography.....	48
2.7.1 Principles of XMT	49
2.7.2 XMT based Studies	51

2.7.3 XMT and Bone.....	51
2.8 Scanning Electron Microscopy.....	56
2.8.1 SEM based studies on bone	58
2.9 Nano-tomography and X-ray Ultra Microscopy.....	59
General Aims and Objectives	61
Part II: Materials and Methods	62
Chapter 3 Materials and Preparation	63
3.1 Non–Pathological Specimen.....	65
3.1.1 Specimen selection.....	65
3.1.2 Categorisation of femoral heads	66
3.1.3 Selection of Normal Specimen	66
3.1.4 Femoral Head Specimen Preparation in Glycerol.....	68
3.2 Pathological Tissue.....	69
3.2.1 Tissue Extraction.....	69
3.2.2 Specimen Selection	70
3.2.3 Specimen History	70
3.2.4 Specimen Storage.....	71
3.2.5 Specimen size.....	71
3.2.6 Specimen mounting.....	72
3.3 Tissue for Mechanical Studies.....	73
3.3.1 Patient History.....	73
3.3.2 Specimen Shape	74
3.3.3 Preparation and orientation of specimens from the femoral head	75
3.3.4 The number of specimens per head.....	79
3.3.5 Specimen size.....	80
3.3.7 Embedding Technique	80
3.4 Preparation of Microcallus formation Specimens for Micro- and Nano- Tomography.....	81
3.5 Tissue for Micro-mechanics Studies	82

3.5.1 Specimen Selection	82
3.5.2 Slice extraction.....	82
3.5.3 Preparation of calcified tissue	83
3.5.4 Trabecula Extraction	84
3.5.5 Specimen Mounting	84
Chapter 4 Methods.....	85
4.1 X-ray Microtomography	85
4.1.1 Experimental equipment	86
4.1.2 ‘Block’ scanning	91
4.1.3 Signal to Noise ratio.....	93
4.1.4 Calibration.....	93
4.2 In-vitro Biomechanical Testing	96
4.2.1 Description of equipment and method	96
4.2.2 Compression testing.....	96
4.2.3 Strain increments.....	98
4.3 Data Processing	98
4.3.1 Data collection	98
4.3.2 Pre-processing and Linearisation	100
4.3.3 Reconstruction	101
4.3.4 Resolution Limitations and Errors	102
4.4 Visualisation and Analysis	105
4.4.1 Co-ordinate System and Data Location	105
4.4.2 Data Orientation.....	106
4.4.4 Object transformation	107
4.5 Qualitative Analysis.....	116
4.5.1 2D Transfer Function and Thresholding.....	117
4.6 Bone Quality Measurements.....	120
4.7 Measurement of Bone Mineral Concentrations	127

4.8 In-vitro Biomechanical Testing Analysis	128
4.9 X-ray Ultra-Microscopy (XuM)	129
4.9.1 Experimental equipment	129
4.9.2 Image acquisition	130
4.9.3 Reconstruction	131
4.9.4 XuM Data Analysis.....	131
Part III Experimental Studies	132
Chapter 5 High Resolution Imaging of a Clinically Normal Femoral Head	133
5.0 Introduction	133
5.1 Materials and Methods	135
5.1.1 Experimental Details.....	135
5.2 Results.....	136
5.3 Qualitative Analysis of Bone Structural Features	136
5.4 Determination and Distribution of Bone Features.....	137
5.4.1 Greyscale Analysis and Feature Observation	137
5.4.2 Microcallus Formations and Load-bearing Mapping.....	140
5.4.3 Distribution of Microcallus Formations.....	142
5.5 Effect of Bone Mineral Concentration	143
5.6 Bone Volume Measurement	145
5.7 Evaluation of Bone Quality Using XMT	146
Chapter 6 High resolution imaging of Pathological Femoral Heads.....	160
6.0 Introduction.....	160
6.1 Materials and Methods	162
6.1.1 Experimental Details.....	162
6.2 Results.....	163
6.3 Qualitative Analysis of Structural Bone Features	163
6.4 Determination and Distribution of Bone Features.....	169
6.4.1 Greyscale Analysis and Feature Observation	169

6.4.2 Microcallus Formations and Load-bearing Mapping.....	170
6.4.3 Distribution of Microcallus Formations.....	173
6.5 Bone Mineral Concentration.....	176
6.6 Bone Volume Fraction Distribution	178
6.7 Evaluation of Bone Quality Using XMT.....	180
Chapter 7 <i>In-Vitro</i> Mechanical testing of trabecular bone using XMT	192
7.0 Introduction	192
7.1 Methods and Materials	193
7.2 Results.....	193
7.2.1 Region of Interest.....	193
7.2.2 Assessment of Bone Quality and Mechanical Properties	194
7.2.3 Regions of Failure	213
Chapter 8 Single Microcallus Formation Study	216
8.0 Introduction	216
8.1 Methods and Materials	217
8.2 Results.....	217
8.2.1 Location and Morphology of Microcallus Formations at 25 μ m.....	217
8.2.2 Analysis of Microcallus Formation at High resolution - 8.8 μ m	220
8.2.3 Bone mineral concentration and Microcallus Formations	222
8.2.4 Evaluation of Nano-structure of Microcallus Formation at 775nm.....	225
Chapter 9 High resolution imaging of a trabecula using XuM.....	229
9.0 Introduction	229
9.1 Materials and Method.....	230
9.2 Results.....	230
9.2.1 Loading of the single trabecula and micro-cracks	230
9.2.2 Qualitative Feature Detection of greyscale images.....	234
9.2.3 Qualitative 3D analysis of a single trabecula.....	235

Part IV General Discussion, Conclusions and Future Work	238
Chapter 10 General discussion, Conclusions and Future Work.....	239
10.1 Discussion.....	239
10.1.1 Clinically Normal Femoral Head.....	239
10.1.2 Pathological Femoral Heads	246
10.1.3 Mechanical Properties of Trabecular Bone.....	252
10.1.4 Multiscale Imaging of Microcallus Formations.....	256
10.1.5 Trabecula Imaging at Nano-scale	259
10.2 General Overview	261
10.3 Conclusions.....	274
10.4 Future Work.....	276
Part V References and Appendices.....	278
References	279
Appendices	300

List of Figures

Figure 1.1: Hierarchical structure of bone	5
Figure 1.2: Bone remodelling. (i) Resorption: stimulated osteoblast precursors release factors that induce osteoclast differentiation and activity. Osteoclasts remove bone mineral and matrix, creating a cutting cone. (ii) Reversal: mononuclear cells prepare bone surface for new osteoblasts to begin forming bone. (iii) Formation: successive waves of osteoblasts synthesize an organic matrix to replace resorbed bone and fill the cavity with new bone (iv) Resting: bone surface is covered with flattened lining cells (Reproduced from Coxon <i>et al.</i> , 2004 with permission from Macmillan Publishers Ltd)	13
Figure 1.3: (a) Open cell. Here l is the cell length and t is the width of the rods contained within it, (b) Closed cell. Here l is the cell length, t_f is the wall width and t_e is the width of the rods	16
Figure 1.4: Typical stress-strain curve for the compression of trabecular bone. The stress-strain curve is divided into elastic and plastic regions, separated by the point of yield. The maximum compressive stress (MCS) represents the ultimate failure stress and the maximum compressive strain (MCSt) represents the strain at ultimate failure strain. Yield stress (YS) is the stress at point of yield, yield strain (YSt) represents the strain at point of yield and elastic modulus (E) is the maximum slope of the elastic region of the curve.....	19
Figure 1.5: Forces acting on the hip joint during single leg stance under conditions of equilibrium. Gravitational force W , abductor muscle force, A , hip joint reaction force F , abductor muscle moment arm I , and force of gravity moment arm d	23
Figure 1.6: Load-bearing regions of a left femoral head.....	25
Figure 1.7: Four morphological types of MCFs; a) rounded nodular, b) fusiform, c) angulated and d) arched bridges, magnification (Reproduced from Vernon-Roberts and Pirie, 1973 with permission from BMJ Publishing Group Ltd).....	28
Figure 1.8: Lumbar vertebral body trabecular bone, 89-year-old female, showing microcallus repair of trabecular micro- fractures. Field width, 850 μm . Combined backscattered, forward scattered and transmitted primary fast electron image, 20 kV	29
Figure 2.1: The Electromagnetic Spectrum.....	38
Figure 2.2: Bremsstrahlung and characteristic radiation spectra are shown for a tungsten anode with X-ray tube operation at 80, 100, 120, and 140 kV and equal tube currents	40

Figure 2.3: X-rays from a molybdenum target at 35 kV. The two sharp peaks in the graph are characteristic X-rays which occur when vacancies are produced in K-shell of the atom and electrons drop down from above to fill the gap. The X-rays produced by transitions from L to K levels are called K-alpha X-rays, and those from M to K transition are called K-beta X-rays. Transitions to the L-shell are designated as L X-rays. The graph also shows the "brehmsstrahlung" radiation which forms the base for the two sharp peaks41

Figure 2.4: Basic components of a micro-focus X-ray unit42

Figure 2.5: Mass attenuation coefficients for various tissues, lead and iodine47

Figure 2.6: A schematic of an XMT set-up.....50

Figure 2.7: Three dimensional XMT reconstruction of a cuboidal VOI (4 x 4 x 4mm³) at 19.5µm voxel size.....56

Figure 2.8: Behaviour of electrons interacting with a specimen.....57

Figure 2.9: Schematic of an SEM set-up.....58

Figure 2.10: Human femoral shaft, post-mortem, compact bone adjacent to metal implant stem, showing mineralized apoptotic debris in osteocyte lacuna in lamellar bone. 20-kV BSE of PMMA-embedded, polished, carbon-coated sample. Field width, 44 µm (Boyde 2003b).....59

Figure 3.1: Flow diagram showing the different processes of the specimens' experience throughout this thesis64

Figure 3.2 Radiograph of the selected normal femoral head (A6, Appendix I), (a) showing normal geometry of the femoral head with no bone cysts present and no subchondral bone thickening (b) clearly visible is the growth plate and(c) the trabeculae bone are oriented clearly perpendicular to the surface of the femoral head67

Figure 3.3: Radiograph of a severely osteoarthritic femoral head (A23 Appendix I), (a) showing abnormal geometry of the femoral head (b) with subchondral sclerosis, (c) the growth plate is slightly visible and (d) osteophyte formations are found at the superior and inferior surfaces of the head-neck joint67

Figure 3.4: Radiograph of a severely osteoporotic femoral head (A20 Appendix I), (a) showing large areas of resorption and (b) fine trabeculae architecture68

Figure 3.5: An image of the OA Femoral Head72

Figure 3.6: A schematic of the specimen mounting set-up used during imaging of whole femoral heads.....73

Figure 3.7: The jig used to trephine cylindrical specimens from each femoral head 75

Figure 3.8: (a) Image of the bone cylinder after removal of the subchondral bone...76

Figure 3.9: The standardised positions of specimen sites on the right femoral head and their relation to load bearing in the femoral head.....	78
Figure 3.10: Specimen set-up for XuM.....	82
Figure 3.11: A ‘bird’s eye view’ schematic highlighting the sectional slices taken from the medio-lateral region of the femoral head, where the dashed line represents the fovea and the anatomical positions are denoted by; A–Anterior, P-Posterior, M-Medial and L-Lateral.....	83
Figure 4.1: An Image of the 4 th generation XMT scanner developed by Davis and Elliott (2003), showing (a) the ultrafocus beam system, (b) the TDI CCD, (c) the sample and (d) the rotational stage.....	85
Figure 4.2: (a) Vertical and (b) horizontal geometry of the XMT set-up developed by Davis and Elliott (2003)	87
Figure 4.3: Example of a circle being imaged and how the CCD reads out the data (Ahmed, 2010).....	88
Figure 4.4: Time Sequence showing TDI CCD read out of the captured image	89
Figure 4.5: Schematic diagram of bird’s eye view of XMT system showing the difference between scanning a sample (a) without and (b) with moving collimator ..	90
Figure 4.6: Schematic diagram of side view showing ‘block’ scanning.....	92
Figure 4.7: Graph showing the LAC of 100% HAP and Aluminium with varying energy (Ahmed, 2010).....	94
Figure 4.8: Ten Step Aluminium step wedge.....	95
Figure 4.9: A schematic of the loading device.....	97
Figure 4.10: The projection window showing the field of view	100
Figure 4.11: Schematic of line profiles taken through (a) a thick trabecula containing several voxels (b) a thin trabecula containing fewer voxels and (c) a very fine trabecula containing very few voxels, for a perfect system	104
Figure 4.12: Schematic of the anatomical positioning of the femoral head (a) orientation as imaged (b) image data rotated to anatomical orientation	106
Figure 4.13: Data orientation of co-ordinates	107
Figure 4.14: Load-bearing regions of a left femoral head; (adapted from Brown and Shaw, 1983; Sharp, 1988), (a) the position of the femoral head during imaging in the XMT, and (b) as orientated <i>in vivo</i>	110
Figure 4.15: Femoral head geometry for radial distribution	111
Figure 4.16: Binned radi.....	112
Figure 4.17: Geometry for angular distribution	114
Figure 4.18: Histogram with single thresholding boundary approach	117

Figure 4.19: 2D transfer function editor has 3 sections; (a) colour-opacity gradient interface, (b) horizontal axis represents the voxel intensities, and vertical axis represents the rate of change of voxel intensity (gradient magnitude) and (c) manager, plotting interface	118
Figure 4.20: Homogenous material with different arrangements of voxels resulting in different gradients, hence different 2D histograms	119
Figure 4.21: Illustration of the parallel-plate model	122
Figure 4.22: An image measuring 130 × 150 pixels (where 1 pixel = 25µm) obtained from ImageJ, where the green circles denote the sphere used to calculate trabeculae thickness,	123
Figure 4.23: A resulting image measuring 130 × 150 pixels (where 1 pixel = 25µm) obtained from ImageJ when calculating trabeculae spacing, where this image is the inverse of the image in Figure 4.22. The green circle defines the sphere used to calculate the trabecular spacing.....	125
Figure 4.24: Assumed linear relationship between LAC and BMC based on theoretical values for pure hydroxyapatite and measured values for collagen (modelled as water) from XMT data sets	128
Figure 4.25: A schematic of the XuM inside the SEM chamber	130
Figure 5.1: Cross section of the normal femoral head (A6, Appendix I) at 26 µm reconstructed voxel size, with a uniform subchondral bone plate (a) and no apparent pathology	136
Figure 5.2: The anterior view of the articular calcified cartilage (ACC) surface of the femoral head with no apparent eburnated surfaces	137
Figure 5.3: XMT image of the central slice from the normal femoral head at 26µm reconstructed voxel size (A6, Appendix I) in the XY plane (field width = 49 mm) showing (a) the growth plate, (b) well connected trabeculae (c) poorly connected trabeculae and (d) the subchondral bone plate	138
Figure 5.4: (i) Single 2D central slice showing microcallus in the XZ plane, where (a) is the plane of Figure 5.3, (b) and (c) are regions of resorption, (d) is the fovea and (e) the principal direction of trabeculae, and (ii) is the microcallus formation enlarged from the 2D slice	139
Figure 5.5: Distributions of Microcallus patches superimposed on contact stress gradients from Brown and Shaw, 1983. Where, A, P, L and M represent the anatomical positions; anterior, posterior, lateral and medial, respectively. Contour units are MNm ⁻²	141
Figure 5.6: Polar coordinates of MCFs mapped onto the load bearing regions of the femoral head.....	142

Figure 5.7: The number of MCFs found in binned radial volumes, showing a steep increase between 15-20mm. The number of MCFs in each binned radial volume, are shown in brackets.	143
Figure 5.8: (a) Graph showing the histogram for the femoral head obtained from the XMT data set. The peaks relate to the LAC of air, glycerol and bone, and (b) the ROI post-thresholding containing bone, with the distribution of LAC for bone	144
Figure 5.9: The distribution of BMC along the Z-direction of the normal femoral head, from superior to inferior, correlated for anatomical positioning with a slice through the reconstructed XMT data set	145
Figure 5.10: Distribution of volume of bone organ occupied by bone tissue throughout the normal femoral head, from superior to inferior, correlated with a slice through the reconstructed XMT data set	146
Figure 5.11: Scatter plot of BVF vs. Trabecular Thickness for major-, partial- and non-load bearing regions of the normal femoral head ($R = 0.882$ $p = 0.000$).....	147
Figure 5.12: Plot for BVF vs. Tb.Sp for major-, partial- and non-load bearing regions in the normal femoral head of the normal femoral head ($R = -0.754$ $p = 0.001$).....	148
Figure 5.13: Linear relationship between BVF and Tb.N for major-, partial- and non-load bearing regions of the normal femoral head ($R = 0.988$ $p = 0.000$).....	149
Figure 5.14: Scatter plot of Bone volume fraction vs. Structural Model Index for major-, partial- and non-load bearing regions of the normal femoral head ($R = -0.543$ $p = 0.036$)	150
Figure 5.15: Trabecular number vs. Structure Model Index for major-, partial- and non-load bearing regions of the normal femoral head ($R = -0.561$ $p = 0.030$)	151
Figure 5.16: Connectivity Density vs. Structure Model Index for major-, partial- and non-load bearing regions of the normal femoral head ($R = 0.092$ $p = 0.745$).....	152
Figure 5.17: Plot showing Trabecular thickness vs. Structure Model Index for major-, partial-, and non-load bearing regions of the normal femoral head ($R = -0.506$ $p = 0.054$).....	153
Figure 5.18: Relationship between BVF and DA, with no direct correlation for major-, partial- and non-load bearing regions of the normal femoral head ($R = -0.186$ $p = 0.508$)	155
Figure 5.19: Plot of Connectivity Density vs. Degree of anisotropy for major-, partial- and non-load bearing regions of the normal femoral head ($R = -0.710$ $p = 0.003$).....	155
Figure 5.20: Scatter plot of Connectivity Density vs. Trabecular Number for major-, partial- and non-load bearing regions of the normal femoral head ($R = 0.469$ $p = 0.078$).....	156

Figure 5.21: Scatter plot of Trabecular Thickness vs. Trabecular Number for major-, partial- and non-load bearing regions of the normal femoral head ($R = 0.925$ $p = 0.000$).....	156
Figure 5.22: Linear relationship between BMC and Tb.Th for major-, partial- and non-load bearing regions of the normal femoral head of the normal femoral head ($R = 0.899$ $p = 0.000$)	157
Figure 6.1: Cross sectional image of the OA head (B7) showing typical features of OA; (a) thickened subchondral bone plate, (b) possible subchondral bone cysts, (c) osteophyte formation, (d) the growth plate and (e) areas of resorption.	164
Figure 6.2: (a) The non-eburnated surface of the OP femoral head (B14), (b) the excised surface and (c) the plane of the femoral neck fracture	165
Figure 6.3: Cross section of femoral head (B14) exhibiting typical features of OP; (a) areas of resorption, (b) uniform thickness of subchondral bone plate and (c) thin trabeculae.....	166
Figure 6.4: Specimen B15 exhibiting typical OA features; (a) eburnated surface, (b) non-eburnated surface and (c) osteophyte formation	167
Figure 6.5: (a) Cross section of specimen B15 exhibiting typical surface and non-surface features of OA and (b) enlarged section taken from B15, showing local variation in bone architecture	168
Figure 6.6: (i) Single 2D image showing the microcallus formation in the YZ central plane (Specimen B7) and (ii) the enlarged MCF	169
Figure 6.7: Distributions of MCFs found in B7 (OA) superimposed on stress gradients (MNm^{-2}) from (Brown and Shaw 1983). A, P, L and M represent the anatomical positions; anterior, posterior, lateral and medial, respectively. The dashed line, represents the fovea.	171
Figure 6.8: Distributions of Microcallus formations found in B15 (OA) superimposed on stress gradients from (Brown and Shaw 1983). A, P, L and M represent the anatomical positions; anterior, posterior, lateral and medial, respectively	171
Figure 6.9: Distributions of MCFs found in B14 (OP) superimposed on loading contours from (Brown and Shaw 1983). A, P, L and M represent the anatomical positions; anterior, posterior, lateral and medial, respectively	172
Figure 6.10: Polar coordinates of MCFs mapped onto the load bearing regions of the OA femoral head (B7), with the fovea marked in red.....	174
Figure 6.11: Polar coordinates of MCFs mapped onto the load bearing regions of the OA femoral head (B15), with the fovea marked in red.....	174

Figure 6.12: Polar coordinates of MCFs mapped onto the load bearing regions of the OP femoral head (B14), with the fovea marked in red	175
Figure 6.13: The density of MCFs found in binned radial volumes (mm^{-3}) for osteoarthritic and osteoporotic femoral heads.....	176
Figure 6.14: (a) Graph showing volume vs. LAC for the pathological femoral heads obtained from the XMT data set. The peaks relate to the LAC of air, glycerol and bone, and (b) the ROI post-thresholding containing bone, with the distribution of LAC for bone.....	177
Figure 6.15: The distribution of BMC along the Z-direction of the pathological femoral heads, from superior to inferior. The grey line denotes Figure 5.9 for reference	178
Figure 6.16: Distribution of the occupied bone tissue throughout the pathological femoral heads. The grey line denotes Figure 5.10 for reference	179
Figure 6.17: Plot of Bone Volume Fraction vs. Trabecular Thickness for major-, partial- and non-load bearing regions of the OA and OP heads ($R = 0.837$ $p = 0.000$). The shaded region represents Figure 5.11 for reference	181
Figure 6.18: Plot of Bone Volume Fraction vs. Trabecular Spacing for major-, partial- and non-load bearing regions of the OA and OP heads ($R = -0.807$ $p = 0.000$). The shaded region represents Figure 5.12 for reference.....	181
Figure 6.19: Plot of Bone Volume Fraction vs. Trabecular Number for major-, partial- and non-load bearing regions of the OA and OP heads ($R = 0.984$ $p = 0.000$). The shaded region represents Figure 5.13 for reference	182
Figure 6.20: Plot of Bone Volume Fraction vs. Structural Model Index for major-, partial- and non-load bearing regions of the OA and OP heads ($R = -0.904$ $p = 0.000$). The shaded region represents Figure 5.14 for reference	183
Figure 6.21: Plot of Structural Model Index vs. Trabecular Number for major-, partial- and non-load bearing regions of the OA and OP heads ($R = -0.879$ $p = 0.000$). The shaded region represents Figure 5.15 for reference	184
Figure 6.22: Plot of Connectivity Density vs. Structural Model Index for major-, partial- and non-load bearing regions of the OA and OP heads ($R = -0.652$ $p = 0.000$). The shaded region represents Figure 5.16 for reference	185
Figure 6.23: Plot of Trabecular Thickness vs. Structural Model Index for major-, partial- and non-load bearing regions of the OA and OP heads ($R = -0.769$ $p = 0.000$). The shaded region represents Figure 5.17 for reference.....	185
Figure 6.24: Plot of Bone Volume Fraction vs. Degree of Anisotropy for major-, partial- and non-load bearing regions of the OA and OP heads ($R = -.030$ $p = 0.846$). The shaded region represents Figure 5.18 for reference	186

Figure 6.25: Plot of Connectivity Density vs. Degree of Anisotropy for major-, partial- and non-load bearing regions of the OA and OP heads ($R = -0.151$ $p = 0.322$). The shaded region represents Figure 5.19 for reference 187

Figure 6.26: Plot of Connectivity Density vs. Trabecular Number for major-, partial- and non-load bearing regions of the OA and OP heads ($R = 0.538$ $p = 0.002$). The shaded region represents Figure 5.20 for reference 188

Figure 6.27: Plot of Trabecular Thickness vs. Trabecular Number for major-, partial- and non-load bearing regions of the OA and OP heads ($R = 0.837$ $p = 0.000$). The shaded region represents Figure 5.21 for reference 189

Figure 6.28: Plot of Trabecular Thickness vs. Bone Mineral Concentration for major-, partial- and non-load bearing regions of the OA and OP heads ($R = 0.770$ $p = 0.000$). The shaded region represents Figure 5.22 for reference 190

Figure 7.1: (a) Graph showing Normalised voxel frequency vs. LAC for bone cylinder data obtained from XMT. The peaks relate to the LAC of air, glycerol and bone, and (b) the ROI post-thresholding containing bone, with the distribution of LAC for bone..... 194

Figure 7.2: Stress-Strain graph of compressed bone cylinders from major-, partial- and non-load bearing regions, with a systematic error of 5% 195

Figure 7.3: Plot of maximum compressive stress vs. Bone volume fraction for bone cylinders from major-load, partial-load and non-load bearing regions ($R = 0.855$ $p = 0.002$)..... 197

Figure 7.4: Plot of maximum compressive stress vs. Structural model index for bone cylinders from major-load, partial-load and non-load bearing regions ($R = -0.784$ $p = 0.007$)..... 198

Figure 7.5: Plot of Maximum Compressive Stress vs. Trabecular Thickness for bone cylinders from major-load, partial-load and non-load bearing regions ($R = 0.871$ $p = 0.001$)..... 199

Figure 7.6: Plot of Bone Volume Fraction vs. Trabecular Thickness for major-, partial- and non-load bearing regions of the OA extracted cylinders ($R = 0.944$ $p = 0.000$). The shaded region represents Figure 5.11, and X represent OA regions from Figure 6.17 for reference. 200

Figure 7.7: Plot of Bone Volume Fraction vs. Trabecular Spacing for major-, partial- and non-load bearing regions of the OA extracted cylinders ($R = -0.199$ $p = 0.582$). The shaded region represents Figure 5.12, and X represent OA regions from Figure 6.18 for reference 201

Figure 7.8: Plot of Bone Volume Fraction vs. Trabecular Number for major-, partial- and non-load bearing regions of the OA extracted cylinders ($R = -0.199$ $p = 0.194$).

The shaded region represents Figure 5.13, and X represent OA regions from Figure 6.19 for reference202

Figure 7.9: Plot of Bone Volume Fraction vs. Structure Model Index for major-, partial- and non-load bearing regions of the OA extracted cylinders ($R = -0.870$ $p = 0.001$). The shaded region represents Figure 5.14, and X represent OA regions from Figure 6.20 for reference203

Figure 7.10: Plot of Trabecular Number vs. Structure Model Index for major-, partial- and non-load bearing regions of the OA extracted cylinders ($R = -0.585$ $p = 0.076$). The shaded region represents Figure 5.15, and X represent OA regions from Figure 6.21 for reference204

Figure 7.11: Plot of Trabecular Number vs. Structure Model Index for major-, partial- and non-load bearing regions of the OA extracted cylinders ($R = -0.414$ $p = 0.235$). The shaded region represents Figure 5.16, and X represent OA regions from Figure 6.22 for reference205

Figure 7.12: Plot of Trabecular Thickness vs. Structure Model Index for major-, partial- and non-load bearing regions of the OA extracted cylinders ($R = -0.797$ $p = 0.006$). The shaded region represents Figure 5.17, and X represent OA regions from Figure 6.23 for reference206

Figure 7.13: Plot of Bone Volume Fraction vs. Degree of Anisotropy for major-, partial- and non-load bearing regions of the OA extracted cylinders ($R = 0.814$ $p = 0.086$). The shaded region represents Figure 5.18, and X represent OA regions from Figure 6.24 for reference207

Figure 7.14: Plot of Connectivity Density vs. Degree of Anisotropy for major-, partial- and non-load bearing regions of the OA extracted cylinders ($R = 0.235$ $p = 0.514$). The shaded region represents Figure 5.19, and X represent OA regions from Figure 6.25 for reference208

Figure 7.15: Plot of Connectivity Density vs. Trabecular Number for major-, partial- and non-load bearing regions of the OA extracted cylinders ($R = -0.147$ $p = 0.686$). The shaded region represents Figure 5.20, and X represent OA regions from Figure 6.26 for reference209

Figure 7.16: Plot of Trabecular Thickness vs. Trabecular Number for major-, partial- and non-load bearing regions of the OA extracted cylinders ($R = 0.380$ $p = 0.279$). The shaded region represents Figure 5.21, and X represent OA regions from Figure 6.27 for reference210

Figure 7.17: Plot of Trabecular Thickness vs. Bone Mineral Concentration for major-, partial- and non-load bearing regions of the OA extracted cylinders ($R = -0.478$ $p =$

0.163). The shaded region represents Figure 5.22, and X represent OA regions from Figure 6.28 for reference	211
Figure 7.18: (a) Superimposed volumes of a major-load bearing specimen illustrating the region of fracture in shear at 4, 6 and 8% strain, imaged at 20 μ m reconstructed voxel size, (b) the enlarged region highlighted between the red lines in (a).....	214
Figure 7.19: Observed failure behaviour of a single trabecula taken from a major load bearing region bone cylinder at 0, 4, 6 and 8 % strains, imaged at 20 μ m reconstructed voxel size, exhibiting buckling	215
Figure 8.1: Sectioned slice taken from the central xy plane of femoral head B14 (Chapter 6) (measuring 7.85 8.92 1.47 mm (X, Y, Z)), imaged at 25 μ m voxel size.....	218
Figure 8.2: A rendered image of a single microcallus formation (sectioned from Figure 8.1) viewed at different angles, with (a) at 0° and (b) at 90° and (c) at 135° rotation, bound by a box measuring 2.6 1.5 1.4 mm (X,Y,Z)	219
Figure 8.3: Rendered images of an MCF imaged at 8.8 μ m voxel size; with (a) and without (b) the trabeculae, bound by box measuring 871 545 660 μ m	221
Figure 8.4: Axial mid-slice of a MCF removed from a major-load bearing region from specimen B6; the trabecula exhibiting a higher BMC than the surrounding MCF determined using superimposed contour maps of mineralisation from the greyscale values.....	223
Figure 8.5: Coronal mid-slice of a MCF removed from a major-load bearing region from specimen B6; the trabecula exhibiting a higher BMC than the surrounding MCF determined using superimposed contour maps of mineralisation from the greyscale values.....	224
Figure 8.6: Location of line (measuring 1.1 mm) from (a) to (b); placed along the centre of the slice to measure LAC	224
Figure 8.7: Histogram of the line probe showing LAC (as a measure of BMC). See Figure 8.6 for positions of (a) and (b).	225
Figure 8.8: A sectional image through the trabecula encapsulated by a MCF, imaged at 775nm reconstructed voxel size, highlighting the micro-crack, which has propagated through the entire strut (Field width = 0.5 mm)	226
Figure 8.9: Micro-crack propogating through a trabecula, encapsulated in a microcallus formation, bound by box measuring 0.495 0.490 0.494 mm ³ (X,Y,Z)	228
Figure 9.1: SEM image highlighting the unloaded, final load and post-fracture condition of the trabecula, taken at 20 kV (scale bar = 300 μ m).	231

Figure 9.2: Final load image highlighting the micro-cracks on the tensile surface of the single trabecula.....	232
Figure 9.3: SEM image of the critical fracture with an inset image highlighting collagen fibre bridging, taken at 20kV, scale bar is 50 μm and in the enlarged image the scale bar is 2 μm	233
Figure 9.4: Greyscale image exhibiting typical features of a single trabecula with mineralised cell spaces (highlighted by red arrows.....	234
Figure 9.5: Greyscale XuM image of the single trabecula exhibiting internal structure. Field width = 0.24mm	235
Figure 9.6: Cross sectional 3D images of the trabecula: anterior to posterior.	236
Figure 9.7: A rendered image showing the distribution of osteocyte lacunae within the trabecula (bound by box measuring 143.5, 125.6, 237.8 μm in the X, Y, Z), with very few present close to the major fracture site.....	237
Figure 10.1: Rendered images of cropped regions, taken from (a) major-load, (b) partial-load and (c) non-load bearing regions of the normal femoral head.....	244
Figure 10.2: Diagram showing the findings of the studies at different scales using XMT and XuM.....	272

List of Tables

Table 1.1: Trabecular Bone Content (volume %) at Various Skeletal Sites (Cullinane <i>et al.</i> , 2002).....	14
Table 2.1: Morphometric parameters of human bone measured using XMT	54
Table 3.1: Patient information on the specimens obtained for the studies carried out in this thesis	70
Table 3.2: The femoral heads and associated anatomical positions of the cylinder used in the mechanical study (Chapter 7)	79
Table 5.1: Parameters used during XMT for the clinically normal head	135
Table 5.3: Summary of the regional and overall variations for bone quality measurements in the normal femoral head.....	159
Table 6.1: Parameters used to obtain the XMT data sets, where, B7 and B15 are osteoarthritic and B14 is osteoporotic	162
Table 6.2: Summary of the regional and overall variations for Bone Quality Measurements in the normal femoral head	191
Table 7.1: Morphometric and mechanical parameters of bone cylinders from major-load, partial-load and non-load bearing regions of OA femoral heads	212

List of Abbreviations

2D	Two Dimensional
3D	Three Dimensional
A	Anterior
A_f	Position of the fovea
AFM	Atomic force microscopy
Al	Aluminium
B	Required position of the fovea
BMC	Bone Mineral Concentration
BMD	Bone Mineral Density
BMU	Basic Multicellular Unit
BS	Bone surface area
BS/BV	Specific surface area
BS/TV	Total Surface
BSE	Backscattered electron microscopy
BUA	Broadband Ultrasound Attenuation
BV	Occupied bone volume
BVF	Bone Volume Fraction
CCD	Charge coupled detector
Conn.D	Connectivity Density
COPD	Chronic Obstructive Pulmonary Disease
CT	Computed Tomography
DA	Degree of Anisotropy
DXA	Dual Energy X-ray Absorptiometry
E	Elastic Modulus
FEA	Finite element analysis
<i>h</i>	Height

HAP	Hydroxyapatite
Hz	Hertz
I_0	Initial intensity of the beam
IDL	Interactive Data Language
IMS	Industrial Methylated Spirit
l	Cell length
L	Lateral
LAC	Linear Attenuation Co-efficient
M	Medial
MAC	Mass attenuation coefficient
MCFs	Microcallus Formations
MCS	Maximum Compressive Stress
MCSt	Maximum Compressive Strain
MIL	Mean Intercept Length
MRI	Magnetic Resonance Imaging
N	Specimen width (in pixels)
N/A	Not applicable
N_f	Number of Features
O	Origin
O'	New origin
OA	Osteoarthritis
OP	Osteoporosis
P	Posterior
PBS	Phosphate Buffered Saline
PMMA	Polymethylmethacrylate
Q	Centre of Fovea
qBSE	Quantitative backscattered electron microscopy
QUS	Quantitative Ultrasound

r	Radius
R	Outer radius
ROI	Region of Interest
SEM	Scanning electron microscopy
SMI	Structure Model Index
SOS	Speed of Sound
SR	Surface Rendering
<i>t</i>	Width of the rod contained within the cell
<i>t_f</i>	Wall width
Tb.Sp	Trabecular Spacing
Tb.Th	Trabecular Thickness
TDI	Time-delay Integration
<i>t_e</i>	width of the cell rods
t_t	Traverse time
TV	Tissue volume
<i>t_x</i>	Exposure time
u	Direction of Vector
vBMD	Volumetric bone mineral density
VOI	Volume of interest
VR	Volume Rendering
x	Thickness of the medium
WHO	World Health Organisation
<i>x_d</i>	Diameter of the specimen (in pixels)
XMT	X-ray Microtomography
XuM	X-ray Ultra-microscopy
YS	Yield Stress
Ys	Yield Strain
α	Angle of Rotation

β_1	Redundant connections
μ	Linear attenuation coefficient
μ_{CT}	Micro-computed Tomography
μ_m	Mass attenuation coefficient
ρ	Density
χ	Euler number

Part I Literature Survey

Pathological diseases in bone affect the elderly population in the hundreds of thousands every year globally. In the UK alone over 67 000 hip replacements were carried out between 2008 and 2009. The NHS diagnosed over 67 000 people with an average age of 68 with osteoarthritis of the hip and over 22 000 people with an average age of 73 with osteoporosis (NHS, Hesonline, 2010).

Undoubtedly with an ageing population in the UK the occurrence of these diseases is set to increase, resulting in an additional cost to the hundreds of millions of pounds already spent each year in the NHS. Although these diseases rarely result in fatalities, they result in high costs in treatment and more importantly exceptionally painful and difficult times for the elderly patient. It is therefore important to understand the compromised structure of bone in these cases to aid in an improved understanding of the diseases, ultimately leading to an improved method of diagnosis and treatment.

Current research techniques such as Scanning Electron Microscopy (SEM) (Boyde, 2003a), Atomic Force Microscopy (AFM) (Hassenkam *et al.*, 2004), Quantitative Backscattered Electron imaging (qBSE) (Loveridge *et al.*, 2004; Ferguson *et al.*, 2003), mechanical testing and histology (Fazzalari *et al.*, 1998a) have provided insight into the phenomena of bone structure, mechanics and fracture (Loveridge *et al.*, 2004). Various studies have looked at the importance of mechanical properties, bone density and architecture in the determination of bone 'quality' (Goldstein, 1987; Zysset *et al.*, 1999; Todoh *et al.*, 2004; Deligianni *et al.*, 1991) and a few have looked into micro-cracks and micro-damage (Fazzalari, 1998b) in relation to pathology.

Clinically, plain radiography has been used for decades as a tool to diagnose skeletal diseases. The main disadvantage of plain radiography is that the understanding of the image is limited to two dimensions. Furthermore, the research techniques mentioned above are not only also limited to 2D analysis but also destructive preparation. The introduction of computed tomography has

opened a new chapter in diagnostic imaging, resulting in a better understanding of the 3D structure of trabecular bone. Furthermore, a detailed insight into the phenomena of bone microdamage and failure is required to aid the understanding in development of bone pathology, hence the need for a 3D non-destructive quantitative approach.

Chapter 1 Bone

1.1 Bone Tissue

Bones are organs that consist of a series of tissue, one of which is bone. Bone differs from other connective tissues in rigidity and hardness. This hardness results from deposition within a soft organic matrix, of a complex mineral substance, composed chiefly of calcium, phosphate, carbonate and citrate. Bone serves a wide range of functions. Its structural functions include providing support for the body against gravity, acting as a rigid lever system for muscular action, and serving as a protective covering for vital internal organs such as the heart, brain and blood forming marrow. Bone also acts as a reservoir for minerals, such as calcium. In addition, bone is a self repairing structural material, able to adapt its mass, shape and properties to changes in mechanical requirements and endures voluntary physical activity for life without breaking or causing pain (Cowin, 2001).

1.2 Bone Composition

Bone consists of both organic and inorganic phases. The organic matrix, which accounts for approximately 35% of the total dry weight of bone, includes bone-specific proteins, osteoclasts, osteoblasts and osteocytes. The osteoid (which forms prior to maturation of bone tissue) includes organic components such as proteoglycans, glycoproteins and collagen elements, all of which are made and deposited by osteoblasts. The flexibility and great tensile strength of bone is in part a contribution of these organic elements, in particular collagen (Currey, 2002; Marieb, 1998).

The inorganic components, which account for approximately 65% of the total dry weight of bone consist primarily of mineral salts, or hydroxyapatites that are predominantly calcium phosphate, $\text{Ca}_{10}(\text{PO}_4)_6(\text{OH})_2$ based. Tiny calcium salt crystals lie within and around the collagen fibres and account for the most notable

characteristic of bone; it's compression resistance. It is the proper combination of organic and inorganic elements that allows bone to be extremely durable and strong without being brittle.

1.3 Organisation of Bone

Bone can be presented on a complex multi-scaled structural level. It is found to be arranged on 3 main structural levels in humans; macro-, micro- and nano-structure as seen in Figure 1.1.

1.3.1 Macro-structure of Bone

There are two types of bone structure in the mature skeleton at macro-scale; cortical (compact) bone, found largely in the shafts of the long bone, which surround the marrow cavities and trabecular bone (also known as cancellous or spongy bone), which is made up of struts and long plates called trabeculae; enclosing cavities that contain either red or fatty marrow (Currey, 2003). Trabecular bone is found in the vertebrae, in the majority of the flat bones, and in the ends of the long bones. The main difference between the structure of cortical and trabecular bone is porosity which varies within positioning of trabecular bone within a bone and is found in the range of 30 – 90% (Carter and Hayes, 1977; Gibson, 1985; Hosokawa, 2010).

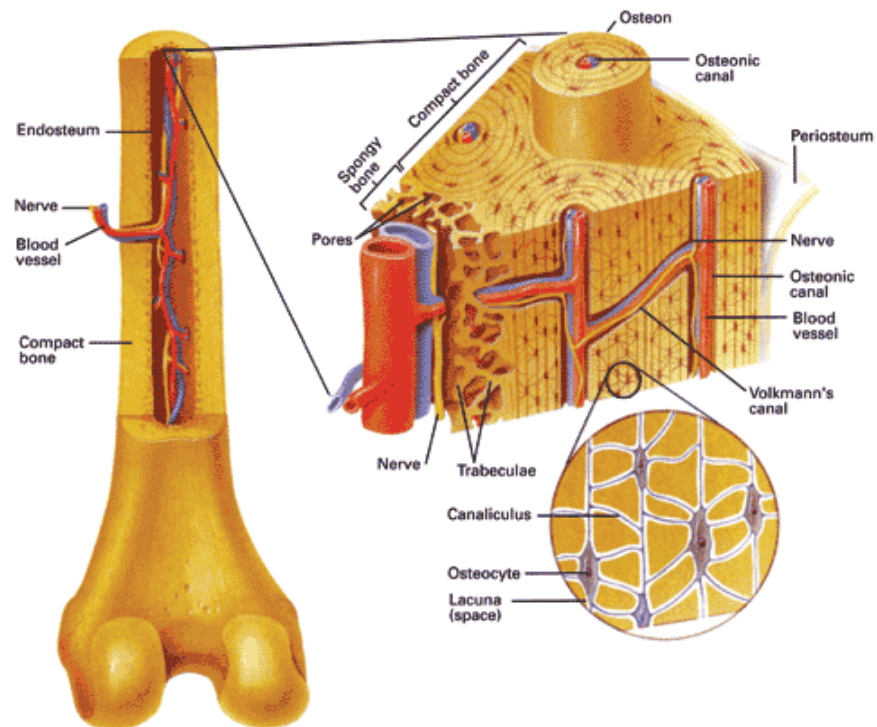


Figure 1.1: Hierarchical structure of bone (Shier *et al.*, 1996)

1.3.2 Micro-Structure

Human bone exists in two fairly distinctive forms on the micro-scale; lamellar bone, and woven or Sharpey fibre bone:

1.3.2.1 Woven (Sharpey Fibre) Bone

Woven (Sharpey fibre) bone is laid down very rapidly particularly in the foetus and in callus formations during fracture repair (more than $4\mu\text{m}$ a day) (Currey, 1984). The collagen in woven bone is fairly varied in size, the fibrils being approximately $0.1\text{-}3\mu\text{m}$ in diameter. The fibrils are also found to be randomly oriented. Various studies have shown that it is difficult to make out any preferred direction over distances greater than 1mm (Boyde, 1980; Boyde and Jones, 1998).

Woven bone is found to be highly porous at the micron level, and this has been reported as a result of mineral free space produced during mineralisation (Boyde, 1980). This study by Boyde (1980) showed that the mineralisation process involves roughly spherical centres, impregnating the collagen and ground substance at the same time, in which the crystals seem to be randomly arranged. The mineral free spaces arise as a product of the mineralisation centres spreading and joining. As in most cases of bone, woven bone contains osteocytes and blood vessels, although the space surrounding osteocytes in woven bone differs greatly from that of lamellar bone.

1.3.2.2 Primary Lamellar Bone

In human long bones, woven bone is replaced by lamellar bone at age 2 and 3 years (Cowin, 2001). Lamellar bone is more precisely arranged, and is laid down much more slowly than woven bone, less than $1\mu\text{m}$ a day (Boyde, 1980). The collagen fibrils and their associated mineral are arranged in sheets (lamellae), which often appear to alternate in thickness. Each lamella is approximately 3 to 7 μm thick and contains fine fibres that run in approximately the same direction, but whose axes can differ by as much as 90° . The final degree of mineralization of lamellar bone is less than that of woven bone. According to the work of Ascenzi *et al.*, (1978) the collagen fibrils in a particular lamella are all oriented in the same direction. However, this may not be the case as suggested by Hobdell and Boyde (1969) and Frasca *et al.*, (1977). As in many lamellae, the fibrils are in small domains about 30-100 μm across and within a domain the fibril orientation is constant, but it changes, within one lamella, from one domain to the next. The collagen fibrils in lamellar bone form branching bundles, 2-3 μm in diameter (Boyde, 1980), thicker than in most woven bone. The osteocyte lacunae in lamellar bone are oblate spheroids, the equatorial diameters being about five times longer than the polar axis. The shorter axis of each lacuna is oriented parallel to the direction of the thickness of the lamella (Currey, 1984).

1.3.3 Nano-structure

At the nano-level, bone exists in the form of three major components; a fibrous protein, typically type I collagen, embedded in calcium phosphate and water. Whereas there is only one type of mineral present, type I collagen is by no means the only protein present.

There are two hundred or more so-called non-collagenous proteins (Delmas *et al.*, 1984), but together they generally contribute to less than 10% of the total protein content, where for some proteins the structure and function is still not fully understood. Type I collagen is characterised by its fibrous nature, with the fibrils in bone generally about 80-100nm in diameter, but because they tend to merge with neighbouring fibrils, their lengths are still unknown (Boyde, 1972; Birk, 1991). Each fibril is made up of three polypeptide chains about 1000 amino acids long. These are wound together in a cylindrical triple helix, with an average diameter of about 1.5nm, and lengths of 300nm and are arranged with a 67nm periodicity (Termine, 1993) and 40nm gaps or holes between the ends of the molecule.

The full structure and morphology of bone mineral is not yet fully understood but since bone mineral contains $\text{Ca}_{10}(\text{PO}_4)_6(\text{OH})_2$, bone mineral is often referred to as impure hydroxyapatite. Ascenzi *et al.*, (1978) claimed that the mineralization process starts off with the small granules, about 4.5nm across, which coalesce or grow into needles about 40nm long. However, the observations of Landis (1995) showed that in mineralized tendon and embryonic chick bone the crystals are plate-like. The apatite crystals occur within the discrete spaces within the collagen fibrils (Gupta and Zioupos, 2008), and are on average 50nm × 25nm in length and width, with a thickness of about 2-3nm (Landis, 1995; Ziv and Weiner, 1994). Currey (1984) suggested that initially the mineral is deposited in an amorphous form, which later on transforms into an apatite form.

1.3.4 Bone Mineral

Bone mineral contributes to both the mechanical strength of bone and to the ability of the skeleton to regulate mineral ion homeostasis. The mineral in bone is an analogue of the naturally occurring mineral hydroxyapatite, whose unit cell can be represented as $(Ca_{10}(PO_4)_6(OH)_2)$. The relative ratio of calcium to phosphorus can vary markedly under different nutritional conditions, the Ca/P ratio on a weight basis varying between 1.3 and 2.0 (Guyton and Hall, 2001; Cowin, 2001).

Bone Mineral Concentration

Various techniques have been described to measure mineral concentration in calcified tissues, although not all of them use the same terms and definitions when describing mineral concentration. For example, it has been defined as volume percentage of mineral in the tissue in BSE imaging (Bloebaum *et al.*, 1990) but it is defined as mass per unit length ($g\ cm^{-1}$) in photon absorptiometry (Jonson, 1993). In this thesis, mineral concentration is defined as mass of mineral per unit volume of tissue. Assuming the mineral phase in bones and teeth to be pure hydroxyapatite, $Ca_{10}(PO_4)_6(OH)_2$, its mineral density will always be $3.15\ gcm^{-3}$ but the mineral concentration will vary according to the maturation of the tissue (Wong, 1995).

1.3.5 Bone Cells

There are 3 main types of bone cells, osteoblasts, osteoclast and osteocytes:

Osteoblasts

Osteoblasts are responsible for the formation of bone and derive from osteoprogenitor cells which are a category of mesenchymal cells, located in the inner layer of the periosteum and inside the medullary cavity. Osteoblasts synthesize and secrete unmineralised bone matrix (the osteoid), participate in the

calcification and resorption of bone, and regulate the flux of calcium and phosphate in and out of bone (Cowin, 2001).

As formation progresses, the number of osteoblasts decreases at the site and the cells become flattened. Each osteoblast has a large nucleus, many mitochondria, and a well-developed Golgi apparatus. These organelles are associated with the secretory functions of the osteoblast. Osteoblasts are always found lining a layer of bone matrix that they are producing and that is not yet calcified. Osteoblastic activity occurs continuously in all living bones; therefore, some new bone is constantly being formed. The lifespan of a team of osteoblasts at a particular site ranges from 3 months to 1.5 years. As bone formation slows, osteoblasts become incorporated into bone as osteocytes or remain on the surface as lining cells (Lian *et al.*, 1999).

Osteoclasts

Osteoclasts are responsible for destroying or resorbing (Lian *et al.*, 1999; Cowin 2001) bone by secretion of acid and proteases. They derive from precursor cells circulating in the blood and are found to be large and multinucleated. Resorption is a physiologic process that results in the loss of bone. Osteoclasts have a discoid shape with a ruffled border and are located on the surfaces of bone in shallow pits called Howship's *lacunae* in trabecular bone, or cylindrical tunnels in cortical bone. These pits are created as osteoclasts resorb bone. The ruffled border contains elements that resorb organic and inorganic components of bone. As the ruffled border adheres to the bone surface, it creates a "sealing zone" or "clear zone" under the cell. It then secretes enzymes that acidify the area under the ruffled border, decalcifying the bone, and other enzymes that digest bone (Lian *et al.*, 1999; Cowin, 2001). The process of decalcification and the breakdown of osteoid results in a saucer-shaped depression in the bone surface (Howship's *lacuna*) (Marcus, 1994; Einhorn, 1996). Resorption releases calcium from the bone to the blood and allows bone modelling and remodelling to occur.

Osteocytes

Osteocytes are the most abundant cell type in mature bone with about ten times more osteocytes than osteoblasts in normal human bone (Cowin, 2001). In general, the larger the animal, the lower the density of osteocytes (Currey, 2002). Osteocytes are responsible for the maintenance of the bone matrix. Osteocytes are osteoblasts that become entrapped in the newly formed bone matrix. Osteocytes reside in *lacunae*; spaces within either the osteoid or the bony tissue. Once osteocytes are entrapped, they lose their ability to secrete the matrix. The osteocyte also develops long fine meshwork processes, or narrow channels, that form a network of communication with adjacent osteocytes and bone surface cells, such as osteoblasts, lining cells, and osteoclasts (Lian *et al.*, 1999). The role of osteocytes is not clearly defined. However, they may play a role in the nonosteoclast-mediated release of mineral from bone tissue. The long processes enable each osteocyte to receive hormonal signals that indicate the need to transfer minerals (e.g., calcium and phosphate) from the surrounding matrix.

Unlike cortical bone in which the osteocytes are located around osteonic canals, the osteocytes are arranged within the trabeculae. These cells perform the daily cellular activities that make the bone a viable, functioning tissue. The osteocytes receive nutrients through small channels in the trabeculae called canaliculi, which extend from the bone cells to the surface of the trabeculae. In some bones, the spaces between the trabeculae are filled with red bone marrow. Because trabecular bone consists of a network of spaces, it is not as tightly packed as cortical bone. Trabecular bone is strong and resilient when subjected to the forces of compression at the ends of bones and in the areas of the joint. This degree of organization of both the trabecular and cortical bone is related to the function of the individual bone cells that control the synthesis and breakdown of bone.

1.4 Bone Physiology

Even though bone appears to be lifeless, and in most people conjures images of graveyards, bone is a very dynamic and active tissue. Large amounts of bone are continually being removed and replaced. Every year 5-10% of the existing bone mass is replaced through a process termed bone remodelling. Through the process of bone resorption and formation, bone remodelling maintains the mechanical integrity of the skeleton by replacing old bone with new. This process is closely coupled and co-ordinated by groups of osteoblasts and osteoclasts. In a young healthy adult skeleton, the total bone mass remains constant, indicating that the rates of resorption and deposition are equal.

1.4.1 Bone remodelling

Remodelling is the term used for the continual process of change in response to physiological (mechanical or metabolic) needs (Frost, 1995). Bone remodelling is continuously active in skeletal tissue through all stages of life, and is managed by teams of osteoclasts and osteoblasts organized into temporary anatomical structures called basic multicellular units (BMUs) (Robling *et al.*, 2006). Each unit is organised into a “cutting cone” of osteoclasts. The processes of bone formation by osteoblasts and bone resorption by osteoclasts produce opposite results; formation increases bone mass and resorption reduces bone mass. These processes can work in two ways. First, they can work at the same time on different surfaces; the net effect is an increase in bone. This process is called modelling and is responsible for shaping or sculpting the skeleton during growth. Second, they can work together on the same area but at different times to renew bone; the net effect is no change or a net loss. This process is called remodelling and is responsible for removing old bone and forming new bone (Einhorn, 1996). Where remodelling occurs in trabecular bone, osteoclasts and osteoblasts work together in a coordinated sequence to replace bone and usually leave the total amount of bone unaltered, in the form of secondary osteons (Haversian systems) (Currey, 2003). In trabecular bone it takes 3-6 months to complete a remodelling cycle, with about 1 month for resorption followed by 5 months for formation

(Baron, 1999). It is estimated that the remodelling cycle takes longer in cortical bone.

Resorption of bone by osteoclasts (Section 1.3.5) allows bone to alter its size and shape as it grows to adult proportions. As a group of osteoclasts form, a cutting cone advances, leaving behind a cylindrical cavity of a diameter measuring approximately 200 μ m. As soon as the cavity forms it begins to fill in. Within each of the tubular spaces cleared by the osteoclasts inside the bone, osteoblasts follow along, laying down layers of new bone to form individual concentric lamellae (Figure 1.2). Cylinders of lamellae form the mature osteon. The blood vessel runs through the osteon, and outside of the osteon between the areas of osteoclastic and osteoblastic activity there is a cement line containing bone matrix, which delineates the ones of resorption (Revell, 1998).

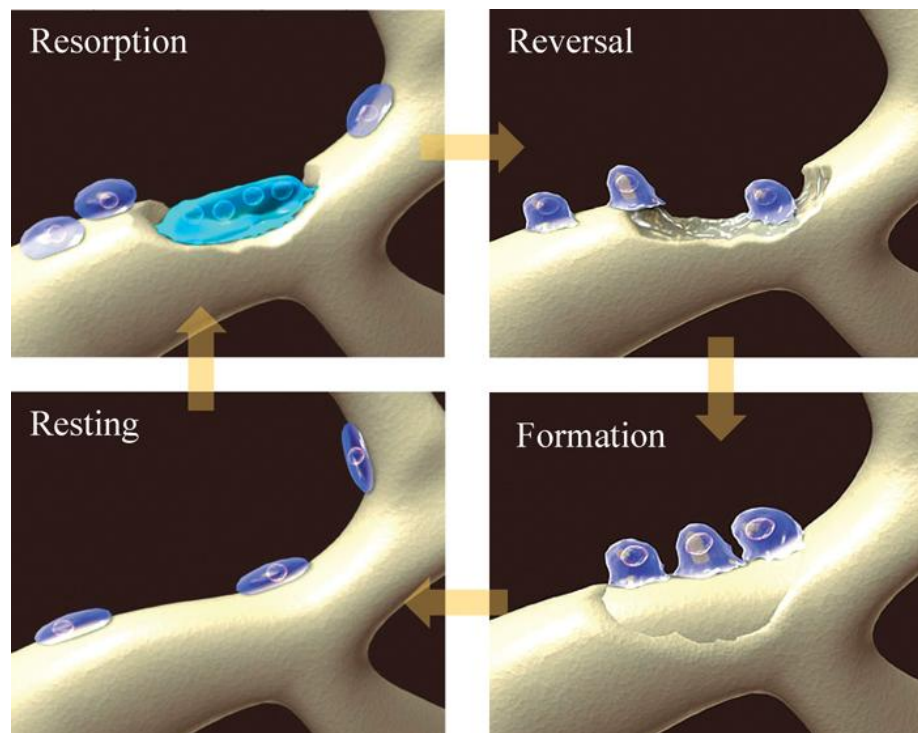


Figure 1.2: Bone remodelling. (i) Resorption: stimulated osteoblast precursors release factors that induce osteoclast differentiation and activity. Osteoclasts remove bone mineral and matrix, creating a cutting cone. (ii) Reversal: mononuclear cells prepare bone surface for new osteoblasts to begin forming bone. (iii) Formation: successive waves of osteoblasts synthesize an organic matrix to replace resorbed bone and fill the cavity with new bone (iv) Resting: bone surface is covered with flattened lining cells (Reproduced from Coxon *et al.*, 2004 with permission from Macmillan Publishers Ltd)

1.4.2 Bone Turnover

A number of stimuli affect bone turnover, including hormones, cytokines and mechanical stimuli. Mechanical loading is considered to be the main factor in stimulating bone cells as it contributes enormously towards improving bone strength and inhibits bone loss with age (Robling *et al.*, 2006). The number of remodelling units activated within a given space over a given period of time determines the rate of bone turnover. Although trabecular bone represents only 20% of skeletal mass, it represents 80% of bone turnover because of its large surface area-to-mass ratio.

This is a far greater percentage of bone turnover compared with cortical bone, which makes up 80% of skeletal mass and accounts for only 20% of total bone turnover in a given period. Any substantial decrease in the rate of remodelling may increase the risk of spontaneous fractures because the skeleton's ability to repair itself is decreased (Einhorn, 1996).

1.4.3 Trabecular Bone Architecture

Since the observations of Galileo it has been recognized that the inherent architecture of bone is not only organized to accommodate normal loading, but is also influenced during ontogeny by the mechanical stresses associated with daily function. Thus, the skeleton is both evolutionary adapted and has the capacity to adapt as a result of change in daily activity (Cullinane *et al.*, 2002). Trabecular bone is prominent near the ends of the long bones and in the vertebral bodies (Einhorn 1996). This is seen in Table 2.1, where percentage of trabecular bone found at any one skeletal site is shown. Trabecular bone has the honeycomb structure of an open network of struts and plates called *trabeculae* (Figure 1.1) which are made up of osteocytes and intercellular material.

Table 1.1: Trabecular Bone Content (volume %) at Various Skeletal Sites
(Cullinane *et al.*, 2002)

Vertebrae	66-90%
Hip (Intertrochanteric)	50%
Hip (femoral head)	25%
Distal Radius	25%
Midradius	1%
Femoral Shaft	5%

An idealized structure for trabecular bone has been presented in many studies (Beaupre and Hayes, 1985; Jensen *et al.*, 1990; Gibson and Ashby, 1997). As trabecular bone is a foam-like structure, careful consideration has to be given to the structural and mechanical properties of foam. Studies conducted by Mosekilde (1988 and 1989) have formed a basis for the conclusion reported by Jensen *et al.*, (1990) for trabecular bone to resemble a cubic lattice of thick vertebral columns with thinner horizontal struts. This has also been reported by Gibson and Ashby (1999) (Figure 1.3) as a low-density equiaxed structure (open cell). This type of cell is mainly associated with older people, approximately 40 years or older (Jensen *et al.*, 1990). In younger persons, a denser, closed-cell architecture as described by Whitehouse *et al.*, (1971) and Arnold (1980) is seen. A closed-cell architecture has been described by Gibson and Ashby (1999) as a high-density equiaxed structure (Figure 1.3).

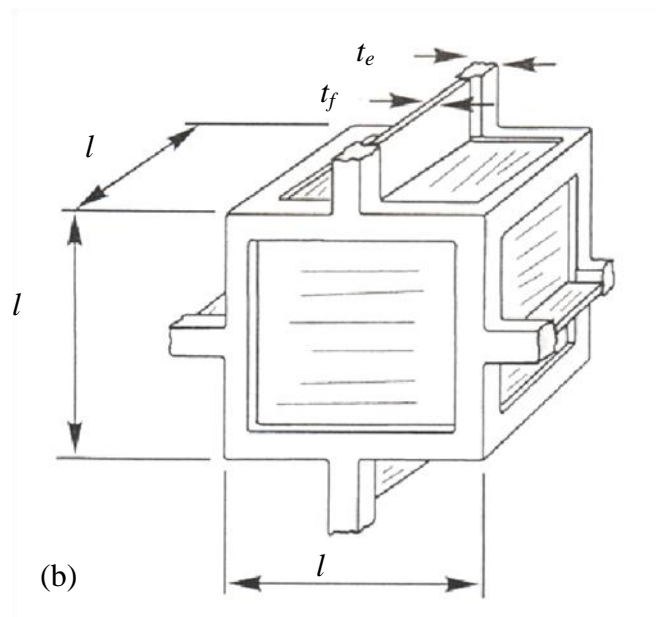
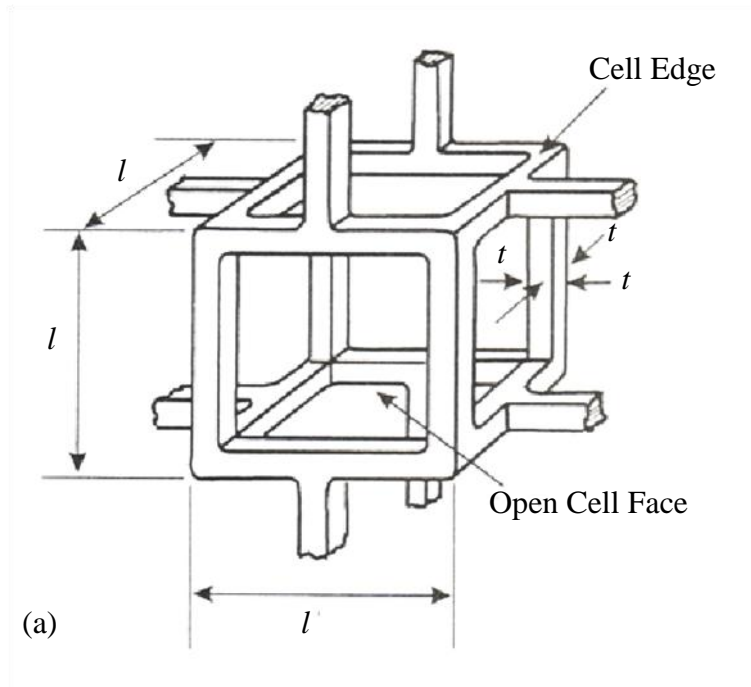


Figure 1.3: (a) Open cell. Here l is the cell length and t is the width of the rods contained within it, (b) Closed cell. Here l is the cell length, t_f is the wall width and t_e is the width of the rods (Gibson and Ashby, 1999)

1.5 Bone Quality

In the simplest sense, bone quality may be defined as a measure of how well the bone is capable of performing its functional role. Bone quality is dependent on a number of factors, including the amount of bone, the microarchitecture, mineralization of bone, organic constituents, activity of cells and the low level molecular signalling. However for the purpose of this thesis, bone quality will be thought of as depending on only the apparent parameters:

- Bone volume fraction (BVF): The amount of bone occupying a given volume
- Bone microarchitecture: The specific alignment, shape and size of trabeculae in given volume. These include Trabecular Thickness (Tb.Th), Trabecular Spacing (Tb.Sp), Connectivity Density (Conn.D), Structure Model Index (SMI) and Structural Anisotropy.
- Bone Mineral Concentration (BMC) (g cm^{-3}): The mass of mineral per unit volume of tissue

Studies have shown BVF to be a strong predictor of mechanical properties, accounting for 89-94% of the variability of ultimate stress (Pothuau *et al.*, 2002) and accounting for 92% of the variability in maximum compressive strength (McCalden *et al.*, 1997). Architectural parameters such as trabeculae thickness and separation, connectivity and spatial geometry have key roles in determining bone quality. Studies have shown bone microarchitecture related factors may explain 10-30% of the variability in bone mechanical competence, beyond that of bone mass (Cortet and Marchandise, 2001). However factors such as age (Section 1.6.5) and pathologies also have an influence on the mechanical competence of bone.

1.6 Mechanical Properties of Trabecular Bone

A formal description of the dynamic structure-function relationship between bone and mechanical load was established in the late 19th century in what has since become known as Wolff's law. Wolff determined that the trabecular elements of the skeleton were not only designed to perform their specific functions, but also responded to load by altering their structural configuration during the lifetime of an individual (Cullinane *et al.*, 2002). This section looks to examine the relationship between trabecular bone and its mechanical properties.

1.6.1 Stress-strain Behaviour

When considering the structure and mechanics of trabecular bone, it can be considered a foam (Gibson and Ashby, 1999). A typical stress-strain curve for vertebral trabecular bone is typical for that of a cellular solid (Gibson and Ashby, 1999) and has a short initial phase where the stiffness increases to a constant value that lasts until collapse of trabeculae occurs at high loads; thereafter stiffness decreases (Mosekilde *et al.*, 1987). As the specimen compresses, it yields and reaches a maximum stress (Figure 1.4). As for typical foams, in trabecular bone the small strain linear-elastic response of low-density trabecular bone derives from the elastic bending of the trabeculae (Pugh *et al.*, 1973; Stone *et al.*, 1983; Gibson, 1985, Taylor *et al.*, 1995).

Also noted to occur in foams, in compression, the load does not fall back to zero because the specimen does not fracture to pieces. Instead, its void spaces collapse and the trabeculae compact against one another. As this process continues, the load is maintained and then rises far above the previous ultimate load. The rod-like trabeculae walls, in low density bone have a higher slenderness ratio (ratio of the length of the column to the thickness) and fail by elastic buckling, both in wet and dry conditions (Hayes and Carter, 1976; Gibson and Ashby, 1999; Kim and Al-Hassani, 2001). At higher densities the slenderness ratio is lower and higher loads are required for buckling; wet specimens microcrack, whilst dry ones

fracture in a brittle manner. Progressive collapse correlates to the long, horizontal plateau of the stress-strain curve which continues until opposite *trabeculae* meet and touch, causing the stress to rise steeply (Hayes and Carter, 1976).

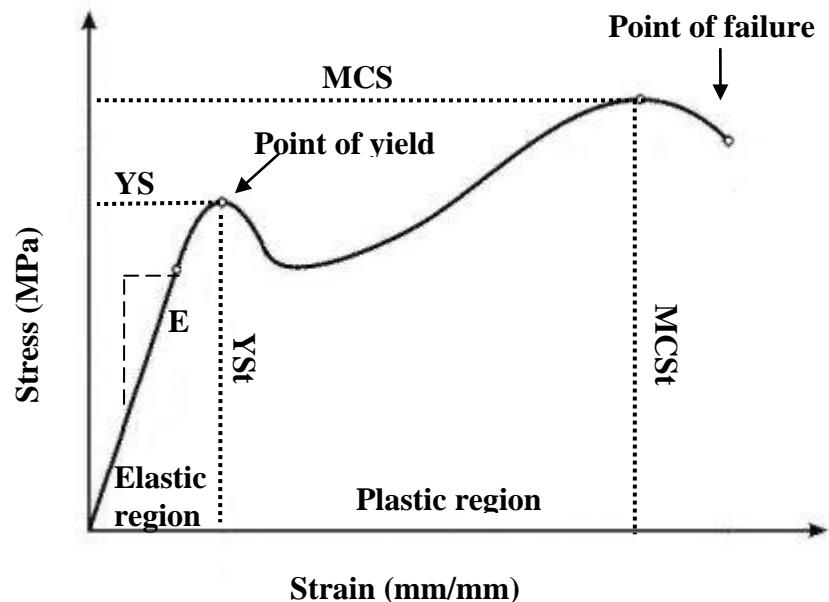


Figure 1.4: Typical stress-strain curve for the compression of trabecular bone. The stress-strain curve is divided into elastic and plastic regions, separated by the point of yield. The maximum compressive stress (MCS) represents the ultimate failure stress and the maximum compressive strain (MCSt) represents the strain at ultimate failure strain. Yield stress (YS) is the stress at point of yield, yield strain (YSt) represents the strain at point of yield and elastic modulus (E) is the maximum slope of the elastic region of the curve

1.6.2 Shear Strength

Ford and Keaveny (1996) have predicted that trabecular bone can fail in shear when subjected to compressive loads that are not aligned with the principle trabecular orientation. Thus shear may be a dominant failure mode during off-axis loading of trabecular bone *in vivo*, such as during falls on the hip. They found that shear failure strains may be independent of architecture. They showed that if changes in trabecular structure with ageing degrade shear properties more than the

compressive properties, then shear will dominate trabecular bone failure for an even larger range of axis-loading.

Therefore, efforts to understand and predict the failure of the proximal femur under traumatic loading conditions may be improved by considering the shear as well as compressive properties of the trabecular bone.

1.6.3 Compressive Strength

The maximum compressive strength (MCS) of trabecular bone is related to the square of its apparent density so that a decline in the latter due to aging or metabolic bone disease is associated with a reduction in compressive strength. Mathematically, therefore, if the apparent density of a bone were to decline by one-third, there would be a reduction in its compressive strength of the order of one-ninth (Carter and Hayes, 1977; Cullinane et al., 2002).

Trabecular bone also exhibits anisotropy. Compressive strength is greatest along the vertical axis of trabeculae in the lumbar vertebrae (Galante *et al.*, 1970; Mosekilde *et al.*, 1985) but parallel to the trabecular elements in the femoral neck (Brown and Ferguson, 1978).

1.6.4 Trabecular Bone Density

Bone density has a profound influence on determining the strength and stiffness of trabecular bone. There is extensive evidence that 75% of the values of strength and stiffness depend on the density (Carter and Hayes, 1977; Deligianni *et al.*, 1991; Goldstein *et al.*, 1993). As bone is a hydrated porous solid, there is no one single density; three different densities can be defined (Sharp *et al.*, 1990):

a) Real density: the density of the trabecular bone material. Careful measurements need to be done to take into account only the structural material.

b) Apparent density: density of the trabecular bone structure with air in the trabecular spaces and is measured using the volume of the overall physical dimensions of the specimens and the mass of the bone in the specimen.

c) Actual density; this is the density of the bone including the intra-trabecular contents and is the density of the bone as present in the body. It is defined as the hydrated tissue mass divided by the bone tissue volume.

The mass of trabecular bone and its densities have the following relationship:

$$\text{Real Density} > \text{Actual Density} > \text{Apparent Density}$$

The typical range of apparent density in trabecular bone is $1000 - 1400 \text{ kgm}^{-3}$ (Cowin, 1989). The decrease in apparent density results primarily from the presence of marrow-filled spaces, but the real density of the calcified matrix of trabecular bone itself is similar to that of compact bone (Cowin, 1989).

1.6.5 Effect of Age

Based on his combinative study Mosekilde (2000) demonstrated that age is the major determinant of vertebral bone strength, mass, and microarchitecture. There is, after the age of 50 years, a higher tendency for disconnections of the trabecular network. Kurutz *et al.*, (2005) demonstrated that during the age period between 40-90 years, the strength properties decrease by 60-70% for both sexes. Mosekilde (1998) also reported that the decline in strength for whole vertebrae during normal ageing for both men and women is 70 – 80%. This was in agreement with the study carried out by Kurutz *et al.*, (2005)

The effect of aging on MCS, have been reported in a number of studies. Mosekilde *et al.*, (1986, 1987, 1988, 1989) showed that MCS is reduced by an average of almost 7% per decade for the human proximal femur and by almost 11% per decade for vertebral bodies from ages 20 to 100 years, due mostly to decreases in BVF. In addition, because trabecular bone is anisotropic, its strength

also depends on the orientation of the specimen with respect to loads. This dependence has also been reported as changing with age (Ciarelli *et al.*, 1991; Mosekilde 1986 and 1988).

1.6.6 Principles of Hip Mechanics

Pauwels, in 1935, was the first to analyse the forces exerted on the hip and their variations. In the years since, his work has been repeated and enlarged upon many times. However, the basic principles as he outlined them still remain unaltered. The interpretation of the mechanical properties of the trabecular bone in the femoral head demands an understanding of the biomechanics of the hip joint

When a subject stands with symmetrical support on both legs, each hip carries half the weight of head, trunk and upper limbs, i.e. a load equivalent to 30% of the body weight. This exerts a vertical force upon each hip. During gait, however, each hip alternately is subject to a change in load, and a consequent increased stress. Figure 1.5 illustrates this effect. The main forces then concerned are three in number;

1. Force W; this consists of the combined effect of a partial body mass (body weight less the weight of the supporting leg), and the forces of inertia generated by acceleration of this mass. Force W acts eccentrically on the hip, with a lever arm d . Its line of action must pass through the centre of gravity.
2. Force A; this is a resultant force, being the effect of the muscular forces which counterbalance force W. Force A acts on the hip with a lever arm l , which is about a third of the length of d .
3. Force F; this force is transmitted across the joint, and is equal to the resultant of the forces W and A, but is opposite in direction. In other words, this resultant is transmitted from the pelvis to the femur and its counterforce F is transmitted from the femur to the pelvis. The line of action of force F must pass through the centre of rotation of the articular surface and through the proximal intersection point of

lines of force W and A . Assuming friction to be a negligible factor, force F will be directed at right angles to the tangent to the articular surfaces where it intersects them.

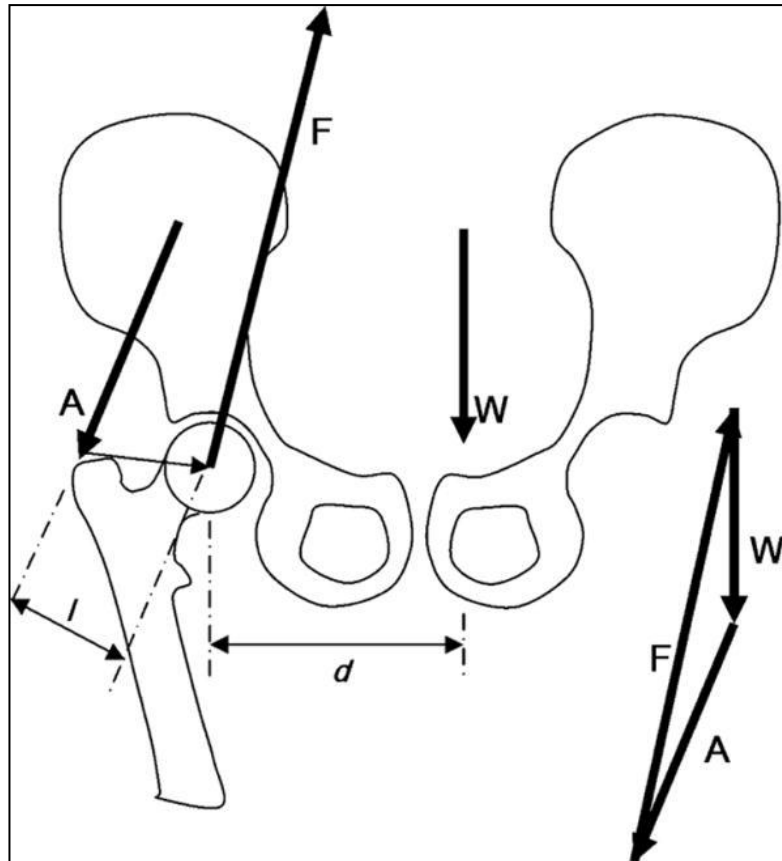


Figure 1.5: Forces acting on the hip joint during single leg stance under conditions of equilibrium. Gravitational force W , abductor muscle force, A , hip joint reaction force F , abductor muscle moment arm l , and force of gravity moment arm d (Polowski and Clohisy 2010)

1.6.6.1 Biomechanics of the normal hip joint

Load bearing areas of the femoral head have been demonstrated precisely by *in vitro* studies using miniature piezoresistive transducers embedded in the articular cartilage of 17 femoral heads (Brown and Shaw, 1983). Oscillatory joint loadings were imposed at frequencies of the order of 1Hz, which corresponds approximately to the frequency of the walking cycle, on specimens held fixed in neutral extension and 10, 20 and 30° of flexion. This demonstrated that the sites of maximal load stress most commonly underlie the general region of the cartilage of the acetabular dome and that the full contact stress pattern was most commonly a central band of pressure elevation orientated approximately antero-posteriorly. As the load was increased, the area of contact increased and ‘saturated’ well in advance of peak load, and in 92% of cases peak local stress was located within 30° of the line of action of the joint load resultant. They were unable to demonstrate the sort of preponderant load bearing at the extreme head periphery which might be expected in highly incongruent joints. The exact mechanism of load transmission across the hip joint does, however remain uncertain.

The functional topography of the femoral head and the determination of the relation of any changes of the mechanical properties with topography are of great importance, and the work of Brown and Shaw has provided the best data available for the use in the analysis of this study.

Figure 1.6 outlines the load bearing regions in the femoral head based on the work of Brown and Shaw (1983). It can be seen that the major load bearing is related to the region where load falls directly onto it from the body weight of the person. The region in the anterior view is highlighted major-load demonstrating the region where every day walking contributes that to the way in which the load is applied to the femoral head. Only two thirds of the femoral head is highlighted in relation to the loading regions as this is the area of the head this study associates with most.

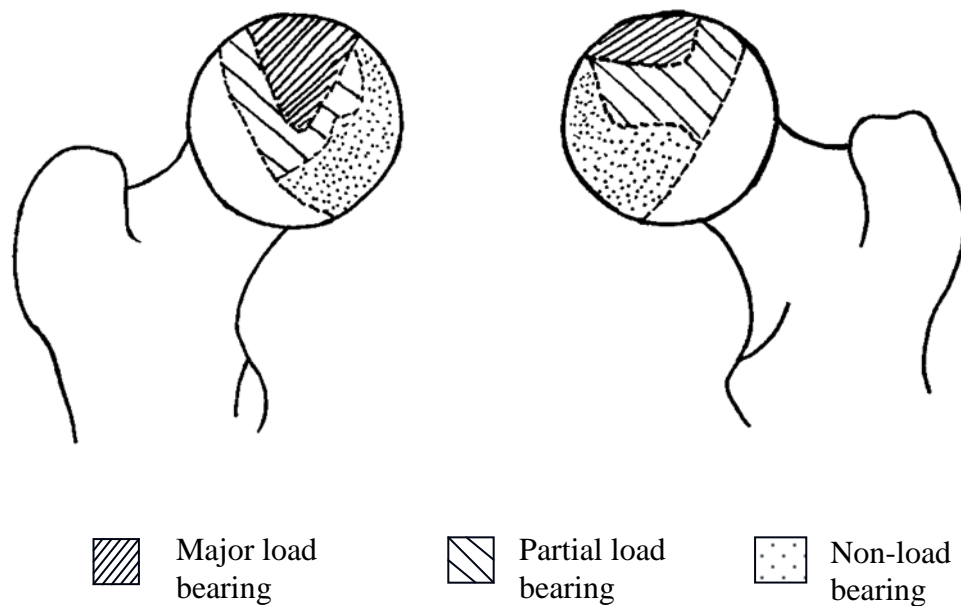


Figure 1.6: Load-bearing regions of a left femoral head (adapted from Brown and Shaw, 1983; Sharp, 1988)

1.7 Bone Fracture and Repair Mechanisms

Daily activities subject both cortical and trabecular bone to cyclic loading. The applied loading interacts with the microarchitecture at multiple length scales (Vashishth, 2007) and forms *in vivo* microdamage in the form of linear microcracks (Schaffler *et al.*, 1995; Wenzel *et al.*, 1996; Norman and Wang, 1997; Fazzalari *et al.*, 1998b) and diffuse damage (Fazzalari *et al.*, 1998a; Fazzalari *et al.*, 1998b; Vashishth *et al.*, 2000a; Diab and Vashishth 2007). The propensity of bone to form linear microcracks and diffuse damage varies with age (Diab *et al.*, 2006) and the two forms of microdamage have different effects on the mechanical properties of bone (Burr *et al.*, 1998; Diab and Vashishth, 2005). One of the bodies' natural repair mechanisms to remove microdamage is bone remodelling (Burr *et al.*, 1985; Bentolila *et al.*, 1998) but recent studies have shown that the efficacy of damage-initiated remodelling decreases with age

(Waldorff *et al.*, 2007). Consequently, with increased age, microdamage may accumulate and may contribute to the increase in age-related fracture risk.

1.7.1 Microdamage

In order to understand the behaviour of bone fracture, it is important to study the fracture mechanics at all levels of the hierarchical structure. More recent developments in research techniques have allowed for investigations into the fracture mechanics of bone at the micro- and sub-micron level (Peterlik *et al.*, 2005; Gupta and Zioupos 2008). Micro damage related to *in vitro* loading can be related to physiological loadings such as tension or compression. Diab *et al.*, (2006) showed that under compressive loading short linear microcracks (100-200 μm) were produced associated strongly with the lamellar orientation of bone. Microdamage resulting from torsional loading produced predominantly time dependant damage in the form of long microcracks (>300 μm) with no or little diffuse damage formation (Caler and Carter, 1989; George and Vashishth, 2005).

1.7.2 Detection of microcracks

Microcracks found in trabecular bone are often detected with traditional histological methods (Boyde, 2003b). Zioupos *et al.*, (1994) confirmed acoustic-emission as a method of microcrack detection and Raman spectroscopic markers for fatigue-induced microdamage have recently been identified (Timlin *et al.*, 2000). By far the most popular method of microcrack detection has been transmitted light microscopy using the common method of *en bloc* staining with 1% basic fuchsin, originally developed by Frost (1960) and modified by Burr and Hooser (1995). However, traditional histological techniques limit understanding of microdamage to 2-dimensions. Very little work has been done to assess microdamage using 3-dimensional techniques such as X-ray Microtomography (XMT) and X-ray Ultra-microscopy (XuM). Where attempts have been made,

there have been limitations, presented by the ability of the scanner, to resolve crack openings (typically in the order of 1 μ m) (Wang *et al.*, 2007).

1.7.3 Microcallus Formations

1.7.3.1 The role of Microcallus Formations

Microcallus formations (MCFs) are small patches of woven bone often found surrounding trabeculae. They are found in people with osteoarthritis, rheumatoid arthritis (Todd *et al.*, 1972) and osteoporosis (Cheng *et al.* 1997), hence relating them to fracture healing. In all cases the ‘quality’ of the bone is jeopardised and several processes are initiated to try and correct for this. It is a general consensus that microcallus formations appear where there are fractures in the trabecular structure (Todd *et al.* 1972; Vernon-Roberts and Pirie, 1973). Whether or not they act as a transient brace, preventing relative movement of the fractured segment and enabling the trabecula to heal, or whether a permanent buttress reducing the stress on the fractured strut, so preventing the healing process, is not known (Fazzalari, 1993).

1.7.3.2 Prevalence of Microcallus

Cheng *et al.*, (1997) carried out a study to investigate the prevalence of microcallus formations in two different regions, the vertebra and femoral neck. They showed that a larger number of microcallus formations were present in the vertebral slices (Hahn *et al.*, 1995; Cheng *et al.*, 1997) than the femoral slices and that the number increased with age, especially with subjects over 60 years old. They concluded that the occurrence of microcallus formations is strongly related to the anatomical site, probably due to the differences in the applied loads and the trabecular structure between sites.

1.7.3.4 Morphology of Microcallus Formations

Vernon-Roberts and Pirie (1973) described four morphological types of microcallus formations; a) rounded nodular, b) fusiform, c) angulated and d) arched bridges, as shown in Figure 1.7 They found the presence of angulated and arched bridges less apparent, and found the rounded nodular type more commonly present.

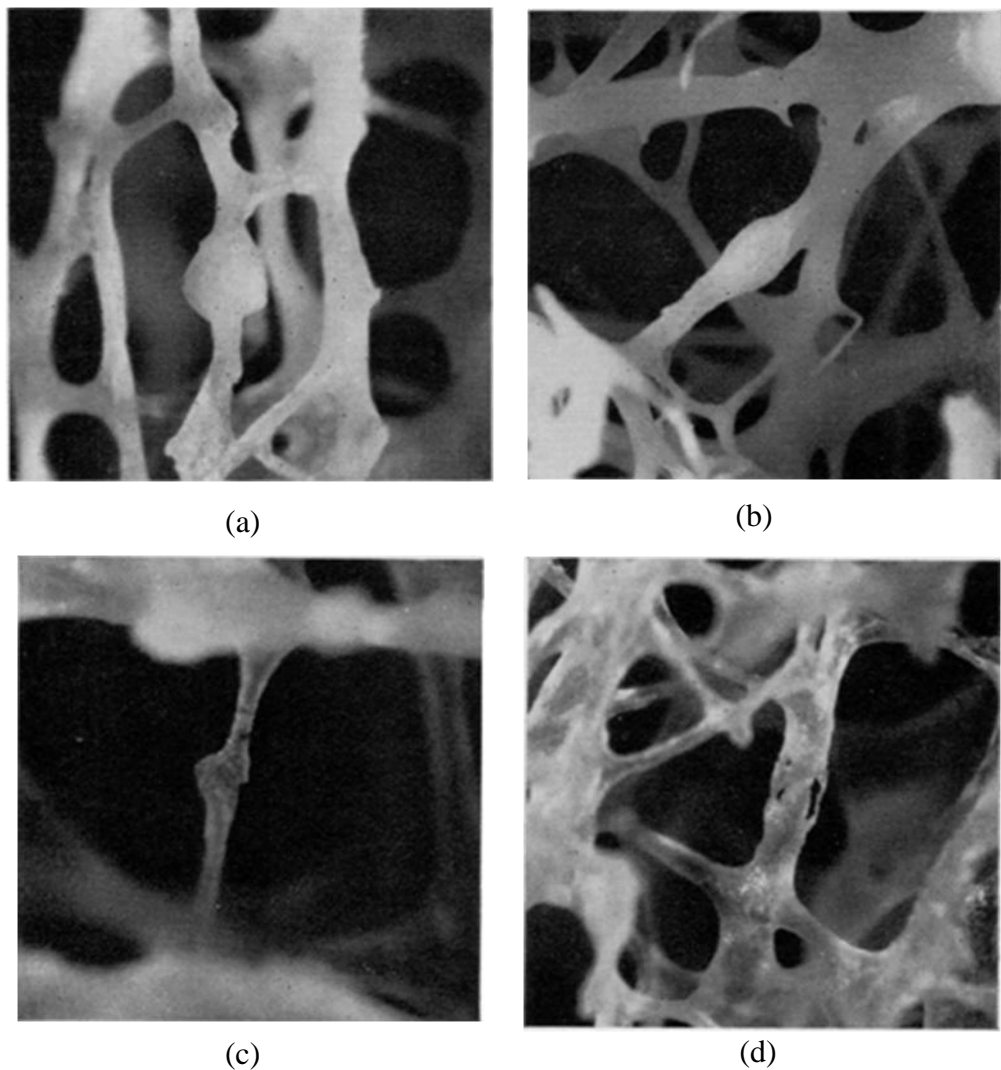


Figure 1.7: Four morphological types of MCFs; a) rounded nodular, b) fusiform, c) angulated and d) arched bridges, magnification (Reproduced from Vernon-Roberts and Pirie, 1973 with permission from BMJ Publishing Group Ltd)

Further developments in 2D imaging analysis have led studies in producing more detailed images of MCFs (Boyde and Jones, 1996; Boyde, 2003b) successfully showing the morphology of a nodular MCF using a combination of a backscattered, forward scattering and transmitted primary fast electron image (Figure 1.8).



Figure 1.8: Lumbar vertebral body trabecular bone, 89-year-old female, showing microcallus repair of trabecular micro- fractures. Field width, 850 μm . Combined backscattered, forward scattered and transmitted primary fast electron image, 20 kV (Boyde and Jones 1996, Boyde 2003b). The arrows denote two beaks either side of the microcallus repair zone.

1.8 Bone Pathology

1.8.1 Osteoarthritis

1.8.1.1 Definitions and terminology

Osteoarthritis (OA) is a ubiquitous, slowly developing non-inflammatory disorder affecting synovial joints (which occurs in response to a variety of insults, both mechanical and biological) and is characterised by deterioration of articular cartilage and formation of new bone at the joint edges (Sokoloff, 1969; Hart and Spector, 1995; Schiphof *et al.*, 2008). It characteristically presents with pain,

stiffness and deformity of the involved joints, but the disparity between pain and pathological change has long been recognised; thus symptomatology is not a precise reflection of either the onset or severity of the disease process (Kellgren, 1983).

The Greek term frequently used for the acute arthritis was one which in literal translation means “the disease which interferes with walking”. There have been many synonyms for such degenerative joint disease including *malum coxae senilis* (literally hip disease in the elderly), *arthritis deformans*, chondromalacic arthrosis, hypertrophic arthritis, degenerative arthritis, osteoarthritis and osteoarthrosis. There are several types of arthritis, such as juvenile chronic arthritis and gouty arthritis that may have a variable appearance compared with that of other common inflammatory arthritis (Jacobson *et al*, 2008). The term coxarthrosis refers to osteoarthritis of the hip joint.

1.8.1.2 The Pathology of OA

A brief description of the pathology of osteoarthritis is included here as this will be of importance in the interpretation of the mechanical findings of this study and for correlation with the imaging data. Once changes have begun in the hip due to this degenerative disease, no matter from what primary cause, they progress to the characteristic bone changes of osteoarthritis, with deformation and eburnation of the bone surface, bony sclerosis, cyst formation, hypervascularity, remodelling and osteophyte formation, and bone death (Collins, 1949; Woods, 1972; Dieppe *et al.*, 1998; Hart and Spector, 2003).

1.8.1.3 Cysts

As the subchondral bone becomes exposed, two alterations are observed within the underlying bone marrow spaces: chondrous tuft formation and the development of cysts (Milgram, 1983; Crema *et al.*, 2010). The presence of

multiple cysts is a common finding in human joints, occurring at an advanced stage of bone necrosis and varying in size from 1mm to 2.5cm , although cysts over 1cm are only found in the femoral head, and are found further away from the subchondral bone (Landells, 1953). An explanation for cysts is described by Ondrouch (1963) in a study simulating the mechanical loads of uneven eburnated bone using polarised light which produced spherical stress patterns, and so the cysts may be due to impaction of the eburnated surface (Rhaney and Lamb, 1955). These match the contours and relative size of bone cysts, suggesting that bone “disintegrates” along the lines of highest stress. A finite element study by Hans *et al.*, (2004) showed that stress-induced bone resorption may cause development of subchondral bone cysts in osteoarthritis. More recently, studies using Magnetic Resonance Imaging (MRI) have investigated the detection of cysts. Zanetti (2000) and Pouders *et al.*, (2008) successfully demonstrated that MRI was able to detect small subchondral cysts in comparison to conventional X-rays, demonstrating well-defined rounded areas of fluid-like signal intensity.

1.8.1.4 Osteophytes

As the disease progresses, reparative responses are also occurring. With the cartilage and subchondral bone changes, the contours of the joint become flattened on the weight bearing areas. New bone is produced in various locations along the joint surface in an attempt to restore joint shape, particularly at the margins of the joint to form osteophytes (Sengupta *et al.*, 2006).

There are four types of osteophyte formation (Ferguson, 1971):

1. Reduplications where the subchondral plate is broken by the passage of the vessels from the medullary bone spaces into the hyaline cartilage. This results in the enlargement of the head, and occurs only in the medial inferior portion of the femoral head and only in OA.
2. The marginal osteophyte, which forms at the junction of cartilage and the femoral neck (Cicutini *et al.*, 1996). The highly vascular transitional

connective tissue which links the cartilage with the synovial tissue in the normal subject is potentially reactive, and the abnormal mechanical stresses in a degenerative joint, stimulates its ossification. Such marginal extoses are characteristic of the normal ageing joint, their growth to form osteophytes being accelerated in osteoarthritis (Danielsson, 1964; Hernborg and Nilsson, 1973).

3. and 4. Hypertrophic and traction osteophytes.

Because of the hard nature of the eburnated bone, erosion is halted in most joints at this stage, but remodelling continues and may result in a very deformed femoral head. (Bullough, 1984)

1.8.1.5 Subchondral bone Plate

The subchondral bone plate supports the articular cartilage in diarthrodial joints. It has a significant mechanical function in transmitting loads from the cartilage into the underlying trabecular bone. Since OA is known as a disease to affect the joint tissue, the underlying bone structure is affected in the absence of the articular cartilage in femoral heads. Sclerosis is a well recognised feature of OA and studies carried out previously have shown the differences between normal and OA subchondral bone. Li *et al.*, (1999) examined sections of subchondral taken from normal and OA femoral head using scanning electron microscopy. They found that the OA subchondral bone appeared more compact, and showed a reduced stiffness, lower density and mineral content in comparison to normal subchondral bone.

1.8.2 Osteoporosis

1.8.2.1 Definitions and terminology

Osteoporosis (OP) refers to a systemic disease where an imbalance of bone remodelling occurs. The composition of the bone matrix, bone mass and architecture are compromised, making the bone lighter and more porous (Marieb, 1998; Jee, 2001; WHO 2003)

The World Health Organisation (WHO) defines OP as a disease that is characterised by a reduction of bone mass and a deterioration of the architecture of the bone, leading to increased bone fragility (WHO, 2003). The WHO have stated that the lifetime risk for hip, vertebral and wrist fractures, resulting from osteoporosis has been estimated at 40%, similar to coronary heart disease, and is three times more likely in women than men. The WHO has developed criteria for diagnosis of osteoporosis, which are used daily worldwide. These criteria are based on comparing bone mineral density (BMD) in a particular patient with those of a referent “normal” population. Values which fall well below the average for the normal (stated statistically as 2.5 standard deviations below the average), are diagnosed as osteoporotic, values less than the normal, but not 2.5 standard deviations below the average are classified as osteopenic (meaning a decreased bone mineral density) (WHO, 2003).

1.9 Clinical Diagnostic Techniques

1.9.1 Radiographs

Often late stage OP and OA can be diagnosed from a 2D radiograph, which, is the most commonly assessable and cheapest imaging modality in the world. Radiographically detected change in apparent bone density, abnormalities in trabecular architecture, cortical width and visible evidence of fracture are all accessible through macroscopic visual inspection of 2D radiographs. More

detailed quantitative assessment of trabecular architecture has also been attempted.

One of the first radiographic techniques was developed by Singh *et al.*, (1970). In this technique, subjective ratings of the appearance of the trabecular patterns were made on the radiographs of the proximal femur. Rockoff (1967a and b) and Rockoff *et al.*, (1971) also pioneered work utilising the information contained in radiographic images for assessing trabecular bone architecture. In more recent years more quantitative techniques have been developed, which are based on textural and fractal analyses of the radiographic trabecular pattern. Geraets *et al.*, (1990, 1991, 1993, 1997, 1998) developed techniques to measure information about the trabecular pattern from binarised radiographs. Luo *et al.*, (1999) were able to demonstrate a clear relationship between 2D projections of trabecular bone and 3D structure. Caldwell *et al.*, (1995) showed that the addition of structural information, measured from 2D radiographs, to that of bone mass was more superior in explaining the variability in mechanical strength than mass alone. Chappard *et al.*, (2005a, 2005b) were able to show textural indices obtained from radiographs correlated with histomorphometric parameters and also demonstrated that a radiographic measure of anisotropy was able to distinguish individuals with vertebral fractures from controls. The use of fractal dimension, Moire pattern and textural anisotropy to characterise trabecular bone microarchitecture have also been investigated by others (Caligiuri *et al.*, 1993; Benhamou *et al.*, 1994; Buckland-Wright *et al.*, 1994; Kaufman 2001).

The classification for OA described by Kellgren and Lawrence (1957) is the most widely used radiological classification to identify and grade OA. Kellgren and Lawrence (1957) defined OA in five grades (0, normal to 4, severe). The radiological signs found to be evidence for OA were combined to define a grading scale for severity. For the femoral head, important changes are: (a) formation of osteophytes on the joint margins, (b) narrowing of the joint space associated with sclerosis of subchondral bone, (c) cystic areas with sclerotic walls situated in the subchondral bone and (d) altered shape of the femoral head itself.

1.9.2 DXA

Dual Energy X-ray absorptiometry (DXA) is considered the gold standard in bone assessment. The dual energy component refers to the dual energy X-ray spectra, obtained either by filtering or dual excitation. In single energy absorptiometry techniques, differences in attenuation due to varying soft tissue thickness cannot be distinguished from bone density differences. As such, single energy absorptiometry techniques commonly require soft tissue equivalent material to be present in order to eliminate soft tissue artefacts. DXA overcomes this problem mathematically subtracting the soft tissue attenuation from the measure attenuation (Faulkner and Pocock, 2001; Kaufman and Siffert, 2001).

DXA is a projection based technique that estimates the amount of bone present in a region using X-ray attenuation information. However measured BMD is an areal density (expressed as g cm^{-2}) and not a true volumetric density (expressed as g cm^{-3}). This makes DXA and BMD measures prone to bone size artefacts. As such, BMD measures from men are observed to be higher than those of women, based purely on skeletal size differences (Faulkner *et al.*, 1991; Faulkner and Pocock, 2001). This same problem creates complications in BMD measurements of young children. Even though the measurement of BMD is a useful clinical tool in predicting fracture risk (WHO 2003), there are significant degrees of discrepancies in BMD measurements of patients who have been diagnosed as high risk and high risk patients who actually fracture (Kanis *et al.*, 2001; Kanis, 2002). BMD explains between 30 – 80% of the variability in bone mechanical competence (Cortet and Marchandise, 2001) and it is this large variability that requires consideration and the development of other techniques and measures. However, despite these shortcomings, DXA is the current gold standard in the assessment of fracture risk prediction and is the clinical assessment tool recognised by the WHO.

1.9.3 Quantitative Ultrasound

Clinical quantitative ultrasound (QUS) utilises the transmission of high frequency sound and the resulting attenuation of that sound through bone, in order to assess the bone material properties (Faulkner and Pocock, 2001; Kanis, 2002; Kaufman, 2001; WHO, 2003). Unlike the electromagnetic wave interrogation of X-ray based techniques, QUS utilizes mechanical vibration. This mechanical interaction of high frequency sound with bone results in two primary measures; the speed of sound (SOS) and the broadband ultrasound attenuation (BUA) (Faulkner and Pocock, 2001; Kanis, 2002). Even though utilizing a completely different mechanism of interaction with the bone, QUS measurements correlate reasonably well with X-ray based DXA BMD measurements (Kanis, 2002). Evidence has also been shown to support their use for assessment of fracture risk (Gregg *et al.*, 1997).

1.9.4 CT Imaging

Quantitative computed tomography (CT) is the only *in vivo* technology capable of true volumetric density measurement (Faulkner and Pocock, 2001; Kanis, 2002). Clinically, quantitative CT is used to measure bone density (g cm^{-3}) in the spine. The standard involves scanning a single 8 to 10mm slice through 3 to 4 vertebral bodies. The scan is always accompanied by a scan of a calibration standard. From the reconstructed CT images, the average attenuation of the vertebral body bone is calculated along with the attenuation of the calibration standard. Then via a transformation of the known attenuation to density of the standard, the volumetric density of the vertebral body and its sub-compartments can be estimated (Faulkner and Pocock, 2001; Kanis, 2002; Kaufman 2001; WHO, 2003). Although quantitative CT does provide information on the shape and architecture of bone, current resolution of clinical CT systems are not capable of resolving the trabecular bone (Faulkner and Pocock, 2001; Kaufman, 2001; WHO, 2003). Other disadvantages include relatively high radiation exposure and costs (WHO, 2003).

Micro-computed tomography (μ CT) systems operate in a similar manner to clinical CT, but are capable of resolutions down to $1\mu\text{m}$ (Kaufman, 2001). The trade-off for achieving such resolutions is that the specimen must be small in size. *In-vivo* imaging at these resolutions is not available for human trabecular bone due to the high dose required. However, the μ CT modality can be utilized as a tool for extracting relevant information from human bone samples at resolutions suitable for trabecular bone assessment (Ruegsegger *et al.*, 1996). This modality can be used as a gold standard in the non-destructive assessment of trabecular bone *ex-vivo* or *in vitro*.

Chapter 2 X-ray Microscopy

2.1 Introduction

Like many important scientific breakthroughs, the discovery of X-rays was accidental. A physicist by the name of Roentgen in 1895, discovered X-rays during a study of cathode rays, and since then they have played a fundamental role in our lives. X-rays are used extensively throughout research encompassed in several techniques: X-ray spectroscopy, X-ray diffraction, computed tomography and micro-radiography to name a few. Their non-destructive nature, in techniques such as computed tomography appeals to the medical and research sectors, and they are now used widely in diagnostic radiology in medicine and dentistry. They also provide an essential role in other industries such as automotive, aeronautic and forensic science.

2.1.1 EM Spectrum

X-rays are electromagnetic radiation, and like light, form part of the electromagnetic spectrum. They can be classed as high frequency electromagnetic rays with a wavelength around 10^{-10} m and frequencies of 3×10^{16} Hz upwards (Figure 2.1).

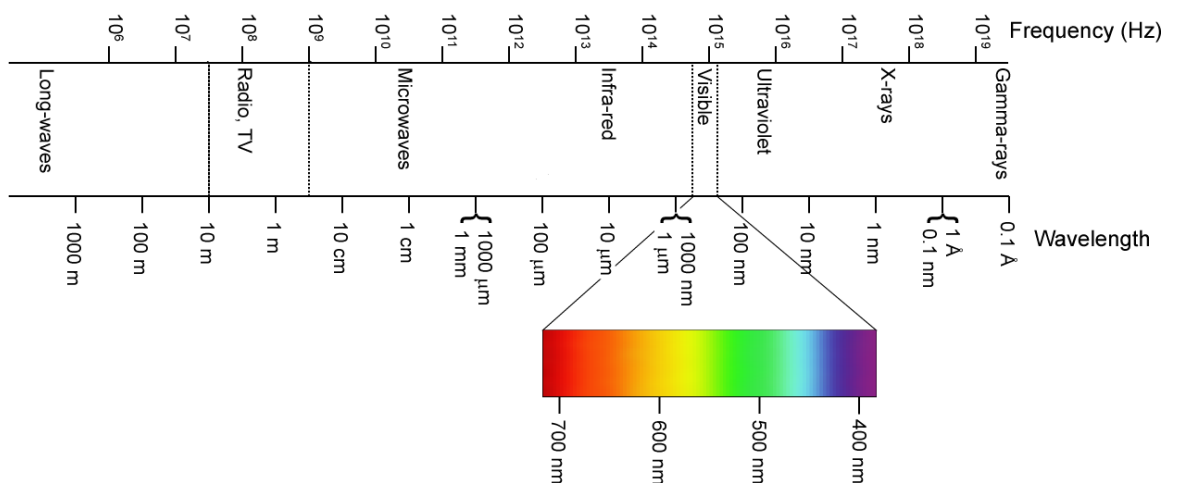


Figure 2.1: The Electromagnetic Spectrum (Adapted from Seibert 2004)

2.2 X-ray production

X-rays are generated when high energy electrons strike a metal target. The kinetic energy of the electron is transformed into electromagnetic energy, and two kinds of X-rays are generated during this process;

- (i) Brehmsstrahlung
- (ii) Characteristic

2.2.1 Bremsstrahlung radiation

Bremsstrahlung radiation also known as “braking radiation” is produced due to electron deceleration. Accelerated charges give off electromagnetic radiation, and when the energy of the bombarding electrons is high enough, that radiation is in the X-ray region of the electromagnetic spectrum. It is characterized by a continuous distribution of radiation called continuous (Bremsstrahlung) X-ray spectrum (Figure 2.2) which becomes more intense and shifts toward higher frequencies when the energy of the bombarding electrons is increased.

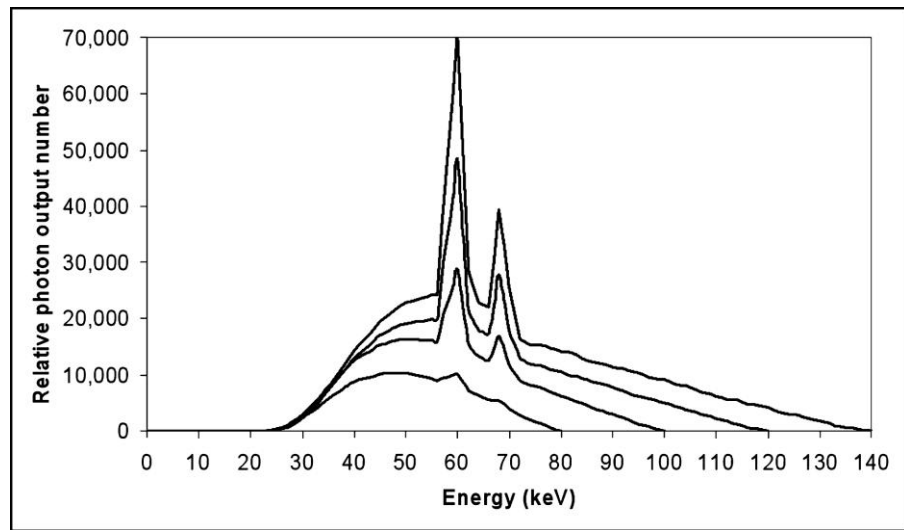


Figure 2.2: Bremsstrahlung and characteristic radiation spectra are shown for a tungsten anode with X-ray tube operation at 80, 100, 120, and 140 kV and equal tube currents (Seibert, 2004)

2.2.2 Characteristic (k-shell) X-rays

These type of X-rays are produced by transitions of orbital electrons from outer to inner shells. This type of X-radiation is called characteristic radiation because it has precisely fixed, or discrete, energies and that these energies are characteristic of the differences between electron binding energies of a particular element. Bombarding electrons can release electrons from inner energy level orbits. Higher electrons can then fall into the vacancy and if the energy gap between the levels is great enough X-rays will be produced (Figure 2.3). Since the electron binding energy for every element is different, the characteristic X-rays produced in the various elements are also different.

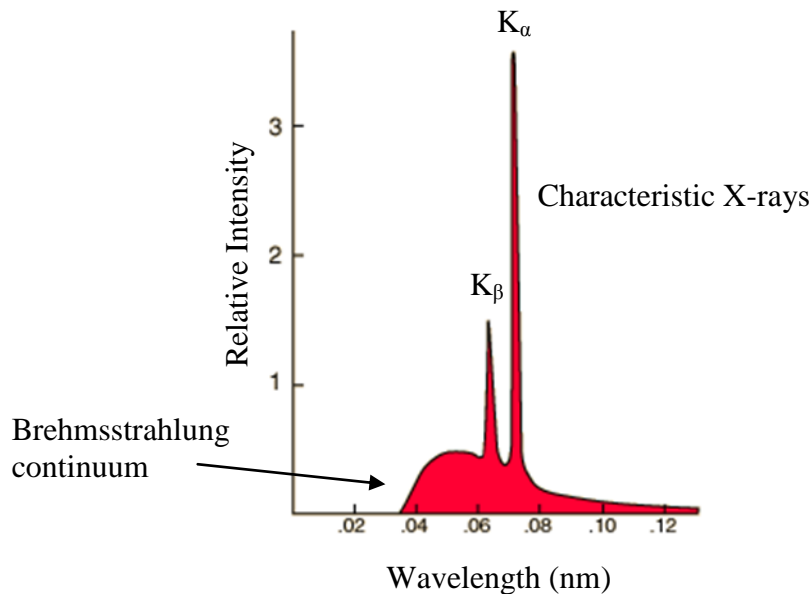


Figure 2.3: X-rays from a molybdenum target at 35 kV. The two sharp peaks in the graph are characteristic X-rays which occur when vacancies are produced in K-shell of the atom and electrons drop down from above to fill the gap. The X-rays produced by transitions from L to K levels are called K-alpha X-rays, and those from M to K transition are called K-beta X-rays. Transitions to the L-shell are designated as L X-rays. The graph also shows the "bremsstrahlung" radiation which forms the base for the two sharp peaks (Adapted from Sprawls 1995)

2.2.3 Impact sources

The source of X-rays is often achieved by using an X-ray tube. The main components of a typical set-up consist of (1) a source of electrons - a filament (2) a vacuum, (3) a high positive potential to accelerate the negative electrons and (4) a target or anode, which the electrons strike (Figure 2.4).

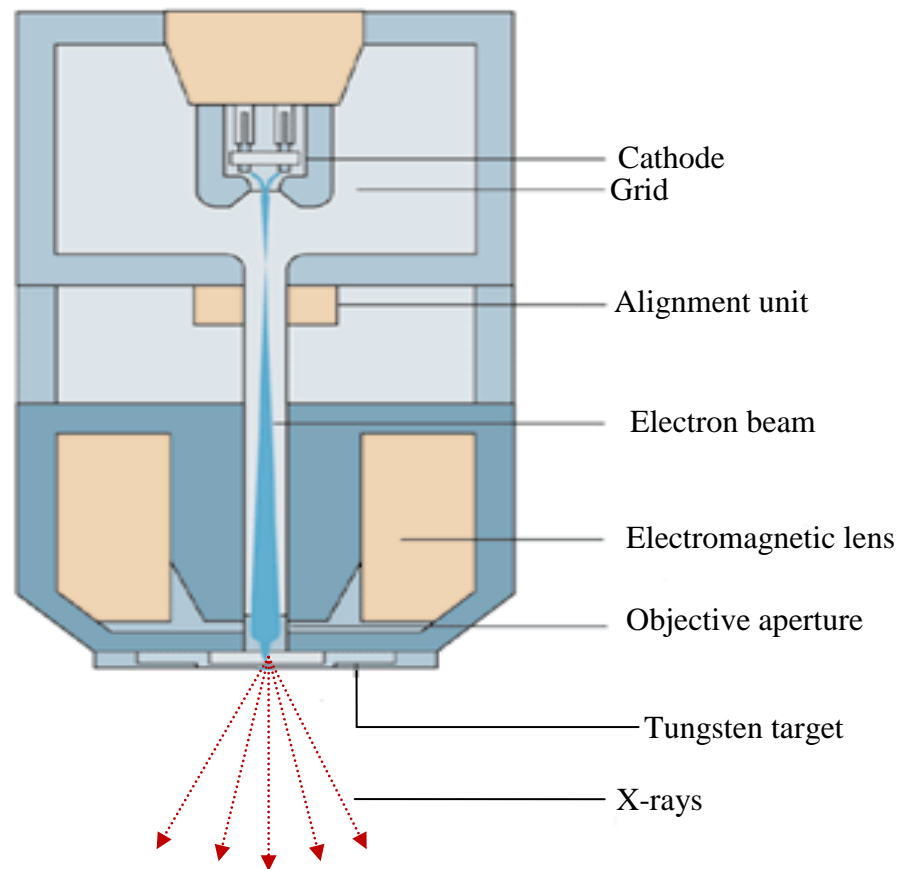


Figure 2.4: Basic components of a micro-focus X-ray unit

In a modern micro focus X-ray tube the number of electrons accelerated toward the anode depends on the temperature of the filament, and the maximum energy of the X-ray photons produced is determined by the accelerating voltage. A microfocus X-ray tube that generates X-rays with a micrometer-sized focal spot is a key device for high resolution X-ray microtomography because X-rays with smaller focal spot size yield finer X-ray images with higher magnification factor (Davis and Wong 1996, Heo *et al.*, 2007).

In a micro-focus X-ray tube, a tungsten filament is heated up (current) until releasing electrons. Due to a difference in potential between filament (cathode) and anode, the electrons travel from cathode to anode, where they strike at the order of one third of the speed of light, dependent on the kV. The filament current is controlled by means of the Wehnelt grid, which is held at a negative potential (voltage).

The beam passes through a hole in the anode and is then directed through an electromagnetic lens by a series of deflecting magnets where it is then collimated and focussed onto the target. The diameter of the focal spot dictates the size of the X-ray source and is only a few microns in size. The target requires a high atomic number (Z) to produce X-rays efficiently. Nearly all X-ray tubes use tungsten targets, as the Z of tungsten is 74 and its melting point is approximately 3400°C (Cameron and Skofronick, 1978). A high melting point is required as heat is produced when the electrons are stopped at the target surface. In most laboratory set-ups a cooling system is also used. In case of transmission targets, the X-ray source is located very close to the outer wall of the microfocuss X-ray tube allowing the user to bring samples very close to the source ensuring highest magnifications.

2.3 Synchrotron Radiation

When relativistic electrons experience centripetal acceleration due to the presence of a magnetic field, they emit electromagnetic waves that are commonly called ‘synchrotron’ radiation (Burattini, 1996). Since the effect occurs under the influence of a magnetic field, it keeps the electrons in a circular trajectory, and is also known as *magnetic brehmsstrahlung* (Podgorsak, 2005). Radiation produced in this manner is intense and virtually parallel, allowing the use of monochromators, resulting in a monochromatic X-ray beam, thus, enabling absolute linear attenuation coefficients to be measured (Davis and Wong, 1996). Due to this ability to provide accurate Linear Attenuation Co-efficient (LAC) measurements at high resolutions, synchrotron radiation is favoured, but difficulty of access and expense limits its use for extensive research.

2.4 X-ray interactions with matter

Attenuation at energies used in the laboratory is due primarily to two processes, absorption and scattering, and is affected by the energy of the X-rays, the density of the attenuating material and the atomic number of the material. In both processes, the X-ray photon interacts with the atoms of the material. In scattering, the X-ray photon continues with a change in direction with or without a loss in energy. In absorption, the energy of the X-ray photon is transferred to the atoms of the material.

2.4.1 Attenuation mechanisms

Photoelectric absorption

A photon can be absorbed by transferring all of its energy to an inner orbital electron in an atom. The electron is ejected from the atom and the photon disappears due to the loss of all its energy. The atom is now left with a vacant inner electron orbit, which it will fill with one of the outer electrons. This results in a small amount of energy in the form of a characteristic photon.

Rayleigh (Simple) Scattering

During simple scatter the incident photon energy is much less than the energy required to remove an electron from its atom (the binding energy). The photon is simply deflected without change of energy (elastic scattering).

Compton Scattering

The Compton effect is named after an American physicist who, in 1922, showed how photons can be scattered by outer or free electrons in an absorber. Here, the incoming photon has a greater energy than the binding energy of the electron in the atom. An interaction with the outer electrons which are not tightly bound to an atom is known as the Compton Effect. This results in the photon giving some of

its energy to the electron and hence changing direction (inelastic scattering). Whereas, the recoil electron distributes its energy via ionisation.

Pair Production

This method of absorption only happens for high-energy photons, and is encountered in clinical diagnosis in Positron Emission Tomography (PET). If the photon has sufficient energy then it can be absorbed by an atomic nucleus in the absorber and results in the production of an electron and a positron. This is a case of energy being converted into mass. The mass of the electron and positron is such that 1.02MeV is needed to produce the pair of particles.

2.5 Beer's Law

For monochromatic radiation a beam of X-rays is attenuated in an exponential fashion as it passes through a medium, this relationship is better known as Beer's or the Beer-Lambert Law:

$$I = I_0 e^{-\mu x} \qquad \text{Equation 2.1}$$

Where

I_0 is the initial intensity of the beam

x is the thickness of the medium

μ is the linear attenuation coefficient (LAC)

Using the transmitted intensity equation above, linear attenuation coefficients can be used to make a number of calculations. These include:

- the intensity of the energy transmitted through a material when the incident X-ray intensity, the material and the material thickness are known.
- the intensity of the incident X-ray energy when the transmitted X-ray intensity, material, and material thickness are known.
- the thickness of the material when the incident and transmitted intensity, and the material are known.
- the density of the material can be determined from the value of μ when the incident and transmitted intensity, and the material thickness, and chemical composition are known.

2.5.1 Attenuation Coefficients

Linear Attenuation Coefficient LAC

The linear attenuation coefficient (μ) describes the fraction of a beam of X-rays that is absorbed or scattered per unit thickness of the material. It is typically expressed in units of cm^{-1} .

Mass Attenuation Coefficient MAC

The values of mass attenuation coefficients are dependent upon the absorption and scattering of the incident radiation caused by the different mechanisms mentioned in section 8.5.1. It is defined as μ_m , which describes the attenuation per unit mass of material traversed (values of μ_m are given in Figure 2.5), and is shown in equation 8.2:

$$\mu_m = \frac{\mu}{\rho} \quad \text{Equation 2.2}$$

Where

μ is the total linear attenuation coefficient

ρ is the density

It is typically expressed in units of $cm^2 g^{-1}$

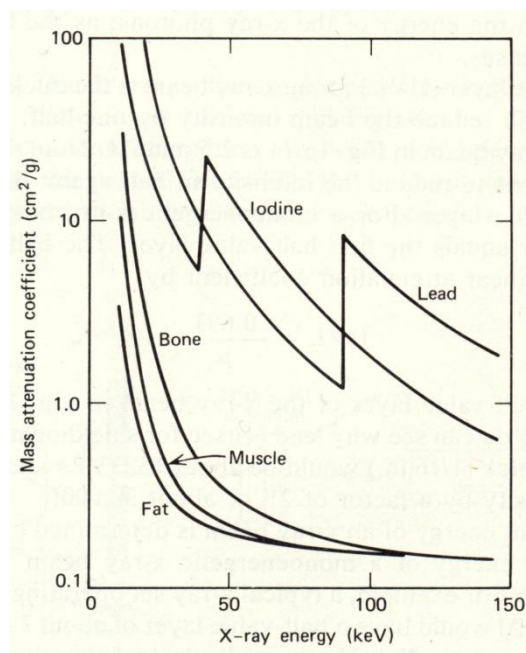


Figure 2.5: Mass attenuation coefficients for various tissues, lead and iodine (Cameron and Skofronick, 1978)

Figure 2.5 shows that tissues with higher atomic numbers such as bone are better absorbers than soft tissues like fat and muscle, and it is to be noted that on a mass basis the attenuation of all tissues is similar above 100 keV.

2.6 Beam Attenuation

Beam Hardening

So far we have discussed monochromatic X-ray beams. X-rays produced using impact sources are in fact polychromatic. As a polychromatic X-ray beam passes through a typical specimen, it becomes not only attenuated but harder (i.e., the distribution of X-ray photon energies is shifted to higher energies as lower energy photons are more attenuated). This results in “dishing” artefacts in X-ray micro-computed tomography (XMT) images, where specimens appear to be less attenuating in the centre (Davis and Elliott, 2003). In order to achieve the same result as an image obtained from a monochromatic beam, a correction is required, which is discussed in more detail in Section 4.1.4.

2.7 X-ray Microtomography

X-ray Microtomography (XMT) is a non-destructive technique that can be used to image specimens at micron scale in 3D, and finds its name from the greek word ‘tomos’, for ‘cut’ or ‘section’. In the field of clinical and scientific research XMT has become a frequently used method for the investigation of bone (Perilli *et al.*, 2007a; Shefelbine *et al.*, 2005; Müller and Ruegsegger, 1997). It allows non-destructive investigation of trabecular and cortical bone specimens without any significant preparation of the sample.

2.7.1 Principles of XMT

XMT was first developed by Elliott and Dover (1982). It is a miniaturised form of CT, with the ability to image at a resolution of a few microns. CT systems that are capable of volumetric CT analysis with isotropic spacing (pixel size identical to the slice thickness) of less than 100 μ m are defined as micro-CT systems (Kalendar, 2000). XMT works with the same fundamental principles of a CT system. There is an X-ray source, an X-ray detector and a specimen stage (Figure 2.6). Where in medical CT scanners the X-ray source and detector are mobile, they are fixed in most XMT systems, and the specimen rotates instead. XMT strongly depends on the characteristics of the X-ray source. In XMT a micro-focused X-ray source illuminates the object of interest, which is positioned precisely within the X-ray beam. The X-ray absorption images are acquired by a sensitive X-ray camera. During the image acquisition the sample is rotated one step at a time through 360 degrees (Figure 2.6). Images are recorded at each rotation. Using complex software 2 dimensional images (or slices) based on X-ray linear attenuation co-efficient can be calculated from the X-ray absorption images.

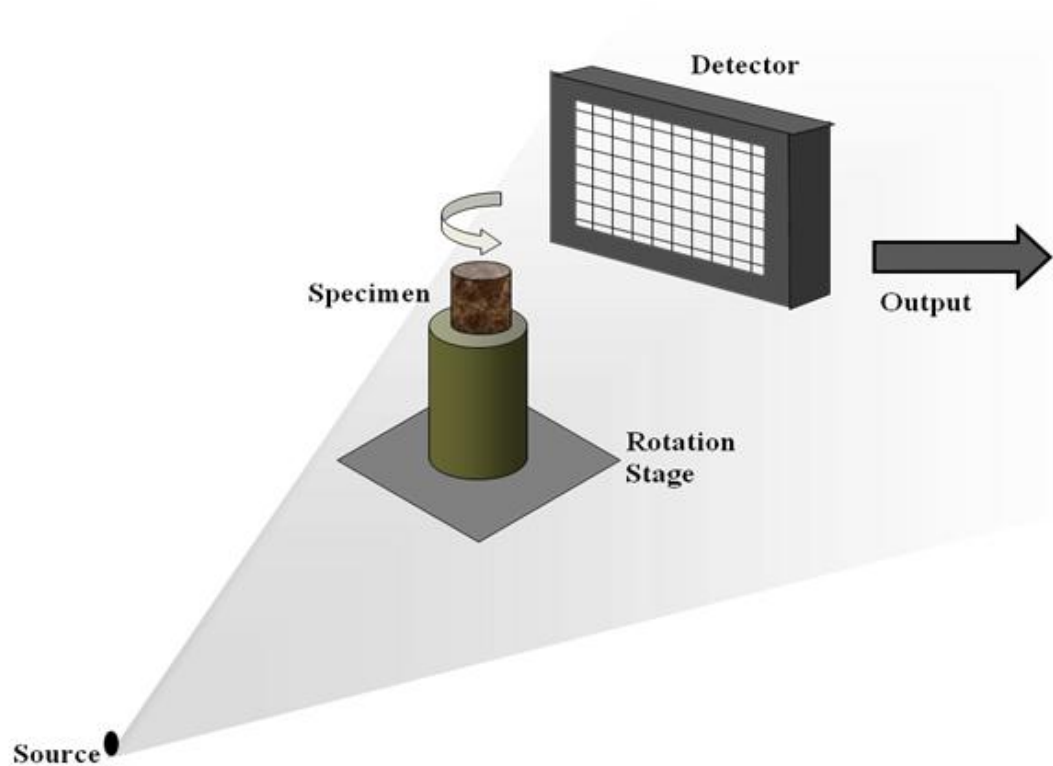


Figure 2.6: A schematic of an XMT set-up

With the recent improvement in compact X-ray tubes, it has been possible to develop systems with a focal spot size down to several microns. This has allowed high resolution and high signal-to-noise ratio imaging, offering the opportunity to obtain significantly improved XMT results (Peyrin *et al.*, 2000). Furthermore, with the conventional impact X-ray source there are disadvantages, such as, beam hardening and artefacts as mentioned previously. However, these can be overcome with the use of a scanner using a high dynamic range CCD X-ray camera, which has a time-delay integration (TDI) readout (Davis and Elliott, 2003) described in detail in Chapter 4.

2.7.2 XMT based Studies

Bone microarchitecture has been assessed for several decades using 2D histological methods (Boyde 1972, 1980, 2003a, 2003b; Boyde and Jones 1996, 1998; Boyde *et al.*, 1999). Standard histomorphometric procedures have some drawbacks: the invasive nature of bone biopsy technique does not allow longitudinal studies on individuals, the biopsies are destroyed during sample preparation and the procedure is 2-dimensional (Ruegsegger *et al.*, 1996). Additionally being truly destructive, serial sectioning techniques do not allow subsequent mechanical testing or other secondary measurements because the samples are destroyed during sample preparation (Müller *et al.*, 1998). A crucial advancement in microscopy was that of stereo-imaging (using SEM), enabling a better qualitative understanding into the structure of bone (Boyde, 1973). More recent developments have introduced a quantitative 3D measure of bone microarchitecture in the form of XMT imaging. Various studies have used XMT for bone assessment (Ruegsegger *et al.*, 1996; Müller and Ruegsegger, 1997; Shefelbine *et al.*, 2005; Perilli *et al.*, 2007a; Nazarian *et al.*, 2008). Some studies have used the data obtained from XMT to further understanding of structure and mechanics in healthy and pathological bone using Finite Element Analysis (FEA) (Taylor *et al.*, 2002; Van Rietbergen *et al.*, 2003; Shefelbine *et al.*, 2005).

2.7.3 XMT and Bone

XMT has proved to be a useful tool in providing a deeper insight into the understanding of OA. *In vivo* studies have been carried out to look at changes of subchondral bone and volumetric bone mineral density (vBMD) (McErlain *et al.*, 2008). Rat models were used to determine progressive changes of trabecular bone during OA. This study demonstrated the capabilities of monitoring changes occurring in the bony tissue during the progression of OA, and measuring significant changes in vBMD and subchondral cyst formations using XMT. Using animal models for *in vivo* studies provides useful insights into

bone pathology and its effects, but care is required in interpreting the results for use in human research. Due to the nature of high dose radiation in XMT, studies on human bone tissue are carried out *in vitro*. Bone tissue is either collected post-mortem or from patients undergoing some form of surgery where bone tissue is excised.

Established histomorphometric parameters such as Bone Volume Fraction (BVF), Trabecular Thickness (Tb.Th), Trabecular Spacing (Tb.Sp) and Trabecular Number (Tb.N) have been used to explain bone architecture calculated indirectly assuming a plate-model (dependant model) (Whitehouse, 1974; Parfitt *et al.*, 1983). More recently these measures have been assessed using 3D independent-models, enabling a more direct measurement into the variation of trabecular micro-architecture (Table 2.1). Measures such as connectivity derived from 2-dimensional sections can only give restricted information of the 3-dimensional topology, but has nevertheless been shown to correlate with the mechanical strength of trabecular bone (Mellish *et al.*, 1991). The availability of three-dimensional measuring techniques has opened new possibilities to analyse the architecture of trabecular bone. Three-dimensional image processing methods allow unbiased morphometric parameters to be derived in a direct way. Examples of such techniques are model independent assessment of thickness (Hildebrand and Ruegsegger, 1997b) and three-dimensional connectivity estimation (Odgaard and Gundersen, 1993). Hildebrand and Ruegsegger (1997b) developed a mathematical model to assess the rod and plate-like structure of bone, known as the Structure Model Index (SMI). Since the development of SMI in 1997, it has been commonly used to look at trabecular structure (Nägele *et al.*, 2004; Stauber and Müller 2006) (Table 2.1), providing an insight into age-related and architectural variation within trabecular bone. The orientation of trabecular bone is also of importance since it is also responsible for the anisotropic material properties of bone. This anisotropy can be associated with the directional variation of a geometric measure called the mean intercept length (MIL) (Whitehouse, 1974). MIL denotes the average distance between two bone/marrow interfaces

and is measured by tracing test lines in different directions in the examined volume of interest. From this measurement, a MIL tensor can be calculated by fitting the MIL values to an ellipsoid. The eigenvalues of the MIL tensor can then be used to define the degree of anisotropy (DA) which denotes the maximum to minimum MIL ratio (Odgaard, 1997 and 2001).

Table 2.1: Morphometric parameters of human bone measured using XMT

Reference	Bone Type	BVF	Tb.Th (μm)	Tb.Sp (μm)	Tb.N (cm^{-1})	SMI	Conn.D (mm^{-3})	DA
Tanck <i>et al.</i> , (2009)	OAFh	0.32	290	-	-	-	-	-
	(cylinders)	(0.07)	(40)					
	OPFh	0.24	240					
	(cylinders)	(0.03)	(30)					
	OAFh	0.18	230					
		(0.04)	(20)					
	OAFh	0.14	190					
		(0.03)	(20)					
	OPFh							
Perilli <i>et al.</i> , (2007a)	OAFh	0.18	244	1071	-	-	-	-
	(In air)	(0.09)	(80)	(238)				
	OAFh	0.18	241	1062				
	(Embedded)	(0.09)	(69)	(228)				
Nazarian <i>et al.</i> , (2006)	LS	0.05	146	-	1.527	2.362	0.767	1.665
		(0.01)	(10)		(0.053)	(0.165)	(0.380)	(0.15)
Nägele <i>et al.</i> , (2004)	F	0.26	207	951	10.9	1.01	3.05	2.31
		(0.12)	(57)	(417)	(3.29)	(0.8)	(2.82)	(0.61)
Müller and Ruegsegger, (1997)	PMFh	0.26	120	360	-	-	-	-
		(0.07)	(30)	(80)				

OA = osteoarthritis OP = osteoporosis H = Human Fh = Femoral head
PM = Post mortem IC = Iliac crest LS2 = Lumbar spine F = Femur
Values refer to mean (SD)

XMT and Biomechanics

XMT studies involved in assessing bone architecture in relation to mechanical loading are often carried out outside of the XMT system. The possibility of real time XMT and mechanical loading of bone may not be very far away but recently various studies have demonstrated the advantageous nature of XMT imaging in providing vast amount of understanding of the mechanical behaviour of bone under compression. Müller and co-workers have recently worked on a number of studies demonstrating the relationship between mechanical properties and bone quality of trabecular bone (Nazarian *et al.*, 2007 and 2008). Nazarian *et al.*, (2008) demonstrated in 3D that incremental compressive strain (0 - 20% at 2% increments) showed highest deformation of trabecular bone at the region with minimum BVF. However, they were unable to quantitatively demonstrate any relationship of the extracted region to the physiological loading condition.

XMT Limitations

All studies looking at bone using XMT are able to provide a qualitative understanding of bone structure and architecture over a micro-scale, and more recently some studies (Müller and Ruegsegger, 1997; Nägele *et al.*, 2004; Nazarian *et al.*, 2006; Perilli *et al.*, 2007a; Chen *et al.*, 2008; Tanck *et al.*, 2009) have been shown to quantify morphometric parameters in 3D, as shown in Table 2.1. Limitations of these studies mean that investigation of bone behaviour is limited to small samples and so, prior to XMT scanning, a form of destructive sample preparation was required of human tissue, i.e. removing small regions from femoral heads or animal tissue was used. XMT has been used to investigate bone architecture in relation to OA and OP (Müller and Ruegsegger, 1997; Perilli *et al.*, 2007a; McErlain *et al.*, 2008), but all these studies have used bone biopsies or cut sections from larger samples (Figure 2.7). This limitation results in limited understanding of bone as a whole.

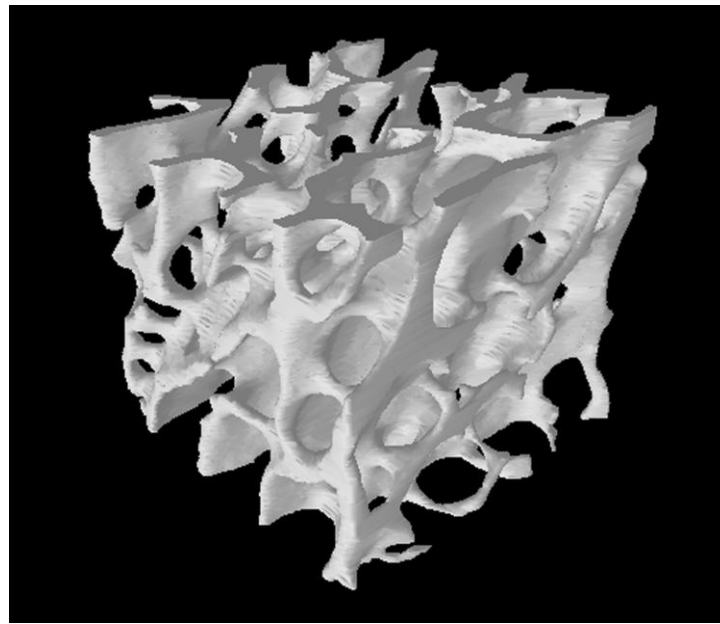


Figure 2.7: Three dimensional XMT reconstruction of a cuboidal VOI ($4 \times 4 \times 4\text{mm}^3$) at $19.5\mu\text{m}$ voxel size (Perilli 2007a)

2.8 Scanning Electron Microscopy

Scanning electron microscopy (SEM) is a method for high-resolution imaging of surfaces. This technique has been used extensively for studying the surface morphology of bone (Boyde, 1980, 2003a, 2003b). The image is formed by a very fine electron beam, typically 1nm-5nm spot size, which is focused on the surface of the specimen. The beam is scanned over the specimen in a series of lines and frames. The raster movement is accomplished by means of small coils of wire carrying the controlling current (scan coils). At any given moment, the specimen is bombarded with electrons over a very small area. Several things may happen to these electrons. They may be elastically scattered from the specimen, with no loss of energy. They may be absorbed by the specimen and give rise to secondary electrons of very low energy, together with X-rays (Figure 2.8). They may be absorbed and give rise to the emission of visible light (an effect known as cathodoluminescence), and they may give rise to electric currents within the specimen.

All these effects can be used to produce an image. By far, the most common, however, is image formation by means of low-energy secondary electrons.

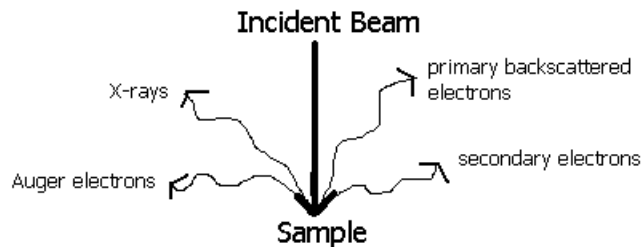


Figure 2.8: Behaviour of electrons interacting with a specimen

The secondary electrons are selectively attracted to a grid held at low positive potential with respect to the specimen. Behind the grid is a disc held at about 10 kilovolts positive with respect to the specimen. The disc consists of a layer of scintillant coated with a thin layer of aluminium. The secondary electrons pass through the grid and strike the disc, causing the emission of light from the scintillant. The light is directed down a light pipe to a photomultiplier tube, which converts the photons of light into a voltage. The strength of this voltage depends on the number of secondary electrons that are striking the disc (Figure 2.9).

Thus the secondary electrons produced from a small area of the specimen give rise to a voltage signal of a particular strength. An image is built up simply by scanning the electron beam across the specimen in exact synchrony with the scan of the electron beam in the cathode ray tube.

Back-scattered electrons (BSE) are beam electrons that are reflected from the sample by scattering. BSE are often used in analytical SEM along with the spectra made from the characteristic X-rays. Because the intensity of the BSE signal is strongly related to the atomic number (Z) of the specimen, BSE images can provide information about the distribution of different elements in the sample.

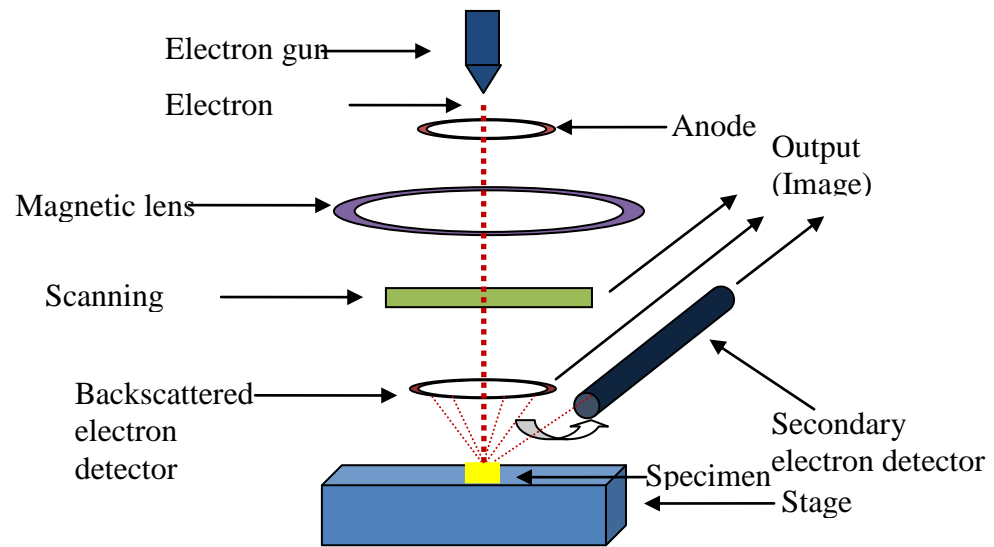


Figure 2.9: Schematic of an SEM set-up

2.8.1 SEM based studies on bone

Investigations into the surface morphology of bone have been extensively studied using Backscattered Electron Microscopy (BSE) (Boyde, 1972; Mosekilde, 1990; Boyde, 1996; Boyde, 2003a, 2003b). BSE imaging also has the ability to assess the microscopic differences in tissue mineralisation (Reid and Boyde, 1987). The resolution of BSE imaging depends on the penetration of electrons into the specimen, which is approximately 5 μm (for an electron beam of 20–30 keV) in bone (Bachus and Bloebaum, 1992) and can go down to 0.5 μm for an electron of 10 keV (Howell & Boyde, 2003). BSE studies have successfully shown trabecular bone morphology at the cellular level (Boyde and Jones 1996), and also enlightened researchers into the phenomenon of remodelling along with microdamage (Boyde, 2003b) and microcallus formations (Boyde, 2003a, 2003b). Boyde (2003b) proved SEM was successful in identifying micro-cracks that mineralised *in vivo* as part of bone's self healing process. He also showed BSE images of osteocyte lacunae apoptosis (cell death) (Figure 2.10) and micro-

damage. However, he was careful to note the damage (micro-cracks) that may arise from sample preparations, which should not be confused with ‘real’ cracks.



Figure 2.10: Human femoral shaft, post-mortem, compact bone adjacent to metal implant stem, showing mineralized apoptotic debris in osteocyte lacuna in lamellar bone. 20-kV BSE of PMMA-embedded, polished, carbon-coated sample. Field width, 44 μm (Boyde 2003b)

2.9 Nano-tomography and X-ray Ultra Microscopy

Analysis of bone for fine-scale architecture and material quality is crucial in facilitating our understanding of bone behaviour at the nano-scale. In order to achieve this, it is essential to overcome current tomographic limitations by attaining submicron resolution ("nano-CT") tomographic imaging and in being able to access any such systems. This has recently been achieved by Skyscan by the development of the 2011 nano-CT scanner. This employs an X-ray source using new technology to obtain a spot size of 0.3 μm , combined with an extremely high precision sample manipulator and highly sensitive X-ray camera. With this instrument, pixel sizes of down to 150 nm are possible.

Structural features linked to bone quality such as osteocytes and microcracks in bone, and resorption lacunae, can be readily visualised (Salmon and Sasov, 2007)

A new approach to X-ray projection microscopy using a scanning electron microscope as a host has recently been developed by Mayo *et al.* (2003). The X-ray Ultra-Microscope is an accessory to a scanning electron microscope (SEM), manufactured by Gatan Inc., which uses X-rays to allow the 2D and 3D-visualisation of the internal structure of specimens in the SEM. It is capable of producing sub-micron 3D computed tomography (CT) of specimens (Howard *et al.*, 2010). The electron beam of the SEM is used to create a cone of X-rays by focusing the beam onto a metal target. The sample, which is off-set to one side of the beam, is placed within the X-ray cone and the resulting X-ray absorption image is projected onto a CCD behind the specimen. This CCD output is essentially a 2D X-ray projection image where differences in grey-scales reflect changes in density and thickness of the specimen (Section 4.9). A recent development, the XuM has proven to be a versatile and useful instrument, with greatly enhanced visibility of weakly absorbing and fine scale features (Gao *et al.*, 2006; Wu *et al.*, 2008).

General Aims and Objectives

The aim of this study is to provide quantitative multi-scaled information to ultimately aid interpretation of imaging data obtained from clinical 2D radiography of pathological and non-pathological trabecular bone.

The specific objectives were:

- To image whole femoral heads at high resolution using TDI XMT.
- To resolve structural features attributing to pathological and non-pathological femoral heads using XMT
- To determine the global and local morphometric parameters of normal, osteoarthritic, and osteoporotic bone, and investigate any micro-architectural differences in 3D
- To identify and relate microdamage and microcallus formations to bone quality and the loading condition of the pathological and non-pathological femoral
- To determine and investigate the differences in bone mineral concentration in pathological and non-pathological femoral heads using XMT
- To analyse the failure behaviour of trabecular bone in 3D using image analysis
- To relate the morphometric parameters and mechanical properties of osteoarthritic bone to loading conditions
- To identify and determine microcallus formations and investigate their morphology and relationship to trabecular microfractures using XMT and XuM
- To image a single trabecula using XuM and correlate to SEM imaging.

Part II: Materials and Methods

Chapters three and four present the materials and methods used throughout this thesis. Chapter three presents the collection and preparation of bone tissue, and describes the origin, basis and categorisation methods for selecting the tissue. Chapter three also describes the storage and mounting techniques required for the experimental studies. The approach taken to identify regions of load bearing in the femoral heads and sample extraction from the different regions along with the combination of embedding techniques used for imaging hard tissue are also presented. A total of eight femoral heads are used and presented in the five separate experimental studies (Chapters 5 - 9). Chapter four outlines the methods and experimental details used in Chapters 5 – 9. It aims to provide an understanding of 3D imaging of pathological and non-pathological bone tissue. Chapter four also describes and discusses the methods used to establish the validity and limitations of Time-Delay Integration XMT for the purpose of imaging large specimens at high resolution. The experimental details of 3D *In vitro* mechanical testing and tomography of small specimens at nano-scale using XuM are also presented.

Chapter 3 Materials and Preparation

The femoral heads and tissue obtained for the purpose of this thesis were processed in several ways and their results are presented in five separate experimental chapters (Chapters 5-9). The specimen processes and their experimental experiences are shown diagrammatically in a flow diagram (Figure 3.1) with the details presented in Chapters three and four.

Bone tissue selected and used throughout this thesis was obtained from a combination of cadaveric (obtained from School of Medicine and Dentistry, QMUL) and fresh femoral heads (obtained from total hip arthroplasty, Barts and The Royal London Hospital). Ethical approval was granted for the collection of bone tissue from Barts and The Royal London, and QMUL SMD by NRes Ethics Committee. In all cases of tissue collection from patients, informed consent was obtained prior to total hip arthroplasty (Appendix III).

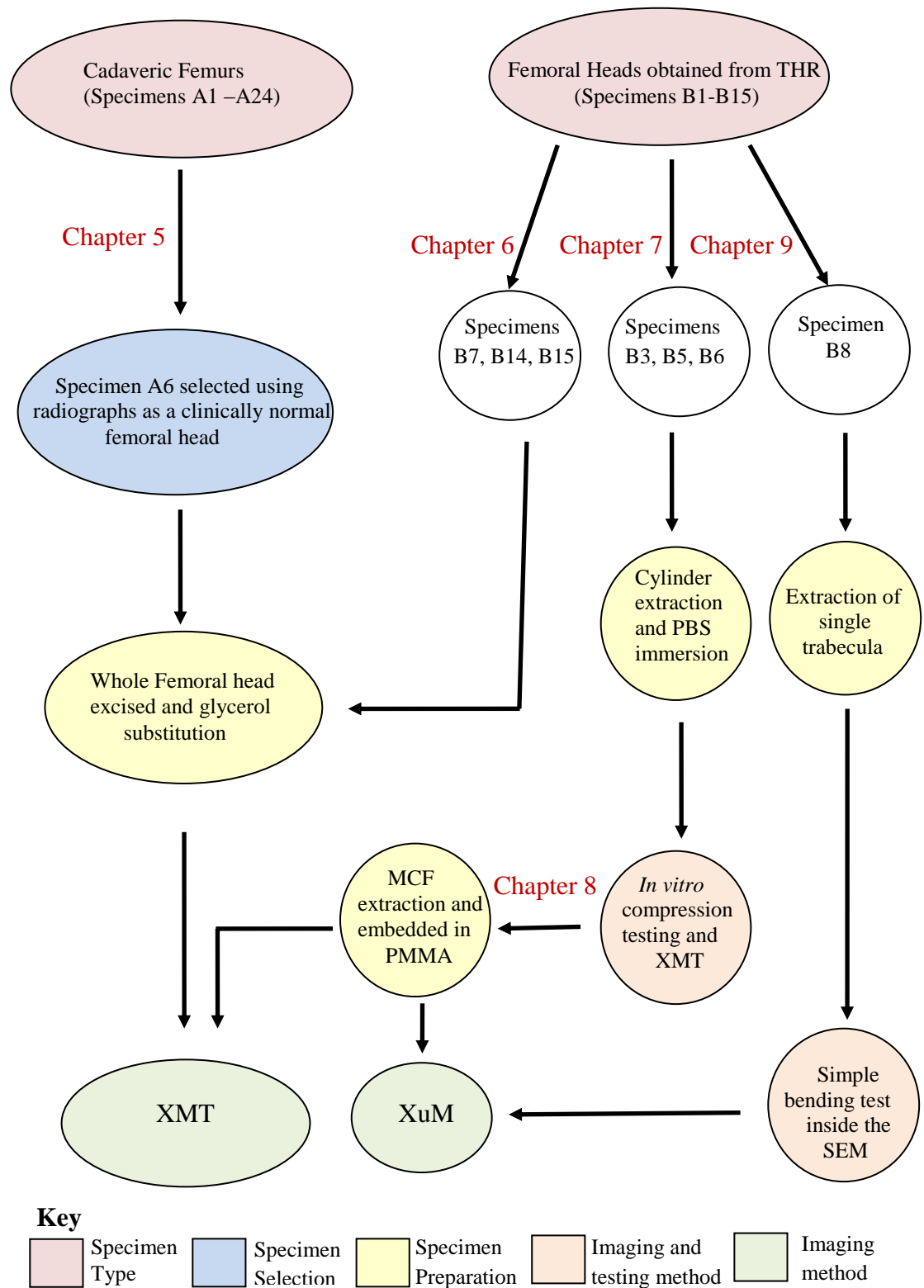


Figure 3.1: Flow diagram showing the different processes of the specimens' experience throughout this thesis

3.1 Non-Pathological Specimen

This section categorises cadaveric femurs and identifies the criteria used for selecting a non-pathological femoral head used in the XMT study outlined in Chapter 5. The preparation and embedding technique is also outlined.

3.1.1 Specimen selection

A total of twenty-four cadaveric femurs were obtained. It was necessary to find an appropriate categorisation criteria to determine a non-pathological femoral head for the purpose of 3D XMT imaging. For the purpose of defining a non-pathological femoral head two common grading systems were used (Kellgren and Lawrence, 1957; Singh *et al.*, 1970). Using these grading systems the cadaveric femoral heads were classified as OA, OP or normal (Appendix I).

The grading system described by Kellgren and Lawrence (1957) uses four main markers for assessing the patient (Section 1.9.1), namely the presence of osteophytes; narrowing of the joint space; bone contour deformity; and sclerosis. Another commonly used system is that described by Singh *et al.*, (1970), where distinguishing features in trabecular architecture are classified (Section 1.9.1). As the femurs obtained in this study are cadaveric, and therefore are not in their anatomical position (bound by muscle and soft tissue, to the acetabulum), a modified version of the Kellgren and Lawrence system was used, (omitting the joint space).

Although, Dual-energy X-ray Absorptiometry (DXA) is now used as the ‘gold standard’ in measuring Bone Mineral Density (BMD) when assessing patients, this was not carried out in this study since the tissue obtained was cadaveric. Instead, the twenty-four cadaveric femurs were classified using radiographs.

3.1.2 Categorisation of femoral heads

The classification of the femoral heads was carried out in collaboration with an experienced Orthopaedic consultant (Mr Gareth Scott, St Bartholemews and The Royal London Hospital) and the main factors considered in line with the Kellgren and Lawrence (1957) grading scale, as mentioned in Section 1.9.1 (subchondral bone thickening, sclerosis, bone cysts, osteophyte formation, the shape of the head, the orientation of the trabeculae and visibility of growth plate). The observations were carried out visually using plain 2D radiographs in the anterior-posterior plane. Limited medical history was available, therefore only the gender, age and cause of death is known (Appendix 1). Table 3.1 below shows the result of the assessment of the twenty four femurs. Out of the twenty four femurs, 14 femoral heads were classified as OA, 2 as OP, 7 as normal and one was excluded due to an implant insertion. Femoral heads exhibiting none of the factors mentioned in the Kellgren and Lawrence (1957) and Singh *et al.*, (1970) classification methods were assumed to be normal with no pathology. For the purpose of this thesis a non-pathological specimen will be referred to as clinically normal. Due to time constraints only one clinically normal femoral head was selected, at random from the qualifying group. The selected specimen is highlighted in red (Appendix I).

3.1.3 Selection of Normal Specimen

The specimen selected for this study (shown in Figure 3.2) was obtained from a male cadaver aged 89 who died of bronchopneumonia secondary to Chronic Obstructive Pulmonary Disease (COPD), which are found to be unrelated to any bone diseases. No further medical history was available. Figures 3.3 and 3.4 can be seen as examples of two of the femoral heads, which were identified as having extreme pathology and excluded from the study.

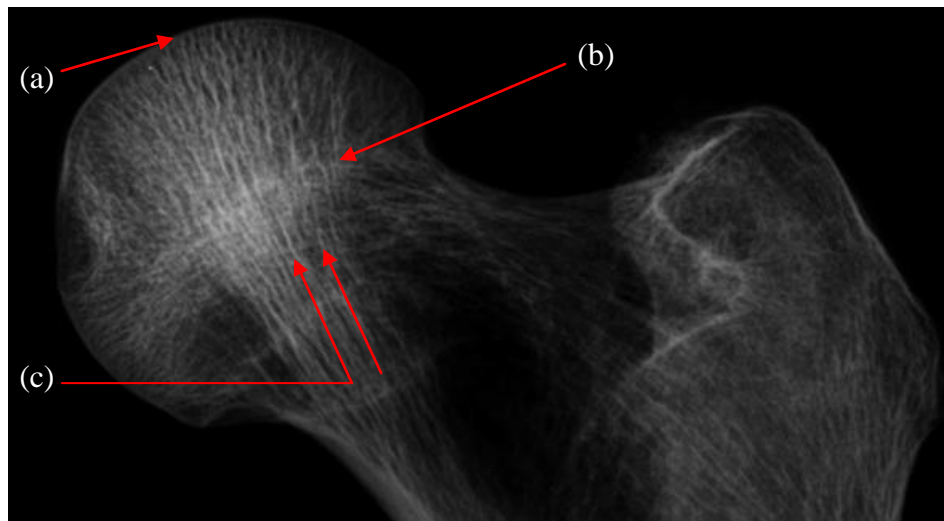


Figure 3.2 Radiograph of the selected normal femoral head (A6, Appendix I), (a) showing normal geometry of the femoral head with no bone cysts present and no subchondral bone thickening (b) clearly visible is the growth plate and (c) the trabeculae bone are oriented clearly perpendicular to the surface of the femoral head

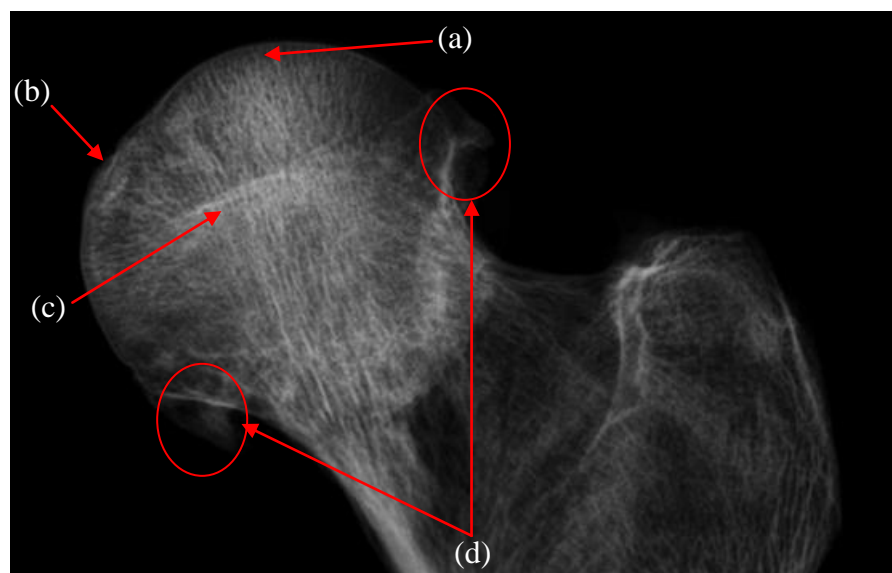


Figure 3.3: Radiograph of a severely osteoarthritic femoral head (A23 Appendix I), (a) showing abnormal geometry of the femoral head (b) with subchondral sclerosis, (c) the growth plate is slightly visible and (d) osteophyte formations are found at the superior and inferior surfaces of the head-neck joint

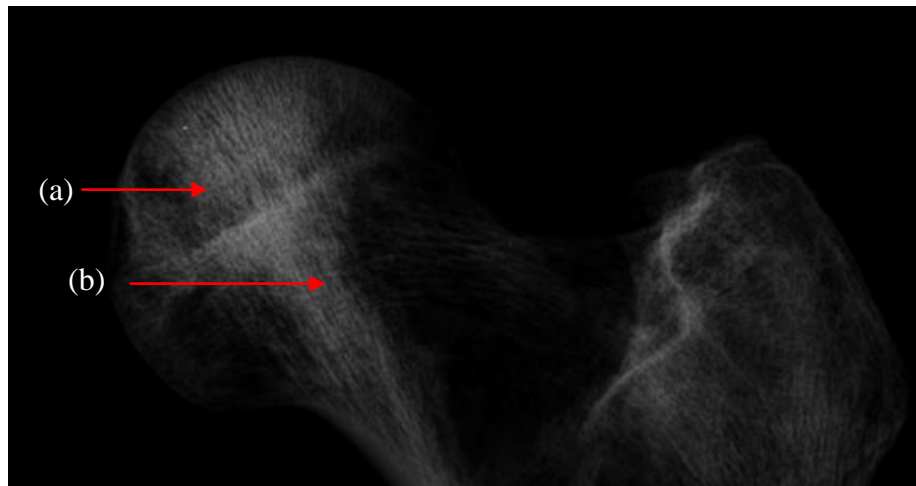


Figure 3.4: Radiograph of a severely osteoporotic femoral head (A20 Appendix I), (a) showing large areas of resorption and (b) fine trabeculae architecture

3.1.4 Femoral Head Specimen Preparation in Glycerol

The femoral head was cut at the femoral neck using a precision diamond band saw to obtain the femoral head. Careful consideration was taken in preparing the excised femoral head for XMT. Various methods for preservation and identification of tissue for imaging techniques are known to be used, including; embedding in methacrylate or epoxy resins, cryopreservation, and various staining techniques (Schenk *et al.*, 1984). These methods vary in suitability dependent upon the imaging technique and type of tissue. The approach in this study was to use a method which would preserve the tissue, prevent dehydration and enable imaging within a given time frame. For these reasons glycerol-substitution was chosen.

Glycerol-substitution was compared to cryopreservation in a study by *Giovani et al.*, (2006). They used trabecular bone specimens, and placed them into 3 groups, cryopreserved, glycerol preserved and a control group. After preservation, the samples were subjected to histomorphological, cell feasibility and microbiological analyses. This study showed that glycerol preservation was similar to cryopreservation in terms of bone matrix preservation; no bacteria or fungi were found in the samples, even after 1 year.

The specimen was first placed in industrial methylated spirit (IMS – 99% ethanol and 1% methanol) at 50°C for 24 hours to de-fat the femoral head. IMS was replaced after 24 hours and the specimen was placed in the oven at 50°C for a further 24 hours. Once the specimen had undergone the cleaning process, it was placed in glycerol and placed in the oven for a further 3 weeks at 50°C. The specimen was removed and the glycerol was replenished. The specimen was immersed in glycerol during the entirety of the experiment.

3.2 Pathological Tissue

Pathological tissue was prepared for the high resolution XMT study which is reported in Chapter 6.

3.2.1 Tissue Extraction

A total of 14 femoral heads were obtained from patients undergoing total hip arthroplasty (Mr. Gareth Scott FRCS, Barts and The Royal London) as a result of osteoarthritis or osteoporosis. Table 3.1 shows the age, gender, diagnosis, the side from which the femoral head was extracted, and which study (if included) the selected specimen relates to. If the specimen was found to be damaged as a result of the surgical procedure, it was rejected. Otherwise, specimens which were found intact with minimal damage (i.e. scratches on the surface) were considered for the study. Furthermore, some selected specimens suffered damage during preparation

and others were found not to have sufficient bone tissue, therefore they were also rejected.

Table 3.1: Patient information on the specimens obtained for the studies carried out in this thesis

Femoral Head	Gender	Age	Diagnosis	Side	Chapter
B1	Female	54	OA	Left	7*
B2	Female	44	Sickle cell	Left	N/A
B3	Female	59	OA	Left	7
B4	Female	53	OA	Left	7*
B5	Female	70	OA	Right	7
B6	Female	73	OA	Left	7
B7	Female	68	OA	Right	6
B8	Female	67	OA	Right	8
B9	Male	55	OA	Right	N/A
B10	Female	73	OA	Left	**
B11	Female	53	OA	Left	**
B12	Female	67	OP	Left	N/A
B13	Female	79	OP	Left	N/A
B14	Female	81	OP	Right	6
B15	Female	69	OA	Right	6

*Rejected due to preparation damage **Not sufficient bone tissue for the study
N/A Not considered due to damage induced during surgical procedure

3.2.2 Specimen Selection

The pre-operative radiographs were assessed and any features contributing to the condition (Section 1.9.1) were noted, including joint space. Immediately following surgical removal from the patient, each femoral head was wrapped in a Phosphate Buffered Saline-soaked (PBS) gauze swab and stored at -20°C.

3.2.3 Specimen History

Three femoral heads were used in this study (Chapter 7) and were obtained from the right hip of female patients ranging 68-81 years old (B7, B14, and B15) (Table 3.2). One femoral head was obtained from a patient who suffered a femoral neck fracture as a result of osteoporosis and two heads were obtained from patients who underwent total hip arthroplasty as a result of osteoarthritis.

3.2.4 Specimen Storage

Beaupied *et al.*, (2006) satisfactorily demonstrated, using dual-energy X-ray absorptiometry and XMT that the densitometric, micro-architectural and biomechanical parameters of rat femurs showed no significant differences when preserved in alcohol or stored in deep-freezing after one month.

Sedlin (1965) also demonstrated in a study of 74 cortical bone specimens that the ultimate fibre stress, elastic modulus, energy absorbed to failure, and total deflection to failure are not significantly altered by freezing at -20°C if the specimen is adequately hydrated and thawed before testing but clearly showed that the other two common methods of preserving specimens; formaldehyde and alcohol fixation, do have a significant effect on some (but not all) of the mechanical properties, and therefore should not be used (Sedlin, 1965). Bushby *et al.*, (2004) investigated the effect of embedding and liquid storage modes on bone micro-mechanical properties. They performed nano-indentation on equine cortical bone after embedding in PMMA, and storing in 70% ethanol. Their findings concluded that the replacing water in bone using PMMA, and ethanol, had a profound effect on the mechanical properties.

Bembey *et al.*, (2006) also reported on the effect of hydration on the micro-mechanical properties of bone. They investigated the effect of acetone, ethanol, water and methanol. They found that the storage mode can have a considerable effect on the mechanical properties, in particular in the organic phase.

3.2.5 Specimen size

OA contributes to the change in geometry in femoral heads, therefore the average dimensions, need to be considered. The dimensions (equatorial diameter) of the femoral heads were measured using vernier callipers. Each measurement was taken five times (at different positions), before the average and standard deviation was calculated since the shape of the femoral head was not uniformly spherical as seen in Figure 3.5.



Figure 3.5: An image of the OA Femoral Head

3.2.6 Specimen mounting

The specimens were placed in a perspex container and were fully submerged in glycerol to prevent dehydration, and cracking of the bone specimen, during XMT imaging (Figure 3.6). The container was centred on an aluminium plate in order to assist in minimising scan length, therefore scan time (see Chapter 4). This was then placed on the rotational stage during scanning (Section 2.7.1). This set-up enabled the sample to remain in a fixed position and prevent any motion instability during XMT Imaging. This set-up was used for imaging all femoral heads throughout this project.

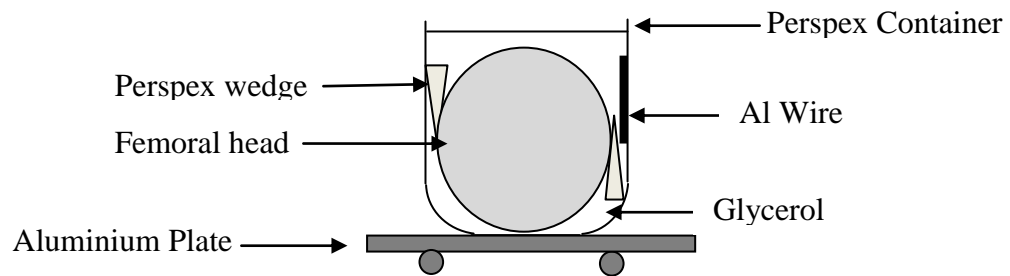


Figure 3.6: A schematic of the specimen mounting set-up used during imaging of whole femoral heads

3.3 Tissue for Mechanical Studies

Tissue considered here (cylindrical specimens) was used for *in vitro* compression testing in the XMT (Chapter 7). Cylindrical samples were taken from femoral heads at different anatomical positions related to load bearing regions. The method of obtaining specimens from the femoral head for mechanical studies was carefully considered, as a basic premise of this study was to relate the mechanical findings, degree of mineralization and micro-morphology over the whole femoral head to load bearing and non-load bearing areas.

3.3.1 Patient History

Femoral heads were taken from patients undergoing total hip arthroplasty as a result of osteoarthritis. Five heads initially qualified for this study, but due to preparation damage only three were used (Chapter 7). Two of the femoral heads were from the right hip and one from the left hip; all obtained from female patients ranging in age from 59-73 years old (B3, B5, and B6 Table 3.2).

3.3.2 Specimen Shape

Specimen shape is an important factor which affects the measurement of compressive mechanical properties of the material. Sagittal slices of the head would, perhaps, be most suitable for histology and microradiography but would not be suitable for compression testing.

When elongated circular or rectangular specimens are used for determining the compressive stress of bone, the effects of column action have to be considered. A column is a relatively slender compression-resisting member, the strength of which depends upon several factors: the material; the cross-sectional shape and area; the restraints at the ends of the column; and the aspect ratio of the smallest dimension of the column to its height. These factors are inter-dependent to some extent, but the cross-sectional shape of the column is the most important. For example, a hollow cylinder will support more weight without bending than will a solid column of the same shape and composed of the same kind and amount of material (Evans, 1973).

No standards have been made for the compression testing of trabecular bone. Methods for testing flexible cellular materials are set out by the British Standards Institution, No BS 4443-17 (2008). Methods for determining compression stress-strain characteristics for intercommunicating flexible low-density materials and for denser non-intercommunicating flexible cellular materials are described, but the terms 'low' and 'high' are not defined. Expanded cellular rubbers are quoted as an example of a denser material. It is stated that at no point should the force-bearing surface of the specimen overlap the compression plate, and recommended that the specimen should be a right parallelepiped with square load-bearing surfaces. For metals, ASTM Standards (2009) recommended that, where feasible, compression test specimens be in the form of solid circular cylinders.

It is uncertain whether trabecular bone would be considered to be of low or high density. It is probably a high density material, but it is also an intercommunicating foam. The standards therefore provided limited help. It was decided to use

cylindrical specimens since this enables the accurate preparation of specimens by use of a trephine from the various functional areas of the femoral head. Carter and Hayes (1977) examined specimens trephined under continuous irrigation for evidence of damage during preparation. The specimens were included in acrylic resin, and using a reflected light microscope they found occasional fracture and tearing of trabeculae on the exposed surfaces. However, the specimen appeared to be undamaged throughout most of their volume, therefore they considered this method as reasonable for specimen preparation.

3.3.3 Preparation and orientation of specimens from the femoral head

The subchondral trabeculae lie perpendicular to the surface (“The chondrogenous bone in the head radiates with the greatest regularity towards a common centre in the head” Ogston 1878). Therefore a jig was designed so that the cylindrical core specimens would all be taken perpendicular to the surface at set reproducible positions from each head (Figure 3.7). This, therefore, ensured that each core specimen was taken in line with the main direction of the subchondral trabeculae.

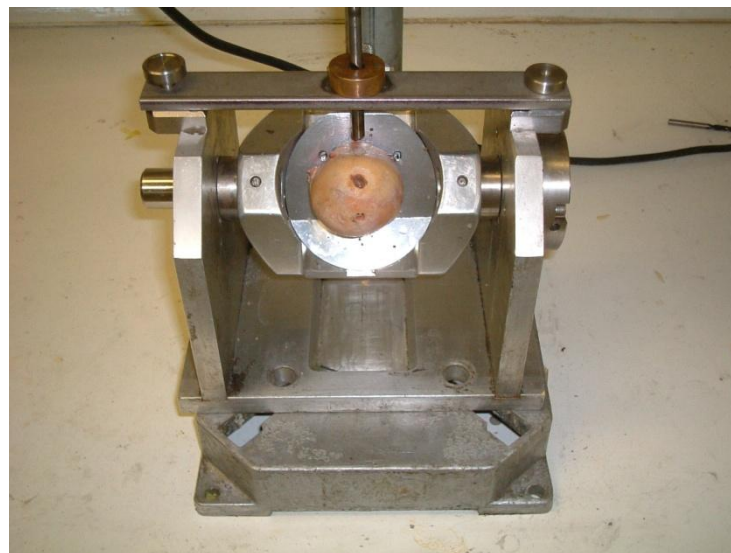


Figure 3.7: The jig used to trephine cylindrical specimens from each femoral head

Each femoral head was thawed to room temperature, and then orientated on the jig using the lateral cortex and fovea as landmarks and by measurement of the neck angle from the pre-operative X-ray. Each was positioned on the jig so that it would conform to a standard reference point on the head with the trephine always directly above the pole position when the jig was in the neutral position.

This was achieved by placing packing under the head so that depth of head + packing = radius of head + 12mm.

Cylinder Extraction

Cylinders were removed from a variety of anatomical positions related to load bearing (Figure 3.9) (Section 3.3.4). At room temperature a 5mm trephine was used at low speed and irrigated with Phosphate buffered saline to prevent thermal damage to obtain 10 – 5mm cylinders of trabecular bone from each femoral head. An example is shown in Figure 3.8. Each specimen was radiographed and then sectioned just below the level of the subchondral plate to remove the subchondral bone.



Figure 3.8: (a) Image of the bone cylinder after removal of the subchondral bone

Each specimen of trabecular bone was cut with ends square to the longitudinal axis using an Exakt precision diamond coated band saw (Exakt Technologies Inc., Oklahoma City, OK) and irrigated with water during sectioning. They were wrapped in a swab soaked in phosphate buffered saline, and stored at -20°C, while awaiting compression testing, and XMT Imaging. The radiograph of each core specimen was checked; specimens in which hidden cysts were present or trabeculae did not run parallel to the long axis were excluded.

The load bearing areas of the femoral heads were determined according to the work of Brown and Shaw (1983) whose work has been discussed in Section 1.6.6.2. Using their contour maps of load bearing configurations, the trephine points were superimposed on topographical maps of each head before removing the core specimens (Figure 3.9). In the osteoarthritic heads, it was clear that the eburnated areas were weight bearing and other areas were considered to be non-weight bearing, but using Brown and Shaw's map it was observed that the weight bearing area was not, in fact, always eburnated.

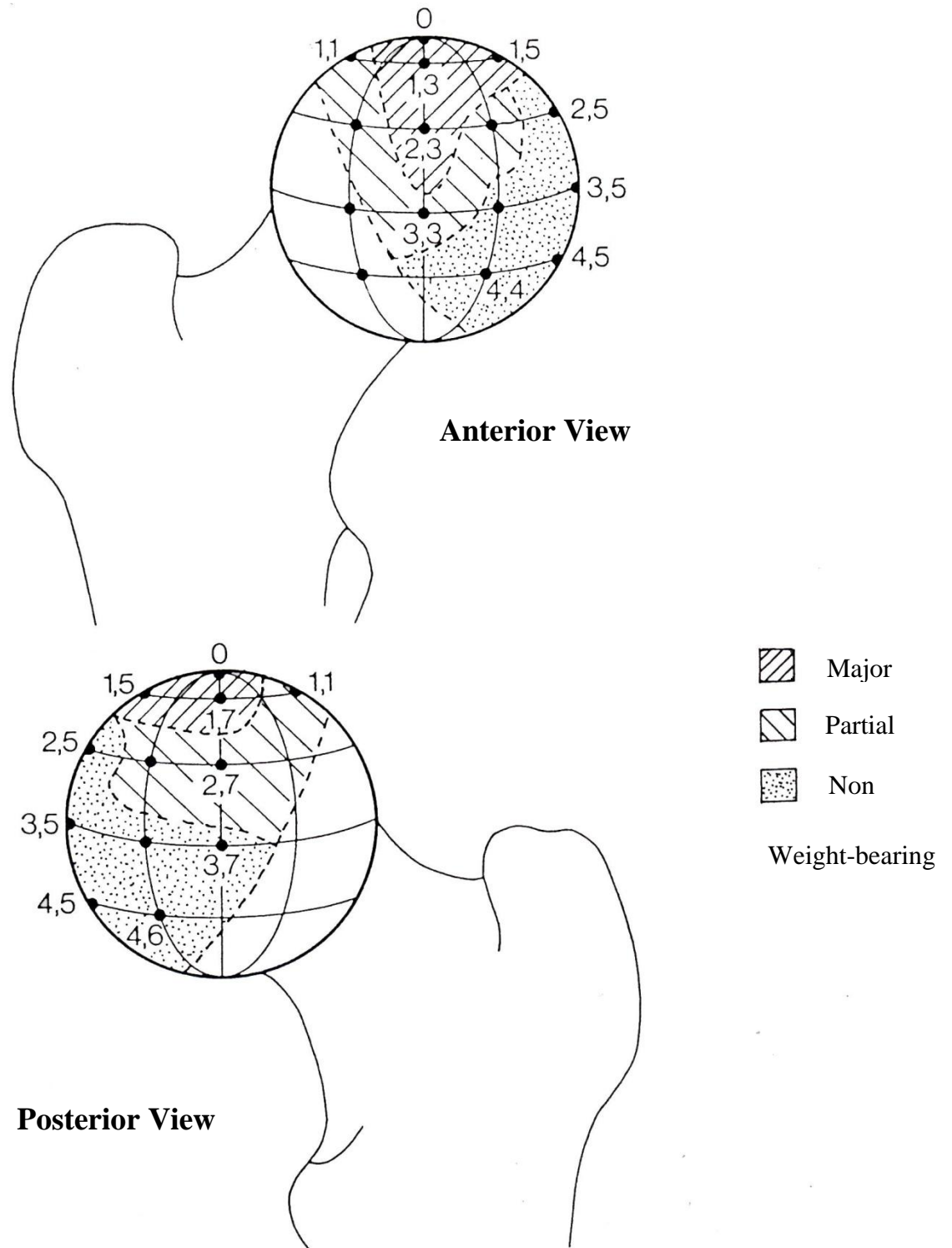


Figure 3.9: The standardised positions of specimen sites on the right femoral head and their relation to load bearing in the femoral head (Adapted from Sharp 1988)

3.3.4 The number of specimens per head

The number of specimens obtained per head varied because of varying head size. Great care had to be taken when trephining the specimens to ensure that the trephines did not cut into each other. Due to the nature of the varying sizes of the head a uniform number of samples could not be removed from each head. The maximum number of specimens obtained from one head was 10, and the minimum 5. A total of 24 cylinders were extracted from the 3 femoral heads, but due to damage induced as a result of extraction, only 10 samples qualified overall for testing. The samples used for the study were taken from the three heads, across all different loading sites; three samples from major-load, two from partial-load and 5 from non-load bearing regions (Table 3.2).

Table 3.2: The femoral heads and associated anatomical positions of the cylinder used in the mechanical study (Chapter 7)

Femoral Head (Table 3.1)	Anatomical Position (Figure 3.8)	Load Bearing
B3	1,7	Partial
B3	2,8	Non
B5	0,0	Major
B5	2,5	Non
B5	2,6	Non
B6	1,3	Major
B6	1,4	Non
B6	1,7	Partial
B6	2,2	Non
B6	2,6	Non

3.3.5 Specimen size

Sharp *et al.*, (1988) carried out a study to determine the effect of varying the specimen length and end effects during compression testing on trabecular bone. This study concluded that specimens of less than 4.0 mm in length should not be used. Therefore careful consideration was taken in deciding to use specimens measuring 5mm in diameter and 10mm in length. Following ASTM D 1621-73 convention for cylindrical compression specimens for foams the ratio 2:1 of length to diameter was preserved.

For stability in axial compression, short specimens are required to avoid Euler buckling, but decreasing the length-to-diameter ratio increases the relative frictional strain at the compression plate-specimen interface. End effects are at the specimen-compression interface and are important when specimens of a relatively low length-to-diameter ratio are tested in compression. End effects can also contribute to ineffective load transfer to trabeculae. For this reason care was taken in sectioning the ends of the cylinders (Section 3.3.3)

3.3.7 Embedding Technique

Immediately after compression testing, the regions of interest (ROI) were identified from the XMT data sets (Chapter 7) and the corresponding cylinders were embedded for further XMT imaging (Chapter 8). The samples were embedded to enable stable and accurate sectioning (Section 3.4) of the ROI. Samples were first dehydrated by placing them in IMS, for 24 hours initially, in an oven at 50°C. The IMS was then changed after 24 hours, and the specimens left for a further 48 hours to enable complete dehydration. The specimens were then placed in xylene for 24 hours at 50°C to clear the IMS and remove any alcohol present in the specimens. The dehydration and clearing steps are important as a thorough infiltration and substitution of the methacrylate is essential, and removal of the fat and lipids greatly improves the quality of the final blocks and reduces cutting problems.

It is also essential to emphasise that degreasing and complete removal of water is required for uniform hardening during polymerisation (Schenk *et al.*, 1984).

After the clearing process, the specimens were placed in a solution of non-catalysed methacrylate monomer. This step was taken for the monomer to infiltrate the entire specimen, therefore the specimens were left for 72 hours at room temperature. After this period of time the specimens were placed in a mixture of catalysed methacrylate monomer and polymerised methylmethacrylate. This step was taken to initiate the polymerisation of the methylmethacrylate. The specimens were left for 48 hours at room temperature, and then placed in the oven at 35°C and removed after 16 days.

3.4 Preparation of Microcallus formation Specimens for Micro- and Nano-Tomography

Regions of interest identified from the mechanical study were furthermore investigated at a higher resolution using the XMT. Those regions were identified (Chapter 7) and embedded prior to sectioning. Microcallus formations (MCFs) were identified from XMT datasets (discussed in Chapters 7 and 8) and located within the tissue. After the sample was embedded (Section 3.3.7), a slow speed diamond saw (Beuhler, Illinois, USA) was used to section the region of interest containing the microcallus formation and the edges of the section were carefully polished to remove any excess embedding material. The specimen was then mounted on the fine tip of a thin metal pin (suitable for using on the rotation stage in the XuM) using Cyanoacrylate (Loctite Superglue Precision, Henkel, UK) (Figure 3.10). The methodology for this study is outlined in Chapter 4, and the results are presented in Chapter 8.

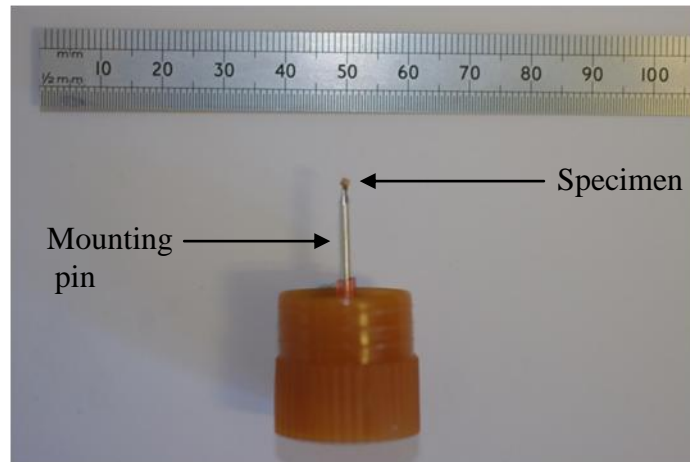


Figure 3.10: Specimen set-up for XuM

3.5 Tissue for Micro-mechanics Studies

Single, isolated trabeculae were required for micro-mechanical studies. In order to extract single trabeculae from the femoral head, it was important to prepare the tissue using the appropriate clearing and preparation techniques (Section 3.5.3). The single trabecula was prepared for the purpose of a simple bending test and X-ray ultra-microscopy (Chapter 9).

3.5.1 Specimen Selection

Specimen B8 (OA) was selected for this study as it was intact after removal from total hip arthroplasty and was found to be undamaged. It was obtained from the right hip of a 68 year old female patient.

3.5.2 Slice extraction

A series of 0.5 mm thick medio-lateral sectional slices, passing through the fovea (physical slices will be referred to as sectional slices throughout this thesis) were extracted from an OA femoral head (Figure 3.11) using a slow speed diamond saw (Buehler, Illinois, USA).

Thin sectioned slices are often used in histology as this enables simpler preparation when using chemicals for ‘clearing’ or embedding. For the purpose of extracting single trabeculae, it was important to use thin sectioned slices to enable trabeculae to be visually located under a light microscope. It was also important to ensure that the slice contained a significant number of trabeculae for extraction, and 0.5 mm slices were therefore used.

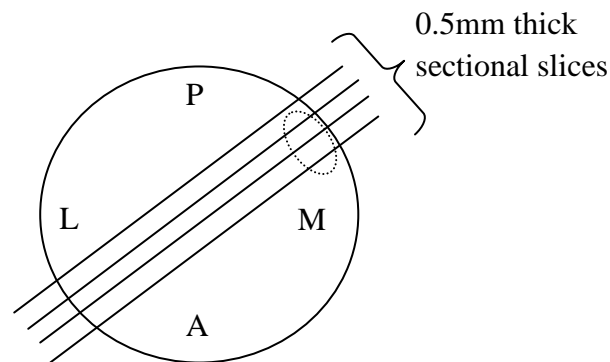


Figure 3.11: A ‘bird’s eye view’ schematic highlighting the sectional slices taken from the medio-lateral region of the femoral head, where the dashed line represents the fovea and the anatomical positions are denoted by; A–Anterior, P-Posterior, M-Medial and L-Lateral

3.5.3 Preparation of calcified tissue

Initially, the specimen slices were placed in IMS, following the same method as discussed in section 3.3.7. Hydrogen peroxide has been used to remove extraneous soft tissue components, leaving mineralised bone or dentine collagen largely intact (Boyde 1984). In this study, the specimens were cleaned using 15% H₂O₂ (50% by volume of stock concentrate).

The specimens were placed in H₂O₂ for 24 hours at 50°C. This is capable of leaving adult osteoid collagen intact, but dissolves cartilage matrix and adult bone ‘ground substance’, (Boyde 1984, Boyde and Jones 1996). The specimens were washed in saline and dried prior to trabeculae extraction.

3.5.4 Trabecula Extraction

Each macerated slice was placed in a glass dish, and submerged in PBS. Dissection was carried out using a fine scalpel (blade size 10) under a light microscope. Trabeculae close to the surface were identified visually through the light microscope and cut manually using a scalpel. Even though this method was found to be time consuming it was proven to be successful as several trabeculae were extracted from one slice, and one trabecula was used for further testing.

3.5.5 Specimen Mounting

The single trabecula was mounted on a stub normally used for SEM, using cyanoacrylate (Loctite Superglue Precision, Henkel, UK). Following bending testing in the ESEM chamber (Chapter 5), the specimen was prepared for nanotomography by careful removal from the stub and mounting onto a thin metal pin using Cyanoacrylate (Loctite Superglue Precision, Henkel, UK).

Chapter 4 Methods

4.1 X-ray Microtomography

This chapter presents the general methodology used throughout this thesis, including an overview of the XMT system, an account of experimental details for different specimens. Section 4.1 presents the experimental details used for the studies in Chapters 5, 6, 7 and 8. This section reports on the 4th generation XMT scanner developed by Davis and Elliott (2003) with Time-Delay Integration (TDI) (Davis *et al.*, 2010).

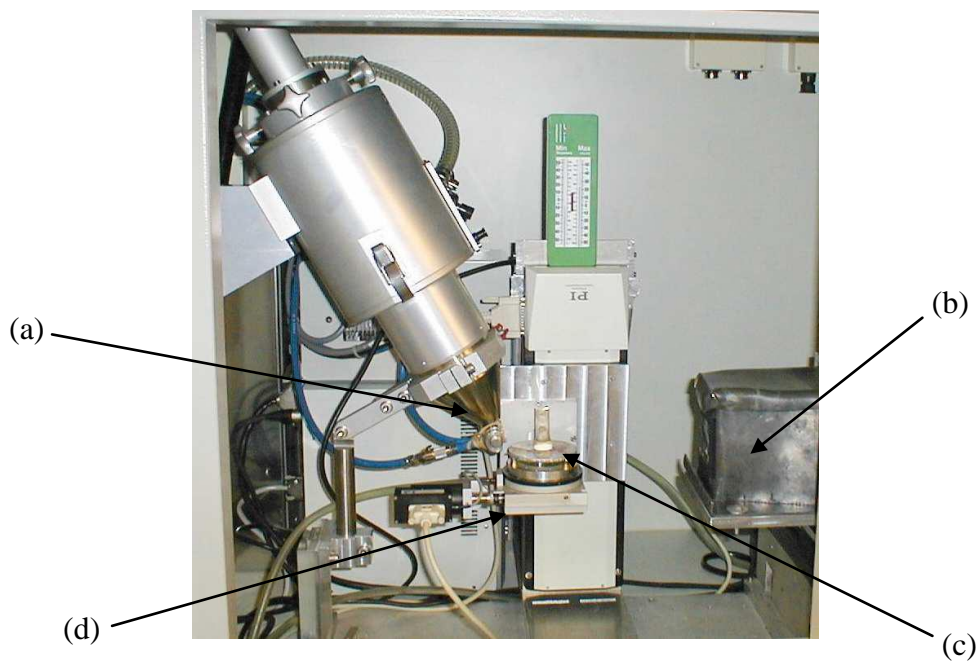
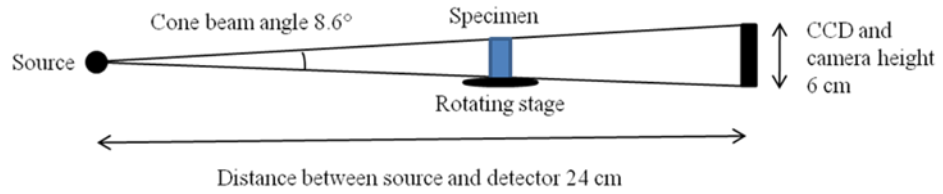


Figure 4.1: An Image of the 4th generation XMT scanner developed by Davis and Elliott (2003), showing (a) the ultrafocus beam system, (b) the TDI CCD, (c) the sample and (d) the rotational stage

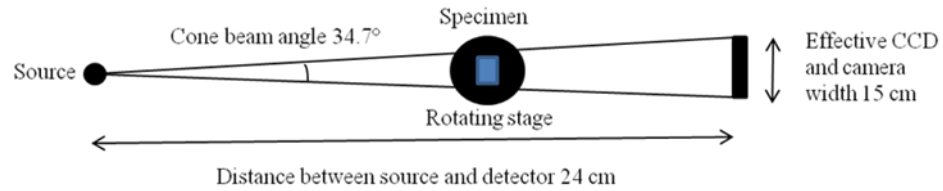
4.1.1 Experimental equipment

An enhanced XMT scanner was used, employing time-delay integration CCD readout, with an X-tek (UK) ultrafocus beam system having a spot size down to 5 μm (highest possible resolution) (Figure 4.1a) and was normally operated at 90 kV, 0.18 mA and with a 0.5mm Al filter. Like 4th generation medical scanners, this system is not susceptible to ring artefacts caused by differences in the characteristics of individual detector elements and is precisely calibrated to minimise the effects of beam hardening (Davis *et al.*, 2008).

A cooled slow scan CCD camera (Spectral Instruments Inc, USA) was used with fibre optic coupling to a 100 μm thick columnar CsI scintillator (Applied Scintillation Technologies Ltd, UK) (Figure 4.1b) The CCD detector had 4096 x 4096 square pixels of dimension 15 μm which are binned 4 x 4 to give 1024 x 1024 square binned pixels of dimension 60 μm . The geometric magnification can be varied to give reconstructed voxel sizes of between 5 and 30 μm . For the purpose of this thesis a 'reconstructed voxel' is defined as a volume element with specific dimensions governed by the resolution. Figure 4.2 shows the set-up geometry of the XMT system.



(a)



(b)

Figure 4.2: (a) Vertical and (b) horizontal geometry of the XMT set-up developed by Davis and Elliott (2003)

The unique TDI CCD (Figure 4.1b) readout method eliminates any ring artefacts by averaging out the characteristics of all the detector elements in each projection. The sample (Figure 4.1c) is placed on the turntable (Figure 4.1d) and at each sequential rotation the camera moves across the X-ray beam and simultaneously the CCD is read out (Figure 4.3). The movement of the camera and the simultaneous CCD read out are timed in a way such that the relative motion of charge along the CCD surface matches that of the focused image (Figure 4.4). Each recorded image pixel is derived from the accumulation of charge as it is moved along the corresponding CCD column. This process takes place for each projection. The air temperature inside the X-ray enclosure is maintained at $26^\circ\text{C} \pm 0.1^\circ\text{C}$ to ensure dimensional stability during data acquisition. Before projections

are taken in this way, a dark reference image is taken, with the CCD shuttered, and then a light reference scan is taken without the specimen in the way of the X-ray beam.

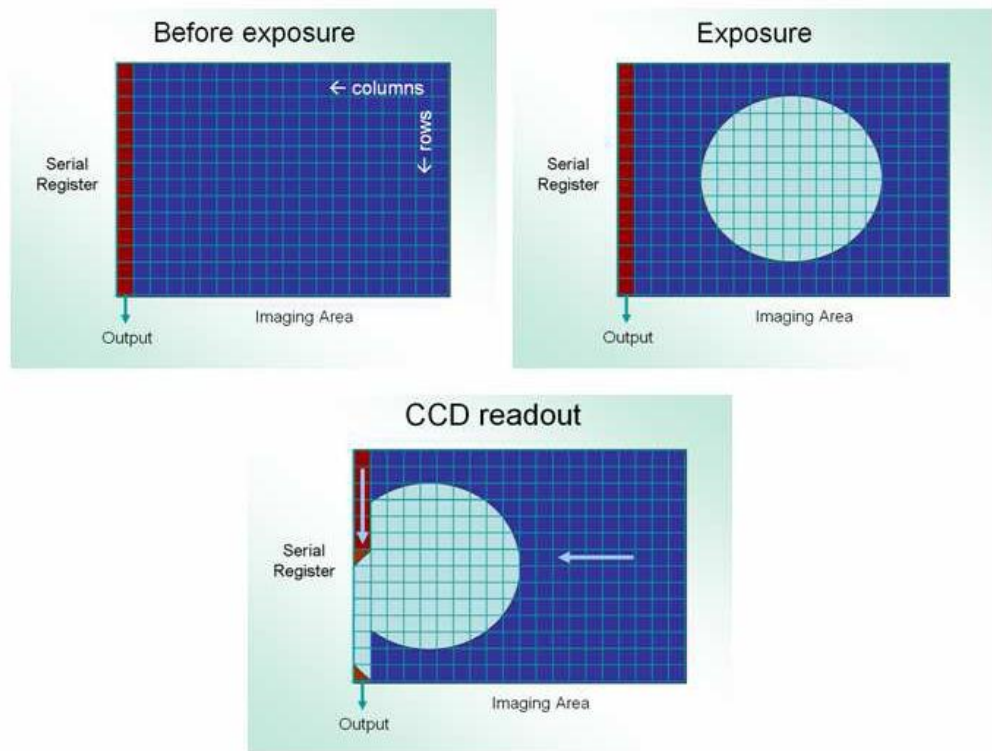


Figure 4.3: Example of a circle being imaged and how the CCD reads out the data (Ahmed, 2010)

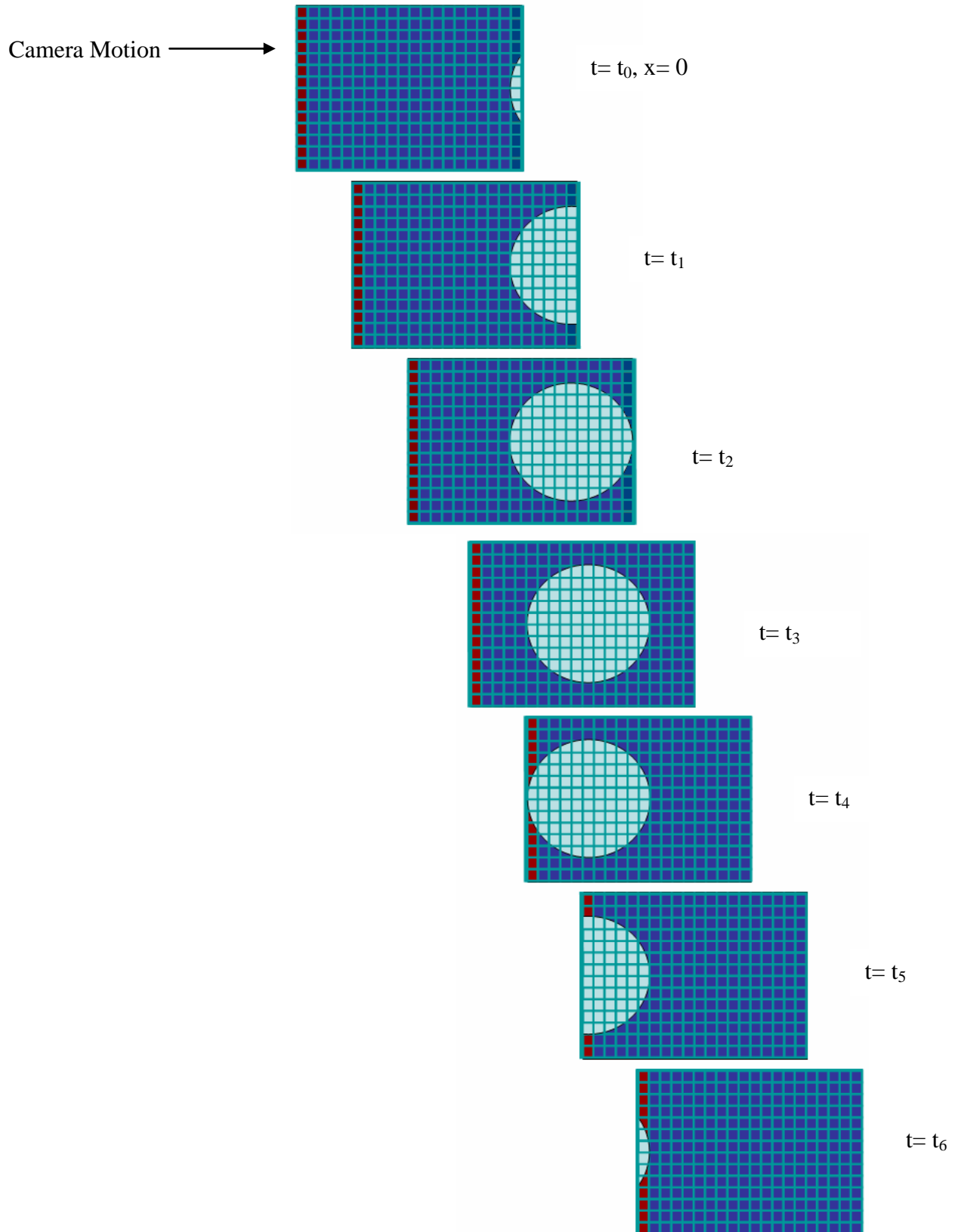


Figure 4.4: Time Sequence showing TDI CCD read out of the captured image (Ahmed, 2010)

A further design feature of the XMT TDI system is its moving collimator. The moving collimator was designed to reduce scattered radiation and thus improve image contrast, resulting in more accurate LAC measurements. It was designed such that it moves in synchrony with the detector thus reducing the portion of the specimen that is illuminated at any point in time. Figure 4.5 shows the difference in scattering with and without the moving collimator.

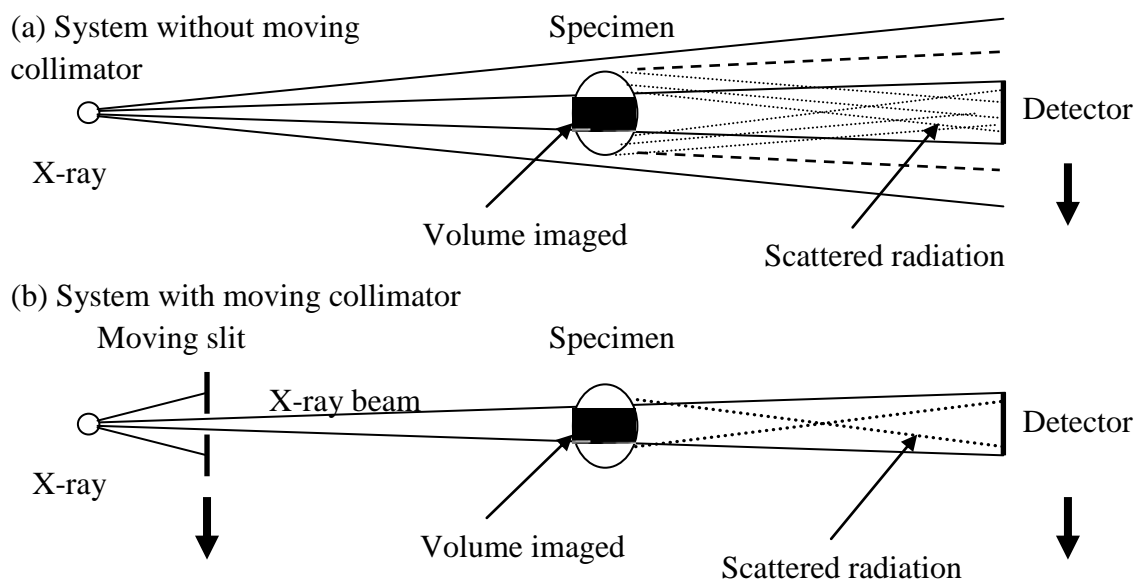


Figure 4.5: Schematic diagram of bird's eye view of XMT system showing the difference between scanning a sample (a) without and (b) with moving collimator (Wassif, 2007)

4.1.2 ‘Block’ scanning

Large specimens were scanned in consecutive blocks of uniform height. The number of blocks and projections for each specimen along with other dimensional parameters are outlined in Chapters 5, 6 and 7 for each study. The specimens were scanned to obtain 3-dimensional volumes of entire specimens at a high resolution. The scan height is limited to the number of ‘slices’ per block, as only a selected volume of the head is covered by the area of the X-ray cone beam.

A slice is defined by the resolution of the image by:

$$\textit{Number of Slices} = \textit{Height/Reconstructed voxel size}$$

i.e. if a specimen is 1mm in height and is imaged at 20µm reconstructed voxel size, there will be 50 resulting virtual slices. For the purpose of this thesis any mention of slices in relation to data interpretation will be defined by virtual slice.

Therefore, in order to build an entire stack of projections for large specimens, they had to be scanned in blocks. This is done by imaging the Region of Interest (ROI) at one full rotation, and then moving the rotating stage to bring in view the next ROI, and so on. It is important to realise here that at no point is the system shut down in between adjusting the height, it is done consecutively, whilst the X-rays are switched on. Figure 4.6 shows a schematic of how ‘block’ scanning was carried out on the femoral heads, imaged in three blocks.

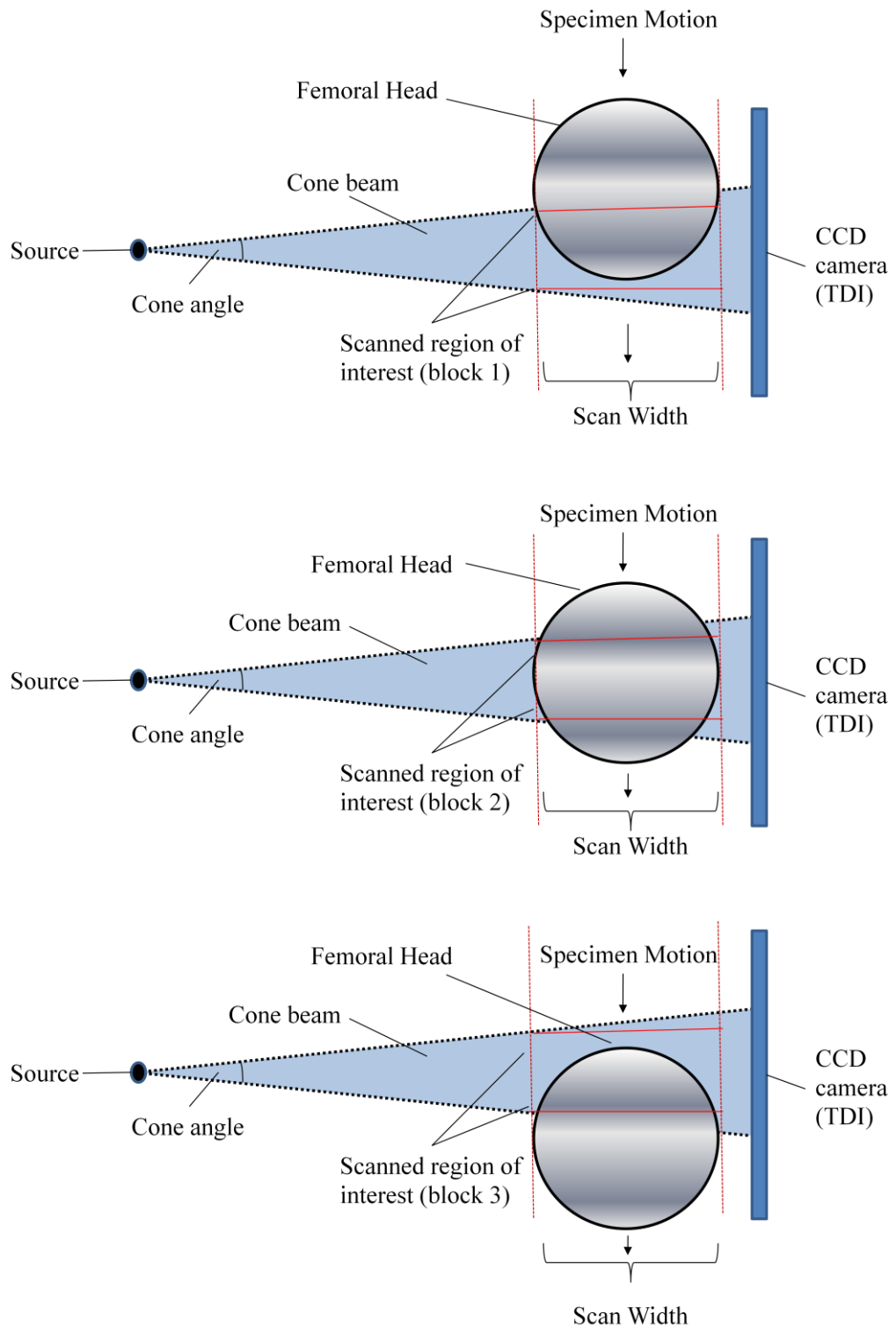


Figure 4.6: Schematic diagram of side view showing 'block' scanning

4.1.3 Signal to Noise ratio

In order to obtain an accurate XMT data set it is important to increase the signal to noise ratio as a high signal to noise ratio is essential for measurements of bone mineral concentration and for accurate segmentation of bone. The noise in the reconstructed image depends on the detected X-ray exposure, the relationship between detected photons and measured X-ray transmission and the reconstruction process (Davis, 1994). To reduce the level of noise in XMT the data collection time is increased. Frame averaging is also carried out; whereby double projections are taken and averaged. This effectively increases the exposure time without saturating the CCD detector, hence contributing to a reduced level of noise.

4.1.4 Calibration

Calibration is an important process to establish the relationship between the recorded X-ray intensity and the attenuating materials in the X-ray beam (Wassif 2007). As discussed in section 2.6, a correction is required for beam hardening due to the nature of polychromatic radiation; this is done by using an appropriate calibration material. It is important to highlight that the calibration material should be of similar nature to the investigated material in regards to its attenuation at any given X-ray energy. Aluminium is considered suitable for the studies of hard tissues, such as bone and teeth (Dowker *et al.*, 1997, Wong *et al.*, 2000) as its behaviour in the absorption of X-rays is similar to that of hard tissues at the X-ray energies of interest. Its attenuation coefficient versus energy relationship is similar to that of hydroxyapatite (HAP) (Figure 4.7) in the low energy range and neither exhibited an absorption edge within the energy range of the MuCAT2 XMT system.

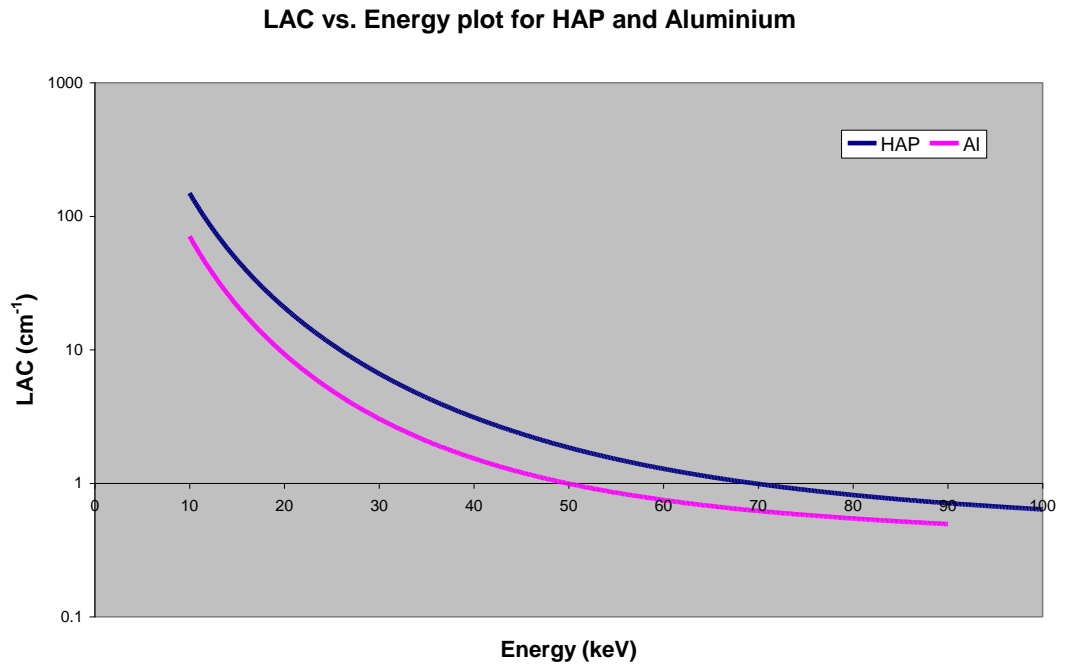


Figure 4.7: Graph showing the LAC of 100% HAP and Aluminium with varying energy (Ahmed, 2010)

A symmetrical ten step wedge (thickest at the centre), made of 99.98% aluminium (Al) was designed to reduce beam hardening artefacts in XMT images (Figure 4.8). Each individual step (each sheet at 0.54mm thickness) was scanned periodically (single projection) at each combination of accelerating potential. This method was described by Davis and Elliott (2003) for beam hardening correction.

In addition, aluminium wire (99.999% purity, Alfa Aesar) was mounted beside the specimen to be scanned simultaneously as a further ‘check’. The LACs of the specimen in the final reconstructed image are calibrated to the measured Al LAC at 40 keV (1.5336 cm^{-1}).

For each CCD column (corresponding to image rows) a 5th order polynomial is fitted to the measured attenuation vs. the calculated attenuation, using published data for a nominal monochromatic radiation, which, for this study was 40 keV (X-ray acceleration voltage 90 kV).

This is because 40 keV is the energy at which the LAC of Al gives 50% attenuation with approximately the same thickness as with the 90 kV polychromatic radiation.

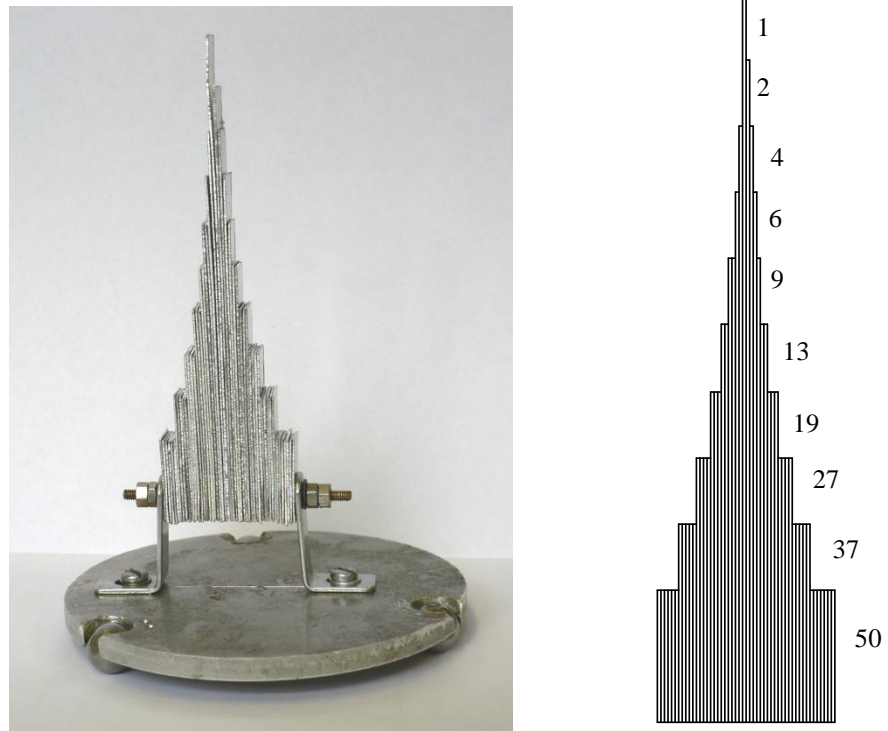


Figure 4.8: Ten Step Aluminium step wedge

4.2 In-vitro Biomechanical Testing

Mechanical testing was carried out inside the XMT system to obtain time-series data. An in-house compression loading device (Figure 4.9) was designed to provide load-extension data for the cylindrical specimens prepared as described in section 3.3.

4.2.1 Description of equipment and method

The loading jig is made of aluminium apart from the internal and external cylinders, which were made of Perspex[®]. A cylindrical geometry was chosen to ensure that the walls of the jig have a uniform contribution to the X-ray attenuation during scanning in the XMT. An initial scan of the strain-device without the specimen was required to measure the attenuation contribution of the strain-device to the overall attenuation of the strain-device plus bone setup. This is subtracted during the reconstruction process so that the resulting attenuation is of the specimen only.

4.2.2 Compression testing

Specimens were compression tested in the XMT system, designed and developed by Prof. Jim Elliott and Dr. Graham Davis, and built by Mr. Steve Figaro (Dental Physical Sciences, Queen Mary University of London) using the schematic shown in Figure 4.9.

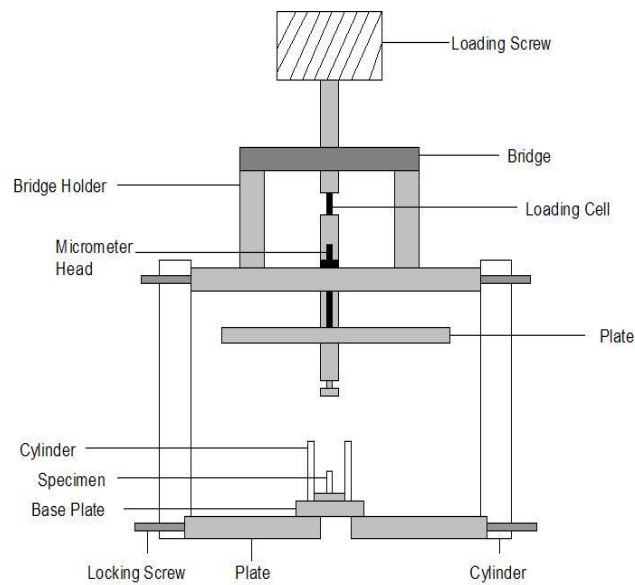


Figure 4.9: A schematic of the loading device

The specimen (Section 3.3) was carefully placed inside the central cylindrical chamber. The compressive load was produced by displacement of a screw-driven upper platen onto unsupported samples placed on a lower fixed platen (Mosekilde *et al.*, 1985; Mosekilde *et al.*, 1987; Fazzalari *et al.*, 1998b; Turner and Burr, 2001). Washers were attached to the platens and the sample placed inside to provide stability for free trabecular ends, minimise effects of misalignment and maximise the contact area between sample and the device. The washers had internal and external diameters of 5.2 mm and 10 mm respectively and a thickness of 1mm. No pre-conditioning was carried out on specimens prior to testing. Extension was measured by displacement of the platen using a micrometer to define the strain increments. Phosphate buffered saline was placed inside the chamber so that the specimen was kept hydrated throughout testing. All load-extension information was recorded manually and converted to stress-strain data (Section 4.8). The device was calibrated to measure compressive load using a dead weight method.

4.2.3 Strain increments

A scan was taken at 0% strain with no load on the sample. Subsequently, scans were taken at 2% increments in the range of 0 to 10% strain. The loading screw was used to drive the upper platen down through the required distance to obtain the 2% strain increment with the displacement measured using the micrometer. The load applied was measured using the integral load cell.

4.3 Data Processing

This section outlines all the methods used to process and analyse the data presented in Chapters 5, 6, 7, 8 and 9.

In order to interpret the data collected using XMT it is essential first to process them into a readable format. The data undergoes three processes:

- Data Collection
- Pre-processing and Linearisation
- Reconstruction

4.3.1 Data collection

The images obtained from XMT are created by directing X-rays through the specimen from different orientations and measuring their resultant intensity. There are a number of variables responsible for the collection of XMT data; the number of projections, exposure time, image resolution, the X-ray tube voltage and current. The specimen rotates step-wise in increments during collection, and each rotation is for a full 360° (Davis, 1994). Each projection represents a rotational interval equal to 360° divided by the total number of views. A specialized algorithm is used to reconstruct the set of projections resulting in a 3D replica of the object.

As a general ‘rule of thumb’ the minimum numbers of projections are calculated for each specimen using equation 4.1,

– **Equation 4.1**

Where, x_d is the diameter of the specimen in pixels (Kak and Slaney, 1998).

Therefore, the greater the diameter of the specimen, the higher the number of projections. The total time for collection of each data set is calculated using the time for each projection multiplied by the number of projections. The total time for each projection includes the fly back time (which is dependent upon sample size but is normally around 2 seconds) and the traverse time. The traverse time is expressed as:

$$t_t = t_x \left(1 + \frac{N + 64}{1024} \right) \quad \text{Equation 4.2}$$

where, N is the specimen width (in pixels) and t_x is the exposure time (minimum 3.3 seconds). 64 is a constant which is derived by adding together the 32 pixels on either side of the specimen. Therefore by adding the constant 64 to N , you get the total distance across the field of view, and the constant 1024 is the width of the CCD detector in binned pixels (Figure 4.10). The resolution of the data (reconstructed voxel size) used during the studies carried out in this thesis ranged from 8.8 μm to 26 μm .

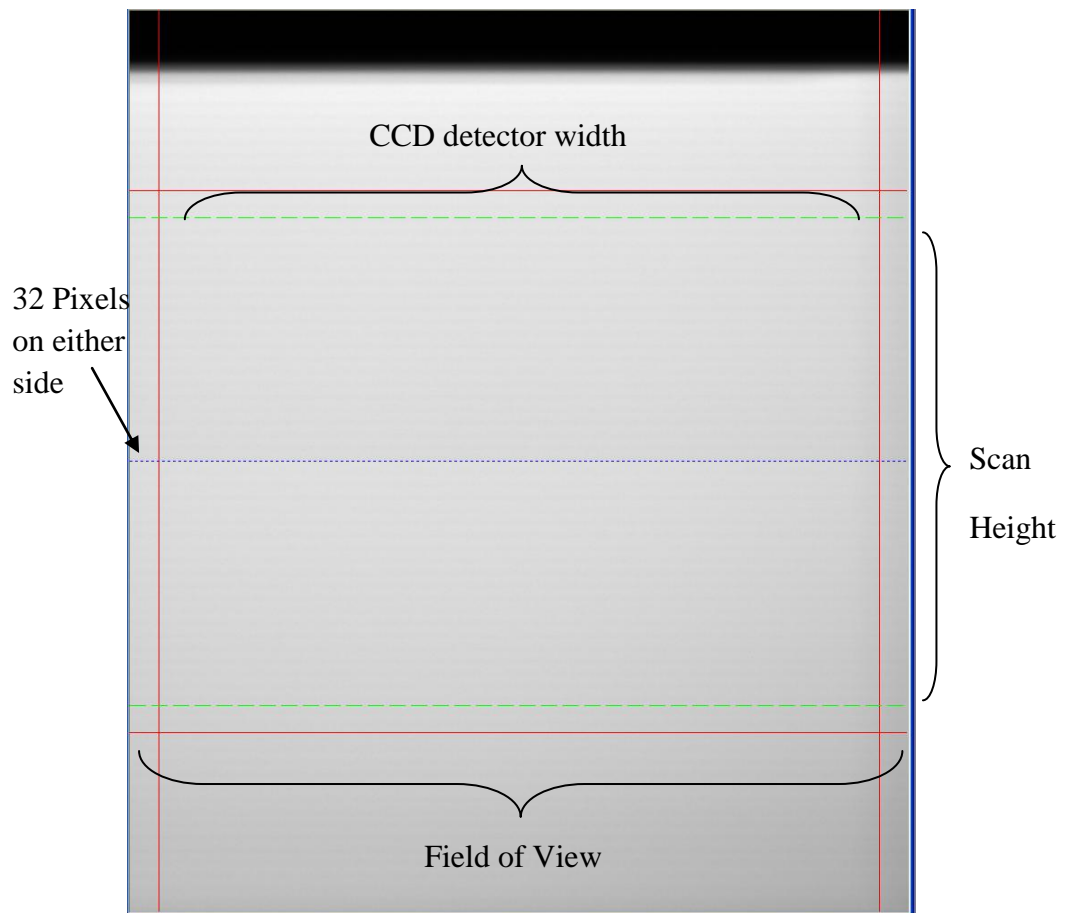


Figure 4.10: The projection window showing the field of view

4.3.2 Pre-processing and Linearisation

A correction, applied for polychromatic radiation (Section 2.6), is carried out during the pre-processing stage of the data reconstruction. This stage of processing is required so that the data can be corrected as though monochromatic radiation was used. The data is corrected so that the values are relative to 40 keV. This is done to normalise all the data to the measured monochromatic LAC value for aluminium. During pre-processing the data, intensity is converted to $\ln \frac{I_0}{I}$ values (Section 2.5) and the polychromatic correction is applied. Initially, the dark reference is deducted from the light reference and the natural log is taken.

A parabola is fitted for each CCD column and for the remaining projections the dark reference is subtracted and the natural log of each projection is taken. It is then necessary to make an adjustment in relation to the mean log of the 32 pixels on either side of the projection, so a further subtraction is made from the appropriate reference parabola and this entire process provides corrected data (described in detail by Kak and Slaney, 2001). Two files are produced here; a .cra text file containing metadata (dimensional parameters) and a .con floating point data file.

4.3.3 Reconstruction

A modified Feldkamp cone beam algorithm (Feldkamp *et al.*, 1984) is used to reconstruct the corrected projections. The floating data point files are loaded into the programme and from each projection the centre of mass is located and the centre of rotation is calculated. The centre of rotation remains constant for all slices. TDI introduces a slight bias in the value for centre of rotation therefore the central slice is reconstructed first. Here, the slice is reconstructed 11 times for a range of centre of rotation offsets (± 5 pixels) with edge enhancements, producing the sharpest possible image. The sharpness is determined from the sum of squares of the edge enhanced image. The centre of rotation is then determined by fitting a parabola to the three highest sharpness values, and finding the peak of the parabola.

After determining the centre of rotation, the entire volume is reconstructed to a 3D volume producing a .bin file containing floating point values corresponding to the reconstructed LAC data (stored in the form of LAC values corresponding to the X, Y, Z co-ordinates of the volume). This processed data is then 'trimmed' (using a program written in IDL[®] Research Systems Inc., Colorado, USA) to reduce the data to the minimum cuboidal volume incorporating the region of interest and converted to 256 grey levels (the user selects a scale determining the ratio between the LAC and grey level). This is done using a histogram showing the grey scale and scale factor; the peak and area under the curve of the histogram determines the ROI.

The relationship is such that,

$$LAC = Greyscale / Scale Factor$$

In addition all the corresponding LAC values of the specimen are altered and normalised to the Al wire, such that the LAC value of the aluminium wire beside the specimen results in a calculated LAC value of 1.5336 cm^{-1} at 40 keV. The mean LAC value for Al can be calculated and using this value an appropriate adjustment factor is applied to the floating point to 8-bit conversion. The final file produced is a .tom file which provides the data in the form of a greyscale image and can be viewed using various visualisation packages.

4.3.4 Resolution Limitations and Errors

It is important to know the cause of different artefacts in XMT images as they can obscure details in the scanned object and they can be problematic in quantitative measurements (Wassif, 2007). One such error, beam hardening, has been discussed in Sections 2.6 and 4.1.4. Ring artefacts can also affect the XMT images, but using the TDI system it is possible to eliminate them (Section 4.1).

It is also important to recognise the effect of voxels containing ‘partial volumes’. In these, a single voxel contains more than one phase and the values of all those phases are averaged to give a single intensity value. These voxels can be either included or excluded during analysis of XMT data depending on the significance. For the purpose of this study partial volume voxels were included (discussed further in Chapter 10).

Balancing the XMT set up with the desired resolution for the XMT data can be challenging. Often, it is recognised that due to sample size, or time constraints a lower resolution may be preferred. Using a lower resolution may not provide all the vital information and so the desired goal may not be achieved. One problem with resolution limitation when imaging specimens such as bone is the edge effect or blurring that can occur. If there are varying sizes of features (as in bone), often

finer structures can be highlighted and appear darker on the greyscale. This can be misleading when quantifying BMC. For example, if one took a bone sample, and the sample contained thick, thin and extremely fine trabeculae, then a line profile of these structures would result in different profiles for a perfect XMT system (Figure 4.11). It can be seen from Figure 4.11c that the profile doesn't plateau in the same manner as for 4.11a and 4.11b; it is this effect that causes the limitation in the XMT image. In any XMT image, at the same reconstructed voxel size, finer features may appear darker on the greyscale simply due to blurring and lack of information.

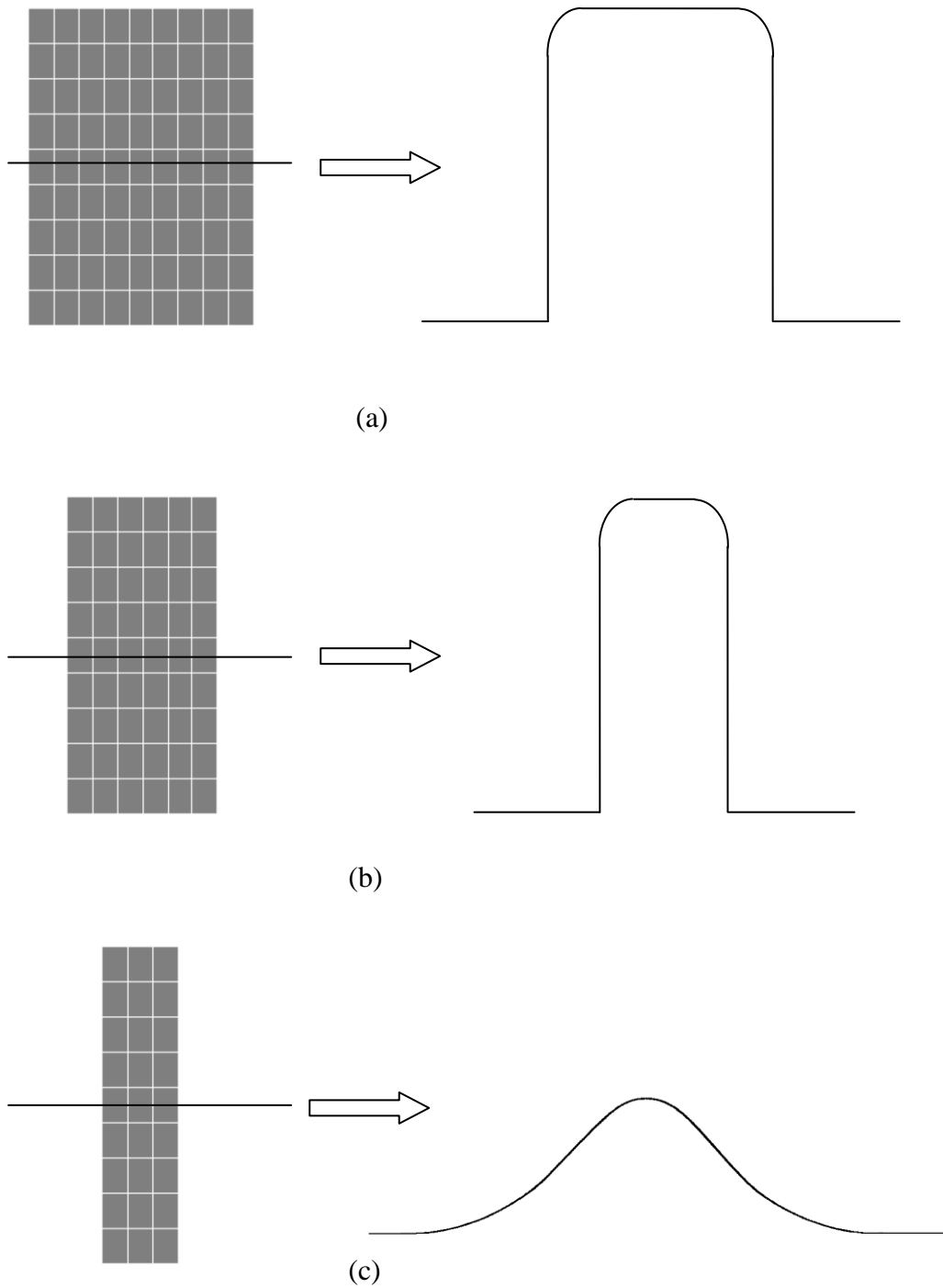


Figure 4.11: Schematic of line profiles taken through (a) a thick trabecula containing several voxels (b) a thin trabecula containing fewer voxels and (c) a very fine trabecula containing very few voxels, for a perfect system

4.4 Visualisation and Analysis

Various types of software used for analysis of the reconstructed XMT data; Drishti (Australia National University, Canberra, Australia), IDL[®], VG Studio Max (Volume Graphics, Germany), Amira[™] (TGS Template Graphics Software, Inc., USA), ImageJ (open source) (with plugin BoneJ, Doube *et al.*, 2010) and Tomview (QMUL, Graham Davis, UK). Drishti was used mainly for manipulation of 3D images, and differentiation of various features of the data set. VG studio was used to handle large data sets for image processing. Amira was used for surface pixel analysis and Tomview (in-house) was used as a reference programme to view the reconstructed data. IDL was used for quantitative analysis using data obtained from reconstructions and ImageJ was used for calculating morphometric parameters from reconstructed data.

4.4.1 Co-ordinate System and Data Location

The image file produced after reconstruction is in the form of a 3D cuboidal volume and can be viewed using Tomview (reference programme). The data is constrained by the x, y and z planes. Therefore any determination of particular features can be defined by a Cartesian co-ordinate system. The data can be viewed in 3 different planes:

- XY
- XZ
- YZ

Using these co-ordinates the location of any particular feature can be defined in 3D. The data is viewed in pixels with the size determined by the resolution used during scanning.

4.4.2 Data Orientation

Chapters 5 and 6 present results for whole femoral heads imaged at high resolution. The femoral heads obtained were either cadaveric or from total hip replacements (THR) as outlined in sections 3.2 and 3.3. Any features determined from the final image volume were defined using the co-ordinate system outlined in section 4.3.1 and are discussed in chapters 5 and 6.

As the head was imaged with the excised (cut) surface down (figure 3.5) , it was not possible to relate the distribution of the features directly to the anatomical loading, therefore, a rotation calculation was needed, so that the data obtained reflected the position of the head in its anatomical position in the body. This rotation is shown schematically in Figure 4.12.

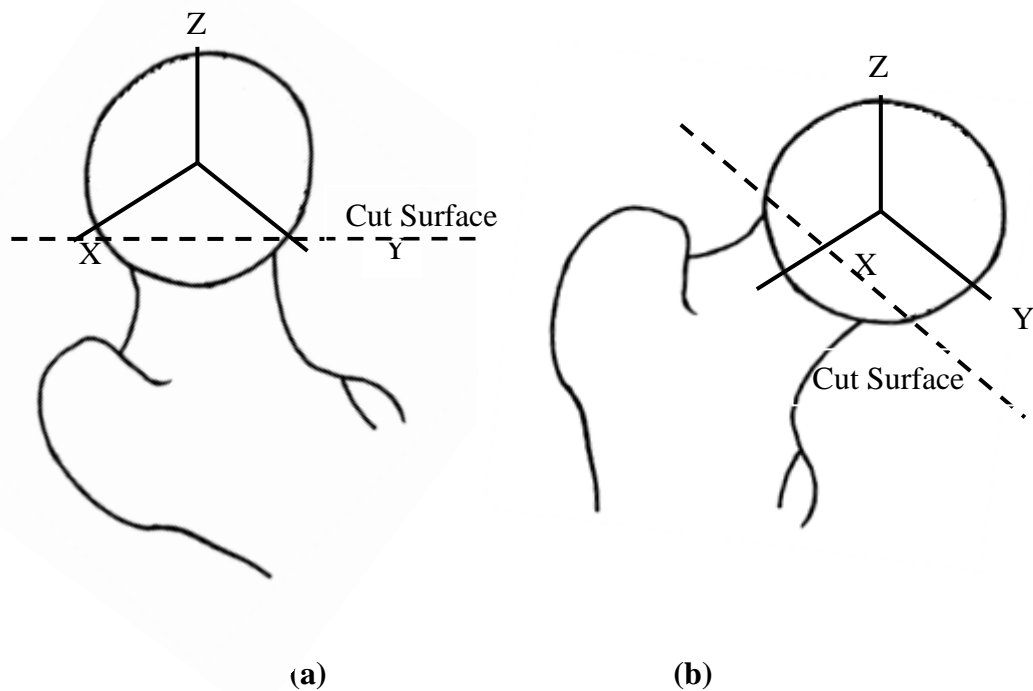


Figure 4.12: Schematic of the anatomical positioning of the femoral head (a) orientation as imaged (b) image data rotated to anatomical orientation

4.4.4 Object transformation

This section presents the system that was developed for identifying the position of features within the 3D XMT data set with respect to anatomical position. The following object transformation was applied to determine the position of the femoral head in its anatomical loading pattern.

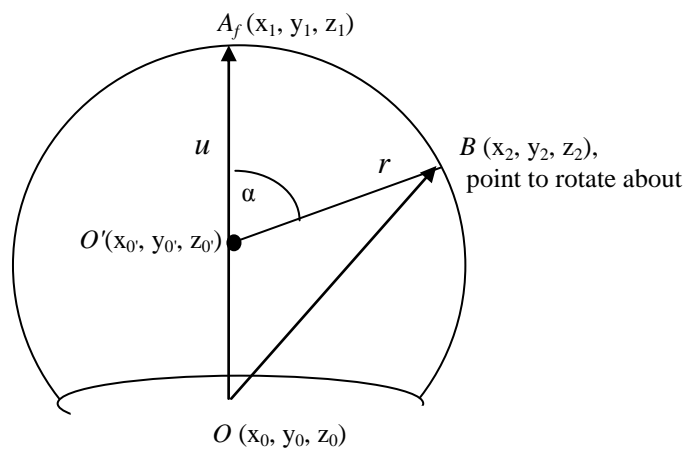


Figure 4.13: Data orientation of co-ordinates

Where,

A_f is the position of the Fovea

B is the required position for the Fovea

O is the origin

O' is the new origin

α is the angle of rotation

The origin is defined as $O(x_0, y_0, z_0)$. Two vectors are defined about the origin $A(x_1, y_1, z_1)$ and $B(x_2, y_2, z_2)$. In order to determine the transformation of coordinates (defining any features) when the axes are rotated through an angle α about an axis through the new origin O' having direction u , we first consider the rotation of a vector \underline{r} about this axis.

where,

$$\vec{O}' = \begin{bmatrix} 0_1 \\ 0_2 \\ 0_3 \\ 1 \end{bmatrix} \quad \vec{A}_f = \begin{bmatrix} a_1 \\ a_2 \\ a_3 \\ 1 \end{bmatrix} \quad \vec{B} = \begin{bmatrix} b_1 \\ b_2 \\ b_3 \\ 1 \end{bmatrix}$$

Where, the magnitude of the cross product is obtained using \underline{a} \underline{b} ,

$$\underline{a} = \vec{A}_f - \vec{O}' = \begin{bmatrix} a_1 \\ a_2 \\ a_3 \\ 0 \end{bmatrix}$$

$$\underline{b} = \vec{B} - \vec{O}' = \begin{bmatrix} b_1 \\ b_2 \\ b_3 \\ 0 \end{bmatrix}$$

The cross product is defined by,

$$\underline{a} \times \underline{b} = \begin{bmatrix} \underline{i} & \underline{j} & \underline{k} \\ a_1 & a_2 & a_3 \\ b_1 & b_2 & b_3 \end{bmatrix} = \begin{bmatrix} C_1 \\ C_2 \\ C_3 \end{bmatrix}$$

Where,

$$\begin{bmatrix} C_1 \\ C_2 \\ C_3 \end{bmatrix}$$

defines a direction perpendicular to both \underline{a} and \underline{b} which allows the calculation of the angle of rotation required, and then enables the rotation around its new axis using the components of its unit vector.

$$|C| = |\underline{a} \wedge \underline{b}| = |\underline{a}||\underline{b}|\sin \alpha \quad \text{Equation 4.3}$$

By re-arranging equation 4.3 it is possible to find $\sin \alpha$, so;

$$\sin \alpha = \frac{|\underline{a} \wedge \underline{b}|}{|\underline{a}||\underline{b}|}$$

and so the unit vector ,

$$\hat{u} = \frac{|\underline{a} \wedge \underline{b}|}{|\underline{a}||\underline{b}|\sin \alpha} \quad \text{Equation 4.4}$$

Here, \hat{u} (unit vector) (Equation 4.4) components are substituted into the following matrix for the rotation calculation,

$$\begin{bmatrix} u_1^2 + \cos \alpha \left(-u_1^2 \right) & u_1 u_2 \left(-\cos \alpha \right) - u_3 \sin \alpha & u_3 u_1 \left(-\cos \alpha \right) + u_2 \sin \alpha \\ u_1 u_2 \left(-\cos \alpha \right) + u_3 \sin \alpha & u_2^2 + \cos \alpha \left(-u_2^2 \right) & u_2 u_3 \left(-\cos \alpha \right) - u_1 \sin \alpha \\ u_3 u_1 \left(-\cos \alpha \right) - u_2 \sin \alpha & u_2 u_3 \left(-\cos \alpha \right) + u_1 \sin \alpha & u_3^2 + \cos \alpha \left(-u_3^2 \right) \end{bmatrix}$$

Now this rotation is applied to the axis directions i, j, k (original co-ordinates of the feature) to find the new axis directions and hence deduce the corresponding co-ordinate transformation.

From Figure 4.14 it can be seen that once the femoral head rotation is applied to the data, the distribution of the features can be related to the anatomical loading based on Figure 3.8.

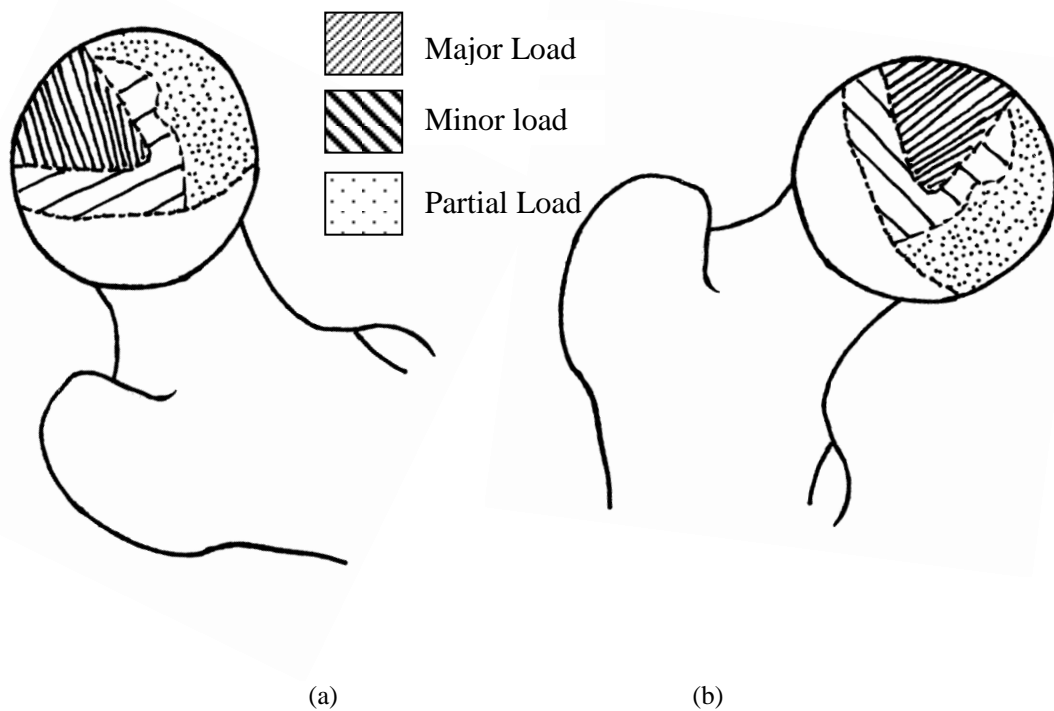


Figure 4.14: Load-bearing regions of a left femoral head; (adapted from Brown and Shaw, 1983; Sharp, 1988), (a) the position of the femoral head during imaging in the XMT, and (b) as orientated *in vivo*

Radial Distribution

In order to determine the radial distribution for the femoral head the centre must be defined

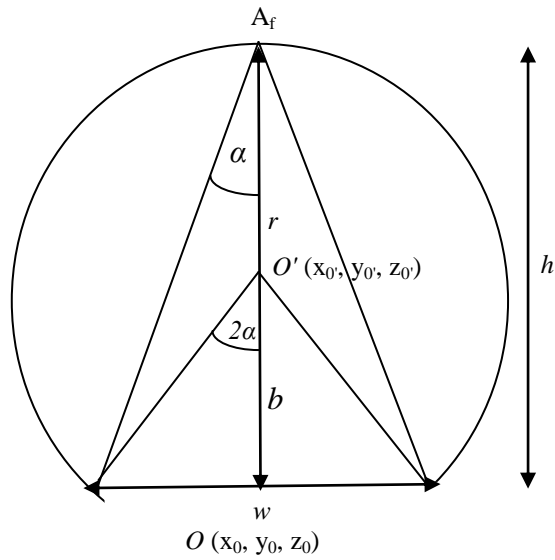


Figure 4.15: Femoral head geometry for radial distribution

The height, h , and width of the base, w , are measured from the reconstructed data set, in microns. The distance r is between the new origin and the top of the femoral head A . The distance between the origin and new origin, b , can be determined by first calculating the angle α ,

$$\tan \alpha = \frac{\frac{1}{2}w}{h} \quad \text{So,} \quad \alpha = \tan^{-1}\left(\frac{w}{2h}\right)$$

As,

$$\tan 2\alpha = \frac{\frac{1}{2}w}{b} \quad \text{therefore,} \quad b = \frac{\frac{1}{2}w}{\tan 2\alpha}$$

$$\text{And } r = \frac{\frac{1}{2}w}{\sin 2\alpha}$$

Now we have the centre of the head as $(0,0,b)$

We then centre all the original co-ordinates, on the centre of the femoral head, by subtracting $(0,0,b)$ from the original (x,y,z) .

In order to measure the density of the sites as a function of distance from the centre of the head the points of interest are binned into consecutive radial shells, as seen in Figure 4.16.

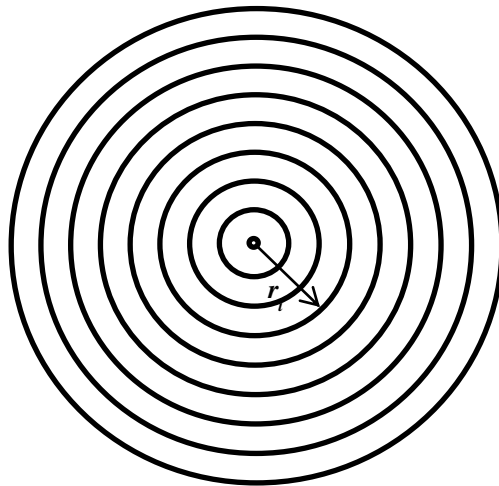


Figure 4.16: Binned radi

So as to normalise each shell to give the density of points per unit volume each shell must be normalised by its volume. Here, the volume for each shell will be;

$$\begin{aligned} \frac{4\pi}{3} (r_{i+1}^3 - r_i^3) &= \frac{4\pi}{3} (r_i^3 + \Delta r^3 - r_i^3) \\ &= \frac{4\pi}{3} (r_i^3 + 3r_i^2\Delta r + 3r_i\Delta r^2 + \Delta r^3 - r_i^3) \end{aligned}$$

Therefore the volume of the shell;

$$= \frac{4\pi}{3} (r_i^2\Delta r + 3r_i\Delta r^2 + \Delta r^3)$$

So if N_f features are found at r_i , the density of points (points per unit volume) will be;

$$P = \frac{N_f}{\frac{4\pi}{3} (r_i^2\Delta r + 3r_i\Delta r^2 + \Delta r^3)}$$

Where,

P is the probability of finding a particular feature at radius r from the centre of the femoral head.

N_f is the number of any particular feature

r is the radius

Angular Distribution

In order to understand the variation in distribution of a feature in relation to load bearing, it is essential to determine the angular distribution corresponding to the longitudinal and latitudinal directions, similar to that of 'co-ordinates on a globe'. This is done by transforming the original co-ordinates (x_0, y_0, z_0) , to the polar co-ordinates (θ, ϕ, r)

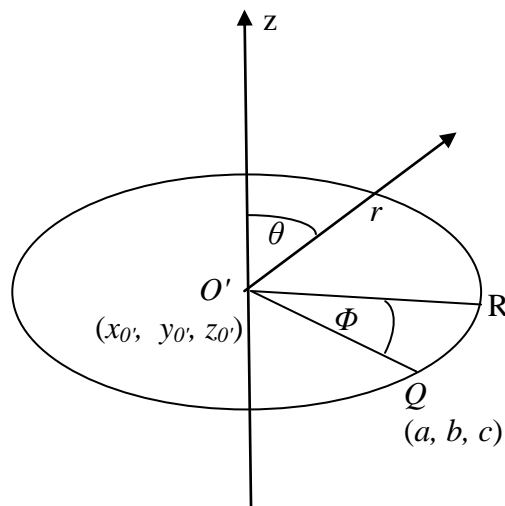


Figure 4.17: Geometry for angular distribution

Q is defined as the centre of the fovea on the femoral head to provide an anatomical reference for any feature, with co-ordinates (a, b, c) and r is the radius.

The original co-ordinates must be centred on the sphere's new origin (x_0', y_0', z_0') , as seen in Figures 4.13 and 4.14. If R is defined as an outer radius of the femoral head, then any internal radius, i.e. the distance from the centre to that point, is r such that $0 \leq r \leq R$

Therefore,

$$R = \begin{bmatrix} a \\ b \\ c \end{bmatrix} = \begin{bmatrix} R \sin \theta \cos \phi \\ R \sin \theta \sin \phi \\ R \cos \theta \end{bmatrix}$$

So as R is known for this point

$$R = \sqrt{a^2 + b^2 + c^2}$$

Hence

$$\cos \theta_0 = \frac{c}{R} \quad \text{so,} \quad \theta_0 = \cos^{-1}\left(\frac{c}{R}\right)$$

Hence

$$\sin \phi_0 = \frac{b}{R \sin \theta_0} \quad \text{so,} \quad \tan \phi = \left(\frac{a}{b}\right); \quad \phi = \tan^{-1}\left(\frac{a}{b}\right)$$

This gives a value of Φ_0 for point Q (the fovea), which has to be subtracted from all other values of Φ calculated for the feature, defining the fovea as Φ equal to 0. This shift of values then gives comparable data sets. It is important to take into account the negative or positive sign of the value as this determines which quadrant the value lies within for the ‘co-ordinate map’.

So for the features centred around point Q with co-ordinates (x_l, y_l, z_l) , we calculate;

$$\begin{bmatrix} x_1 \\ y_1 \\ z_1 \end{bmatrix} = \begin{bmatrix} r \sin \theta \cos \phi \\ r \sin \theta \sin \phi \\ r \cos \theta \end{bmatrix}$$

$$\text{So,} \quad r = \sqrt{x_1^2 + y_1^2 + z_1^2}$$

Therefore;

$$\theta = \cos^{-1}\left(\frac{z_1}{r}\right) \quad \text{and} \quad \tan \phi = \left(\frac{x_1}{y_1}\right); \quad \phi = \tan^{-1}\left(\frac{x_1}{y_1}\right)$$

$$\text{Which, becomes } \phi' = \phi_1 - \phi_0 \quad \text{and} \quad \theta' = \theta$$

4.5 Qualitative Analysis

All qualitative analysis was carried out using Drishti , VG Studio and Amira, with Drishti introducing a 2D transfer function approach which is described in this section (Volume rendering), along with the more conventional single thresholding boundary method (Surface rendering).

Surface Rendering

Surface Rendering (SR) is the visualisation of a surface, from a geometric approximation of an isosurface, within a volume data set; where an isosurface is a surface formed from a cross connection of data points, within a volume, of equal value or density (Roberts, 1993).

This method works by interpreting data-sets by generating a set of polygons that represent the anatomical surface, and displaying a three dimensional model representation. Polygons representing the outer surface of an object can be calculated using a variant of a “marching cubes” algorithm (Lorenson and Cline, 1987). The method of identifying surfaces of interest is often referred to as segmentation or thresholding. Programmes used in this project, such as ImageJ (to determine Bone Quality) and Amira (to analyse line profiles) use the surface rendering approach.

Volume rendering

Volume Rendering (VR) is the direct visualisation of any three dimensional volume data set; without the use of an intermediate geometric representation for isosurfaces' and is a more direct way for reconstruction of 3D structures (Roberts, 1993). Volume rendering represents 3D objects as a collection of cube-like building blocks called voxels, or volume elements. Each voxel is a sample of the original volume, a 3D pixel on a regular 3D grid. Each voxel has associated with it one or more values quantifying some measured or calculated property of the original object, such as transparency and density.

Drishti and VG Studio Max were used throughout this project for qualitative image analysis and use volume rendering (further discussed in Section 4.5.1). The main advantage of this type of rendering is its ability to preserve the integrity of the original data throughout the visualization process.

4.5.1 2D Transfer Function and Thresholding

In general a segmented data set is a required for most quantitative analysis. Segmentation of CT data can be difficult due to the artefacts in micro CT images such as blurred interfaces due to resolution limitation and the partial volume effect (Section 4.3.4). Therefore the segmentation can be biased and prone to errors. Most commonly, a histogram resulting from the image data is thresholded using a single value to determine where one phase ends and another begins (Figure 4.18).

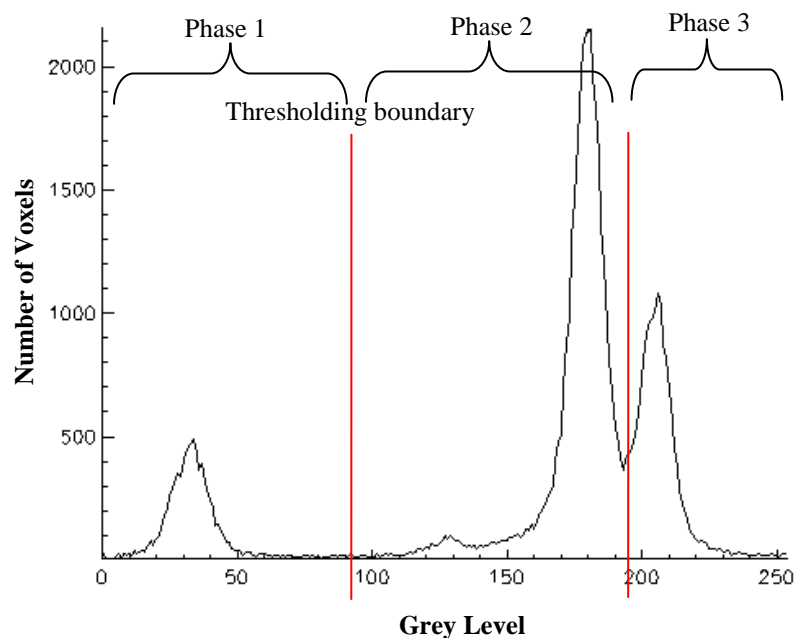


Figure 4.18: Histogram with single thresholding boundary approach

More recently methods using 2 dimensional histograms have been proposed and implemented using XMT data sets (Limaye, 2006; Zou *et al.*, 2007). For qualitative analysis, this project mainly uses Drishti (Australia National University, Canberra, Australia) to define particular features in the XMT data sets using the 2D histogram approach (Figure 4.19).

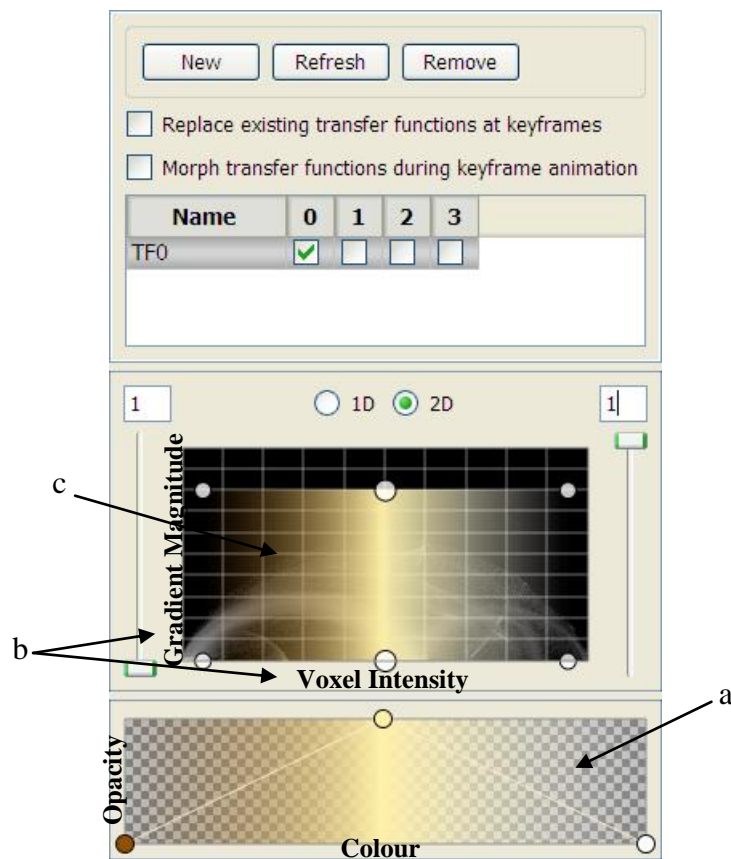


Figure 4.19: 2D transfer function editor has 3 sections; (a) colour-opacity gradient interface, (b) horizontal axis represents the voxel intensities, and vertical axis represents the rate of change of voxel intensity (gradient magnitude) and (c) manager, plotting interface

In Drishti, transfer functions map voxel information in the form of volume rendering (Section 4.5). Drishti implements the transfer function as 256 × 256 lookup table of colours and opacities (Figure 4.19a). The transfer function is used to determine the interface between two phases. The gradient magnitude is defined by the gradient between one voxel to its neighbouring voxels. Gradients are always at the interface and homogenous material is always at zero (Figure 4.20). Using the gradient magnitude and the voxel intensity the 2D histograms are formed representing the data set (Figure 4.19b). Furthermore, the 2D histogram can then be thresholded by manipulating various shapes and colours from the transfer function editor using the plotting interface (Figure 4.19c) to define boundaries between features. It is important to note that two voxels of the same greyscale value cannot be differentiated using the single thresholding approach, whereas with the 2D transfer function using Drishti, it is possible.

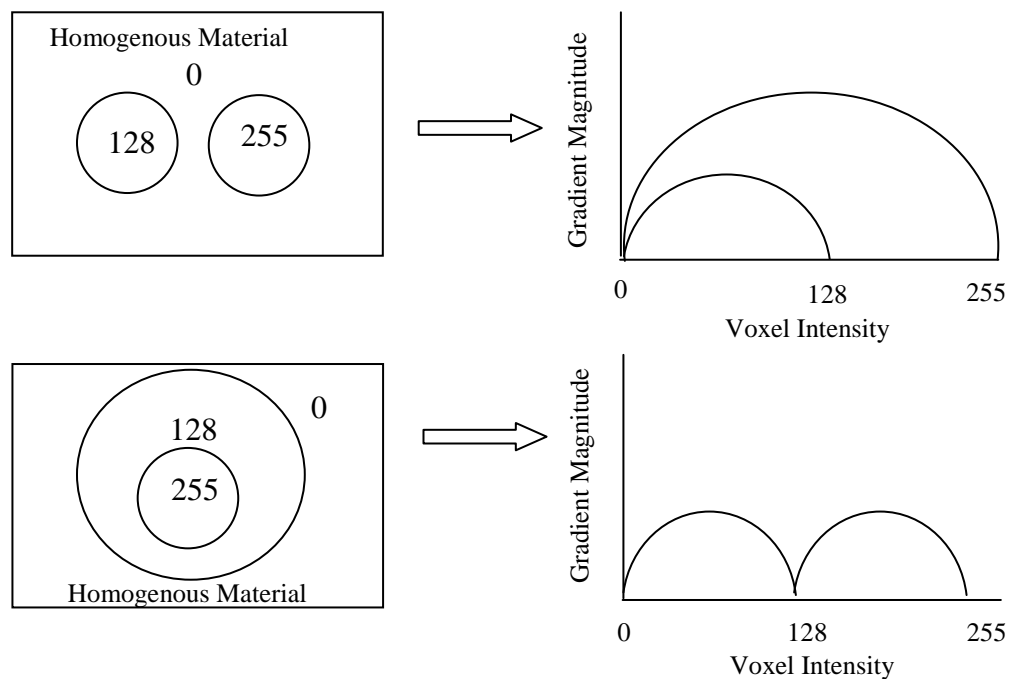


Figure 4.20: Homogenous material with different arrangements of voxels resulting in different gradients, hence different 2D histograms

4.6 Bone Quality Measurements

Bone Quality has been defined for this project in Section 1.5. A total of eight morphometric parameters were measured using ImageJ software (open source), and their definitions are given below.

Bone Volume Fraction

Bone volume fraction (BVF) represents the fraction of the volume of interest (VOI) that is occupied by bone, where BV represents the occupied bone volume and TV the tissue volume (total volume). TV is defined as the union of trabecular bone volume and marrow space volume ($TV = |Bone \cup Marrow|$).

Therefore,

$$BVF = \frac{BV}{TV}$$

and

$$\text{Marrow Volume Fraction} = \frac{MV}{TV},$$

therefore,

$$BVF + \text{Marrow Volume Fraction} = 1$$

Specific Surface area

Specific surface area (BS/BV) represents the bone surface area (BS) relative to the bone volume (BV). BS is calculated as the total area of triangles resulting from the triangulation of the surface of voxels in the 3D model using the well established marching cubes algorithm (Lorensen and Cline, 1987).

Total Surface area

Total surface (BS/TV) represents the bone surface area (BS) relative to the tissue volume (TV) of the volume of interest. Bone surface area (BS) was calculated in the same manner as for specific surface area (BS/BV).

Trabecular Thickness

Trabecular thickness (Tb.Th) represents the mean thickness of trabecular elements in the volume of interest (VOI) and can be measured using either model-dependent or model-independent measures of thickness.

Model-dependent measures of geometric parameters are based on assumptions of fixed structural models. These methods allow derivation of 3D structural parameters from 2D histological measurements of bone area fraction and bone perimeter through well established stereological principles (Parfitt *et al.*, 1987; Russ and Dehoff, 2000). The parallel-plate model (Hildebrand and Ruegsegger, 1997; Parfitt *et al.*, 1987) models the trabecular structure as a series of parallel plates (Figure 4.21). Given the measurement of BVF and BS/TV described above,

— **Equation 4.5**

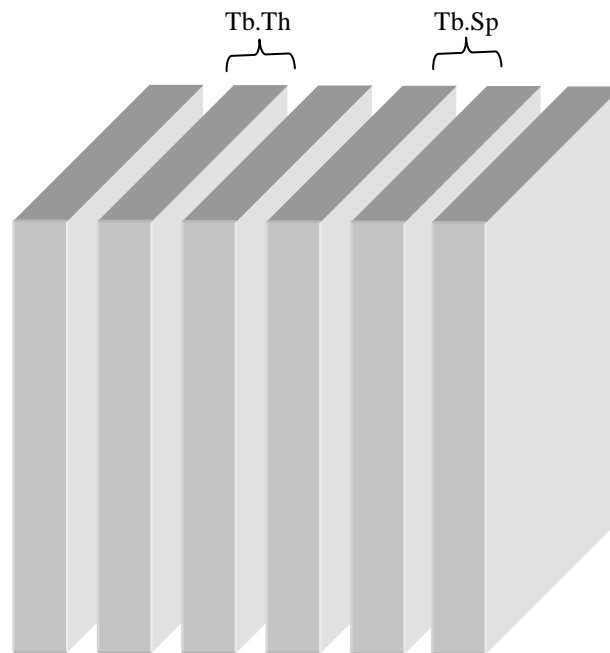


Figure 4.21: Illustration of the parallel-plate model

3D model independent measurements of Tb.Th were calculated via direct 3D morphometric analyses using ImageJ software described by Dougherty and Kunzelmann (2007) based on Hildebrand and Ruedegger (1997b), and Saito and Toriwaki (1994).

Here, Tb.Th is defined as the thickness at a point, being the diameter of the greatest sphere that fits within the structure and which contains that point (Hildebrand and Ruedegger, 1997a, 1997b; Dougherty and Kunzelmann, 2007), (Figure 4.22).

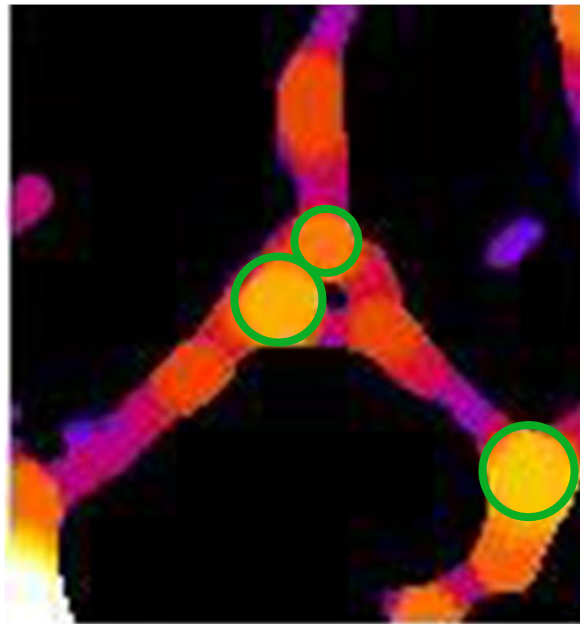


Figure 4.22: An image measuring 130 150 pixels (where 1 pixel = 25 μ m) obtained from ImageJ, where the green circles denote the sphere used to calculate trabeculae thickness,

Trabecular Number

Trabecular Number (Tb.N) is a linear density measure representing the number of intersections made across a trabecular structure for a linear path through the trabecular structure (Parfitt *et al.*, 1987, Russ and Dehoff 2000). For the parallel plate model:

————— **Equation 4.6**

3D model independent measurement employs use of 3D model independent Tb.Th and BVF measured from the 3D structure. Thus, for the 3D model-independent technique,

— **Equation 4.7**

Trabecular Spacing

Trabecular Spacing (Tb.Sp) is a measure of the separation between the edges of trabecular bone elements (Figure 4.21). Similar to Tb.Th, Tb.Sp can be measured using both model-dependent and model independent techniques. Using the parallel-plate model (Parfitt *et al.*, 1987),

— **Equation 4.8**

3D model-independent measurements of Tb.Sp are made using the same technique as that for calculating Tb.Th except that the algorithm is applied to non-bone voxels of the 3D structure (Hildebrand and Ruesgsegger, 1997a and 1997b; Dougherty and Kunzelmann, 2007) as shown in Figure 4.23.

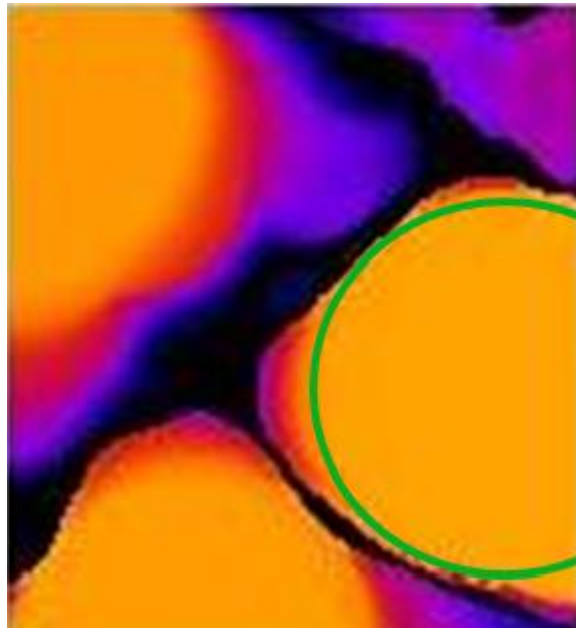


Figure 4.23: A resulting image measuring 130 x 150 pixels (where 1 pixel = 25 μ m) obtained from ImageJ when calculating trabeculae spacing, where this image is the inverse of the image in Figure 4.22. The green circle defines the sphere used to calculate the trabecular spacing

Connectivity Density

Connectivity Density is a measure of the number of redundant elements in the trabecular bone structure (Odgaard, 2001). Connectivity centres around the Euler number (χ) (Odgaard, 1997 and 2001), where in a 3D trabecular structure with β_1 redundant connections,

Equation 4.9

ImageJ uses the BoneJ plug-in (Doube *et al.*, 2010) for connectivity; using voxel neighbourhoods to calculate the Euler characteristic of the volume, and adjusts this to give the contribution of the volume to the connectivity of the structure it

was cut from. The assumption made is that there is only one particle in the foreground. Connectivity Density (Conn.D) is defined as,

— **Equation 4.10**

Structure Model Index

The Structure Model Index (SMI) was developed by Hildebrand and Ruesegger (1997b) as a way of quantifying the prevalence of plate-like and rod-like elements within a trabecular structure (Hildebrand and Ruesegger, 1997b). SMI is based on a calculation of bone volume and bone surface (BS). SMI calculates the BS before and after simulated dilation and is defined as,

———— **Equation 4.11**

In the case of an ideal plate, ideal cylinder and ideal sphere, the SMI has values of 0, 3, and 4, respectively (Hildebrand and Ruesegger, 1997b).

Degree of Anisotropy

Degree of Anisotropy (DA) is a measure of preferential alignment. DA is calculated using information obtained from assessment of the mean intercept length (MIL) (Whitehouse, 1974). The MIL is found by dividing the length of test lines in 3D by the number of intersections between these test lines and the trabecular structure.

The DA is then derived from the eigenvalues resulting from the best-fitting ellipsoid to the 3D MIL data, where DA is the ratio of maximum eigenvalue to minimum eigenvalue (Odgaard, 1997 and 2001).

4.7 Measurement of Bone Mineral Concentrations

BMC was calculated using IDL software with IDL calculating the LAC of each voxel in a given data set. The mean LAC of each data set was calculated and used to define the BMC for each data set or region of interest. A uniform thresholding value approach was used to determine the region of interest (Figure 4.18). This was then normalised using the assumptions that pure hydroxyapatite (3.15 g cm^{-3}) attenuated at 3.16 cm^{-1} (using published data) using the in-house Xabs programme (Graham Davis, QMUL, UK). The LAC value for space (or solution) was used to define pure collagen, by making the assumption that pure collagen attenuates at the same value as water (or glycerol). This was measured from the resulting XMT data sets and found to be 0.27 cm^{-1} . a linear relationship was assumed (Figure 4.24) to give relative measure of BMC between the specimens.

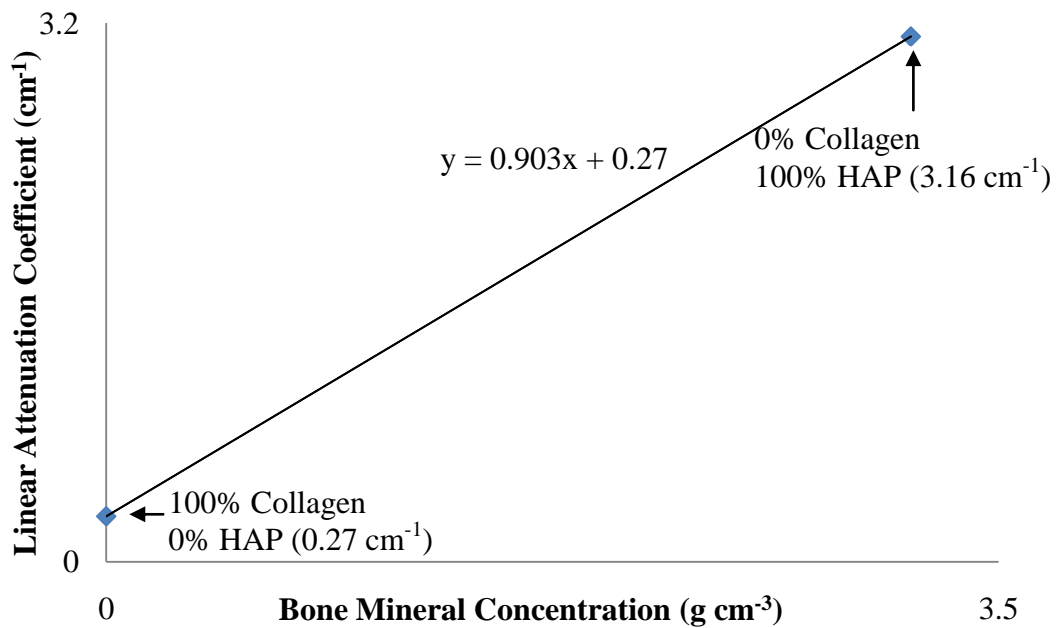


Figure 4.24: Assumed linear relationship between LAC and BMC based on theoretical values for pure hydroxyapatite and measured values for collagen (modelled as water) from XMT data sets

4.8 In-vitro Biomechanical Testing Analysis

All mechanical testing was carried out *In-vitro* using the in-house strain device (Section 4.2). Load was converted to stress by normalizing the instantaneous load by the surface area to which the load was being applied

————— **Equation 4.12**

Extension (mm) was converted to strain (%) by normalising the dimension of the cylinder parallel to the load-train (original height),

————— **Equation 4.13**

4.9 X-ray Ultra-Microscopy (XuM)

The X-ray Ultra-Microscope (Gatan Inc.) is an accessory to a scanning electron microscope (SEM), which uses X-rays generated by the electron beam striking a metal target, to allow the 2D and 3D-visualisation of the internal structure of specimens in the SEM. It is capable of producing sub-micron 3D computed tomography (CT) of specimens (Howard *et al.*, 2010). XuM was used in the work carried out in Chapters eight and nine.

4.9.1 Experimental equipment

The Gatan XuM is mounted onto a Philips XL30, high vacuum, field emission gun SEM (Natural History Museum, London). The XuM is fully integrated with the SEM, allowing easy conversion between SEM mode and XuM mode. The specimen preparation is outlined in Sections 3.4 and 3.5.

As in the original Cosslett-Nixon X-ray microscope, the electron beam of the SEM is used to create a cone of X-rays by focusing the beam onto a gold target. The minimum acceleration voltage used was 20 kV, resulting in a 9.7155 keV X-ray energy and spot 6 setting for beam current. The smaller the excitation volume, the smaller the X-ray ‘source’, and the greater the resolution. As the acceleration voltage (kV) of the electron beam is increased the X-ray excitation volume also increases, thus, in order to achieve the best resolution, lower acceleration voltage was used which was sufficient to generate a high flux of characteristic X-rays.

The specimen, which is offset to one side of the electron beam, is placed within the X-ray cone and the resulting X-ray absorption image is projected onto a CCD (1340 x 1340 pixels) behind the specimen as shown in Figure 4.25. The fundamental principles are similar to those of a microtomography system, only differing in the initial source used to generate the X-rays, and a static CCD camera.

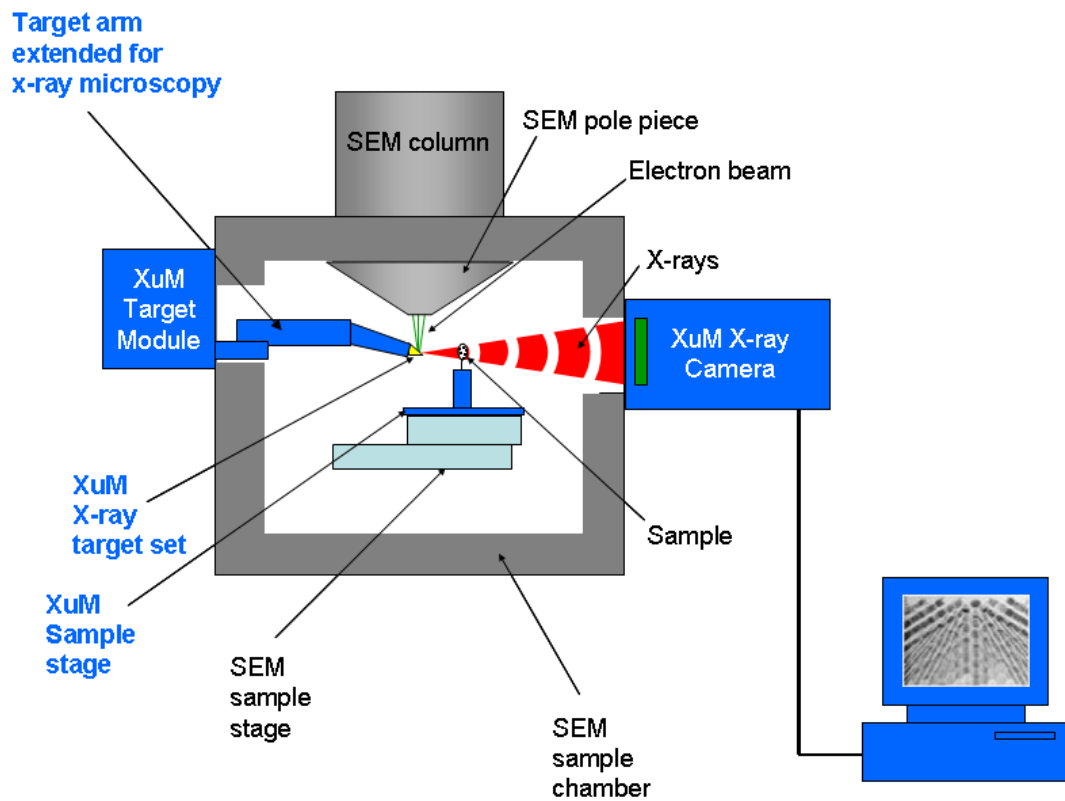


Figure 4.25: A schematic of the XuM inside the SEM chamber (Howard *et al.*, 2010, adapted from Mayo *et al.*, 2002)

4.9.2 Image acquisition

One of the limitations of such a technique is that fewer X-rays are generated at low kV. This therefore results in an image with better resolution but with fewer X-ray counts and hence more noise than an image acquired at higher kV (Howard *et al.*, 2010). To improve the signal to noise ratio, the acquisition time is increased. Data acquisition took between 12 to 24 hours.

The optimal number of 2D X-ray projection images required for the dataset is calculated from the diameter of the sample in pixels; $\pi/2$ X diameter of sample in pixels.

The maximum diameter occurs when the sample fills the entire width of the CCD panel and thus, the ideal number of projections is $\pi/2 \times 1340 = 4210$ projections over 360° , resulting in a 0.09° increment of rotation between each image. This will allow each voxel in the reconstruction to contain at least 1 projection, negating the need to interpolate the data and thus, giving the maximum resolution. In order to keep the acquisition times sensible, fewer projections were acquired, thus reducing the ultimate resolution of the system.

Specimens could be imaged at 360 projections (at 1° rotation increments). However, with this number of projections, instabilities frequently influenced the 3D reconstruction. Thus, the minimum number of projections used for this study was 186 ($180 + \text{cone beam angle}$) at 0.5° increments.

4.9.3 Reconstruction

A 3-dimensional X-ray computed tomography volume of a specimen is created by reconstructing a series of 2D X-ray projection images. All reconstructions were carried out using Digital Micrograph software (Gatan Inc.,) facilitating the XuM. Specimens imaged using the XuM were imaged at 200nm and 775nm, further discussed in Chapters 8 and 9 respectively.

4.9.4 XuM Data Analysis

All visualisation and analysis carried out on the data obtained from XuM followed the procedures outlined earlier in Sections 4.4 and 4.5.

Part III Experimental Studies

Chapters 5-9 present the experimental details of this project.

Chapter 5 High Resolution Imaging of a Clinically Normal Femoral Head

5.0 Introduction

The structure of trabecular bone has been the focus of investigations for centuries. Using radiographs and dissections, early anatomists correlated the microstructure of trabecular bone to their presumed mechanical environments during normal function, and began to perceive trabecular bone as a material of optimised design. Various studies have described different trabecular arrangements in different regions of human bone. Singh *et al.*, (1970) found different characteristics in various regions of the human metaphyses and incorporated these distinguishing features into a classification scheme for trabecular architectures. Kellgren and Lawrence (1957) described a classification system using feature identification to determine the degree of pathology in osteoarthritis. These classification systems are currently widely used for clinical diagnosis and contribute to the diagnosis and choice of treatment for hundreds of thousands of patients every year throughout the United States and the United Kingdom. There is no certain method distinguishing between pathological and non-pathological femoral heads. Orthopaedic surgeons continue to diagnose patients with assumed pathology, yet there may be cases where the pathology, or its phenomenon is not so apparent with current classification techniques. The aim of this study is to determine the bone micro-architecture, bone quality and mineralisation of a clinically normal femoral head, using high definition XMT. The assessment of the clinically normal femoral head will determine the control measure for the purpose of this thesis and highlight any features contributing to bone failure phenomenon.

The objectives for this study were:

- To resolve structural bone features, at high resolution, of a femoral head with normal pathology using XMT.
- To identify and determine the distribution of microcallus formations, or any other significant features in 3D in relation to normal load bearing of the femoral head.
- To determine the BMC and bone quality of the normal head, and to relate to load bearing regions.

5.1 Materials and Methods

5.1.1 Experimental Details

The clinically normal head was identified using radiographs, from 24 cadaveric specimens (Section 3.1). It was prepared as outlined in Section 3.2.6 and imaged using XMT (Chapter 4). The specimen was imaged wet in glycerol to prevent dehydration (Section 3.1.4). The number of projections and dimensional parameters used during XMT imaging are given in Table 5.1. The specimen took a total of 132 hours to image.

Table 5.1: Parameters used during XMT for the clinically normal head

Sample	Number of Blocks	Number of projections per block	Total number of projections	Reconstructed Dimensions (x, y, z)/voxels	Voxel size/μm
A6	4	2801	11204	1888 1888 1316	26

5.2 Results

5.3 Qualitative Analysis of Bone Structural Features

The clinically normal femoral head was rendered to determine any obvious features which may relate to bone pathology. Any such features which are outlined by Kellgren and Lawrence (1957) and Singh *et al.*, (1970) were noted. Figure 5.1 shows that there are no obvious features contributing to OP as the bone structures appears to be well connected, with a uniform thickness of the subchondral bone plate. The structure appears as a combination of struts and plates, with no obvious ‘thinning’ of the structure. One of the signs of OA is eburnated surfaces (Section 1.8.1.2). In Figure 5.2, the articulating surface of the femoral head appears to be non-eburnated showing that there are no obvious signs of OA in this specimen. There are also no obvious signs of bone cysts or osteophytes. The fovea is also observed along with the femoral neck. These results show qualitatively that the specimen has no obvious bone pathology (Video 1, Appendix V).

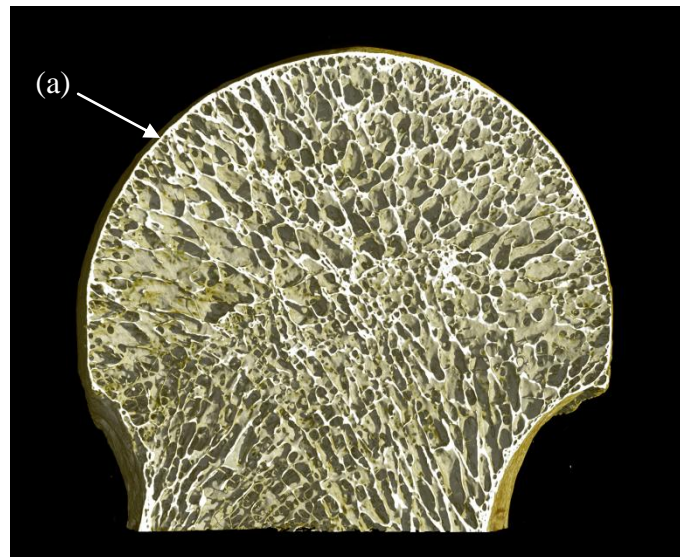


Figure 5.1: Cross section of the normal femoral head (A6, Appendix I) at 26 μm reconstructed voxel size, with a uniform subchondral bone plate (a) and no apparent pathology

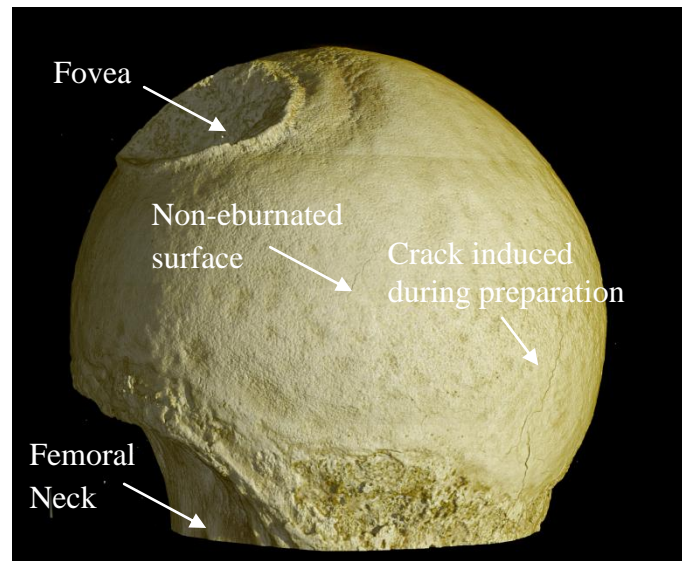


Figure 5.2: The anterior view of the articular calcified cartilage (ACC) surface of the femoral head with no apparent eburnated surfaces

5.4 Determination and Distribution of Bone Features

5.4.1 Greyscale Analysis and Feature Observation

The structure and micro-architecture of bone is clearly visible from the images in the reconstructed data (Figures 5.3 and 5.4). Figure 5.3 shows the dimensions of the central slice in the XY plane of the data set. A virtual slice is measured as $26\mu\text{m}$ voxels. The growth plate is clearly visible (a), and the region to the left (b) appears to show a well connected trabecular network with large trabecular spacing in comparison to the right region. The region to the right (c) of the image appears to be less well connected with smaller trabecular spacing. It can also be observed that the subchondral bone plate also appears of relatively uniform thickness (d).

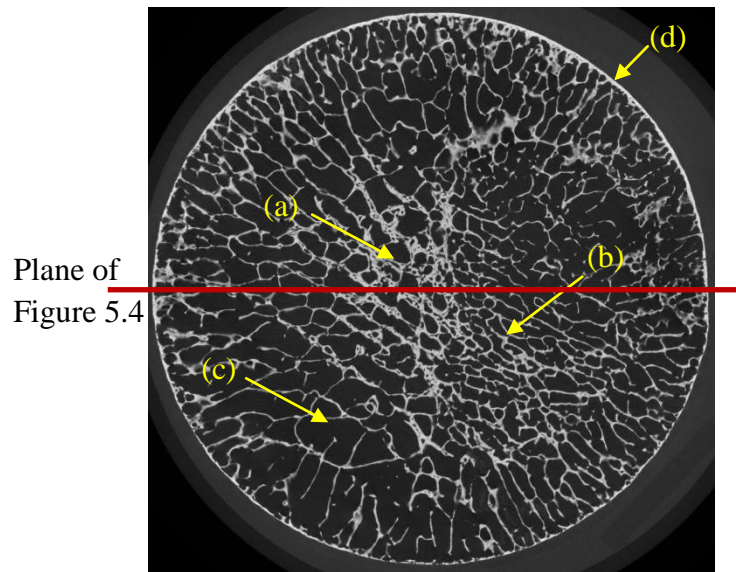


Figure 5.3: XMT image of the central slice from the normal femoral head at $26\mu\text{m}$ reconstructed voxel size (A6, Appendix I) in the XY plane (field width = 49 mm) showing (a) the growth plate, (b) well connected trabeculae (c) poorly connected trabeculae and (d) the subchondral bone plate

Detection of Microcallus Formations

MCFs have been described as woven bone with variable degrees of mineralisation (inhomogeneous grey level) with large osteocyte lacunae, and pores for vessels (Banse *et al.*, 2005). Using greyscale analysis and looking at the reconstructions in all the different planes it was possible to differentiate between the different features present in the specimens.

The criteria used to determine the presence of microcallus formations was to observe differences in the structural properties between bone and microcallus formations. MCFs differed hugely in appearance when compared to the surrounding trabecular structure. They appeared as very fine, porous, bulky, disorganised structures, and did not appear either strut or plate-shaped, like trabecular bone. The MCFs also appeared to be less mineralised, with the trabeculae appearing lighter on the greyscale than the surrounding patch, but this, in fact could have resulted from resolution limitation (Section 4.3.4).

One such example used to identify these patches is seen in Figure 5.4, where the microarchitecture of bone and the MCF is clearly visible in the image obtained from the reconstructed data.

Using greyscale analysis and looking at the reconstructions in all the different planes it was possible to differentiate between the different features present in the clinically normal femoral head.

The MCFs differ hugely in appearance when compared to the surrounding trabecular structure. As per criteria, they appear as porous, bulky, unorganised structures, and do not appear either strut or plate-shaped like trabecular bone. The plane of Figure 5.3 is indicated in Figure 5.4i. It can be seen clearly that the MCF has formed around the trabecular strut (Figure 5.4ii). Areas of resorption are observed in Figures 5.4b and 5.4c, along with an indication of the principal direction of the trabeculae (Figure 5.4e). The fovea is also very clearly shown in Figure 5.4d.

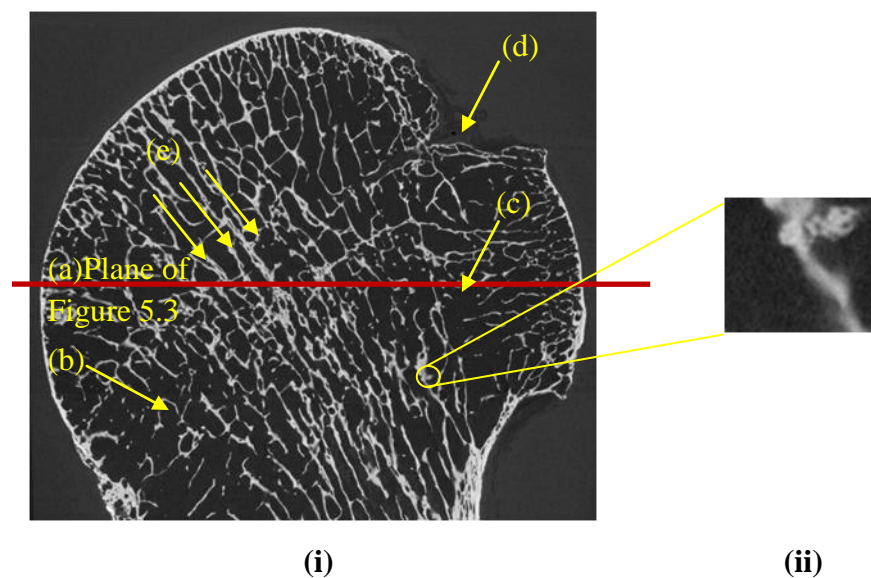


Figure 5.4: (i) Single 2D central slice showing microcallus in the XZ plane, where (a) is the plane of Figure 5.3, (b) and (c) are regions of resorption, (d) is the fovea and (e) the principal direction of trabeculae, and (ii) is the microcallus formation enlarged from the 2D slice

The MCFs were defined as a function of height in the intensity from greyscale images. Since a microcallus formation was larger than one slice in height (where one slice is equivalent to the reconstructed voxel size), the mid slice value was taken as the origin of the location of the MCF. All positions of the observed MCFs were recorded and analysed (discussed in Chapters 5, 6 and 8).

5.4.2 Microcallus Formations and Load-bearing Mapping

A total of 17 MCFs were found in the femoral head. The distribution of the MCFs is superimposed on the stress pattern map produced by Brown and Shaw (1983) (Figure 5.5). There are more MCFs present in the posterior part of the femoral head in comparison to the anterior. Figure 5.5 also suggests that the MCFs appear to have formed on the less loaded region of the femoral head. The majority of MCFs lie between 4.8 and 0.69 MNm⁻² (Figure 5.5). (For 3D visual reference, refer to video 2, Appendix V).

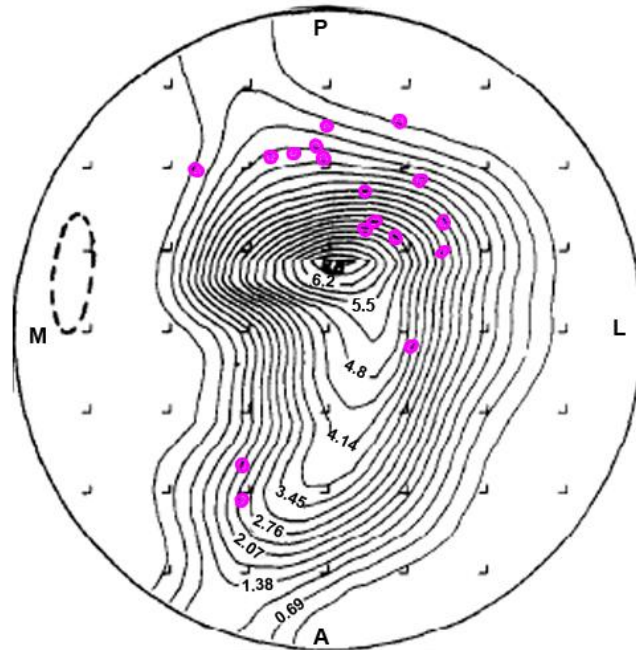


Figure 5.5: Distributions of Microcallus patches superimposed on contact stress gradients from Brown and Shaw, 1983. Where, A, P, L and M represent the anatomical positions; anterior, posterior, lateral and medial, respectively. Contour units are MNm^{-2} .

5.4.3 Distribution of Microcallus Formations

The polar coordinates of the MCFs were calculated as outlined in Section 4.4.4. Furthermore, the polar coordinates of the load bearing boundaries were calculated based on the Brown and Shaw stress map (Figure 3.8).

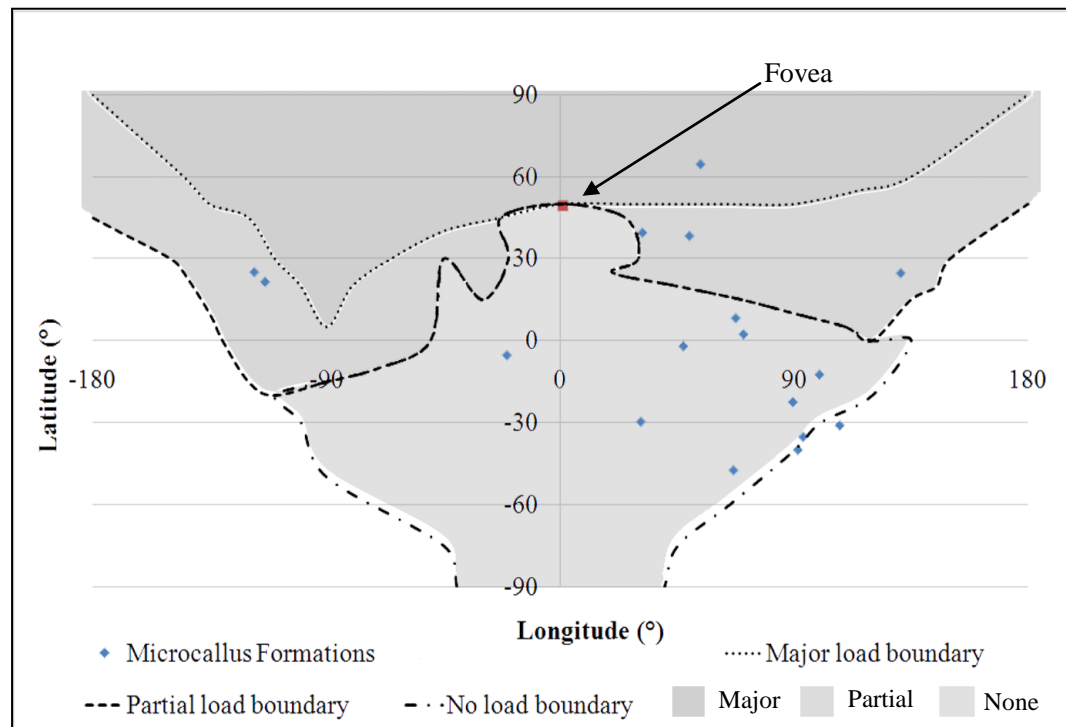


Figure 5.6: Polar coordinates of MCFs mapped onto the load bearing regions of the femoral head

Load bearing regions are defined by dotted and dashed boundaries (Figure 5.6). From Figure 5.6, it can be seen that the majority of MCFs lie within the non-load bearing region, with few MCFs present in the partial-load bearing region and only one MCF in the major-load bearing region.

The density of the MCFs was calculated from the radial distribution (Section 4.4.4). The MCFs are more concentrated between 15-20 mm from the centre of the femoral head, with $0.0042 \text{ MCFs per mm}^{-3}$ (Figure 5.7). There appears to be a large increase in the number of MCFs from 15-20 mm.

There were no MCFs present from centre of the femoral head to 5 mm. However, it should be noted that the number of MCFs are very low in the clinically normal head.

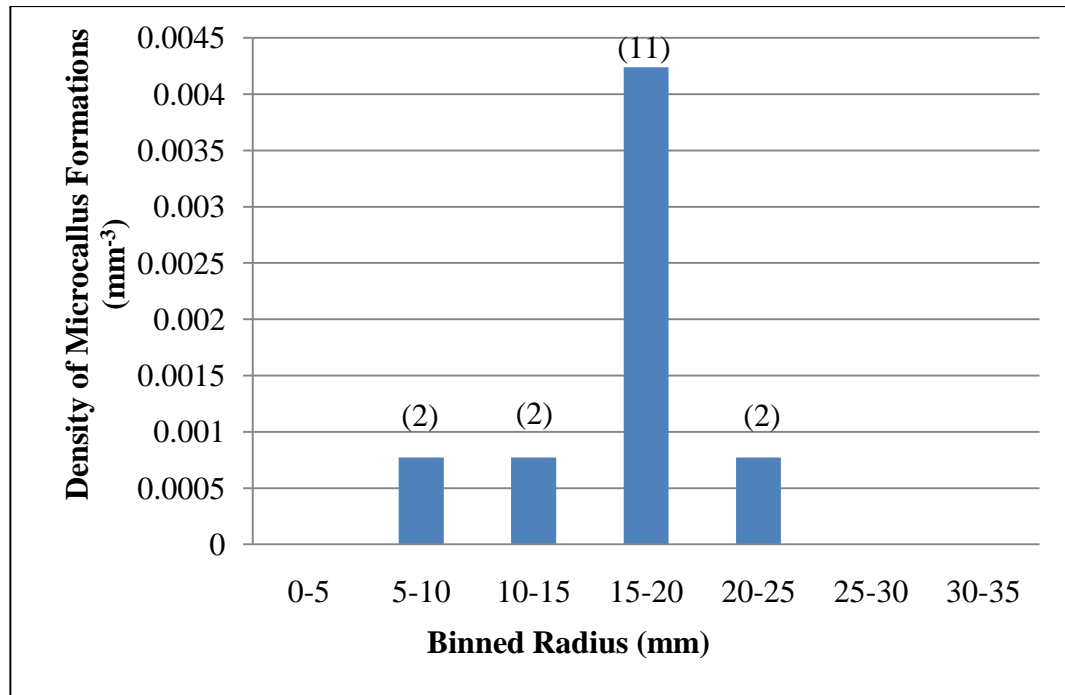


Figure 5.7: The number of MCFs found in binned radial volumes, showing a steep increase between 15-20mm. The number of MCFs in each binned radial volume, are shown in brackets.

5.5 Effect of Bone Mineral Concentration

Histograms obtained from the XMT data set showing the number of voxels versus LAC were used to determine the BMC and the distribution of the BVF throughout the femoral head. The histograms were converted to plots showing the volume of the various phases and their resulting LAC (Figure 5.8). The graph showing the plot for LAC against volume (Figure 5.8) was thresholded using the method described in Section 4.5.1 (Figure 4.18), with the boundary set at 0.82 cm^{-1} , and was used throughout this entire project. This was calculated by taking the LAC of the two peaks, summing the values and dividing by 2 (standard thresholding approach) (Figure 5.8). The ROI was determined post thresholding (Figure 5.8b).

This shows the mean LAC at 40 keV for the bone in the normal femoral head to be 1.27 cm^{-1} . All other phases contributing to the XMT data set (air, space and glycerol) were eliminated using this approach.

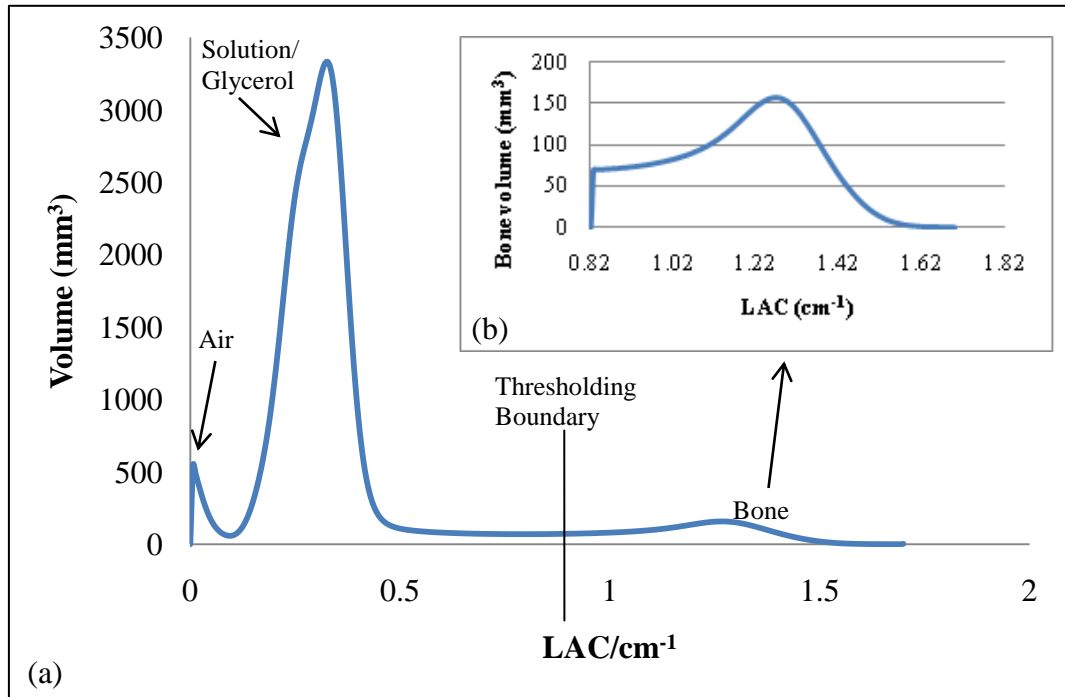


Figure 5.8: (a) Graph showing the histogram for the femoral head obtained from the XMT data set. The peaks relate to the LAC of air, glycerol and bone, and (b) the ROI post-thresholding containing bone, with the distribution of LAC for bone

BMC was calculated using the method outlined in Section 4.7. The superior region of the head has a higher mineral concentration in the occupied bone volume than the medio-lateral region. Also, the medio-lateral region appears to have a lower mineral concentration than the inferior region. The BMC ranges from $0.9 - 1.14 \text{ g cm}^{-3}$ for the entire femoral head and the standard deviation for BMC ranges from $0.1 - 0.145 \text{ g cm}^{-3}$. The mean BMC for the entire femoral head is calculated to be $0.991 \text{ g cm}^{-3} (\pm 0.132 \text{ g cm}^{-3})$. It is observed that apart from the initial 5 mm into the depth of the superior region the remaining volume of the clinically normal head has a fairly constant distribution of mineral concentration.

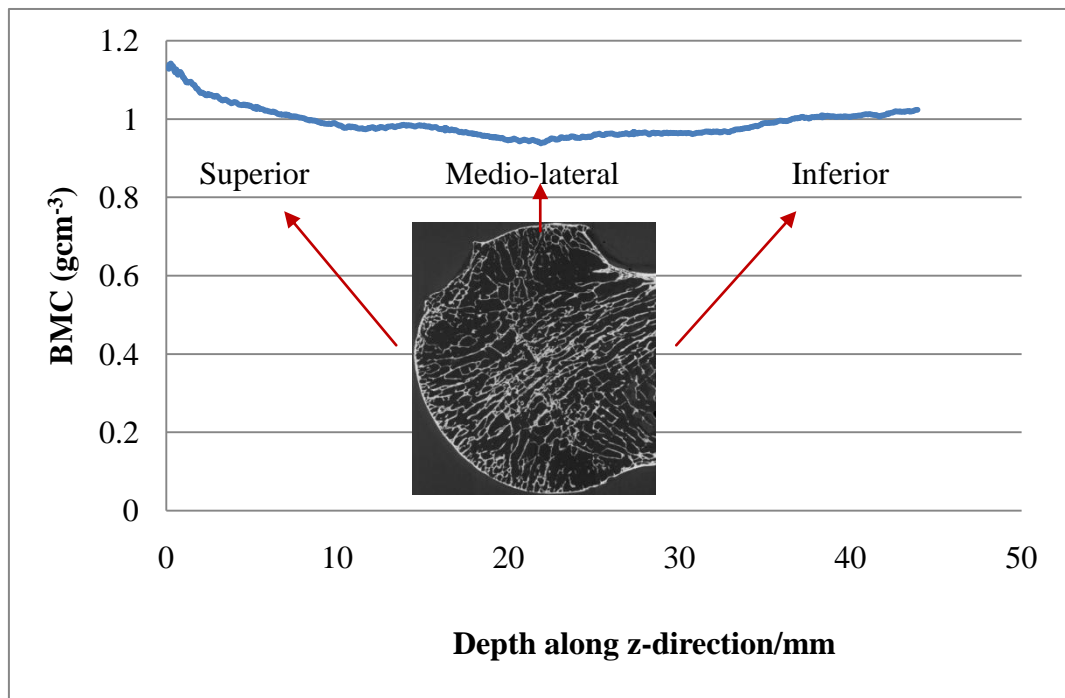


Figure 5.9: The distribution of BMC along the Z-direction of the normal femoral head, from superior to inferior, correlated for anatomical positioning with a slice through the reconstructed XMT data set

5.6 Bone Volume Measurement

Bone volume fraction (BVF; voxels occupied by bone only) was calculated from the histogram obtained for the XMT data set. The distribution of bone volume fraction is shown from the superior to inferior region of the normal femoral head. The cross section image (inset in Figure 5.10) shows how the ROI in the image relating to the superior, inferior and medio-lateral regions of the normal femoral head. The medio-lateral region has higher bone volume than the superior and inferior regions. This result is further investigated in Section 5.7 using cropped regions.

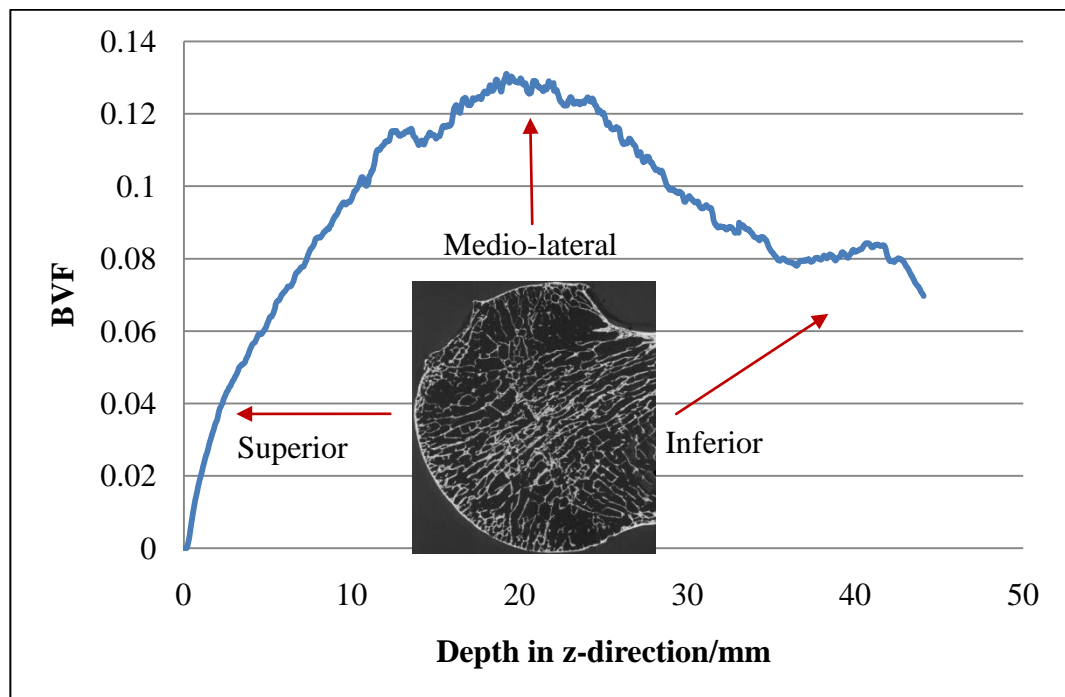


Figure 5.10: Distribution of volume of bone organ occupied by bone tissue throughout the normal femoral head, from superior to inferior, correlated with a slice through the reconstructed XMT data set

5.7 Evaluation of Bone Quality Using XMT

A number of morphometric factors were measured for all the specimens (Section 4.6). A total of 5 randomised cuboidal volumes measuring 3 × 3 × 9 mm per load bearing region were extracted from the femoral heads using Tomview software. Statistical analysis was performed with SPSS software version 17.0 (SPSS Inc., Chicago, IL, USA). Normality of the data was tested with a one-sample Shapiro-Wilk test to indicate the appropriateness of parametric testing. The correlation coefficients were calculated by Pearson Rank correlation analyses due to normal distribution of the histomorphometric factors. P-values of < 0.05 were considered as statistically significant.

From Figure 5.11, a significant positive correlation was found between bone volume fraction (BVF) and trabecular thickness (Tb.Th) ($R = 0.882$, $p = 0.000$), where Tb.Th increases with BVF. The median values for BVF were 0.253, 0.16 and 0.115 and for Tb.Th were 0.214, 0.172 and 0.158 mm; for major-, partial and non-load bearing regions, respectively (Table 5.3). There was a significant negative correlation between Bone volume fraction and trabecular spacing (Tb.Sp) ($R = -0.754$, $p = 0.001$), as seen in Figure 5.12. Figures 5.11 and 5.12 showed that as the trabeculae increase in thickness they are further apart. In general, Tb.Sp lies between 0.984 and 1.467mm, for the entire femoral head (Table 5.3).

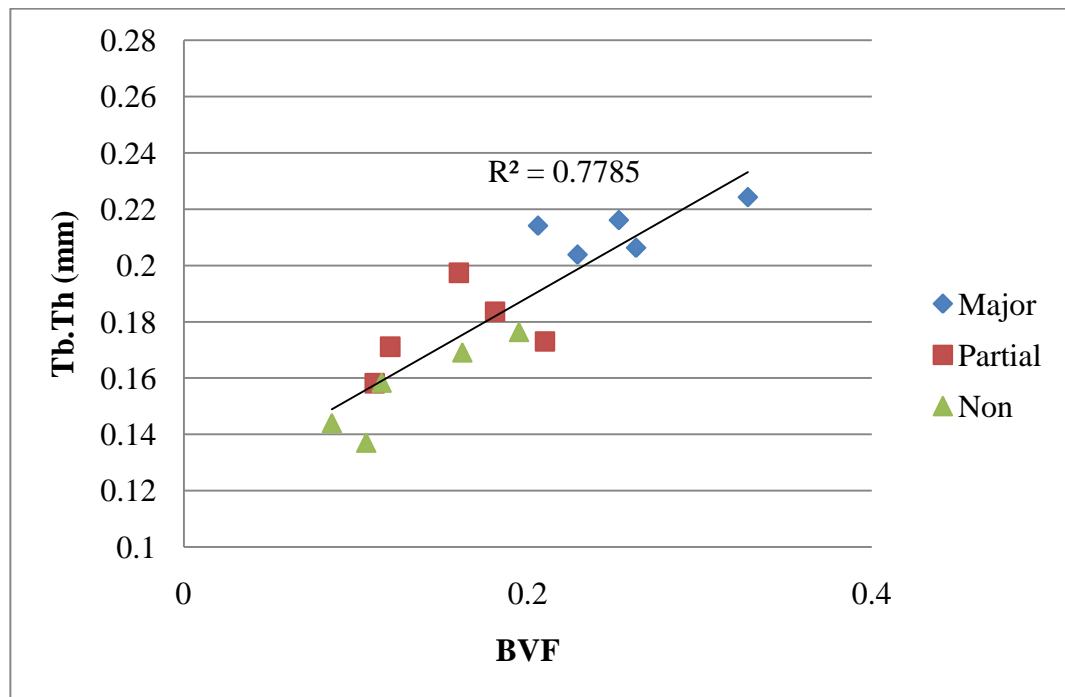


Figure 5.11: Scatter plot of BVF vs. Trabecular Thickness for major-, partial- and non-load bearing regions of the normal femoral head ($R = 0.882$, $p = 0.000$)

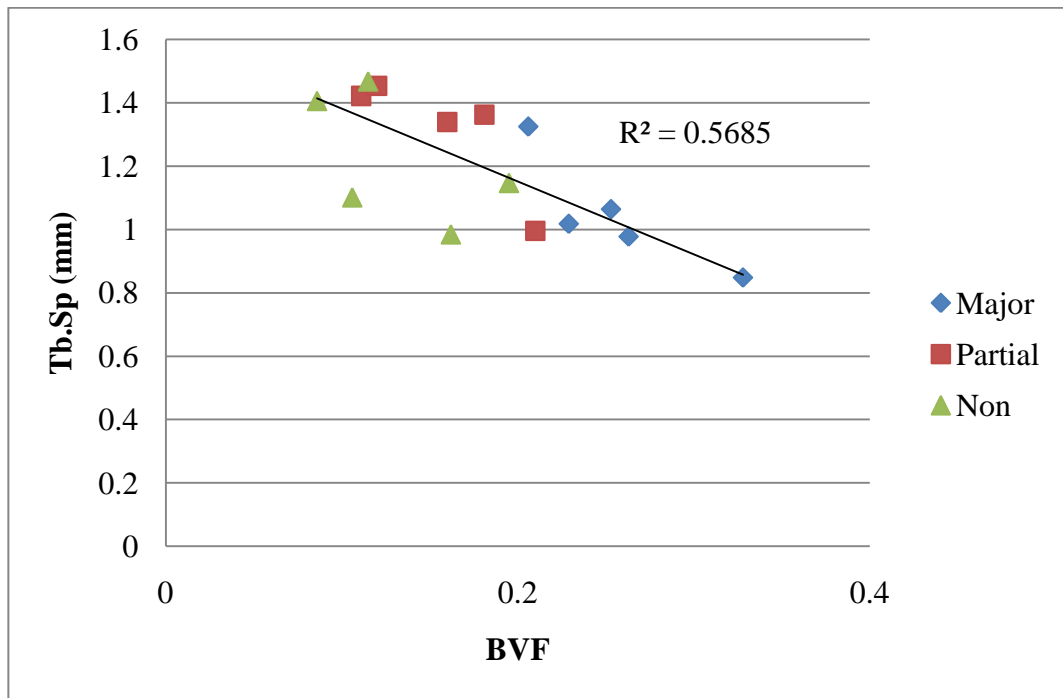


Figure 5.12: Plot for BVF vs. Tb.Sp for major-, partial- and non-load bearing regions in the normal femoral head of the normal femoral head ($R = -0.754$ $p = 0.001$)

Figure 5.13 shows a strong positive correlation between bone volume fraction (BVF) and trabecular number (Tb.N) ($R = 0.988$ $p = 0.000$). There is a linear increase from the non- and partial-load regions to the major load region. The median values for Tb.N are 1.129 , 0.764 and 0.582mm^{-1} for major-, partial- and non-load bearing regions respectively.

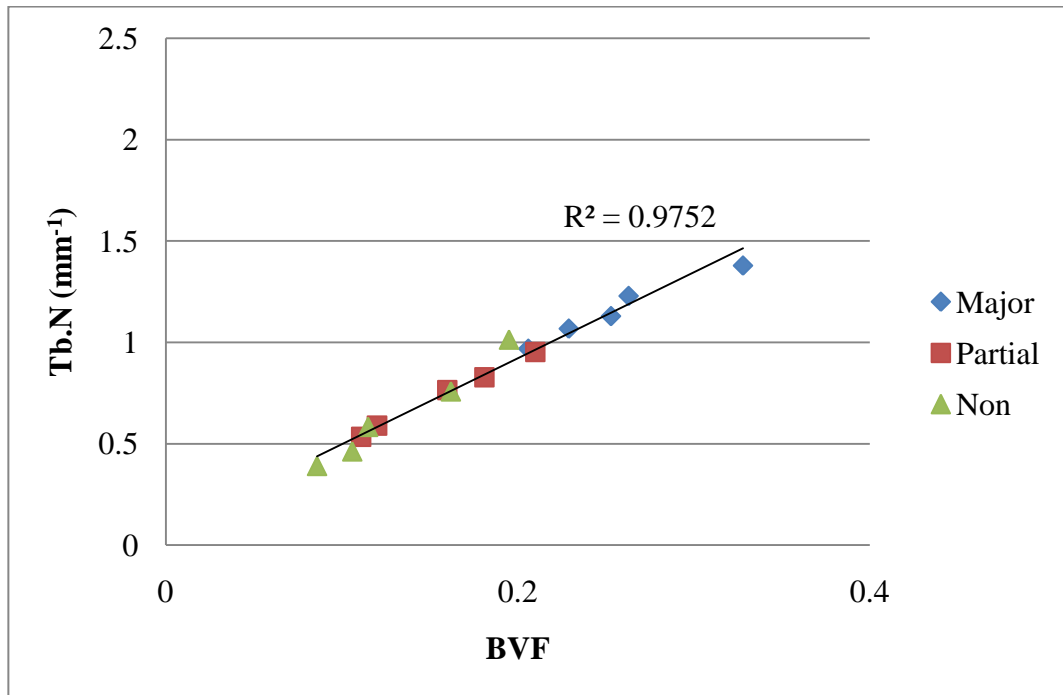


Figure 5.13: Linear relationship between BVF and Tb.N for major-, partial- and non-load bearing regions of the normal femoral head ($R = 0.988$ $p = 0.000$)

There was a weak negative correlation between Bone volume fraction and Structure model index ($R = -0.543$ $p = 0.036$). Figure 5.14 suggests that partial-load bearing appears to be more rod-like with a median value of 2.747 for SMI, in comparison to the other two regions. The major load bearing region, with a median value of 1.683 for SMI appeared to be a combination of rod and plates, whereas the non-load bearing region with a median SMI of 1.856 also appeared as a combination of both rods and plates but was more inclined towards the rod-like structure.

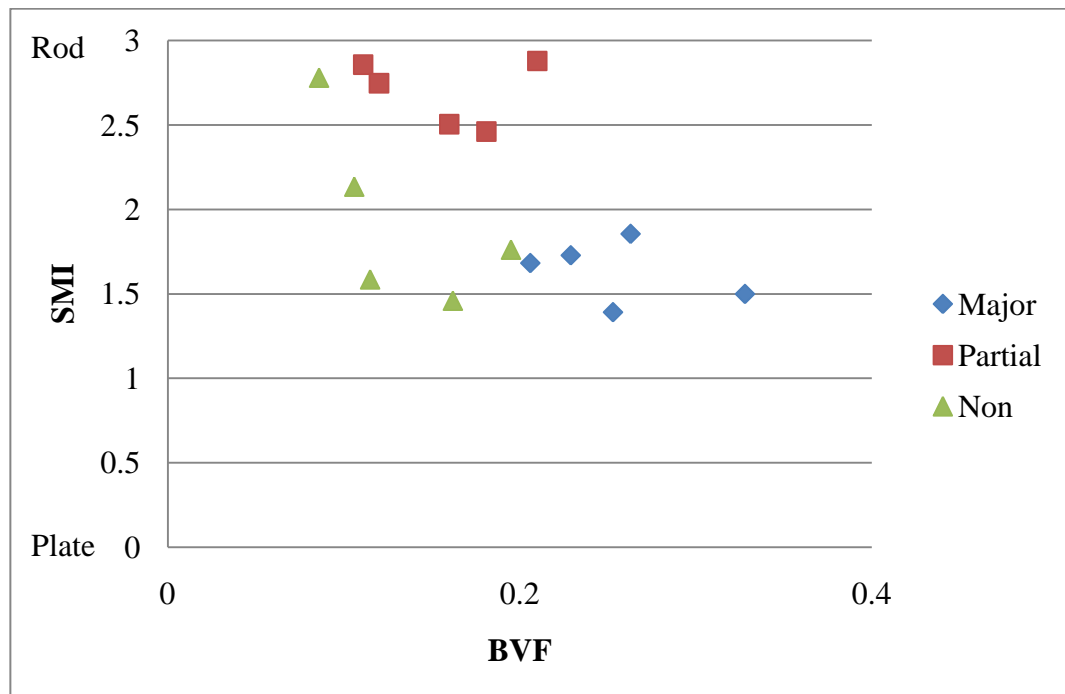


Figure 5.14: Scatter plot of Bone volume fraction vs. Structural Model Index for major-, partial- and non-load bearing regions of the normal femoral head ($R = -0.543$ $p = 0.036$)

There was also a significant negative correlation between Tb.N and SMI ($R = -0.561$ $p = 0.030$). From Figure 5.15, it can be seen that the partial-load bearing region appears to be more plate like, also in agreement with Figure 5.14. There was no correlation between Conn.D and SMI ($R = 0.092$ $p = 0.745$) (Figure 5.16). The Conn. D showed a high level of variability within each loading region and had no direct effect on the SMI.

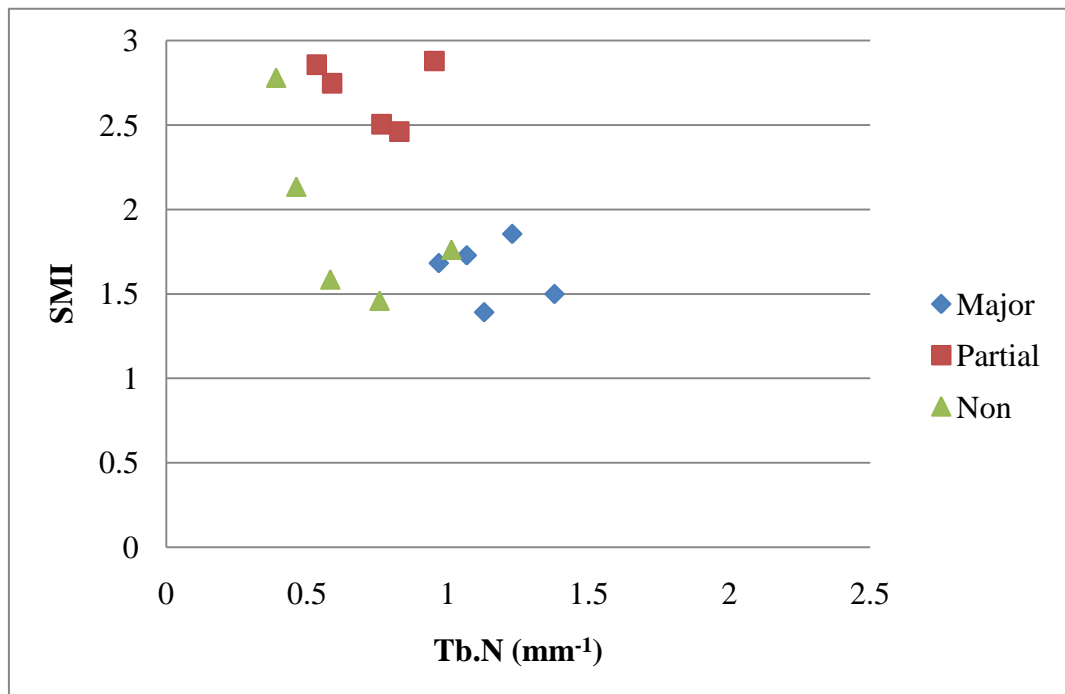


Figure 5.15: Trabecular number vs. Structure Model Index for major-, partial- and non-load bearing regions of the normal femoral head ($R = -0.561$ $p = 0.030$)

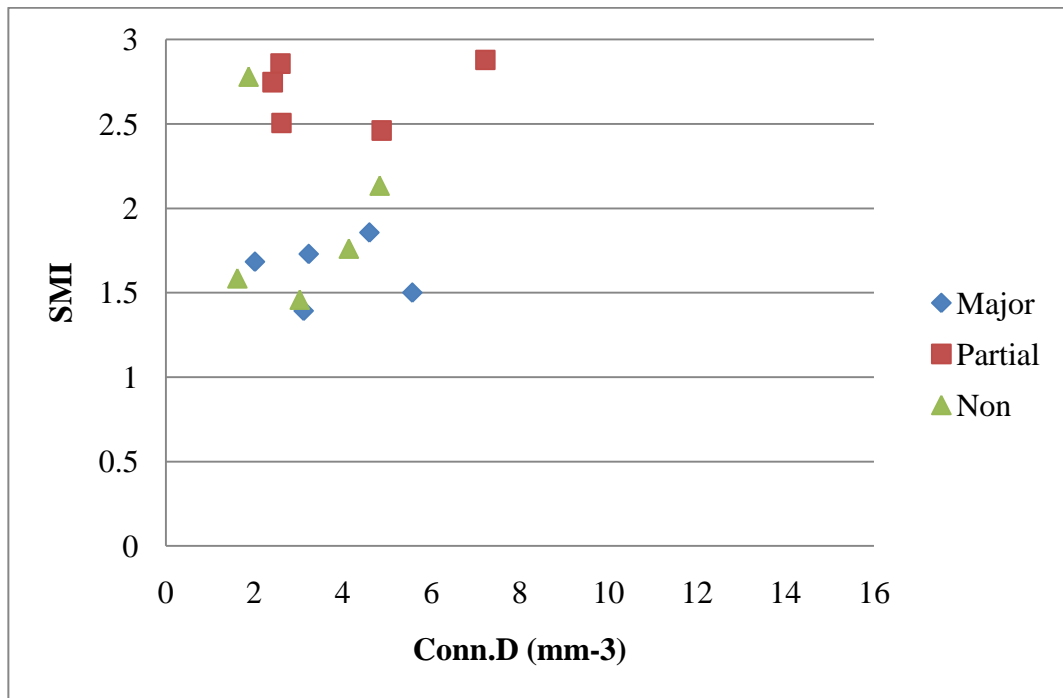


Figure 5.16: Connectivity Density vs. Structure Model Index for major-, partial- and non-load bearing regions of the normal femoral head ($R = 0.092$ $p = 0.745$)

Figure 5.17 showed that trabeculae within the major-load bearing region were thicker than in the other regions, and structured with a combination of rods and plates. The median values for major-load are 1.683 and 0.214 mm (Table 5.3), for SMI and Tb.Th, respectively. The partial-load region has a median Tb.Th of 0.172 mm but was more significantly plate-like with a median SMI of 2.747. There was no significant correlation between SMI and Tb.Th ($R = 0.506$, $p = 0.054$).

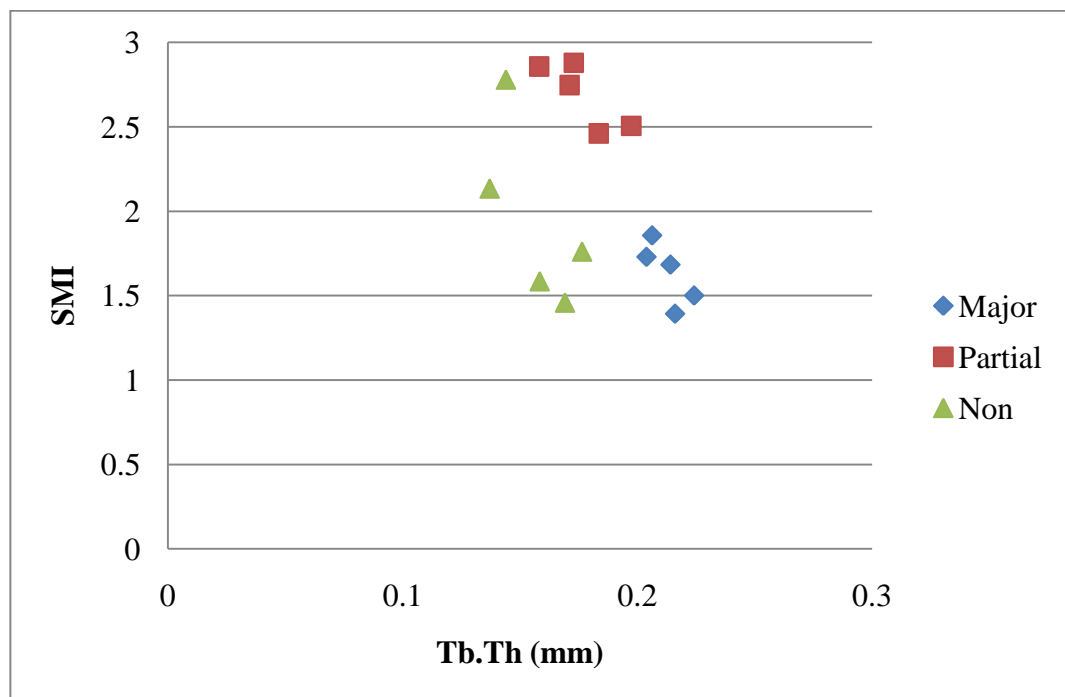


Figure 5.18 shows no direct correlation between DA and BVF ($R = -0.186$ $p = 0.508$). There was considerable amount of variability within partial and non-load bearing regions for DA, with ranges, 0.204-0.495 and 0.232-0.503, respectively. The median DA for the entire head was 0.378, thus exhibiting a low degree of anisotropy overall (Table 5.3). Conn.D was significantly correlated with DA ($R = -0.710$ $p = 0.003$) (Figure 5.19), showing that as degree of anisotropy decreases and when the bone becomes more isotropic there is an increase in the Conn.D. There was a significant overlap in all regions, indicating a high amount of variability in these two measures. There was no correlation between Tb.N and Conn.D ($R = 0.469$ $p = 0.078$) (Figure 5.20). There was a strong linear correlation between Tb.Th and Tb.N ($R = 0.925$ $p = 0.000$) (Figure 5.21). The number of trabeculae and trabecular thickness increased with loading region. There were a higher number of trabeculae present in the major loaded regions and were also thicker, in comparison to the partial and non-load bearing regions. The partial and non-load bearing regions showed a significant overlap in both trabecular number and thickness.

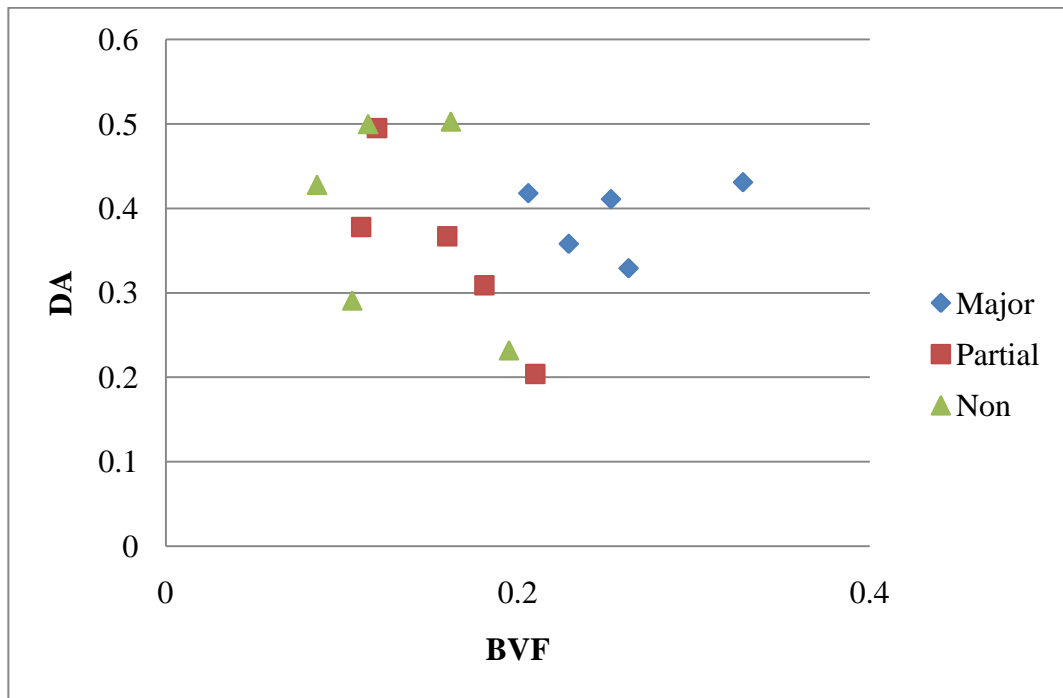


Figure 5.18: Relationship between BVF and DA, with no direct correlation for major-, partial- and non-load bearing regions of the normal femoral head ($R = -0.186$ $p = 0.508$)

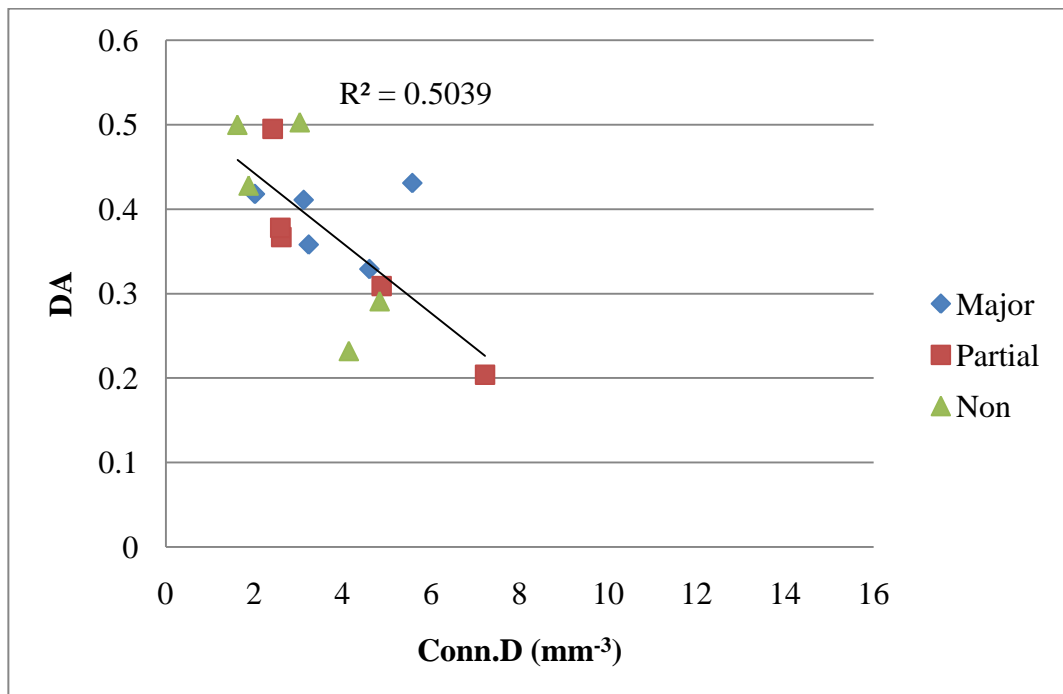


Figure 5.19: Plot of Connectivity Density vs. Degree of anisotropy for major-, partial- and non-load bearing regions of the normal femoral head ($R = -0.710$ $p = 0.003$)

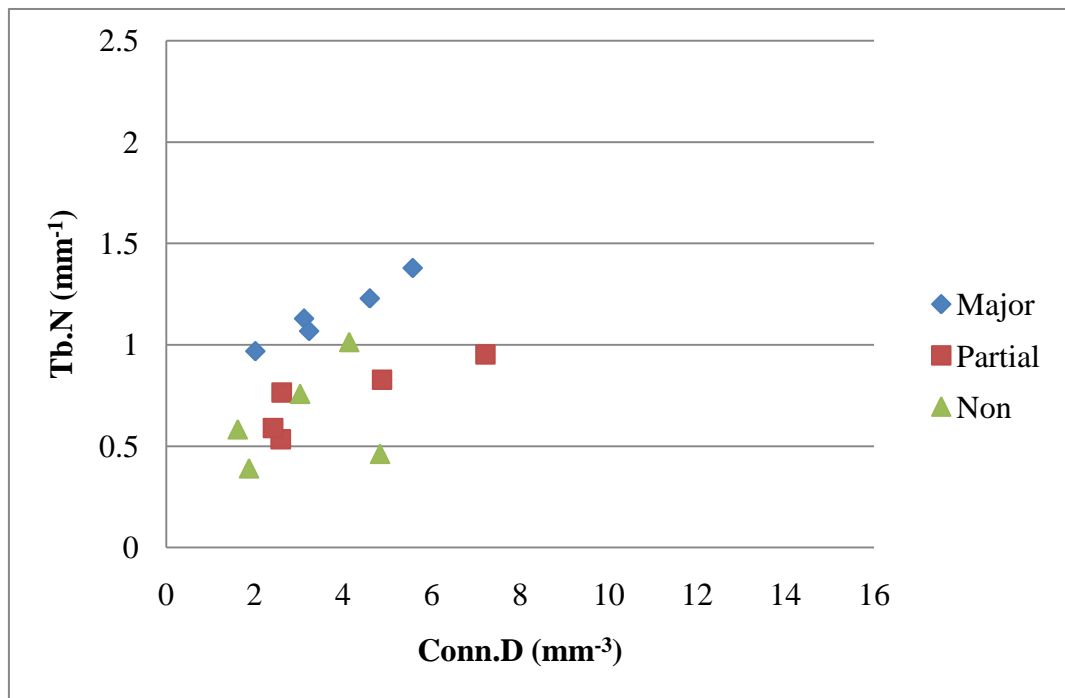


Figure 5.20: Scatter plot of Connectivity Density vs. Trabecular Number for major-, partial- and non-load bearing regions of the normal femoral head ($R = 0.469$ $p = 0.078$)

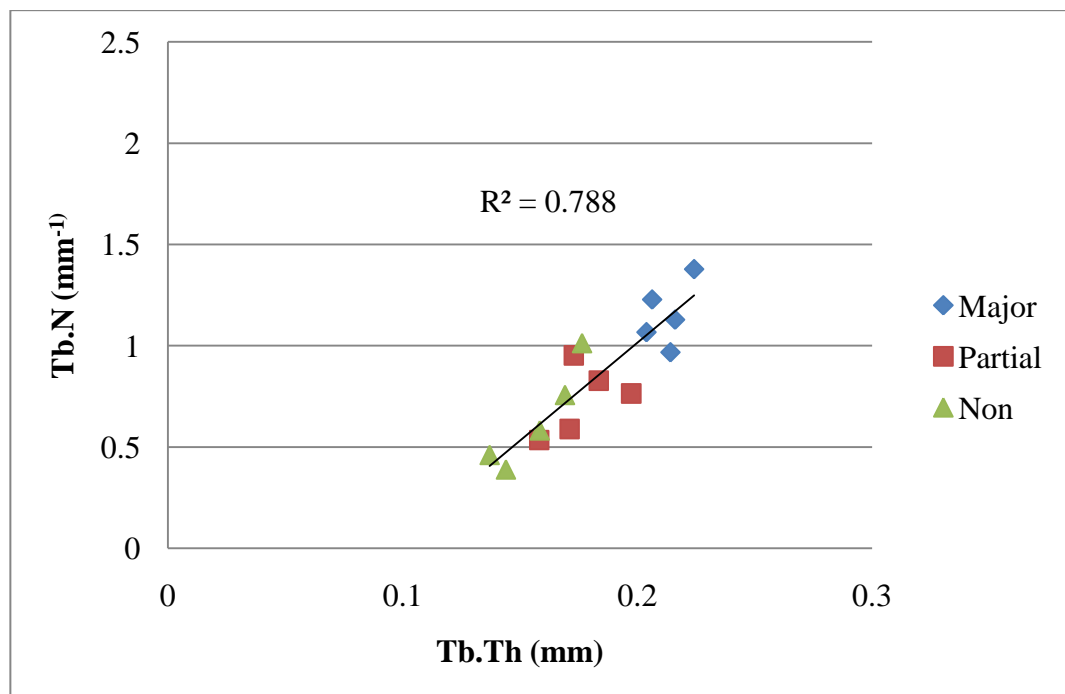


Figure 5.21: Scatter plot of Trabecular Thickness vs. Trabecular Number for major-, partial- and non-load bearing regions of the normal femoral head ($R = 0.925$ $p = 0.000$)

There was a strong linear correlation between BMC and Tb.Th ($R = 0.899$ $p = 0.000$) (Figure 5.22). There was a marked difference between the major load bearing region and the partial and non-load bearing regions. The trabeculae in the major load bearing region were thicker and had a higher mineral concentration than the trabeculae in the partial- and non-load bearing regions. The median BMC for the normal femoral head was 0.935 g cm^{-3} (Table 5.3), which was below the range of the major-load bearing region ($0.964\text{-}0.990 \text{ g cm}^{-3}$), indicating that the BMC for all major-load values was above the overall median value. There was a significant overlap between partial- and non-load bearing regions, as seen in Figure 5.22.

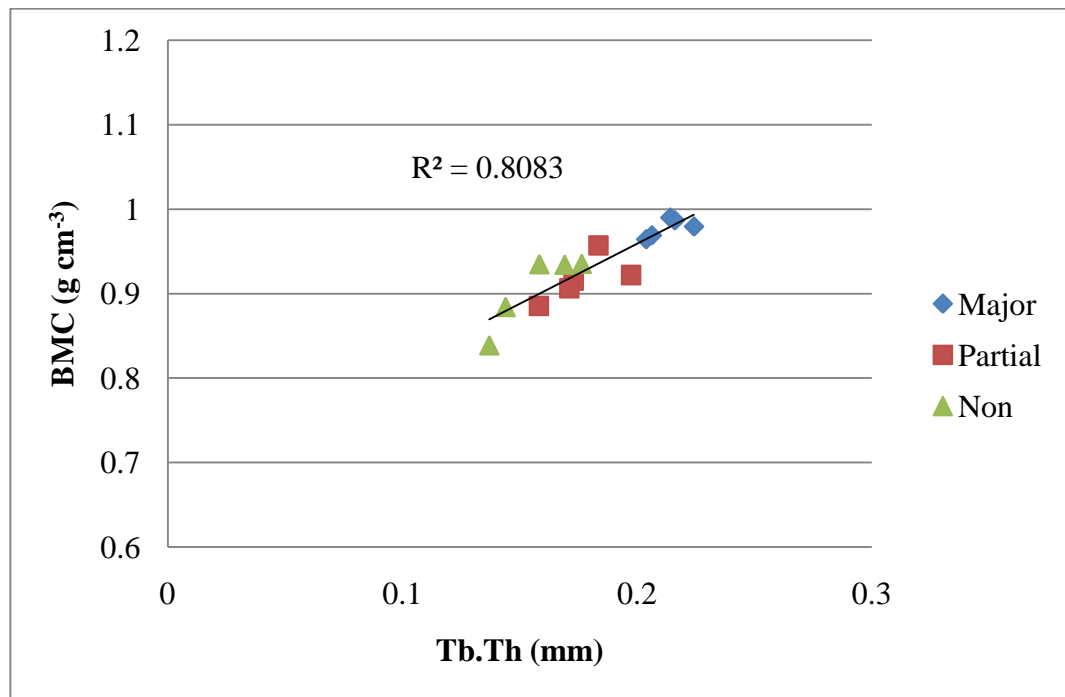


Figure 5.22: Linear relationship between BMC and Tb.Th for major-, partial- and non-load bearing regions of the normal femoral head of the normal femoral head ($R = 0.899$ $p = 0.000$)

Table 5.3 shows a summary of all the bone quality measure for the normal femoral head, indicating median and ranges for the entire head and corresponding load bearing regions. It can be seen that BVF, Tb.N and Tb.Th increased with load bearing. Partial load bearing had a higher Tb.Sp (1.362 mm), and major-load bearing had a higher connectivity density (3.228 mm^{-3}). Partial load bearing appeared to be significantly more plate-like with a median SMI 2.747, in comparison to the other regions, and was also more anisotropic. The major load region was more highly mineralised (0.990 g cm^{-3}), whereas the partial and non-load bearing regions were more closely related with mean BMC, 0.915 and 0.935, respectively.

Table 5.3: Summary of the regional and overall variations for bone quality measurements in the normal femoral head

	BVF	Tb.Th (mm)	Tb.Sp (mm)	Conn.D (mm⁻³)	Tb.N (mm⁻¹)	SMI	DA	BMC (g cm⁻³)
Major Load	0.253* (0.206-0.328) †	0.214* (0.203-0.224) †	1.017* (0.977-1.324) †	3.228* (2.013-5.569) †	1.129* (0.968-1.378) †	1.683* (1.392-1.856) †	0.411* (0.329-0.431) †	0.979* (0.964-0.990) †
Partial Load	0.160* (0.111-0.181) †	0.172* (0.158-0.197) †	1.362* (0.996-1.453) †	2.611* (2.414-7.217) †	0.764* (0.534-0.952) †	2.747* (2.461-2.879) †	0.367* (0.204-0.495) †	0.915* (0.885-0.957) †
Non Load	0.115* (0.086-0.195) †	0.158* (0.137-0.176) †	1.147* (0.984-1.467) †	3.027* (1.619-4.831) †	0.582* (0.389-1.013) †	1.762* (1.460-2.135) †	0.428* (0.232-0.503) †	0.934* (0.839-0.935) †
Entire Femoral head	0.181* (0.086-0.328) †	0.176* (0.137-0.224) †	1.147* (0.984-1.467) †	3.114* (1.619-7.217) †	0.827* (0.389-1.378) †	1.856* (1.392-2.879) †	0.378* (0.204-0.503) †	0.935* (0.839-0.990) †

*Median †Range (min-max)

Chapter 6 High resolution imaging of Pathological Femoral Heads

6.0 Introduction

Radiographic evaluation is an extremely valuable tool that allows the orthopaedic surgeon to characterize and classify bone pathology by its appearance. Careful analytical characterization of bone architecture on plain radiographs often enables the surgeon to greatly narrow the differential diagnosis. Both osteoarthritis and osteoporosis result in a change in trabecular bone architecture. These changes in architecture occur through the action of osteoclasts and osteoblasts in selectively removing and adding bone. As a result of bone pathology a change in trabecular architecture results in the formation of various features (osteophytes, subchondral bone cysts, subchondral bone plate thickening, joint space narrowing and femoral head deformity in OA, and thinning of trabeculae and low bone mineral density in OP) which are generally determined by plain 2D radiography. Although valuable, plain radiographs as a tool, provide limited information due to their 2-dimensional nature and the variability in interpretation from one physician to the next. The aim of this study was to characterise the bone micro-architecture, bone quality and mineralisation of pathological femoral heads, using high definition XMT. The femoral heads used in this study were clinically diagnosed as osteoarthritic and osteoporotic. The non-clinical assessment of the femoral heads aimed to determine the factors and architectural features contributing to bone failure phenomenon in pathological trabecular bone.

The objectives for this study were:

- To resolve structural bone features at high resolution of a femoral head with pathology using XMT.

- To quantify BMC of the pathological femoral heads, and relate this to load bearing regions.
- To analyse the distribution of microcallus formations in the different pathologies and relate this to the different load bearing regions of the femoral heads.
- To analyse bone micro-architecture and bone quality non-destructively, using X-ray micro-computed tomography and relate this to the different pathologies.

6.1 Materials and Methods

6.1.1 Experimental Details

The specimens (Section 3.2) were mounted (Section 3.2.6) and imaged wet in glycerol as described in Section 3.1.4. The parameters used for XMT imaging (Table 6.1) are highlighted. Note, the change in resolution for B15, was due to the specimen size being significantly larger than the other specimens, therefore to fit the scan width, the resolution was decreased. The specimens were scanned using XMT as outlined in Chapter 4.

Two osteoarthritic heads and one osteoporotic head were used for this study. They were clinically diagnosed by an experienced consultant (Mr. Gareth Scott, St. Bartholomew's and The Royal London) prior to being excised during total hip arthroplasty (Section 3.2). They were prepared as outlined in Section 3.2.6 and imaged using XMT (Chapter 4). The specimens were imaged wet in glycerol to prevent dehydration (Section 3.1.4). The specimens took a total of 132, 110 and 144.5 hours to image for specimens, B7 (OA), B14 (OP) and B15 (OA) respectively.

Table 6.1: Parameters used to obtain the XMT data sets, where, B7 and B15 are osteoarthritic and B14 is osteoporotic

Sample	Number of Blocks	Number of projections per block	Total number of projections	Dimensions (X, Y, Z) (Voxels)	Reconstructed Voxel size (μm)
B7 (OA)	3	2801	8403	1798 2168 1316	25
B15 (OA)	5	2801	14005	1944 1914 1815	26
B14 (OP)	3	2801	8403	1658 1848 1314	25

6.2 Results

This section presents the results for this study. Some results have also been presented with the results from the Chapter 5 (normal head study) and these are for reference purpose only.

6.3 Qualitative Analysis of Structural Bone Features

XMT is a technique that provides a 3D understanding of the data. One aspect is to assess images and inspect the data qualitatively. This section reports the findings of the bone feature analysis. Features attributing to OA and OP are reported for each specimen.

Figure 6.1 is a cross section of the OA femoral head (B7) showing typical features of OA; (a) thickened subchondral bone plate, (b) possible subchondral bone cysts, (c) osteophyte formation, (d) the growth plate and (e) areas of resorption. Figures 6.2 and 6.3 show the morphology of the osteoporotic femoral head. The surface of the OP femoral head is highlighted in Figure 6.2. It exhibits a non-eburnated surface (a), showing that the articular calcified cartilage is intact, due to its rough appearance. The excised surface (b) and the fracture plane is also clearly visible (c), where the femoral head collapsed into the femoral neck during the OP fracture. The cross-section image of the OP femoral head shows typical signs of OP associated with the Singh Index (1970). Large areas of resorption (b) can be seen with a uniform thickness of subchondral bone plate. It is also to be noted that the trabeculae appear extremely thin overall (c). (For visual reference refer to video 3 (OA femoral head) and video 4 (OP femoral head), Appendix V)

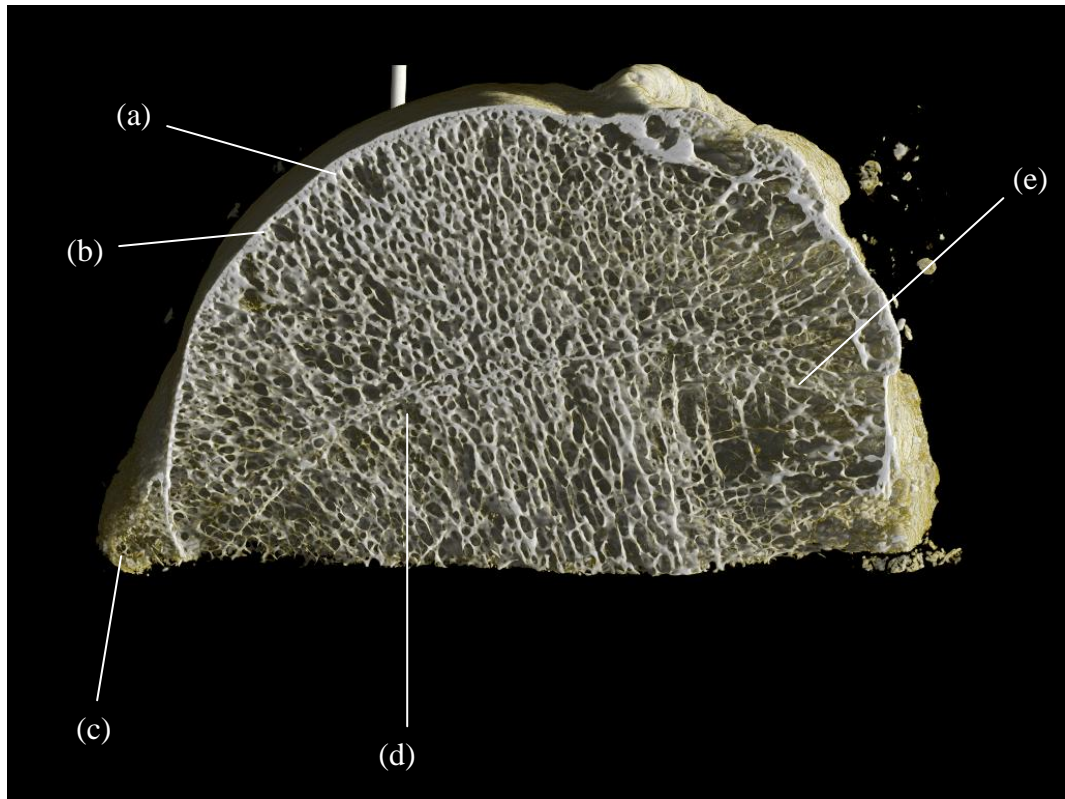


Figure 6.1: Cross sectional image of the OA head (B7) showing typical features of OA; (a) thickened subchondral bone plate, (b) possible subchondral bone cysts, (c) osteophyte formation, (d) the growth plate and (e) areas of resorption.

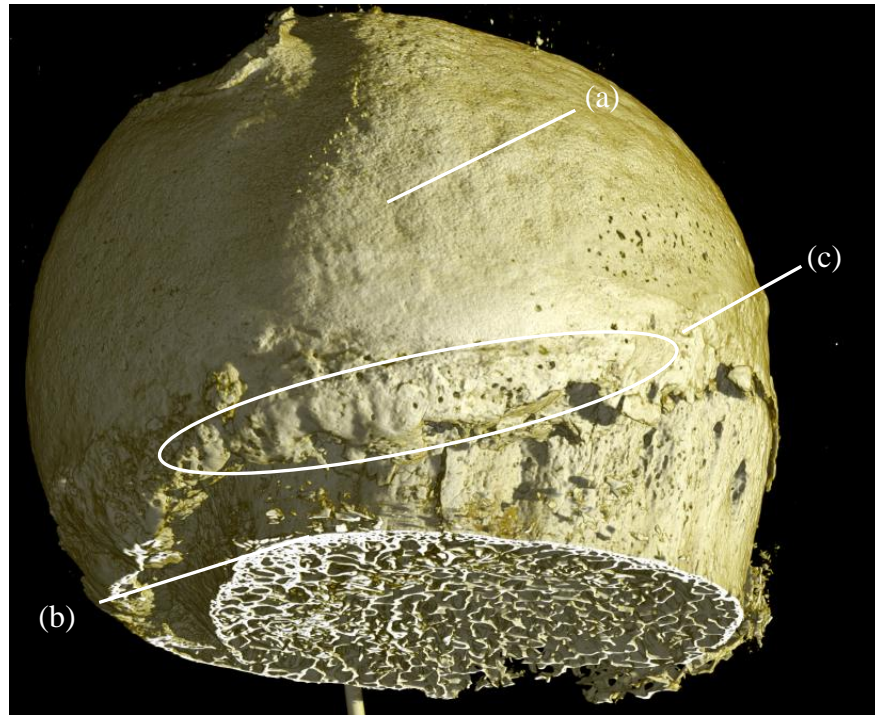


Figure 6.2: (a) The non-eburnated surface of the OP femoral head (B14), (b) the excised surface and (c) the plane of the femoral neck fracture

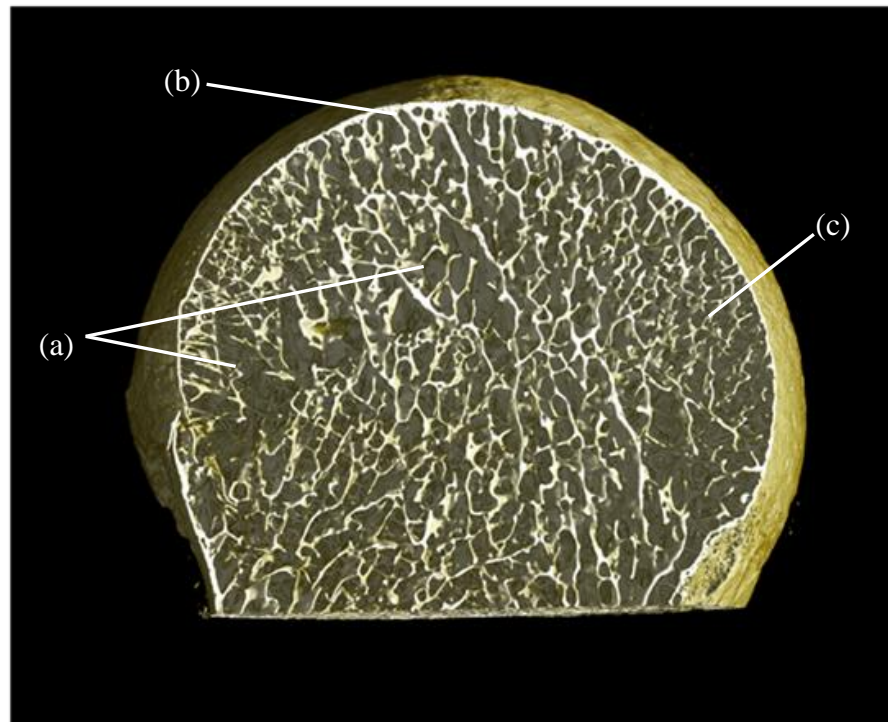


Figure 6.3: Cross section of femoral head (B14) exhibiting typical features of OP; (a) areas of resorption, (b) uniform thickness of subchondral bone plate and (c) thin trabeculae

Figures 6.4 and 6.5 show the morphology of specimen B15, which is osteoarthritic. Figure 6.4a clearly exhibits typical OA features. The eburnated surface (a) appears smooth and polished whereas the non-eburnated surface (b) appears rough. The bony spurs often associated with OA (osteophyte formations) were also observed (c). The cross-sectional image of the OA femoral head (B15) illustrates the internal features contributing to the bone pathology (Figure 6.5). Clearly, a difference in the thickening of the subchondral bone plate is observed along with subchondral bone cysts. The cysts appear to have formed beneath the eburnated region, whereas the subchondral bone plate has thickened in this region following the principal loading direction. In general, osteophytes and regions of resorption are also observed.

The section enlarged from Figure 6.5b illustrates the local variation in the bone structure, along with features associated with bone fracture. Both plate-like and rod-like structures are seen, and a MCF is also observed. Exceptionally thin rod-like trabeculae are observed in close proximity to large plate-like trabeculae. The MCF appears to have formed on trabeculae bordering the rod-like and plate-like regions.

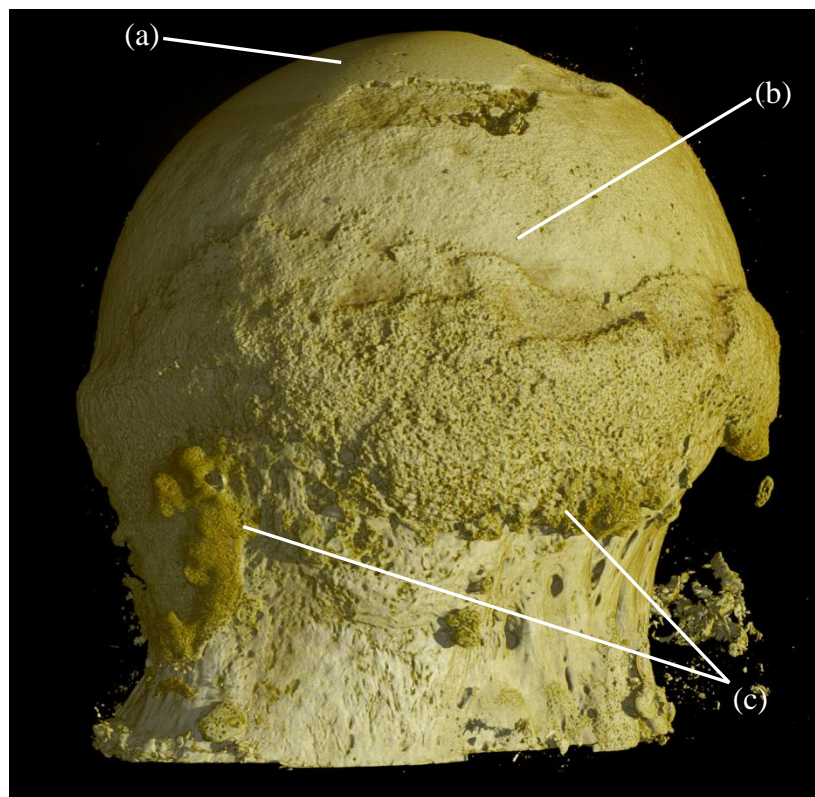


Figure 6.4: Specimen B15 exhibiting typical OA features; (a) eburnated surface, (b) non-eburnated surface and (c) osteophyte formation

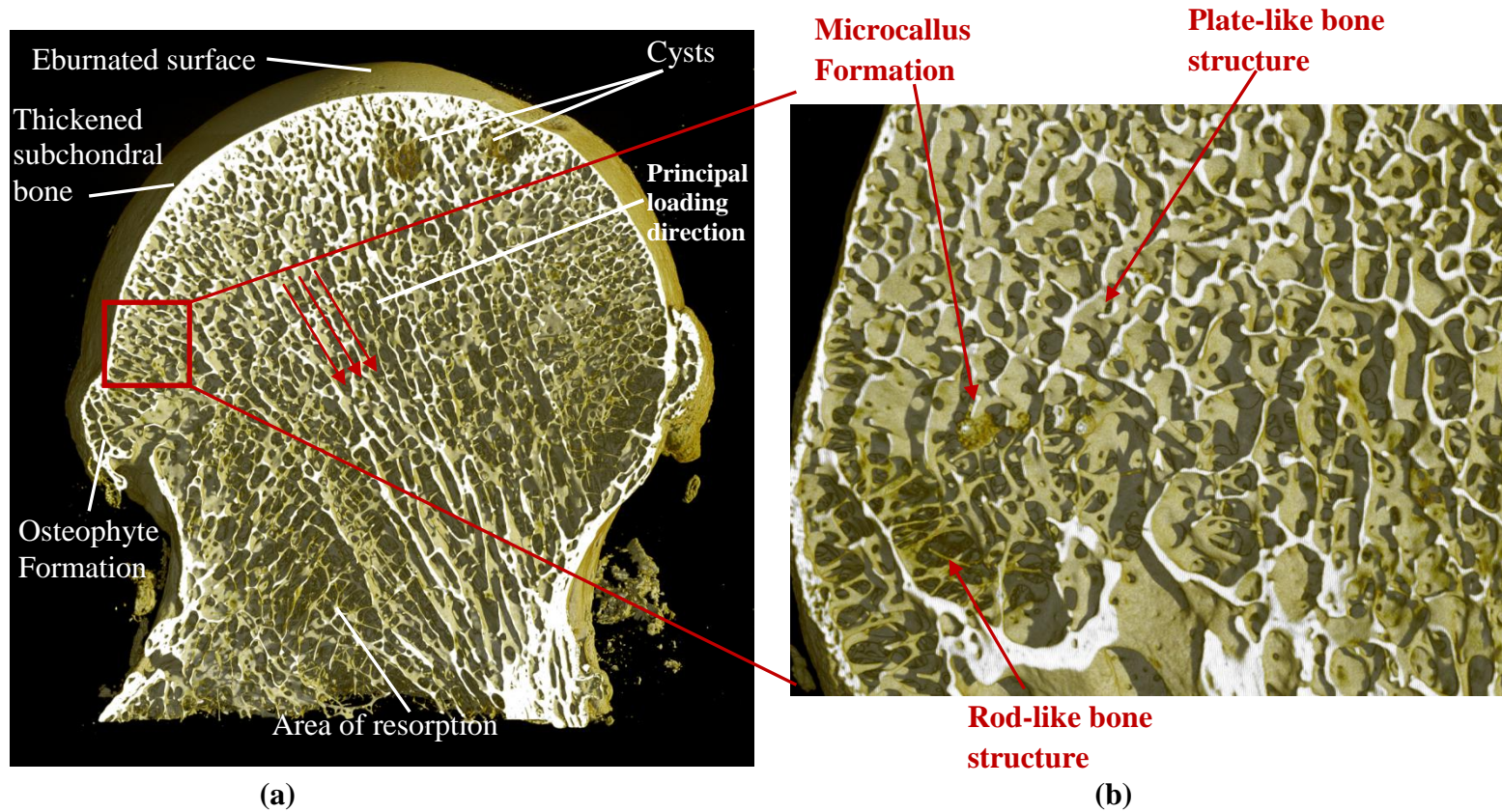


Figure 6.5: (a) Cross section of specimen B15 exhibiting typical surface and non-surface features of OA and (b) enlarged section taken from B15, showing local variation in bone architecture

6.4 Determination and Distribution of Bone Features

6.4.1 Greyscale Analysis and Feature Observation

The structure and micro-architecture of bone is clearly visible from reconstructed images (Figures 6.6). Figure 6.6 shows the central slice in the YZ plane of the data set. A data slice is measured in $25\mu\text{m}$ voxels (specimen B7). Large resorption areas are seen, where there is almost no bone structure present (Figure 6.6a), and large regions also appear less connected (6.6b). In fact, the overall bone connectivity appears to be low, with varied size in trabecular spacing. It can also be observed that the subchondral bone plate appears to be of a non-uniform thickness, with regions thicker in some sections of the subchondral bone plate than others (Figure 6.6c). Using greyscale analysis and looking at the reconstructions in all the different planes it was possible to differentiate between the different features present in the pathological femoral head. In particular, Microcallus formations (MCFs) were observed (Figure 6.6d). The criteria to determine MCFs is presented in Section 5.4. The MCF appears porous, bulky, smaller in size compared to trabeculae, and darker on the grey scale and has formed around a rod-like trabecula (Figure 6.6ii).

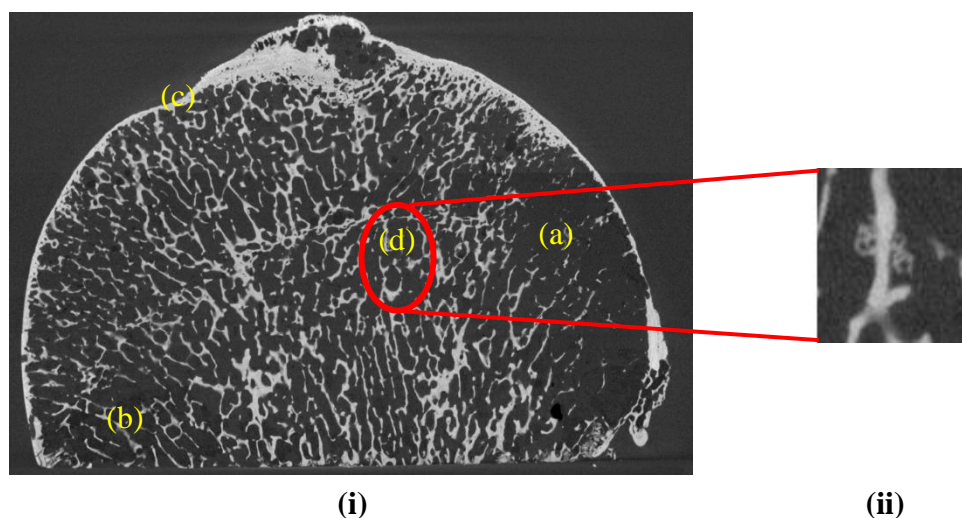


Figure 6.6: (i) Single 2D image showing the microcallus formation in the YZ central plane (Specimen B7) and (ii) the enlarged MCF

6.4.2 Microcallus Formations and Load-bearing Mapping

This section reports on the distribution of MCFs. A total of 101, 132 and 585 MCFs were found in specimens B7 (OA), B15 (OA) and B14 (OP) respectively. The distribution of the MCFs is superimposed on the stress pattern map produced by Brown and Shaw (1983). There is a distinct difference in the number of MCFs and their distribution in the OA femoral heads compared to the OP femoral head (Figures 6.7, 6.8 and 6.9). There is a significant increase in the number of MCFs found in the OP head. From Figure 6.7 (OA) it can be seen that few MCFs have formed in the most highly stressed region, with the majority present between 4.8 and 0.69 MNm^{-2} . They have formed fairly indiscriminately in the anterior-posterior plane, but appear to have formed more dominantly in the lateral region when compared to the medio-lateral plane. Localised clusters are also observed, close to the fovea and in the lateral region. Localised clusters of MCFs are also observed in specimen B15 (OA) (Figure 6.8). Here, the clusters have formed on the less loaded regions of the femoral head and in particular the clusters are observed in the anterior region of the femoral head. The majority of MCFs appear to be in the localised clusters with 2 MCFs in the most highly stressed region, and the more isolated incidence of MCFs present in the posterior region. It can also be observed that the majority of MCFs lie below 1.38 MNm^{-2} on the stress map. In the OP femoral head, the MCFs have formed throughout the entire bone structure in a fairly random manner, with MCFs more dominant in the medial region of the head (Figure 6.9).

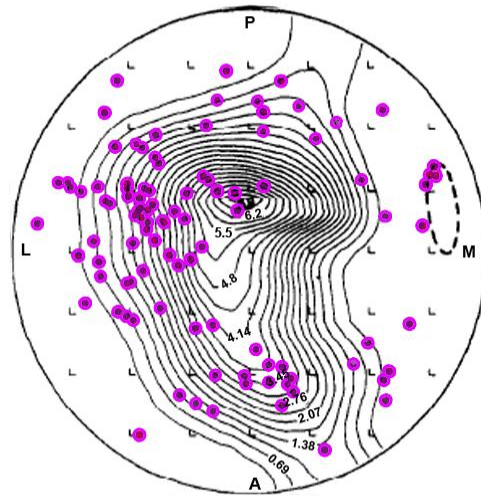


Figure 6.7: Distributions of MCFs found in B7 (OA) superimposed on stress gradients (MNm^{-2}) from (Brown and Shaw 1983). A, P, L and M represent the anatomical positions; anterior, posterior, lateral and medial, respectively. The dashed line, represents the fovea.

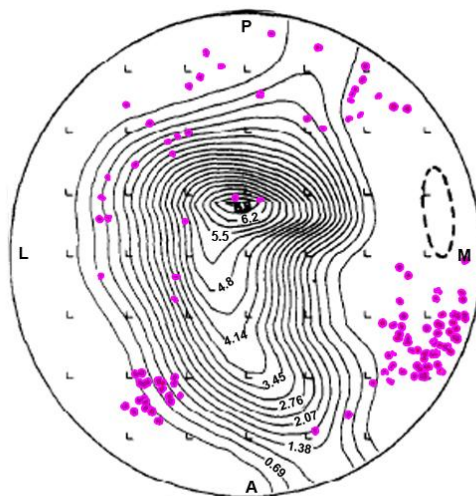


Figure 6.8: Distributions of Microcallus formations found in B15 (OA) superimposed on stress gradients from (Brown and Shaw 1983). A, P, L and M represent the anatomical positions; anterior, posterior, lateral and medial, respectively

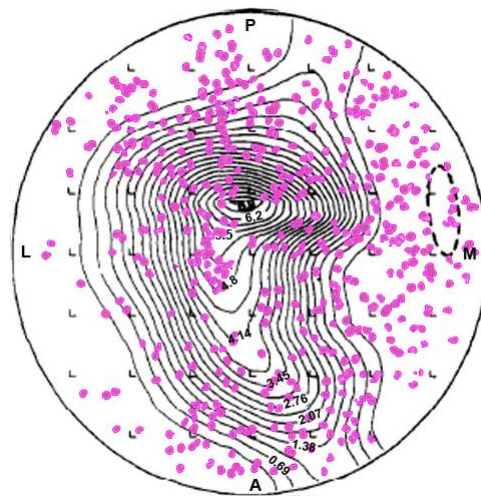


Figure 6.9: Distributions of MCFs found in B14 (OP) superimposed on loading contours from (Brown and Shaw 1983). A, P, L and M represent the anatomical positions; anterior, posterior, lateral and medial, respectively

6.4.3 Distribution of Microcallus Formations

The polar coordinates of the MCFs were calculated as outlined in Section 4.4.4. Furthermore the polar coordinates of the load bearing boundaries were calculated based on the Brown and Shaw stress map (Figure 3.8)

A total of 101 MCFs were found in specimen B7 (OA). Localised clusters of MCFs in the non- and partially-loaded regions were observed. In particular, a larger cluster was found on the partial- and non-loaded boundary. All MCFs were found in the superior region of the femoral head with isolated MCFs mainly observed in the major- and partially- loaded region. No MCFs were found in the inferior region (Figure 6.10). In Figure 6.11, two extremely defined localised clusters are observed; in the major- and non-loaded regions. This clustered trend was also observed in Figure 6.10, with two obvious clusters; in the non- and partially-loaded region. Out of the 132 MCFs found in specimen B15 (OA), very few appear isolated (mainly in the non-loaded region) but the majority appear as part of the clusters. Only 8 MCFs were found in the partially-loaded region with the majority present in the mid-section region of the head. Specimen B14 (OP) was found to have a significantly large number of MCFs, 585. This is illustrated in Figure 6.12. The MCFs in the OP femoral head appear to have formed indiscriminately in the loaded regions, except more have formed in the superior region of the femoral head. A significant number of MCFs have also formed in the region of loading which is not defined by Brown and Shaw 1983 (least shaded) (Figure 6.12).

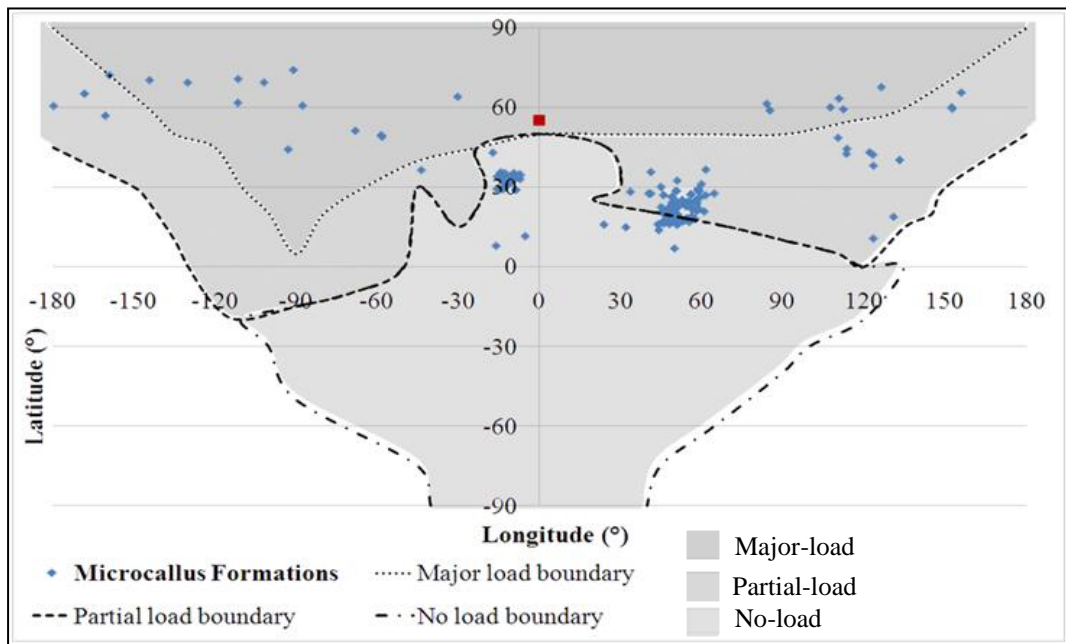


Figure 6.10: Polar coordinates of MCFs mapped onto the load bearing regions of the OA femoral head (B7), with the fovea marked in red

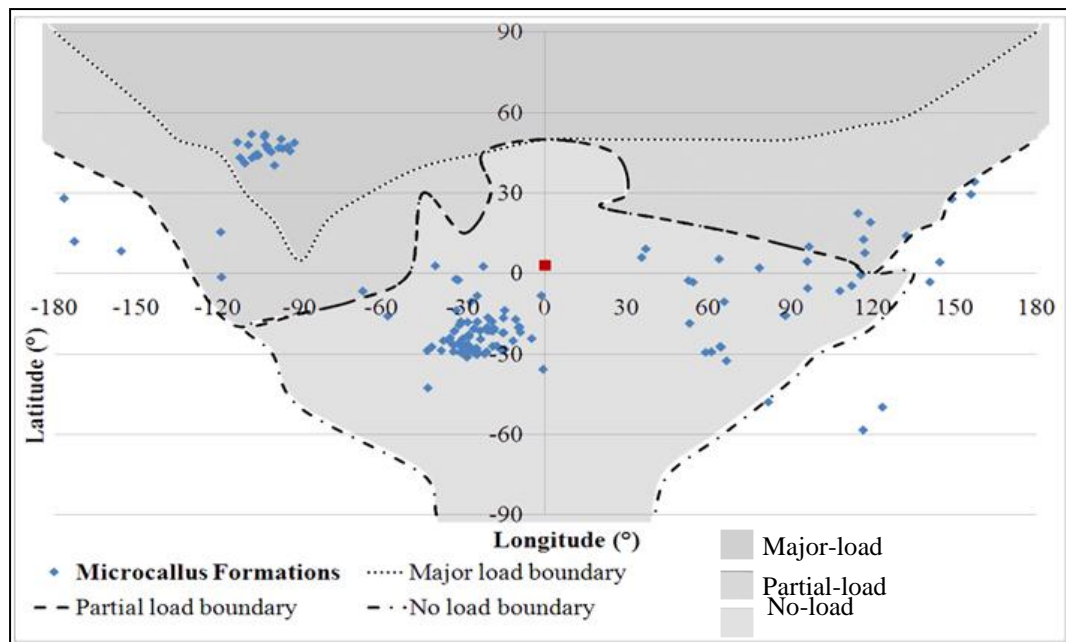


Figure 6.11: Polar coordinates of MCFs mapped onto the load bearing regions of the OA femoral head (B15), with the fovea marked in red

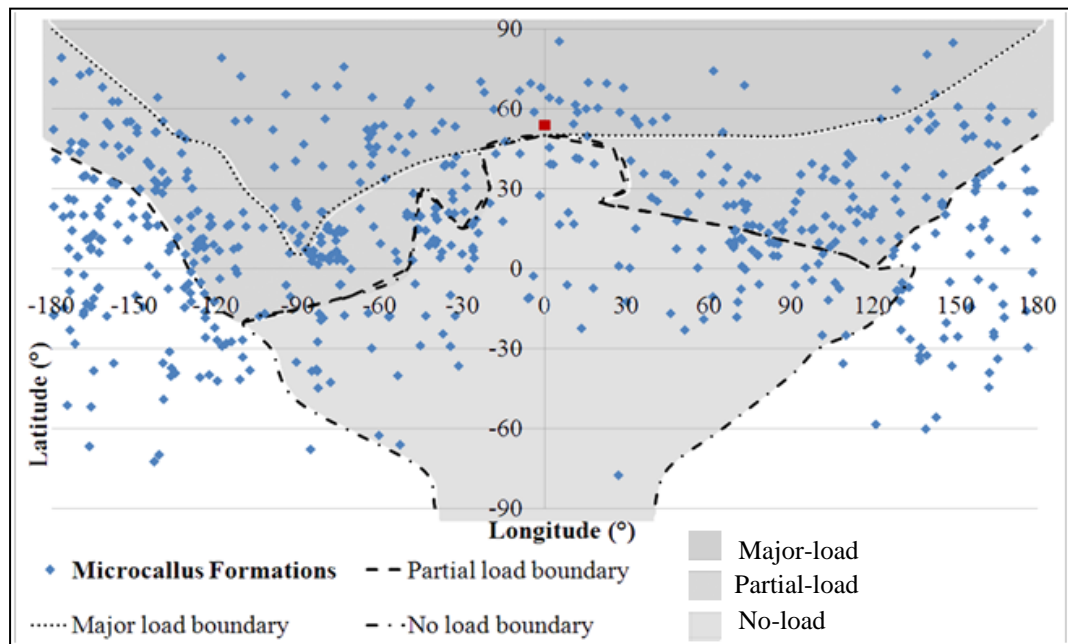


Figure 6.12: Polar coordinates of MCFs mapped onto the load bearing regions of the OP femoral head (B14), with the fovea marked in red

The densities of the MCFs were calculated from the radial distributions (section 4.4.4). In comparison, the OP head (B14) showed the highest density of MCFs between 10-15 mm (0.0129 mm^{-3}), from the centre of the femoral head. It showed very few MCFs present in the centre of the head, with a small decrease to 20mm from the centre of the head, with a marked steep decrease to 25mm (0.0008 mm^{-3}) (Figure 6.13). Both OA femoral heads show a very low density of MCFs up until 15 mm, where there is a marked increase in the density of MCFs for specimen B15, with a small drop between 20-25 mm. Whereas, for specimen B7, there is a small increase after 25 mm, with MCFs present from 25-35 mm only in specimen B7. In comparing the distribution of the density of MCFs, it was noted that in all cases the highest density of MCFs was found in different radial bins in each head. It is to be noted that the radial bins for the OP (B14) femoral head do not extend to the same degree as the OA heads due to the small size of the OP femoral head.

(For visual reference of the microcallus distribution, refer to video 5 for the OA femoral head and video 6 for the OP femoral head, Appendix V).

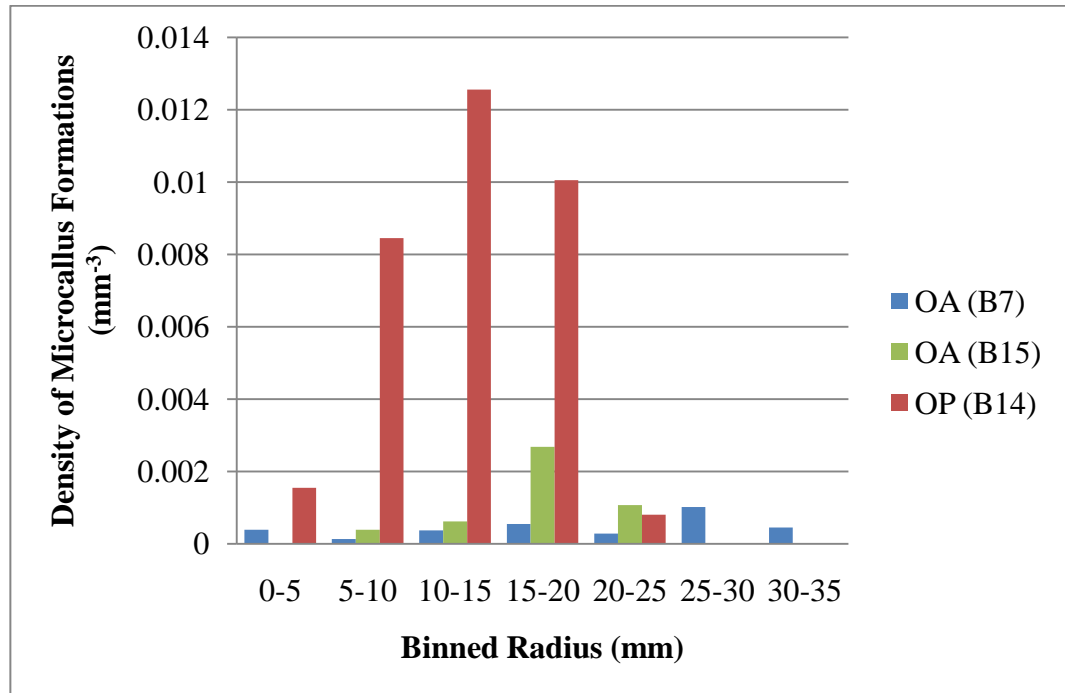


Figure 6.13: The density of MCFs found in binned radial volumes (mm^{-3}) for osteoarthritic and osteoporotic femoral heads

6.5 Bone Mineral Concentration

Data sets obtained from XMT were used to determine the BMC and the distribution of occupied bone volume throughout the pathological femoral heads. The thresholding boundary was set at 0.82 cm^{-1} , as mentioned in Section 5.5 and described in Section 4.5.1 (Figure 4.18). Post-thresholding, all phases other than bone were eliminated. The mean (standard deviation) LAC for B7 (OA), B15 (OA) and B14 (OP) was determined as $1.134 (\pm 0.045)$, $1.150 (\pm 0.052)$ and $1.189 (\pm 0.053) \text{ cm}^{-1}$ ((a) in Figure 6.14). BMC was calculated using the method described in Section 4.7. BMC was calculated from the superior to the inferior region as a function of depth in the Z-direction (Figure 6.15).

The mean BMC was $0.936 (\pm 0.041)$, $0.960 (\pm 0.538)$ and $1.00 (\pm 0.047)$ g cm^{-3} , for specimens B7 (OA), B15 (OA) and B14 (OP) respectively. The medio-lateral regions of all the femoral heads have a lower mineral concentration than the superior and inferior regions.

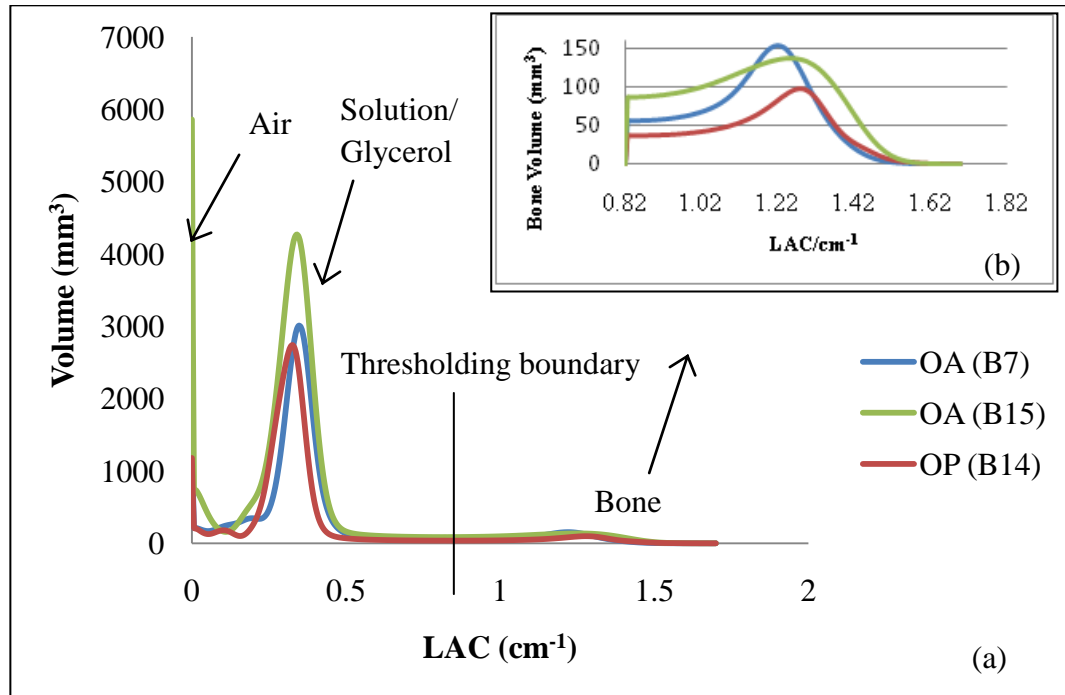


Figure 6.14: (a) Graph showing volume vs. LAC for the pathological femoral heads obtained from the XMT data set. The peaks relate to the LAC of air, glycerol and bone, and (b) the ROI post-thresholding containing bone, with the distribution of LAC for bone

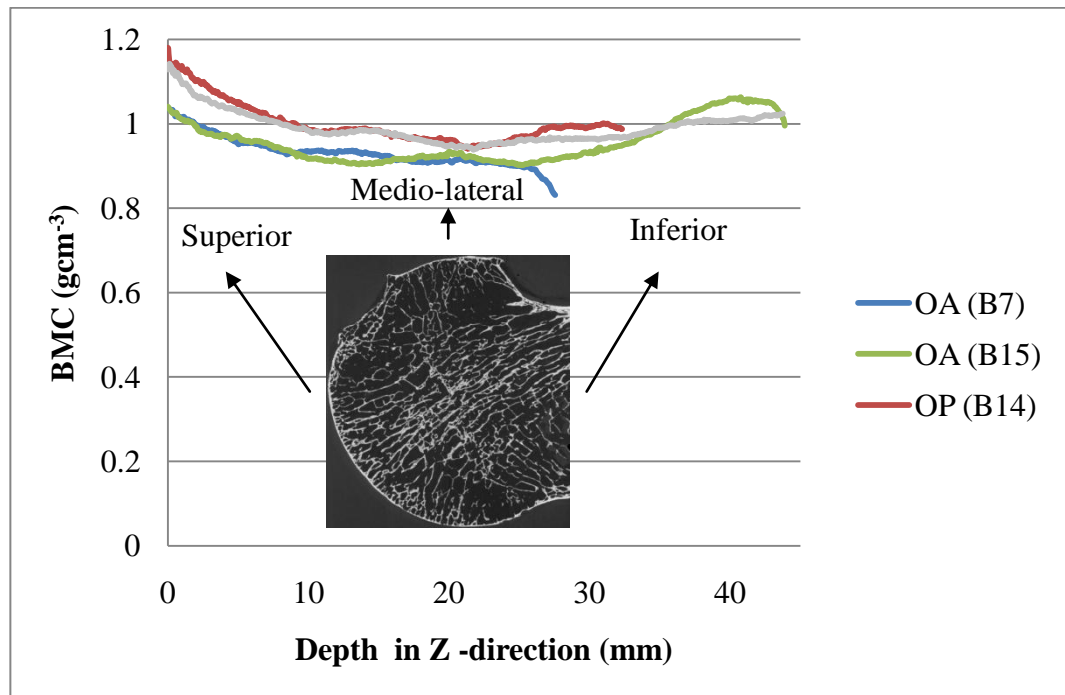


Figure 6.15: The distribution of BMC along the Z-direction of the pathological femoral heads, from superior to inferior. The grey line denotes Figure 5.9 for reference

6.6 Bone Volume Fraction Distribution

Bone volume fraction (occupied bone volume) was calculated from histograms obtained from XMT data sets. The distribution of bone volume fraction is shown from the superior to the inferior region of the femoral heads (Figure 6.16). In all cases, an increase in BVF was observed to the medio-lateral region of the femoral heads with a decrease from there on to the inferior region. An increase in BVF in the OP is also observed between 20 and 30 mm. A significant decrease in BVF is observed in specimen B15 (OA) from the superior to the inferior region (Figure 6.16). To further investigate the BVF, regions were cropped and are reported in Section 6.7.

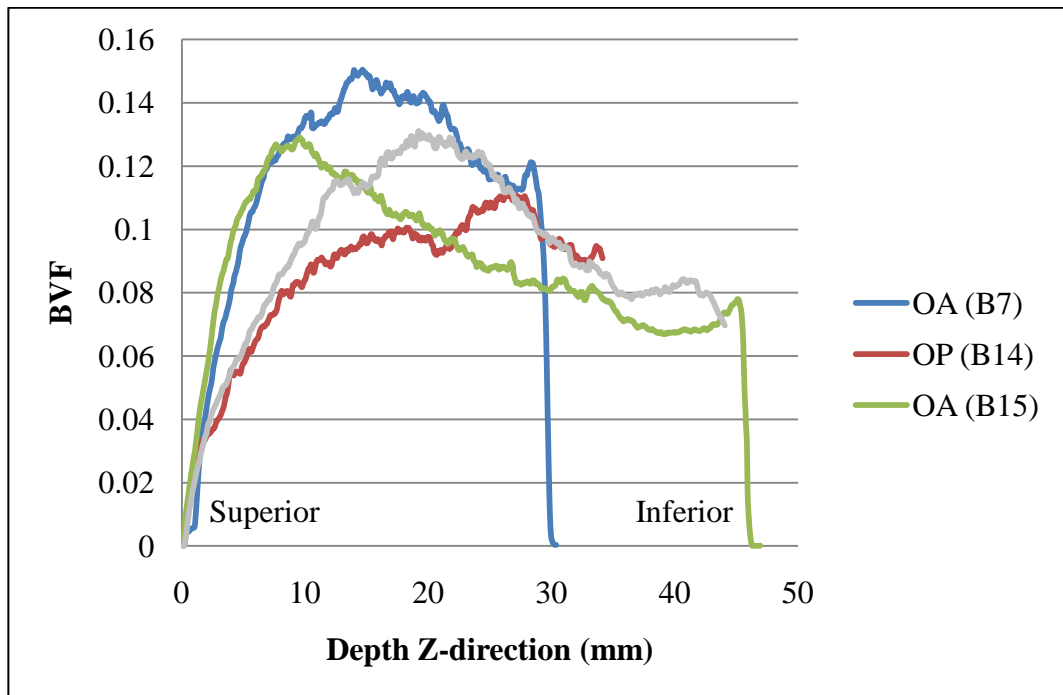


Figure 6.16: Distribution of the occupied bone tissue throughout the pathological femoral heads. The grey line denotes Figure 5.10 for reference

6.7 Evaluation of Bone Quality Using XMT

A number of morphometric factors were measured for all the specimens (Section 4.6). A total of 5 randomised cuboidal volumes measuring 3 × 3 mm per load bearing region were extracted from the femoral heads using Tomview software. Statistical analysis was performed with SPSS software version 17.0 (SPSS Inc., Chicago, IL, USA). Normality of the data was tested with a one-sample Shapiro-Wilk test to indicate the appropriateness of parametric testing. The correlation coefficients were calculated by Pearson Rank correlation analyses due to normal distribution of the histomorphometric factors. P-values of < 0.05 were considered as statistically significant.

Bone volume fraction (BVF) was significantly correlated with Trabecular Thickness (Tb.Th) ($R = 0.837$ $p = 0.000$) as shown in Figure 6.17. The major-loaded region in the OA heads showed a higher BVF and thicker trabeculae than the OP head and all other loading regions in the OA femoral heads. A greater localised variation in BVF and Tb.Th was observed in the OA femoral heads in comparison to the OP head, with the OP head showing a median of 0.195 for BVF with range 0.115 – 0.269, and 0.181 mm Tb.Th with the range 0.163 – 0.212 mm. Whereas for specimen B15 (OA) the median value for BVF was 0.226, with the values ranging from 0.092 - 0.415, and for Tb.Th the overall median value was 0.191 mm, with the range 0.125 – 0.264 mm. Specimen B15 (OA) varied highly in bone quality measures within the structure, whereas in the OP femoral head a close relationship was observed between occupied bone volume (BVF) and Tb.Th. A significant negative correlation was observed between Trabecular Spacing (Tb.Sp) and BVF ($R = -0.807$ $p = 0.000$) (Figure 6.18). Here, it was observed that in the partially-loaded region of the OP femoral head the lowest occupied bone volume with the highest trabecular spacing was exhibited. Also, the major-load regions of the OA femoral heads exhibited the trabeculae more closely arranged with less trabecular spacing. BVF and trabeculae number (Tb.N) scale well as seen in Figure 6.19, where a positive linear relationship is observed ($R = 0.984$ $p = 0.000$).

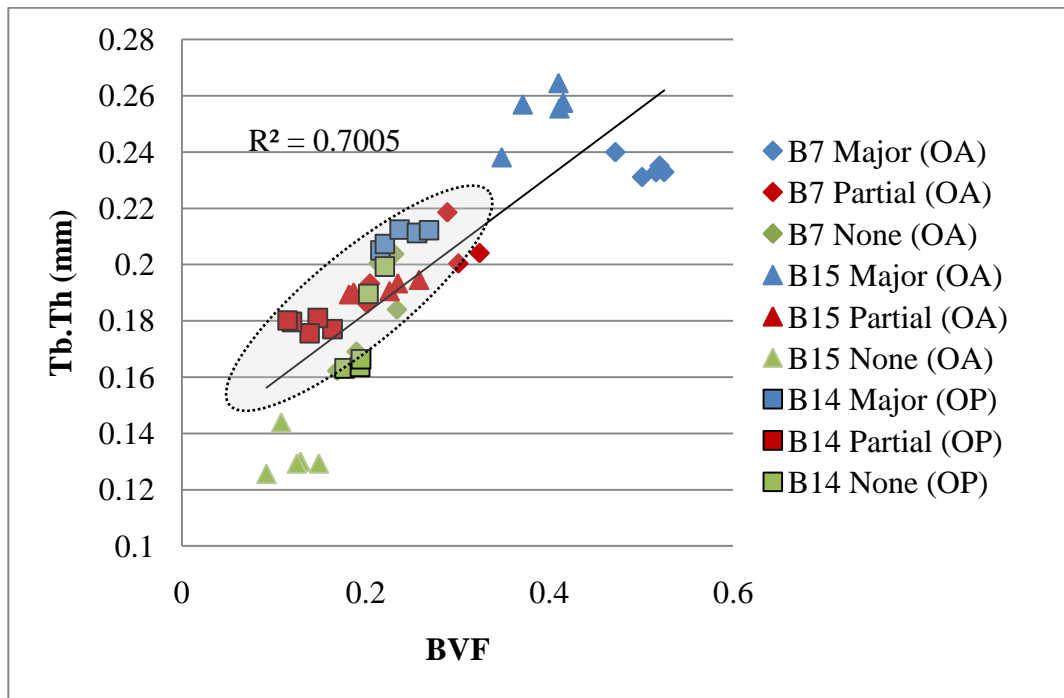


Figure 6.17: Plot of Bone Volume Fraction vs. Trabecular Thickness for major-, partial- and non-load bearing regions of the OA and OP heads ($R = 0.837$ $p = 0.000$). The shaded region represents Figure 5.11 for reference

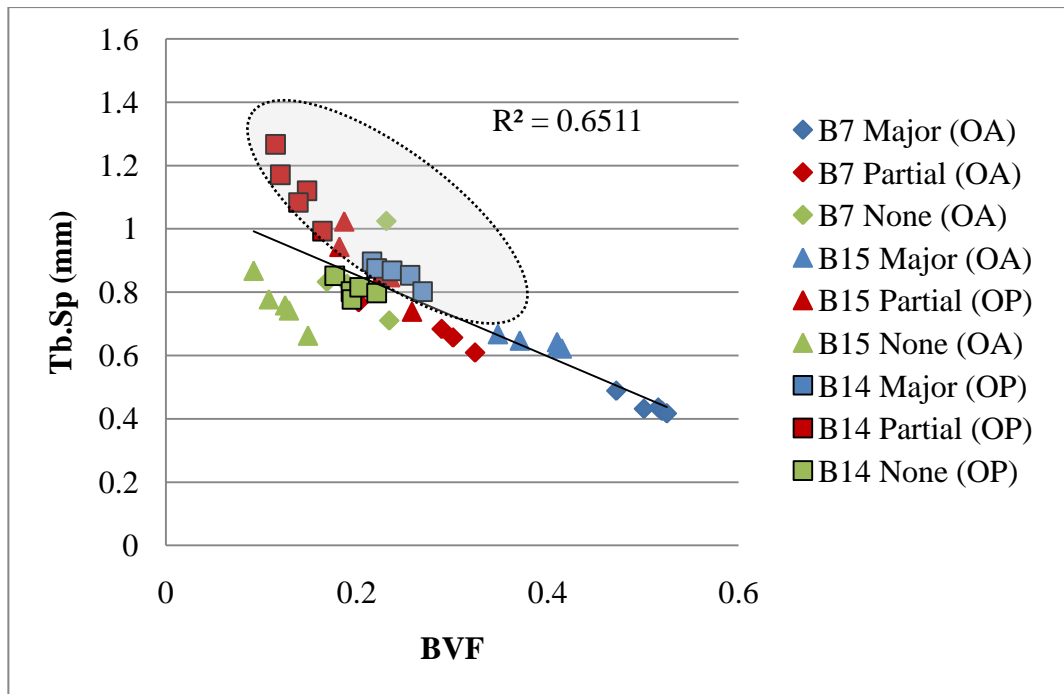


Figure 6.18: Plot of Bone Volume Fraction vs. Trabecular Spacing for major-, partial- and non-load bearing regions of the OA and OP heads ($R = -0.807$ $p = 0.000$). The shaded region represents Figure 5.12 for reference.

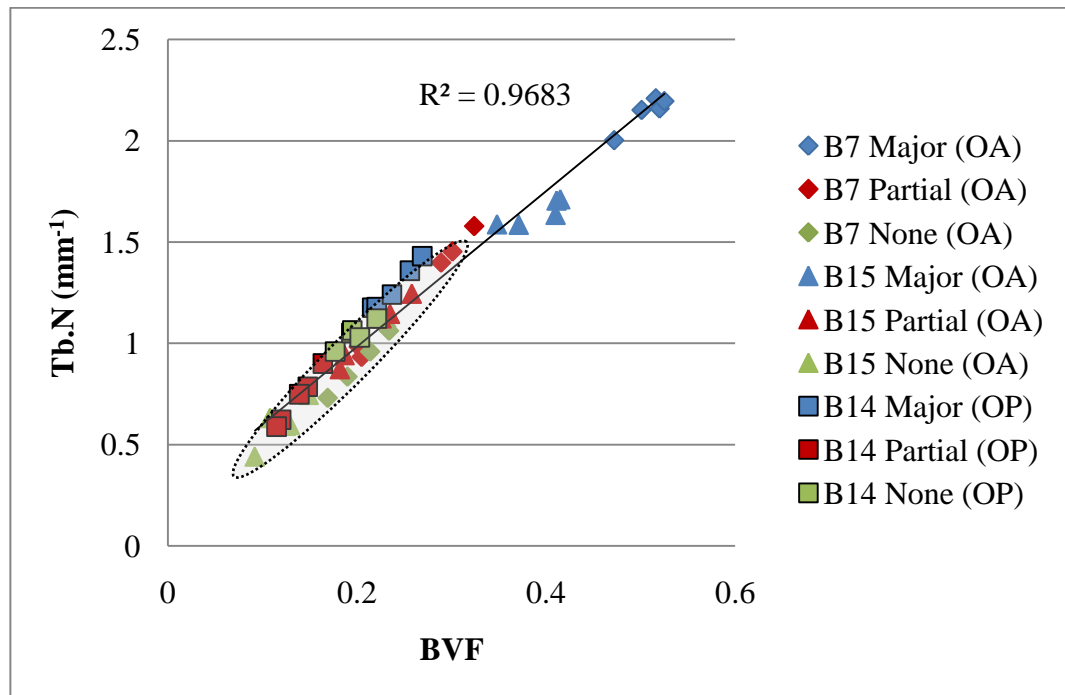


Figure 6.19: Plot of Bone Volume Fraction vs. Trabecular Number for major-, partial- and non-load bearing regions of the OA and OP heads ($R = 0.984$ $p = 0.000$). The shaded region represents Figure 5.13 for reference

BVF was significantly correlated with Structural Model Index (SMI). A negative linear correlation was observed (Figure 6.20). The major-loaded regions of the OA femoral heads exhibited more plate-like structure with more occupied bone volume whereas the partial- and non-loaded regions exhibited a more rod-like structure with less occupied bone volume. The median SMI and range for major – loaded regions of B7 (OA) and B15 (OA) were shown to be 0.89 (0.859-1.272) and 1.236 (1.179-1.7090) respectively. Overall, the OP head exhibited a more rod-like structure with a median SMI 2.595 ranging from 1.848 - 2.948 (Table 6.2). As Trabecular number is so closely correlated with BVF, it is not surprising that a similar trend was found when correlating Tb.N with SMI (Figure 6.21) ($R = -0.879$ $p = 0.000$).

Connectivity Density (Conn.D) was significantly correlated with SMI. Higher variability in the Conn.D of the plate-like major-loaded regions was observed, ranging from 4.373-15.342 mm^{-3} (Figure 6.22). However all other groups exhibited a more rod-like, less connected structure, ranging from 1.651-8.687 mm^{-3} . Figure 6.23 showed that the plate-like trabeculae in the major-loaded regions of the OA femoral heads were thicker than the rod-like trabeculae in all other sample groups. Trabecular thickness was significantly correlated with SMI ($R = -0.769$ $p = 0.000$) and negative correlation was observed. Similar median Tb.Th for major-loaded regions of B7, B14 and B15 were observed at 0.232, 0.211, 0.256 mm, respectively, but a marked difference in the median SMI was found; 0.890, 2.280, 1.236 respectively.

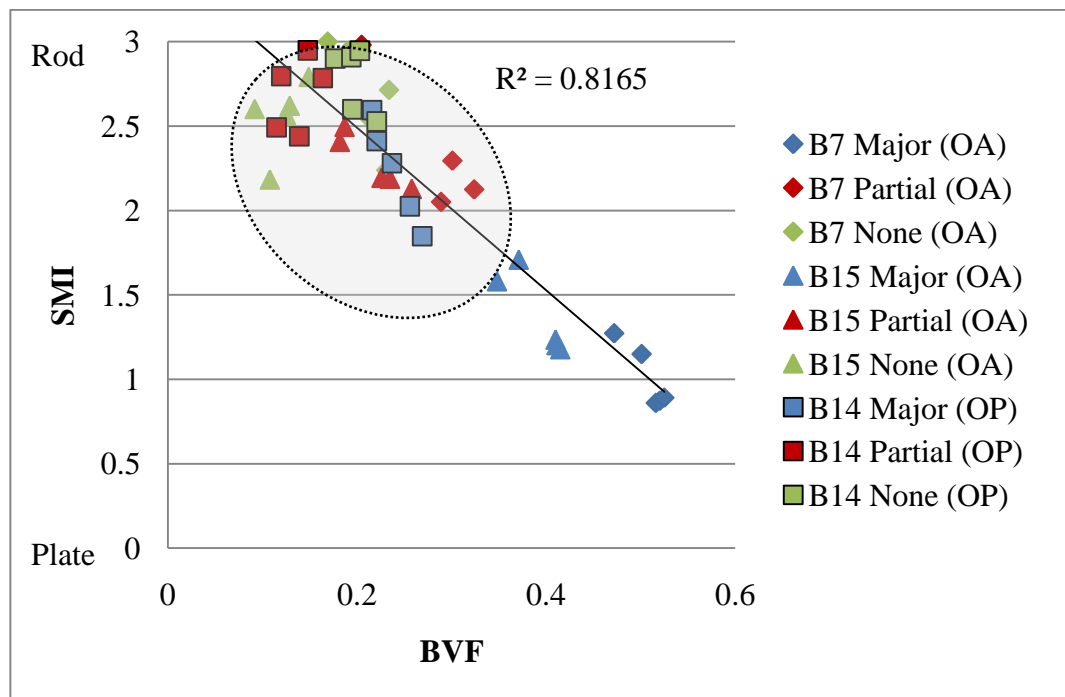


Figure 6.20: Plot of Bone Volume Fraction vs. Structural Model Index for major-, partial- and non-load bearing regions of the OA and OP heads ($R = -0.904$ $p = 0.000$). The shaded region represents Figure 5.14 for reference

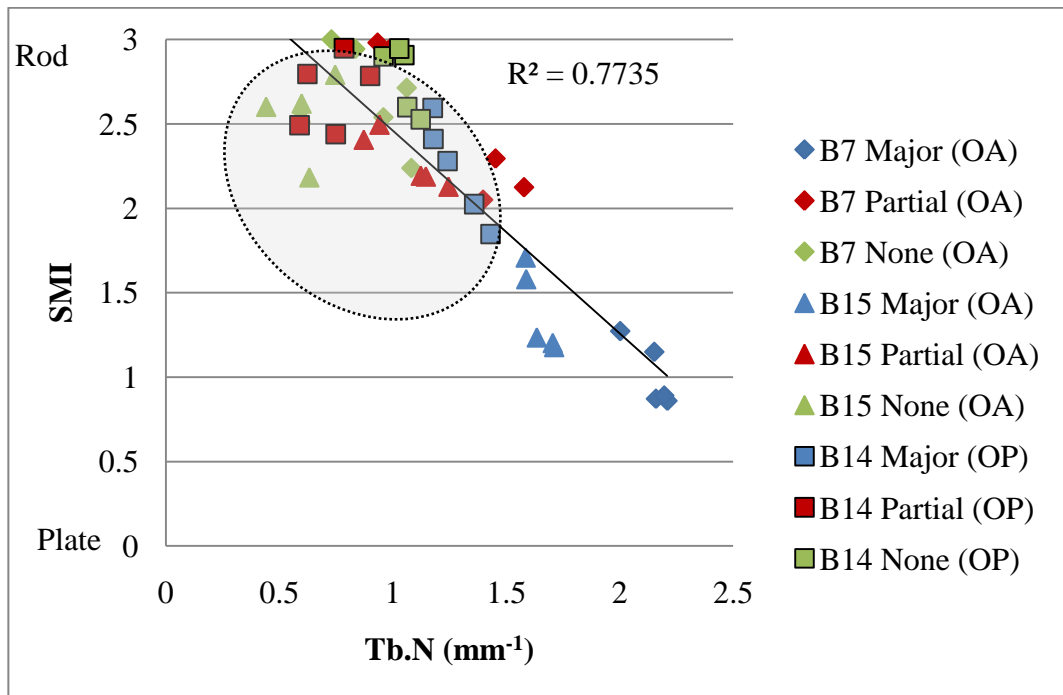


Figure 6.21: Plot of Structural Model Index vs. Trabecular Number for major-, partial- and non-load bearing regions of the OA and OP heads ($R = -0.879$ $p = 0.000$). The shaded region represents Figure 5.15 for reference

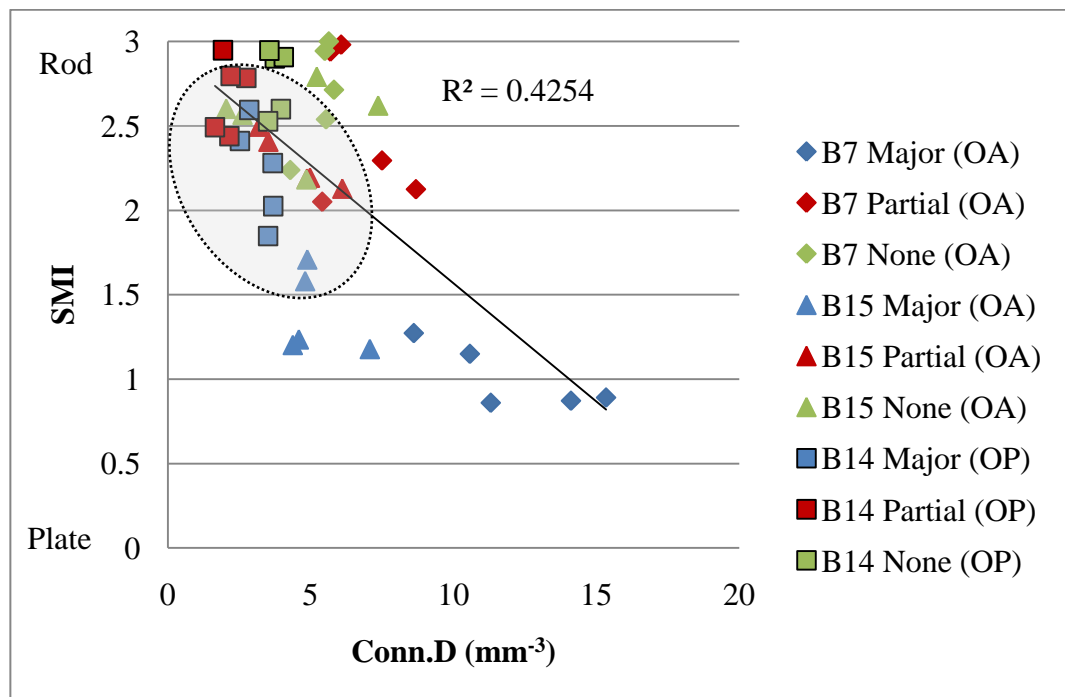


Figure 6.22: Plot of Connectivity Density vs. Structural Model Index for major-, partial- and non-load bearing regions of the OA and OP heads ($R = -0.652$ $p = 0.000$). The shaded region represents Figure 5.16 for reference

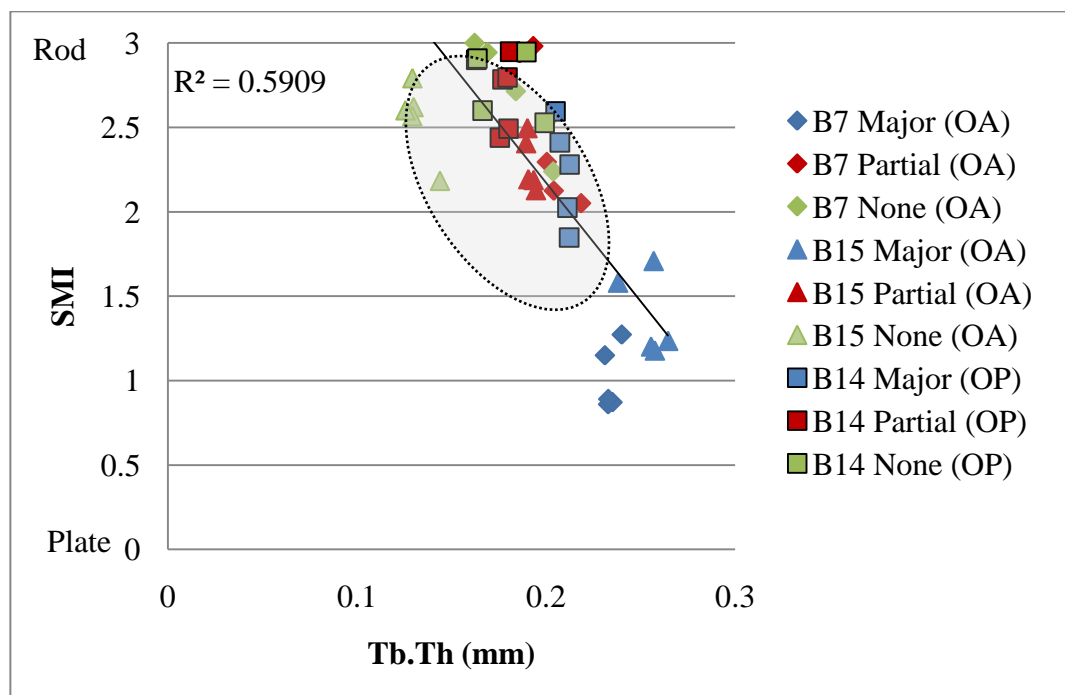


Figure 6.23: Plot of Trabecular Thickness vs. Structural Model Index for major-, partial- and non-load bearing regions of the OA and OP heads ($R = -0.769$ $p = 0.000$). The shaded region represents Figure 5.17 for reference.

From Figure 6.24 the OP femoral head is seen to exhibit a higher degree of anisotropy (DA) than the OA heads, especially in the partial- and non-loaded regions. No significant correlation was found between BVF and DA ($R = -0.030$ $p = 0.846$). There was also no significant correlation between Conn.D and DA ($R = -0.151$ $p = 0.322$) (Figure 6.25). The major load region of specimen B7 exhibited a higher variability in Conn.D but similar anisotropy in comparison to other regions and Specimens B15 (OA), but was less anisotropic compared to B14 (OP). The OP trabeculae exhibited a less connected and more anisotropic structure in comparison to the OA trabeculae.

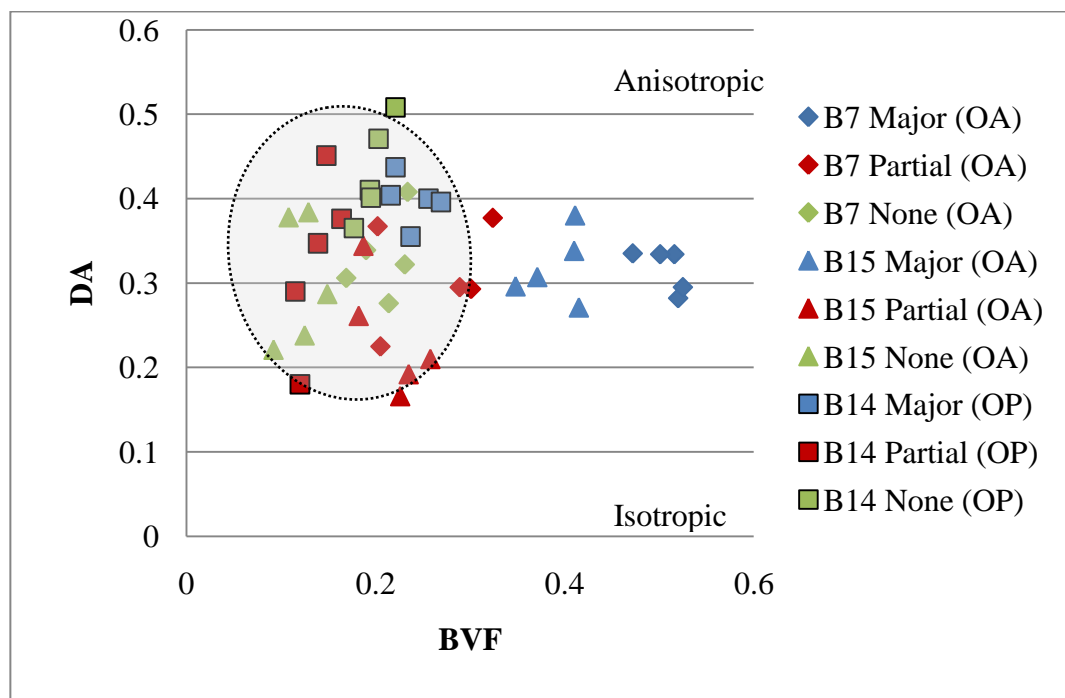


Figure 6.24: Plot of Bone Volume Fraction vs. Degree of Anisotropy for major-, partial- and non-load bearing regions of the OA and OP heads ($R = -0.030$ $p = 0.846$). The shaded region represents Figure 5.18 for reference

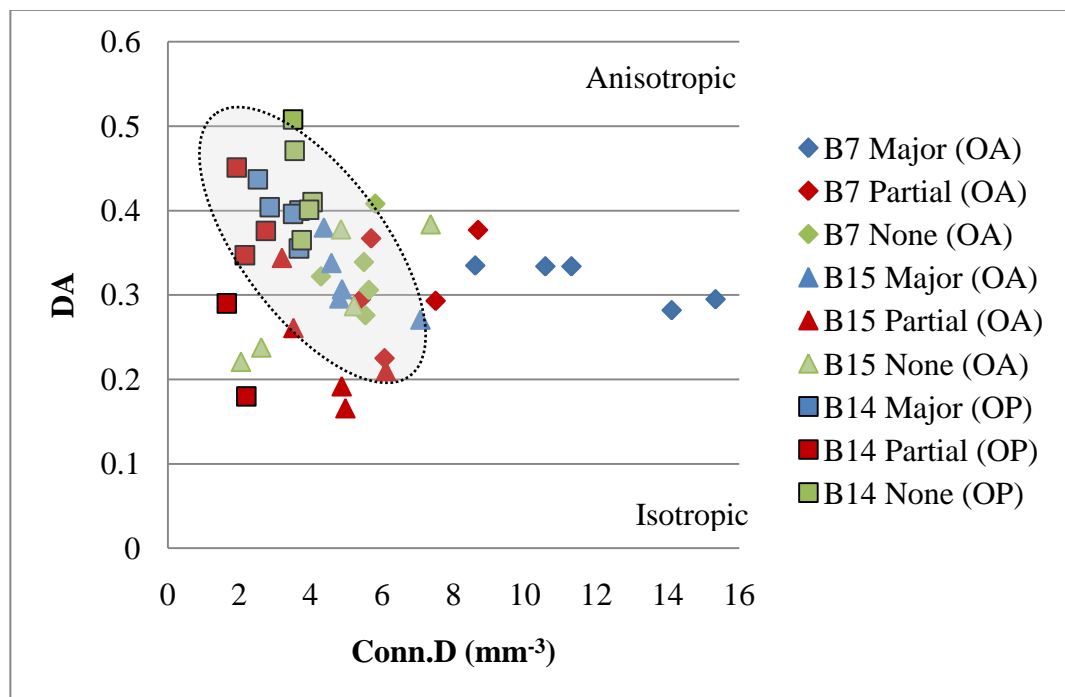


Figure 6.25: Plot of Connectivity Density vs. Degree of Anisotropy for major-, partial- and non-load bearing regions of the OA and OP heads ($R = -0.151$ $p = 0.322$). The shaded region represents Figure 5.19 for reference

Conn.D correlated strongly with Tb.N ($R = 0.538$ $p = 0.002$) (Figure 6.26). The major load region of B7 (OA) exhibited a highly varied connected structure with a higher number of trabeculae present, with Conn.D ranging from $8.606 - 15.342\text{mm}^{-3}$. The major load region of B15 (OA) also exhibited a higher number of trabeculae but showed a similar connectivity density when compared to other OA regions of both OA femoral heads. The less connected OP structure exhibited similar number of trabeculae as the partial and non-loading regions of the OA trabeculae.

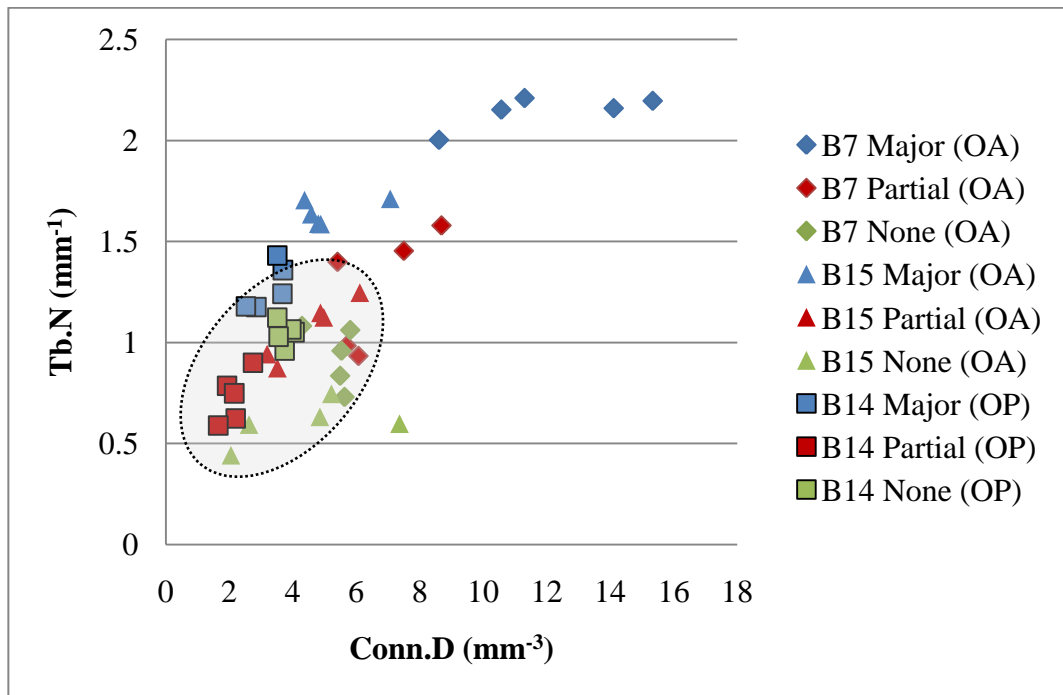


Figure 6.26: Plot of Connectivity Density vs. Trabecular Number for major-, partial- and non-load bearing regions of the OA and OP heads ($R = 0.538$ $p = 0.002$). The shaded region represents Figure 5.20 for reference

A significant correlation was observed between Tb.Th and Tb.N ($R = 0.837$ $p = 0.000$). Figure 6.27 showed that overall as trabecular thickness increases the trabecular number also increased with the highest number and thickest trabeculae present in the major-loaded regions of the OA heads and the thinnest and least number of trabeculae present in the non-loaded region of specimen B15 (OA). The OP head exhibited little variation in trabecular thickness but ranged in trabeculae number from 0.589 to 1.430 mm^{-1} . The partially-loaded regions of the OA head showed a similar pattern in results to that of the OP femoral head.

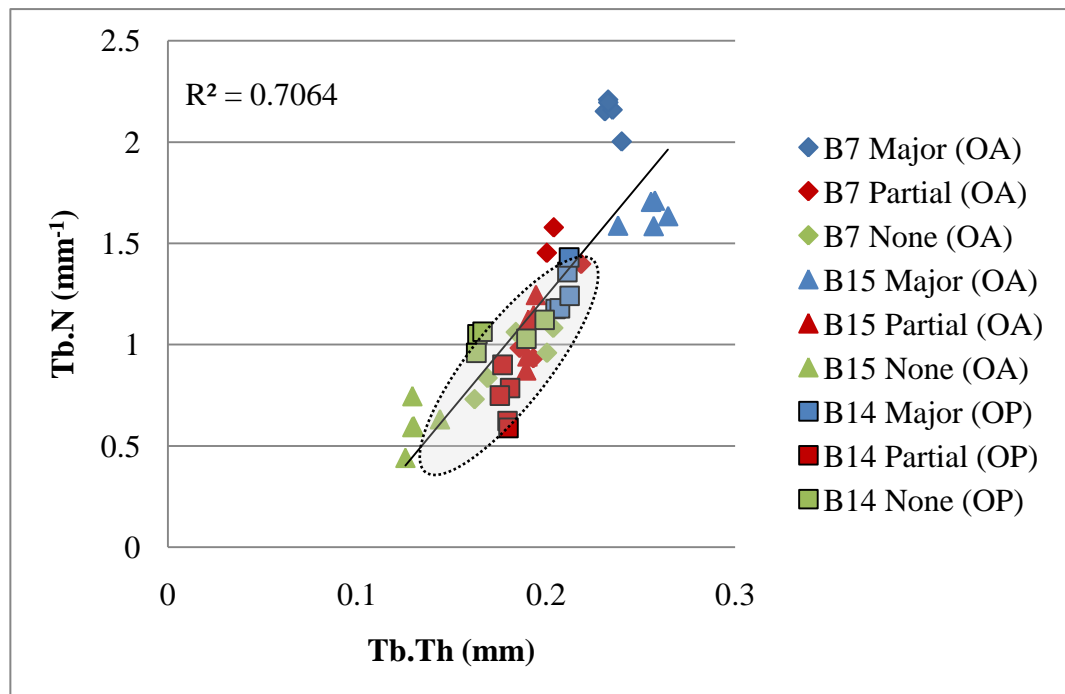


Figure 6.27: Plot of Trabecular Thickness vs. Trabecular Number for major-, partial- and non-load bearing regions of the OA and OP heads ($R = 0.837$ $p = 0.000$). The shaded region represents Figure 5.21 for reference

BMC was significantly correlated with Tb.Th ($R = 0.770$ $p = 0.000$). All sample groups apart from the non-loading OA (B15) group were found to have similar bone mineral concentration with values between $0.890 - 1.013 \text{ g cm}^{-3}$ (Table 6.2). The non-loaded OA group exhibited a lower bone mineral concentration (Figure 6.28), with a median value of 0.770 , with range $0.762-0.810$ (Table 6.2).

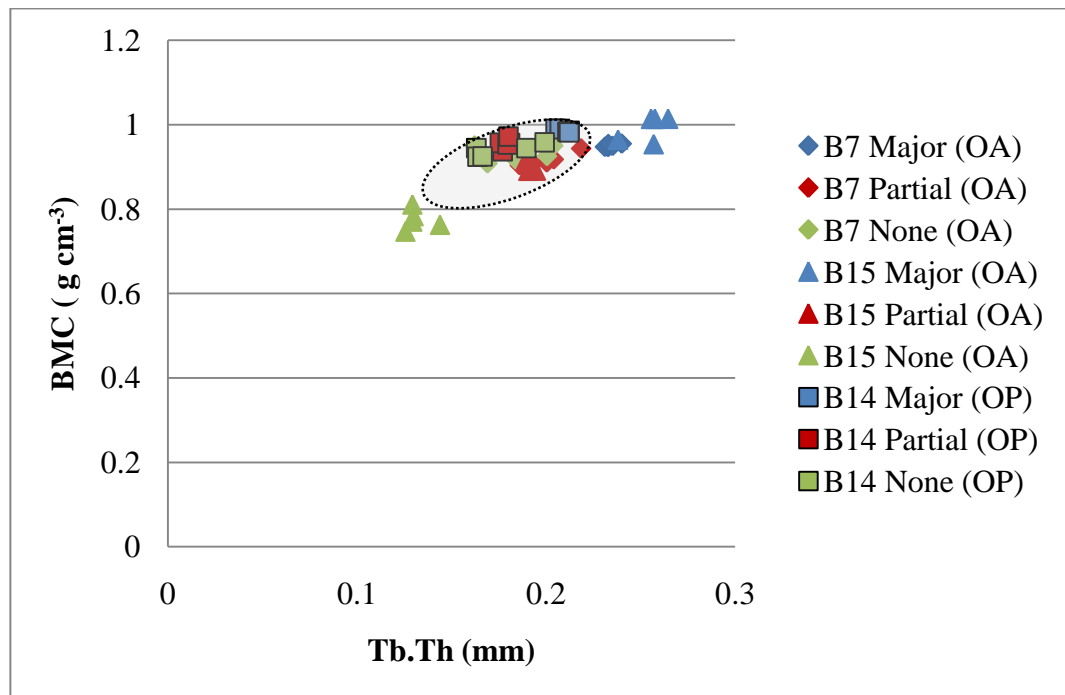


Figure 6.28: Plot of Trabecular Thickness vs. Bone Mineral Concentration for major-, partial- and non-load bearing regions of the OA and OP heads ($R = 0.770$ $p = 0.000$). The shaded region represents Figure 5.22 for reference

Table 6.2: Summary of the regional and overall variations for Bone Quality Measurements in the normal femoral head

*Median †Range (min-max)

Loading Region	BVF	SMI	Conn.D (mm ³)	Tb.Th (mm)	Tb.Sp (mm)	Tb.N (mm ⁻¹)	DA	BMC (gm ⁻³)
B7 Major (OA)	0.516* (0.472-0.525) †	0.890* (0.859-1.272) †	11.303* (8.606-15.342) †	0.232* (0.231-0.239) †	0.4328* (0.417-0.488) †	2.159* (2.002-2.209) †	0.334* (0.282-0.330) †	0.949* (0.947-0.955) †
B7 Partial (OA)	0.289* (0.202-0.324) †	2.295* (2.051-2.981) †	6.608* (5.407-8.687) †	0.200* (0.186-0.218) †	0.683* (0.608-0.814) †	1.398* (0.933-1.578) †	0.295* (0.225-0.377) †	0.910* (0.903-0.943) †
B7 None (OA)	0.207* (0.169-0.234) †	2.714* (2.239-3.00) †	5.535* (4.287-5.812) †	0.184* (0.162-0.203) †	0.826* (0.709-1.024) †	0.959* (0.835-1.082) †	0.322* (0.276-0.408) †	0.925* (0.908-0.950) †
B14 Major (OP)	0.237* (0.216-0.269) †	2.280* (1.848-2.595) †	3.509* (2.523-3.688) †	0.211* (0.205-0.212) †	0.867* (0.801-0.896) †	1.241* (1.175-1.430) †	0.400* (0.355-0.437) †	0.985* (0.981-0.989) †
B14 Partial (OP)	0.139* (0.115-0.164) †	2.784* (2.439-2.948) †	2.157* (1.651-2.746) †	0.179* (0.175-0.181) †	1.120* (0.992-1.267) †	0.745* (0.589-0.900) †	0.347* (0.180-0.451) †	0.956* (0.936-0.971) †
B14 None (OP)	0.195* (0.177-0.221) †	2.900* (2.527-2.946) †	3.747* (3.509-4.05) †	0.166* (0.163-0.199) †	0.801* (0.777-0.851) †	1.050* (0.959-1.122) †	0.410* (0.365-0.508) †	0.944* (0.923-0.958) †
B14 Major (OA)	0.410* (0.371-0.415) †	1.236* (1.179-1.709) †	4.806* (4.373-7.071) †	0.256* (0.238-0.264) †	0.642* (0.622-0.667) †	1.634* (1.585-1.711) †	0.307* (0.271-0.380) †	1.013* (0.984-1.013) †
B14 Partial (OA)	0.226* (0.182-0.258) †	2.194* (2.129-2.496) †	4.872* (3.196-6.109) †	0.190* (0.189-0.193) †	0.854* (0.739-1.023) †	1.12* (0.872-1.245) †	0.210* (0.166-0.344) †	0.891* (0.890-0.916) †
B14 None (OA)	0.125* (0.092-0.149) †	2.602* (2.184-2.792) †	4.850* (2.048-7.36) †	0.129* (0.125-0.143) †	0.759* (0.663-0.868) †	0.598* (0.441-0.746) †	0.287* (0.221-0.384) †	0.770* (0.762-0.810) †

Chapter 7 *In-Vitro* Mechanical testing of trabecular bone using XMT

7.0 Introduction

Age related bone fractures impose a significant social and economic problem on our increasingly ageing population. Understanding the underlying mechanisms of those devastating fractures may help to generate strategies for prevention and treatment. Quantification of bone tissue mechanical quality is important in delineating the underlying mechanisms of many metabolic diseases. In addition, bone tissue may constantly undergo adaptational changes in response to local alterations in mechanical conditions. These adaptational processes are very important in the pathogenesis of age related bone fragility. Quantification of bone tissue properties is prerequisite to characterizing the mechanical environment in which bone cells reside. This study aims to relate the mechanical properties to the load bearing regions in osteoarthritic femoral heads and determine the relationship between mechanical properties and bone quality.

The objectives were:

- To analyse osteoarthritic bone micro-architecture and bone quality, and relate this to mechanical properties of osteoarthritic trabecular bone
- To analyse the failure behaviour of osteoarthritic trabecular bone in 3D using image analysis

7.1 Methods and Materials

Ten cylindrical specimens measuring 5 mm × 10 mm (diameter × length) were extracted from 3 OA femoral heads (Specimens B3, B4 and B5) (Section 3.2.1) and loaded in compression inside the XMT system using an in-house device (Section 4.2.2). The specimens were strained at 2% increments from 0 - 10%. The specimens were imaged at each increment using the XMT system; all force-displacement data was recorded (Section 4.2.2), and converted to Stress-Strain data for analysis (Section 4.8). Morphometric parameters were recorded and used as a measure of Bone Quality (Section 4.6), and furthermore correlated to mechanical findings.

7.2 Results

7.2.1 Region of Interest

Data sets obtained from XMT were used to determine the region of interest. The thresholding boundary was set at 0.82 cm^{-1} as described in Section 4.5.1 (Figure 4.18). Post-thresholding, all phases other than bone were eliminated. Histograms obtained from the XMT data sets were normalised for voxel frequency for comparison (Figure 7.1). Figure 7.1 shows an example of a major-load bearing specimen where the region of interest remained the same for all strains. All further calculations were based on this ROI.

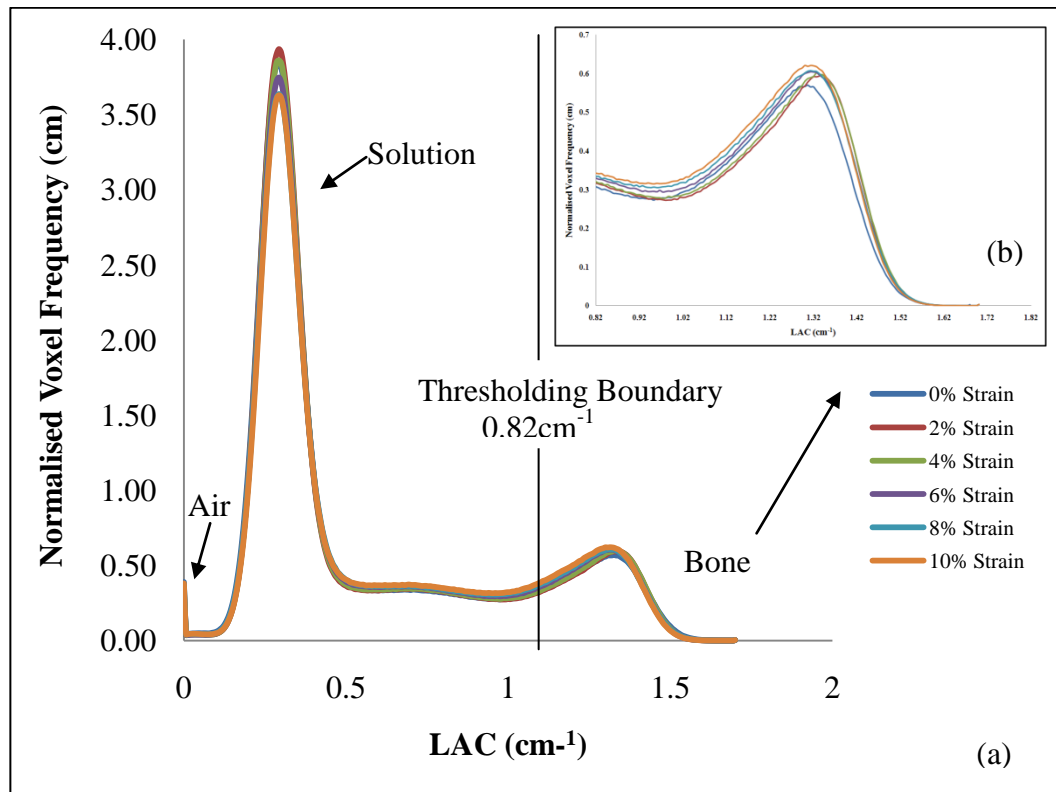


Figure 7.1: (a) Graph showing Normalised voxel frequency vs. LAC for bone cylinder data obtained from XMT. The peaks relate to the LAC of air, glycerol and bone, and (b) the ROI post-thresholding containing bone, with the distribution of LAC for bone

7.2.2 Assessment of Bone Quality and Mechanical Properties

Mechanical Properties

Mechanical properties of the compressed bone cylinders were calculated from load-displacement data noted during the *In-vitro* compression testing inside the XMT system (Section 4.2.2). Bone quality measurements were calculated using data sets obtained from XMT (Section 4.6). This section reports on the findings and correlations between bone quality and mechanical properties. Mechanical properties were calculated for 10 specimens taken from different load bearing regions (Section 3.3).

Figure 7.2 shows the resulting stress-strain curves with a calculated systematic error of 5%. Specimen B3 partial-load bearing, exhibited significantly different mechanical properties to all other specimens. Specimen B3 non-load bearing, B5 major-load bearing, B5 major-load bearing, and B8 partial-load bearing; were all taken from different femoral heads and are from different load bearing regions but appear grouped together, with all other specimens showing similar stress-strain curves to each other.

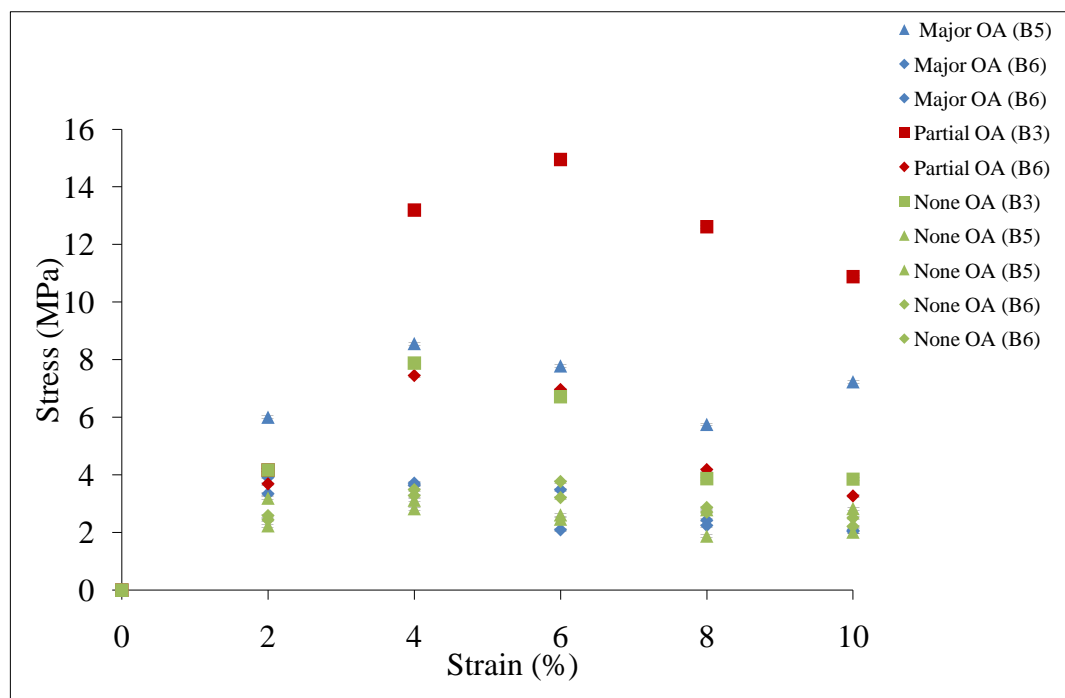


Figure 7.2: Stress-Strain graph of compressed bone cylinders from major-, partial- and non-load bearing regions, with a systematic error of 5%

Bone Quality and Mechanical Properties

A number of morphometric factors were measured for all the specimens (Section 4.6). All specimens were cropped to measure 3 × 3 mm using Tomview software. Statistical analysis was performed with SPSS software version 17.0 (SPSS Inc., Chicago, IL, USA). Normality of the data was tested with a one-sample Shapiro-Wilk test to indicate the appropriateness of parametric testing. The correlation coefficients were calculated by Pearson Rank correlation analyses due to normal distribution of the histomorphometric and mechanical parameters. P-values of <0.05 were considered as statistically significantly.

Bone volume fraction (BVF) was significantly correlated to Maximum Compressive Stress (MCS) ($R = 0.855$ $p = 0.002$). Specimens B6 major-load bearing exhibited similar MCS (3.91 and 3.71MPa) to B6 non-load bearing (3.76 and 3.28MPa), and B5 non-load bearing (3.19MPa). B6 major-load bearing, also exhibited lower BVF than all other specimens (Table 7.1). A negative correlation was determined between MCS and SMI ($R = -0.784$ $p = 0.007$) (Figure 7.4). Specimens exhibiting more rod-like structure were found to have lower MCS, in particular specimens from major- and non-load bearing regions of femoral head B6 (Table 7.1). Non-load bearing specimens from femoral head B5 also showed low MCS in comparison to specimens from femoral head B3. Where, specimens from B3 and B5 major-load bearing showed a higher MCS and were more inclined towards a rod-like structure (Table 7.1). Overall, a more plate-like structure was more closely related to a lower MCS. Trabecular thickness (Tb.Th) was positively correlated with MCS ($R = 0.871$ $p = 0.001$). A general trend of increase in Tb.Th resulting in an increase of MCS was observed. The non-load bearing trabeculae were thinner with lower MCS (Figure 7.5) along with major-load bearing specimens from B6 which also showed a similar trend. No other correlations were observed between any of the parameters shown in Table 7.1.

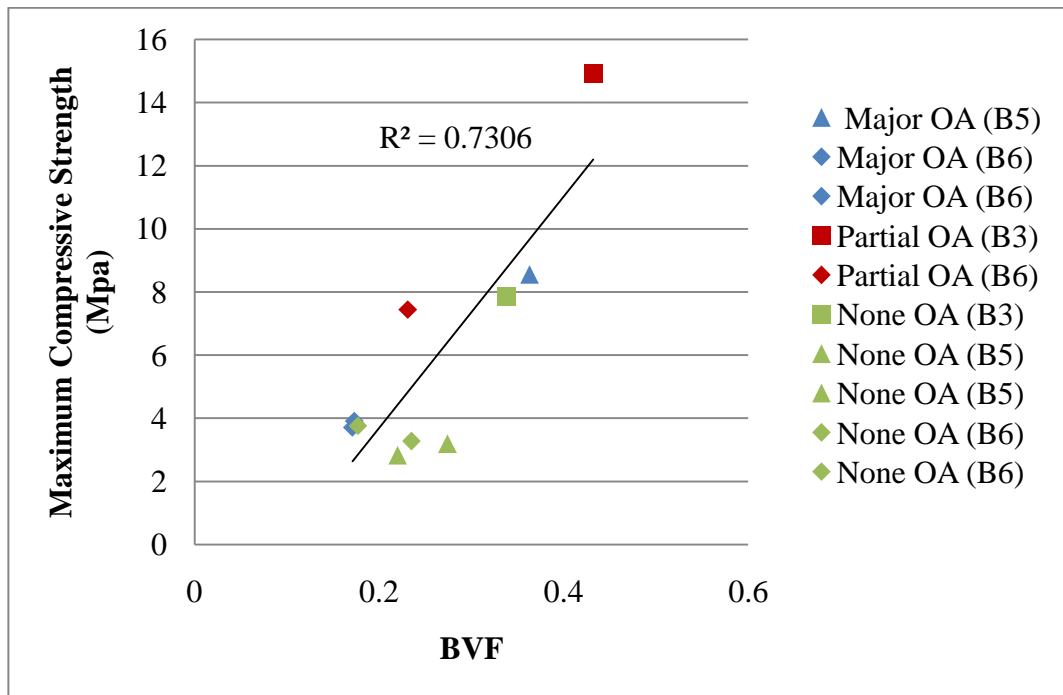


Figure 7.3: Plot of maximum compressive stress vs. Bone volume fraction for bone cylinders from major-load, partial-load and non-load bearing regions ($R = 0.855$ $p = 0.002$)

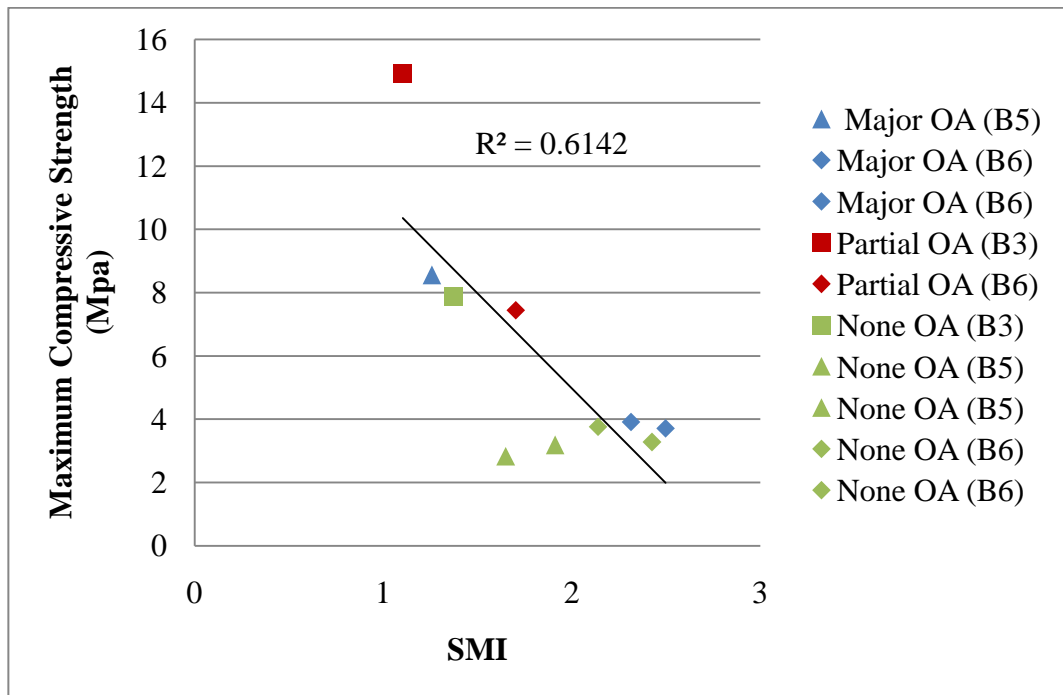


Figure 7.4: Plot of maximum compressive stress vs. Structural model index for bone cylinders from major-load, partial-load and non-load bearing regions ($R = -0.784$ $p = 0.007$)

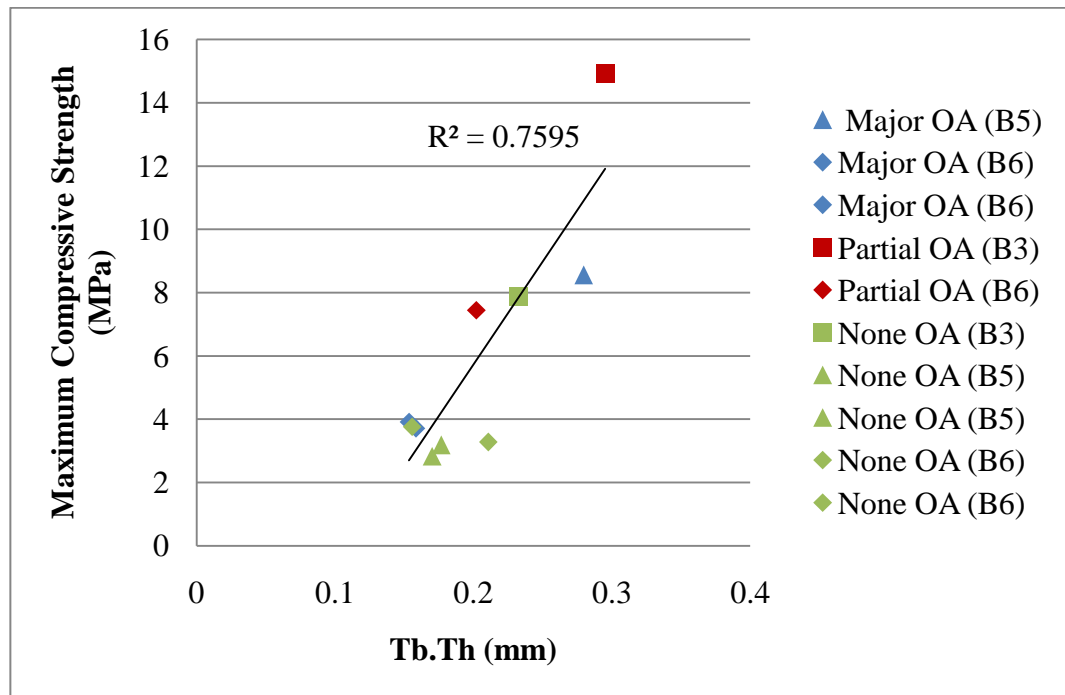


Figure 7.5: Plot of Maximum Compressive Stress vs. Trabecular Thickness for bone cylinders from major-load, partial-load and non-load bearing regions ($R = 0.871$ $p = 0.001$).

BVF correlated significantly with Tb.Th ($R = 0.944$ $p = 0.000$) (Figure 7.6). Trabeculae occupying a higher bone volume exhibited higher thickness. The highest BVF (0.432 ± 0.089) (Table 7.1) and Tb.Th (0.295 ± 0.051 mm) (Table 7.1) was exhibited by a partially loaded specimen (B3). Significant overlap in all loading regions was observed. There was no significant correlation between BVF and Tb.S ($R = -0.199$ $p = 0.582$) (Figure 7.7). The BVF ranged from 0.171 – 0.432 (Table 7.1), and the Tb.S ranged from 0.592 – 0.731 mm (Table 7.1) for all specimens showing that an increase in occupied volume did not result in larger trabecular spacing. There was no correlation between BVF and Tb.N ($R = -0.199$ $p = 0.194$). There was large variability in the non-loaded trabecular specimens in BVF ranging from 0.177 – 0.338 (Table 7.1) but were more closely related in Tb.N ranging from 1.640 – 1.884 mm^{-1} (Table 7.1). BVF was negatively correlated with SMI ($R = -0.870$ $p = 0.001$) (Figure 7.9). As the occupied bone volume increased the trabeculae exhibited a more plate like structure. There was no correlation for loading regions, with BVF and SMI. Specimens from femoral

head B3 exhibited a more plate-like structure in comparison to other femoral heads, with the exception of the specimen from the major-loaded region taken from B5 (OA)

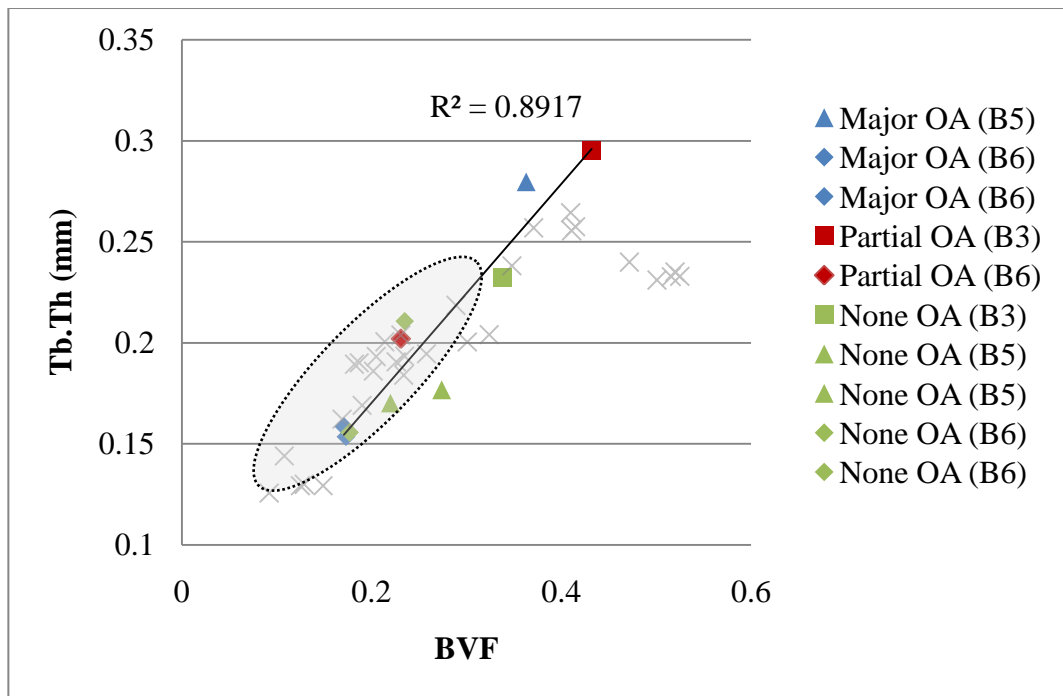


Figure 7.6: Plot of Bone Volume Fraction vs. Trabecular Thickness for major-, partial- and non-load bearing regions of the OA extracted cylinders ($R = 0.944$ $p = 0.000$). The shaded region represents Figure 5.11, and X represent OA regions from Figure 6.17 for reference.

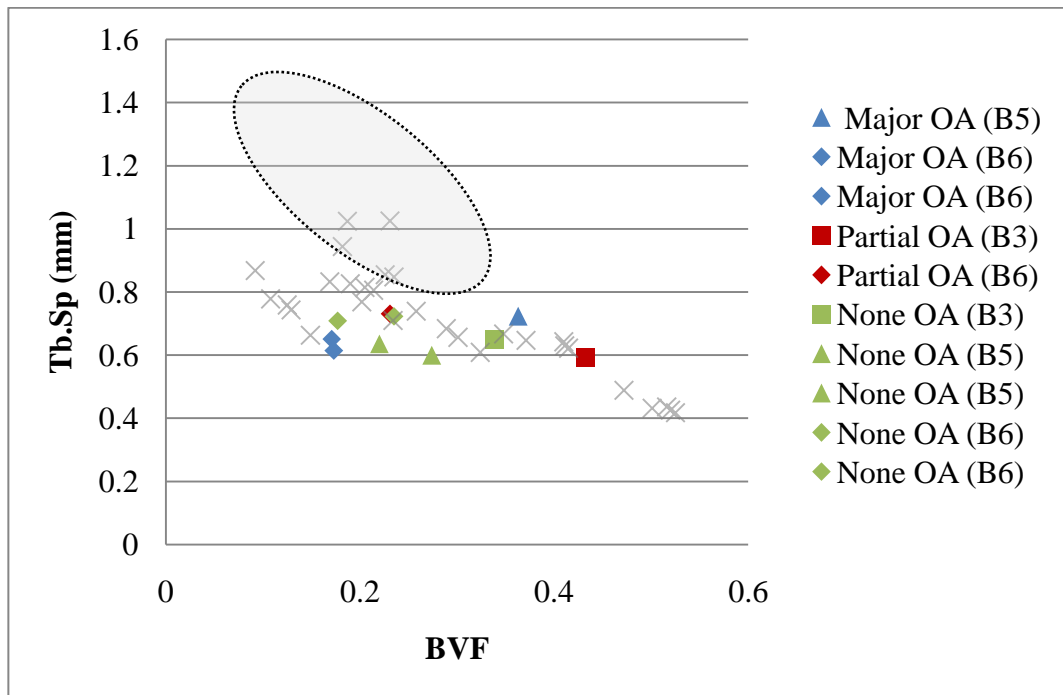


Figure 7.7: Plot of Bone Volume Fraction vs. Trabecular Spacing for major-, partial- and non-load bearing regions of the OA extracted cylinders ($R = -0.199$ $p = 0.582$). The shaded region represents Figure 5.12, and X represent OA regions from Figure 6.18 for reference

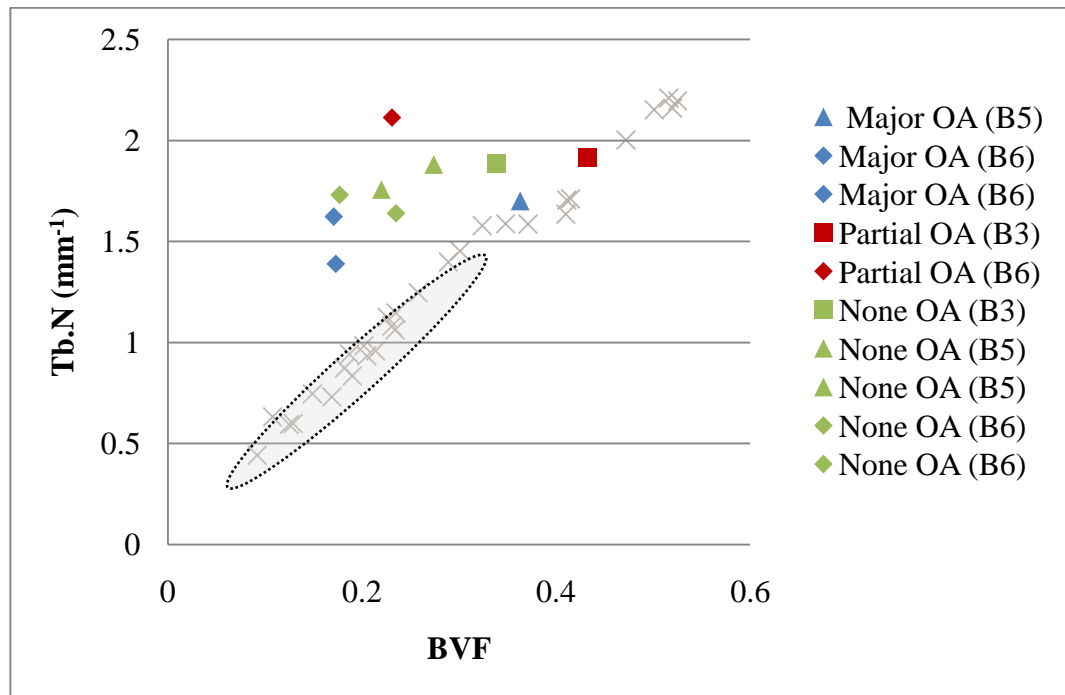


Figure 7.8: Plot of Bone Volume Fraction vs. Trabecular Number for major-, partial- and non-load bearing regions of the OA extracted cylinders ($R = -0.199$ $p = 0.194$). The shaded region represents Figure 5.13, and X represent OA regions from Figure 6.19 for reference

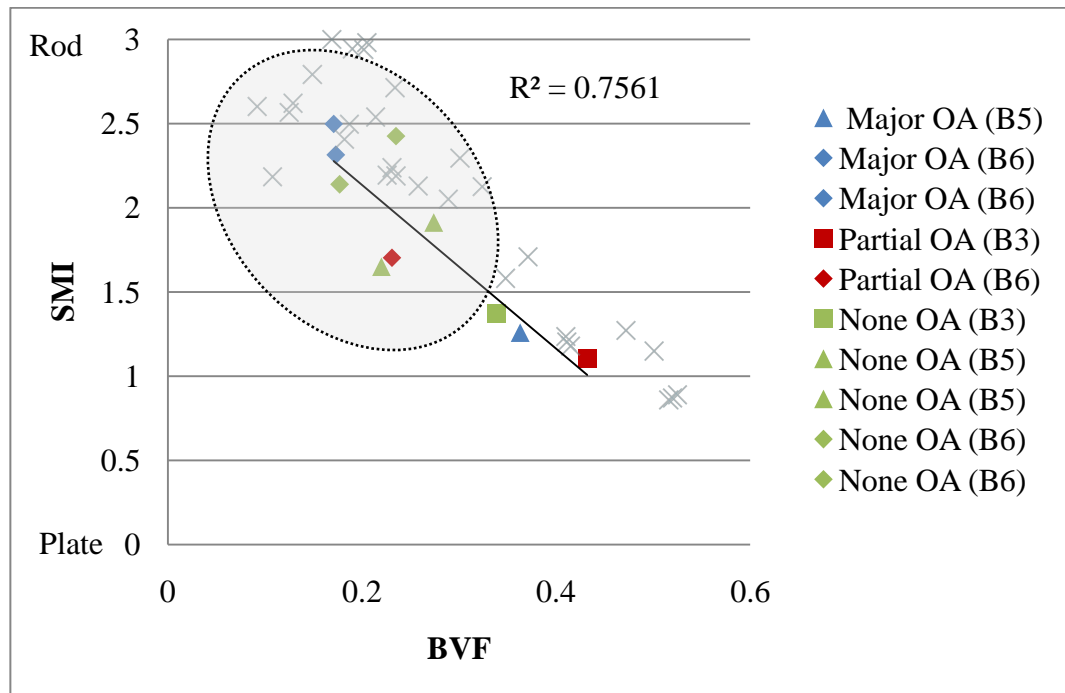


Figure 7.9: Plot of Bone Volume Fraction vs. Structure Model Index for major-, partial- and non-load bearing regions of the OA extracted cylinders ($R = -0.870$ $p = 0.001$). The shaded region represents Figure 5.14, and X represent OA regions from Figure 6.20 for reference

There was no correlation between Tb.N and SMI ($R = -0.585$ $p = 0.076$) (Figure 7.10). All specimens were closely related in terms of Tb.N but showed a high degree of variability in SMI (ranging from 1.104 – 2.498) (Table 7.1). There was no correlation between Conn.D and SMI ($R = -0.414$ $p = 0.235$) (Figure 7.11). All specimens with the exception of Partial OA (B3) exhibited similar Conn.D but varied in SMI. Partial load bearing specimen B3 exhibited a significantly higher connectivity density than all other specimens (12.152 mm^{-3}) (Table 7.1). Tb.Th correlated negatively with SMI ($R = -0.797$ $p = 0.006$). A decrease in SMI was observed with an increase in Tb.Th (Figure 7.12) Major-load specimens from femoral head B6 exhibited a thin rod-like trabecular structure with the least amount of occupied bone volume.

Whereas, partially loaded specimen from B3 and major-loaded specimen from B5 exhibited the highest occupied bone volume with a plate-like trabecular structure. The non-loaded specimen lay in between both of these extremes, with a significant level of variability.

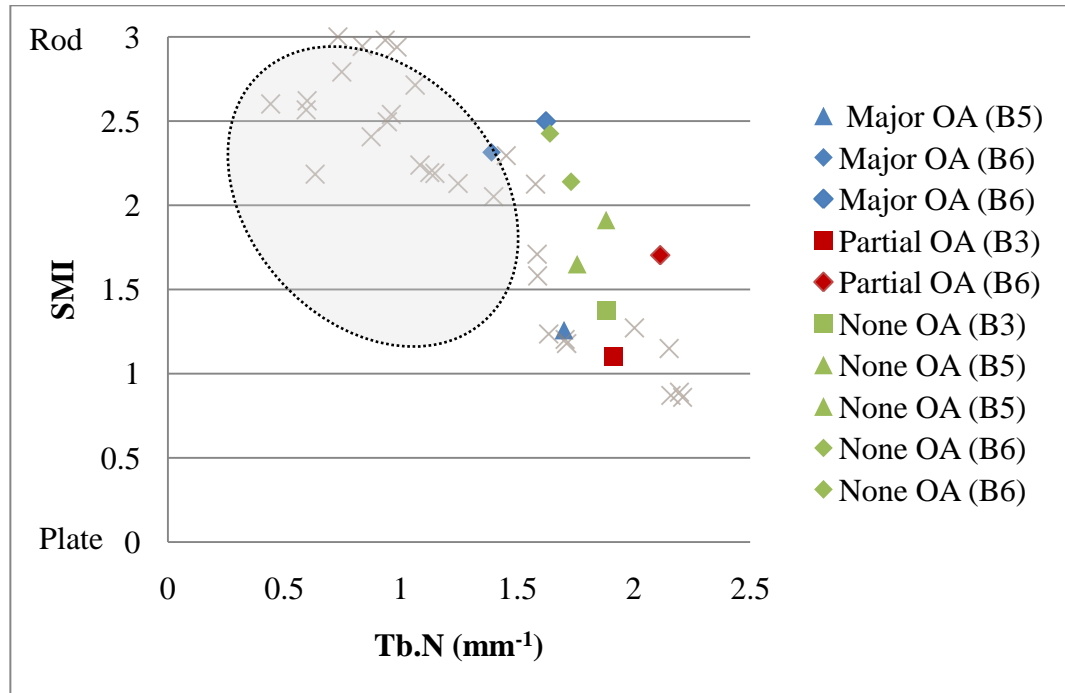


Figure 7.10: Plot of Trabecular Number vs. Structure Model Index for major-, partial- and non-load bearing regions of the OA extracted cylinders ($R = -0.585$ $p = 0.076$). The shaded region represents Figure 5.15, and X represent OA regions from Figure 6.21 for reference

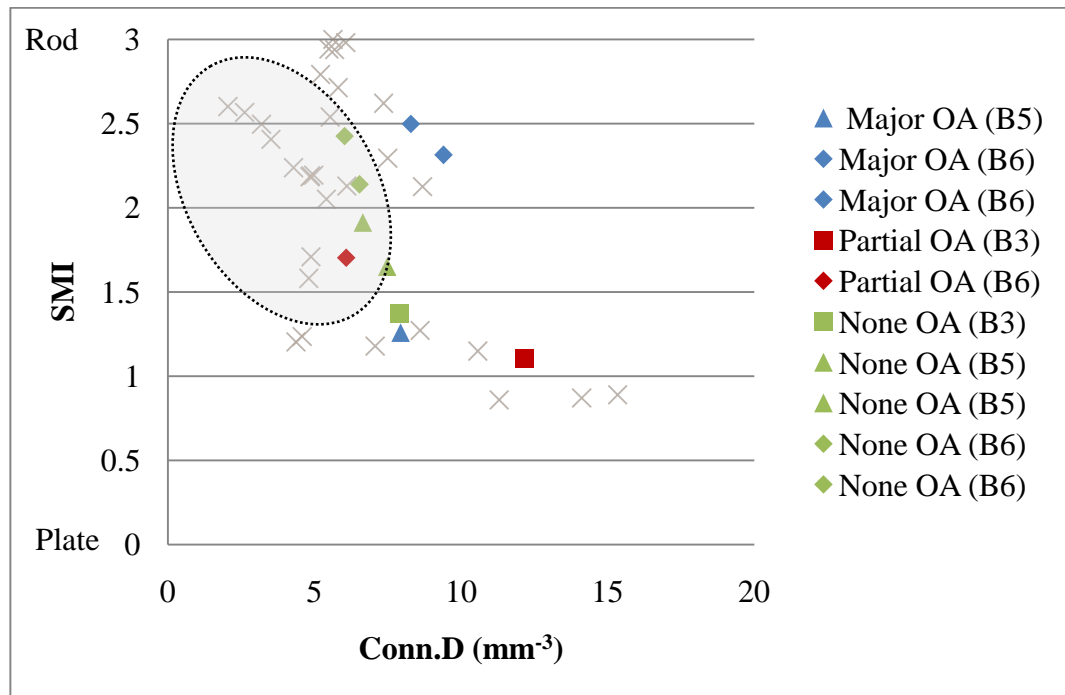


Figure 7.11: Plot of Trabecular Number vs. Structure Model Index for major-, partial- and non-load bearing regions of the OA extracted cylinders ($R = -0.414$ $p = 0.235$). The shaded region represents Figure 5.16, and X represent OA regions from Figure 6.22 for reference

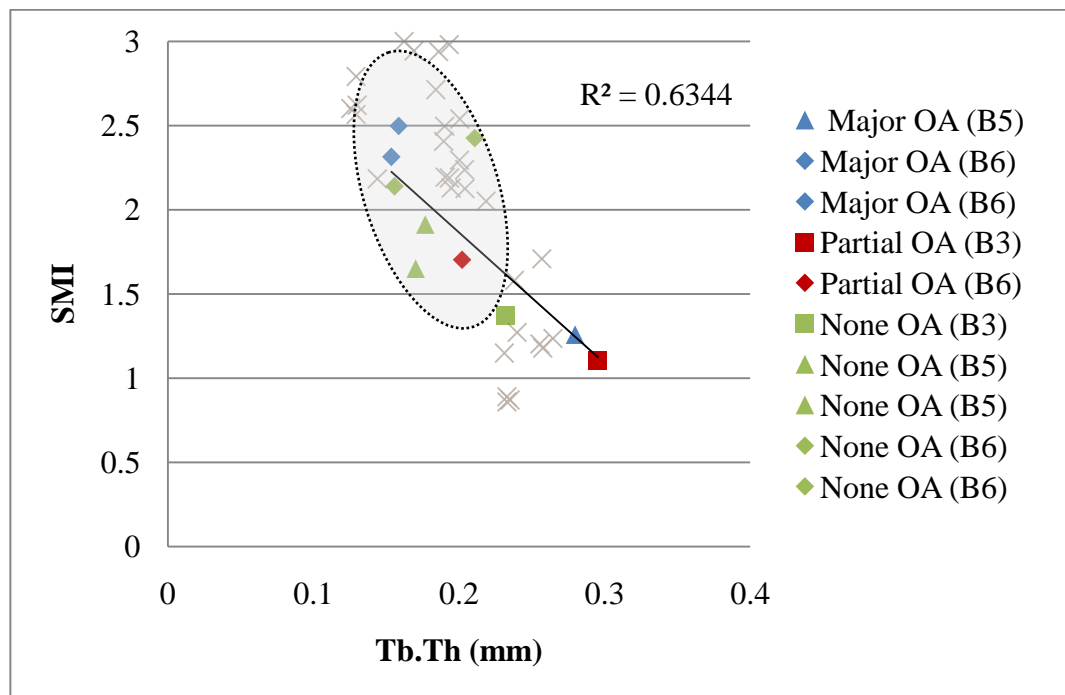


Figure 7.12: Plot of Trabecular Thickness vs. Structure Model Index for major-, partial- and non-load bearing regions of the OA extracted cylinders ($R = -0.797$ $p = 0.006$). The shaded region represents Figure 5.17, and X represent OA regions from Figure 6.23 for reference

There was no correlation between BVF and DA ($R = 0.814$ $p = 0.086$). The non-loaded (B5) specimens exhibited the highest level of anisotropy (Figure 7.13). There was also no correlation observed between Conn.D and DA ($R = 0.235$ $p = 0.514$). This showed that connectivity density had no effect on degree of anisotropy (Figure 7.14). There was no correlation between Conn.D and Tb.N ($R = -0.147$ $p = 0.686$) (Figure 7.15). There was also no correlation between Tb.Th and Tb.N ($R = 0.380$ $p = 0.279$) (Figure 7.16). This also showed that there was no correlation between loading regions. There was no correlation between Tb.Th and BMC ($R = -0.478$ $p = 0.163$). All specimens exhibited a similar BMC ranging from $(1.000 - 1.072 \text{ g cm}^{-3})$ (Table 7.1).

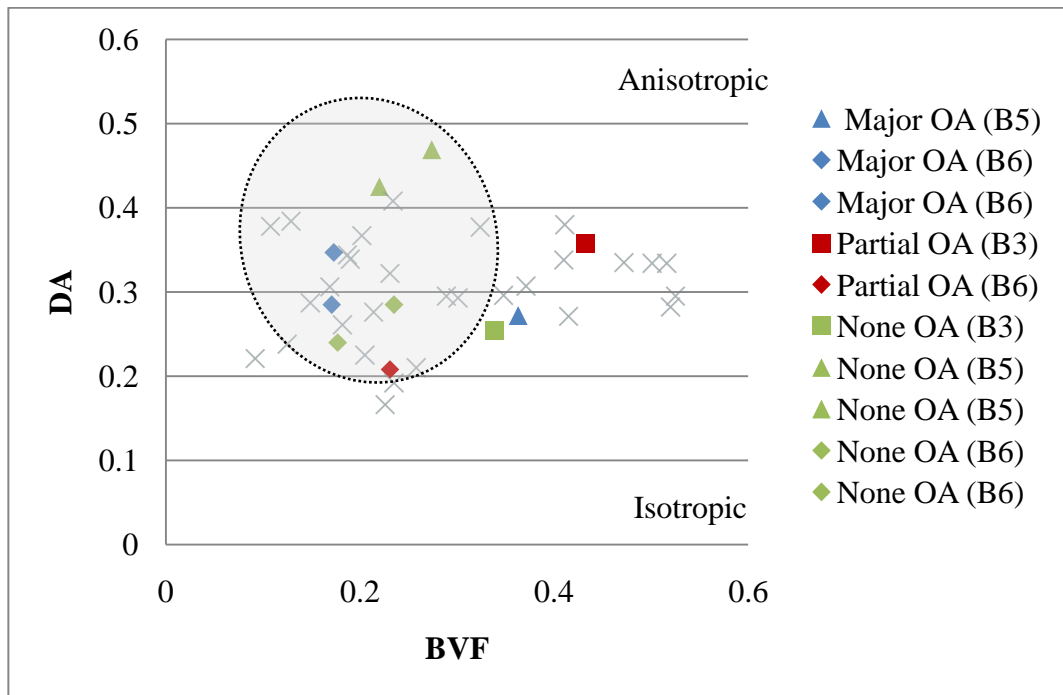


Figure 7.13: Plot of Bone Volume Fraction vs. Degree of Anisotropy for major-, partial- and non-load bearing regions of the OA extracted cylinders ($R = 0.814$ $p = 0.086$). The shaded region represents Figure 5.18, and X represent OA regions from Figure 6.24 for reference

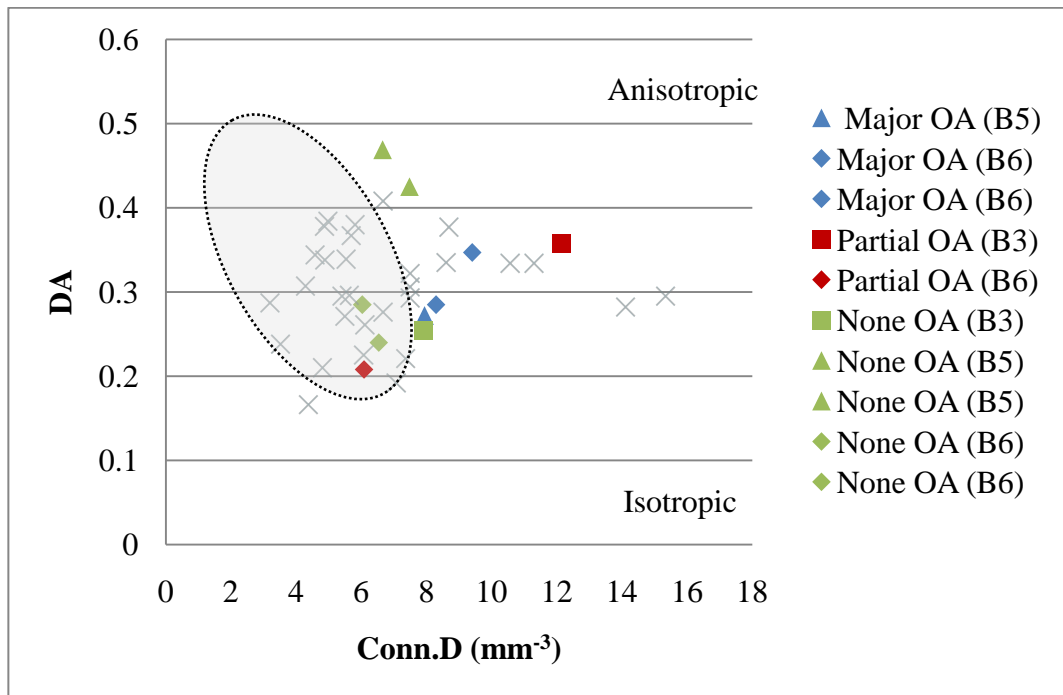


Figure 7.14: Plot of Connectivity Density vs. Degree of Anisotropy for major-, partial- and non-load bearing regions of the OA extracted cylinders ($R = 0.235$ $p = 0.514$). The shaded region represents Figure 5.19, and X represent OA regions from Figure 6.25 for reference

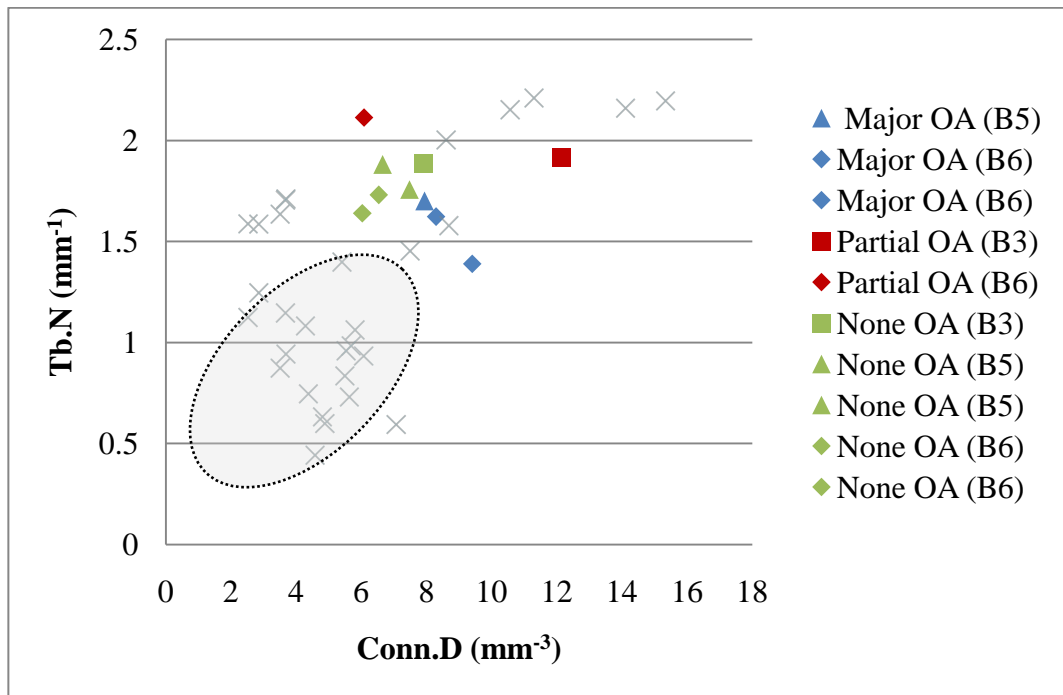


Figure 7.15: Plot of Connectivity Density vs. Trabecular Number for major-, partial- and non-load bearing regions of the OA extracted cylinders ($R = -0.147$ $p = 0.686$). The shaded region represents Figure 5.20, and X represent OA regions from Figure 6.26 for reference

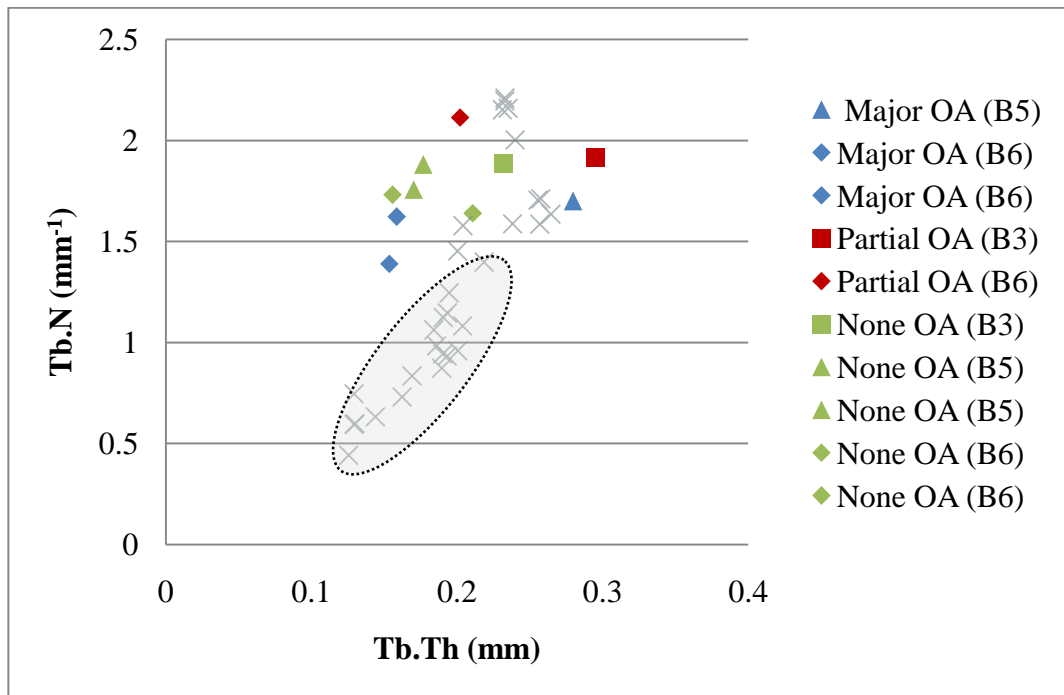


Figure 7.16: Plot of Trabecular Thickness vs. Trabecular Number for major-, partial- and non-load bearing regions of the OA extracted cylinders ($R = 0.380$ $p = 0.279$). The shaded region represents Figure 5.21, and X represent OA regions from Figure 6.27 for reference

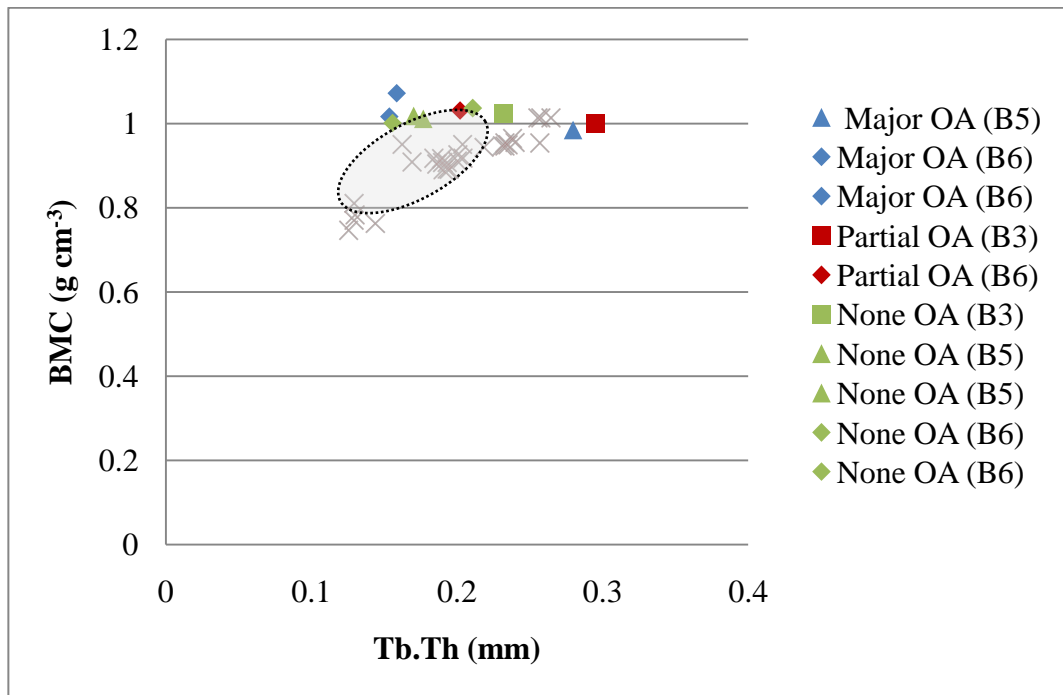


Figure 7.17: Plot of Trabecular Thickness vs. Bone Mineral Concentration for major-, partial- and non-load bearing regions of the OA extracted cylinders ($R = -0.478$ $p = 0.163$). The shaded region represents Figure 5.22, and X represent OA regions from Figure 6.28 for reference

Table 7.1: Morphometric and mechanical parameters of bone cylinders from major-load, partial-load and non-load bearing regions of OA femoral heads

Specimen	BVF	Tb.Th (mm)	Tb.Sp (mm)	Conn.D (mm ³)	Tb.N (mm ⁻¹)	SMI	DA	BMC (g cm ⁻³)	σ_{mcs} (MPa)	ϵ_f (%)	E (MPa)
B3 Partial OA	0.432 (±0.089)	0.295 (±0.051)	0.592 (±0.054)	12.152 (±1.851)	1.914 (±0.198)	1.104 (±0.499)	0.357 (±0.083)	1.000 (±0.024)	14.94 (±3.82)	6 (±1.33)	2.08 (±0.55)
B3 None OA	0.338 (±0.089)	0.232 (±0.051)	0.651 (±0.054)	7.897 (±1.851)	1.884 (±0.198)	1.373 (±0.499)	0.254 (±0.083)	1.024 (±0.024)	7.87 (±3.82)	4 (±1.33)	3.00 (±0.55)
B5 Major OA	0.363 (±0.089)	0.280 (±0.051)	0.723 (±0.054)	7.940 (±1.851)	1.700 (±0.198)	1.259 (±0.499)	0.272 (±0.083)	0.985 (±0.024)	8.56 (±3.82)	4 (±1.33)	2.08 (±0.55)
B5 None OA	0.274 (±0.089)	0.177 (±0.051)	0.600 (±0.054)	6.654 (±1.851)	1.881 (±0.198)	1.912 (±0.499)	0.469 (±0.083)	1.012 (±0.024)	3.19 (±3.82)	2 (±1.33)	1.59 (±0.55)
B5 None OA	0.22 (±0.089)	0.170 (±0.051)	0.636 (±0.054)	7.480 (±1.851)	1.757 (±0.198)	1.65 (±0.499)	0.425 (±0.083)	1.018 (±0.024)	2.83 (±3.82)	4 (±1.33)	1.12 (±0.55)
B6 Major OA	0.173 (±0.089)	0.154 (±0.051)	0.614 (±0.054)	9.405 (±1.851)	1.389 (±0.198)	2.315 (±0.499)	0.347 (±0.083)	1.017 (±0.024)	3.91 (±3.82)	2 (±1.33)	1.96 (±0.55)
B6 Major OA	0.171 (±0.089)	0.159 (±0.051)	0.651 (±0.054)	8.292 (±1.851)	1.622 (±0.198)	2.498 (±0.499)	0.285 (±0.083)	1.072 (±0.024)	3.71 (±3.82)	4 (±1.33)	1.67 (±0.55)
B6 Partial OA	0.231 (±0.089)	0.202 (±0.051)	0.731 (±0.054)	6.086 (±1.851)	2.113 (±0.198)	1.703 (±0.499)	0.208 (±0.083)	1.031 (±0.024)	7.44 (±3.82)	4 (±1.33)	1.84 (±0.55)
B6 None OA	0.177 (±0.089)	0.156 (±0.051)	0.708 (±0.054)	6.538 (±1.851)	1.730 (±0.198)	2.14 (±0.499)	0.24 (±0.083)	1.002 (±0.024)	3.76 (±3.82)	6 (±1.33)	1.22 (±0.55)
B6 None OA	0.235 (±0.089)	0.211 (±0.051)	0.723 (±0.054)	6.030 (±1.851)	1.640 (±0.198)	2.426 (±0.499)	0.285 (±0.083)	1.037 (±0.024)	3.28 (±3.82)	4 (±1.33)	1.29 (±0.55)

Mean (Standard Deviation)

7.2.3 Regions of Failure

Rendered images obtained from XMT data sets were used to determine qualitative failure of the trabecular structure under stress during compression testing. Figure 7.18 is an example of where the images obtained from different strains were superimposed to determine the mode of failure. Shear failure was clearly observed in all specimens. Figure 7.18a shows the XMT data sets superimposed at 4, 6 and 8% strains; the specimen has shown to fail along a shear plane which is enlarged in (b), highlighting where the trabecular structure has failed.

Smaller regions were further analysed to observe failure of individual trabeculae. Figure 7.19 shows an example of failure of a single trabecula, which was loaded in compression as part of a bone cylinder and was computationally sectioned to highlight individual trabecula failure. At 0% strain an intact unloaded trabecula was observed, which was dramatically buckling under 4% strain with catastrophic fracture at 6%, resulting in a collapse of the surrounding trabeculae into the intra-trabecular space at 8% (Figure 7.19). At the individual trabecula scale (constrained within a structure), the trabeculae exhibited buckling or bending failure. (For visual reference, refer to video 7, Appendix V).

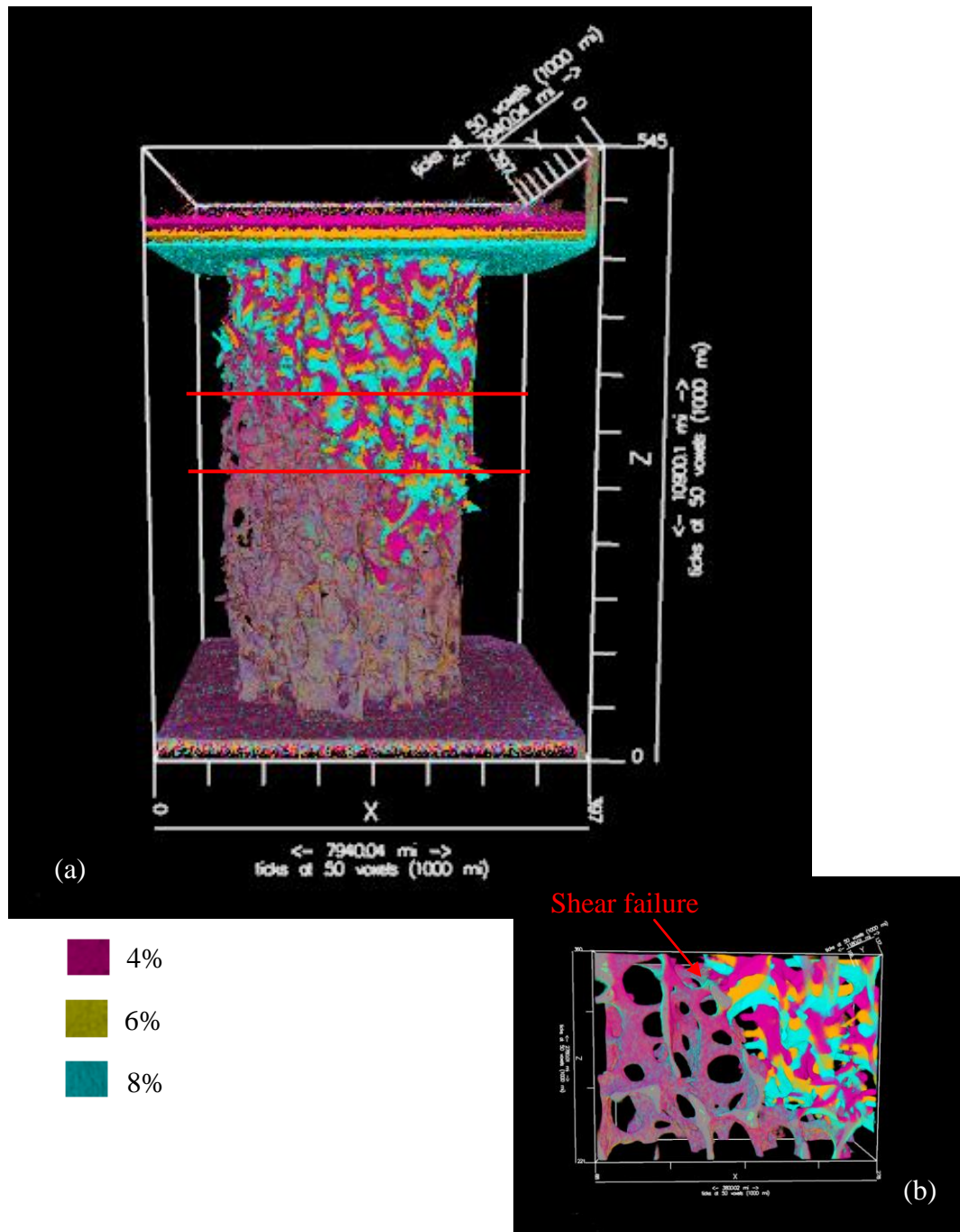


Figure 7.18: (a) Superimposed volumes of a major-load bearing specimen illustrating the region of fracture in shear at 4, 6 and 8% strain, imaged at $20\mu\text{m}$ reconstructed voxel size, (b) the enlarged region highlighted between the red lines in (a)

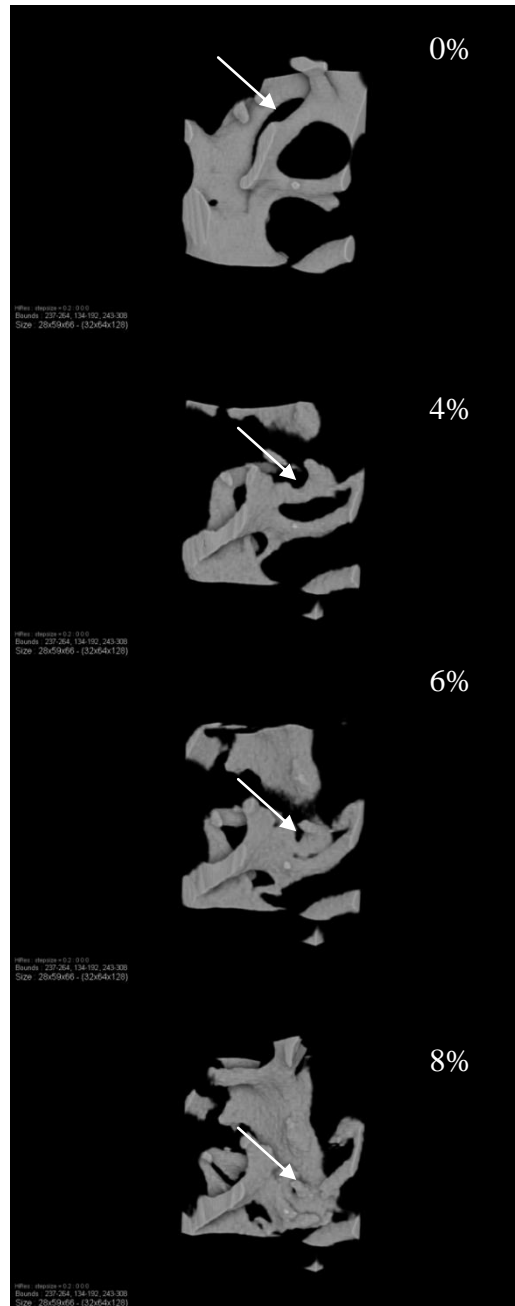


Figure 7.19: Observed failure behaviour of a single trabecula taken from a major load bearing region bone cylinder at 0, 4, 6 and 8 % strains, imaged at $20\mu\text{m}$ reconstructed voxel size, exhibiting buckling

Chapter 8 Single Microcallus Formation Study

8.0 Introduction

The structure and architecture of microcallus formations have been reported in various studies (Vernon-Roberts and Pirie, 1973; Müller and Ruegsegger, 1997; Fazzalari, 1993; Cheng *et al.*, 1997; Hahn *et al.*, 1995), but 3D tomographic data has only really been produced over the last 15 years. Microcallus formations (MCFs) have a function in trabecular microfracture, yet their exact role is unclear. They have been described as occurring in bone having a range of pathological conditions (osteoarthrosis, rheumatoid arthritis, subcapital fracture and degeneration of the articular cartilage) (Blackburn, 1992). Several studies have been carried out looking at the morphology of microcallus formations with very few looking at the mineralisation of the MCFs in relation to the surrounding tissue using XMT. Previous studies using tomography have only used a resolution of around 100 μm to investigate the microarchitecture of MCFs (Müller and Ruegsegger, 1997), but this only allows for limited understanding of the morphology. The aim of this study is to investigate the morphology of microcallus formations at multi-scale using XMT and XuM.

The objectives were:

- To qualitatively compare the morphology of microcallus formations at different resolutions using XMT and XuM
- To quantitatively measure the differences in BMC between trabeculae and the surrounding microcallus formations.
- To determine the presence of microcracks in trabeculae surrounded by microcallus formations

8.1 Methods and Materials

MCFs were identified from reconstructed images obtained from XMT data sets (Chapters 5 and 6). MCFs identified from bone cylinder data sets (Chapter 7) were imaged at higher resolution (8.8 μm) using XMT. Furthermore the bone cylinder containing an identified MCF was embedded, polished (Section 3.4) and imaged using the XuM at 775nm reconstructed voxel size (Section 4.9).

8.2 Results

This section reports on the 3D morphology and BMC of MCFs at micro- and sub-micron level.

8.2.1 Location and Morphology of Microcallus Formations at 25 μm

Figure 8.1 is a rendered image of a slice taken from the central xy plane of a whole femoral head (Specimen B14 Chapter 6) and rendered using a 2D transfer function (Section 4.5.1) (Drishti, Australia National University, Canberra) at 25 μm reconstructed voxel size. Two very clear MCFs are observed in Figure 8.1. The smaller of the two appears to have formed around a strut and the larger has formed around the junction of a trabecular plate with a trabecular rod. They have formed in relatively close proximity to each other and appear as nodular accretions, which have a fine porous structure and are significantly different in size. Figure 8.2 is an enlarged image of the larger MCF cropped from Figure 8.1. Here, it was noted that when the MCF was visualised in 360°, it had formed in particular around the junction and had not formed onto the neighbouring trabecular struts. This MCF in particular exhibited a site specific formation, and although an unorganised, bulky and porous structure, it only formed around a particular element of the trabecular structure (Figure 8.2).

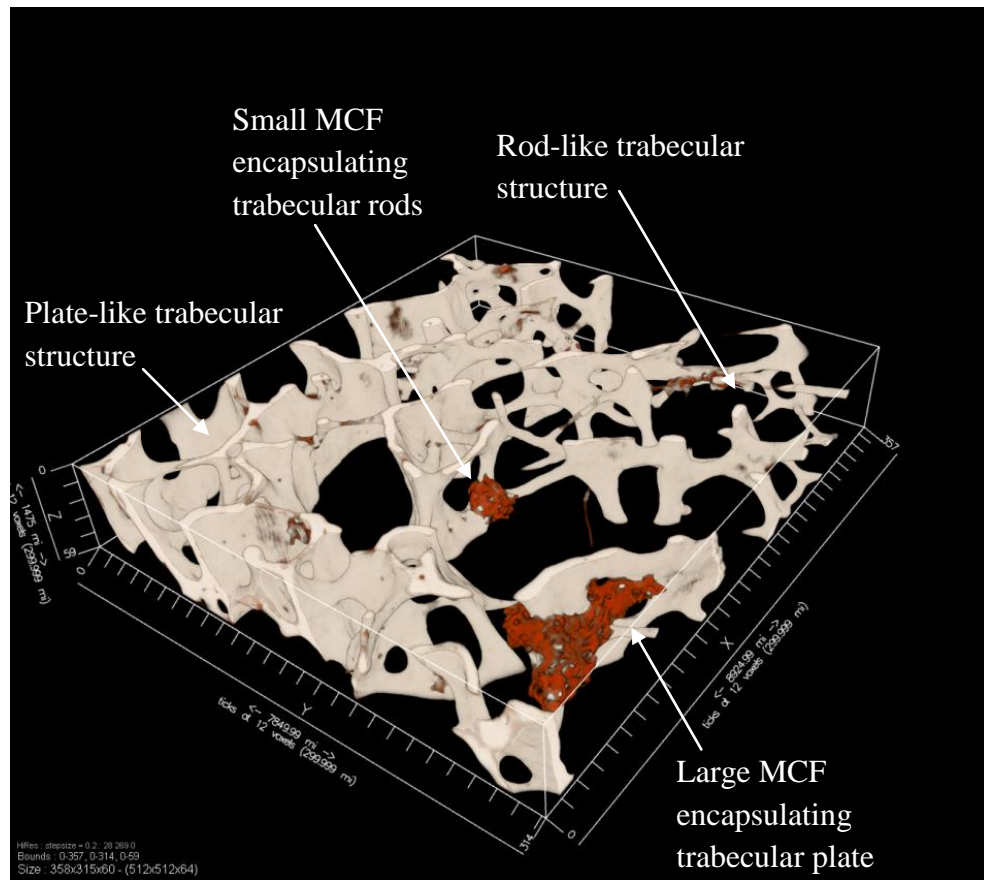


Figure 8.1: Sectioned slice taken from the central xy plane of femoral head B14 (Chapter 6) (measuring 7.85 8.92 1.47 mm (X, Y, Z)), imaged at 25 μ m voxel size

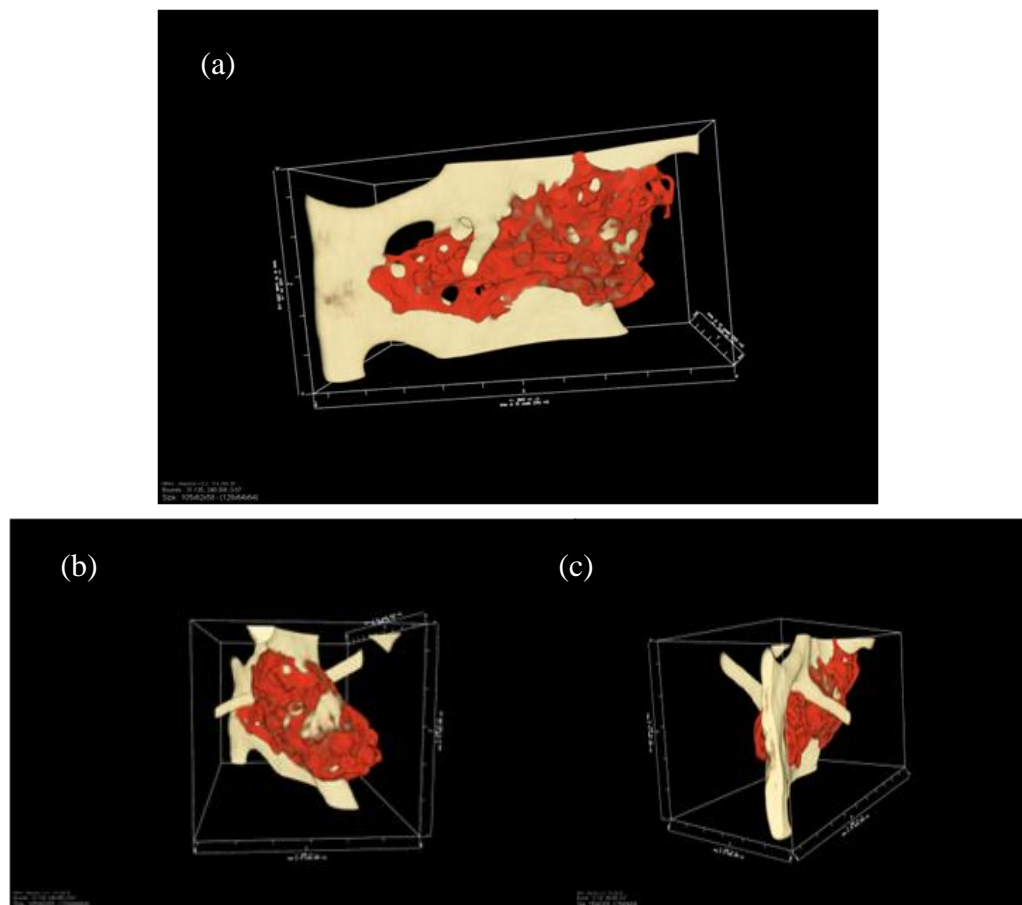


Figure 8.2: A rendered image of a single microcallus formation (sectioned from Figure 8.1) viewed at different angles, with (a) at 0° and (b) at 90° and (c) at 135° rotation, bound by a box measuring 2.6 1.5 1.4 mm (X,Y,Z)

8.2.2 Analysis of Microcallus Formation at High resolution - 8.8 μ m

A single MCF was identified from a bone cylinder taken from a major-load bearing region of specimen B6. It was sectioned and imaged at 8.8 μ m using XMT, reconstructed and rendered (Figure 8.2). Furthermore, it was analysed for Bone Mineral Concentration using Amira.

Figure 8.3 is a rendered image of MCF determined from a bone cylinder, with (a) and without (b) the trabeculae. The MCF has formed around a trabecula encapsulating it completely. Fibrous bone and large pores were observed. The MCF appeared as an unorganised foam-like structure with connective fibres varying in length and diameter (b). The MCF had formed more heavily towards the left of the trabecula (a),

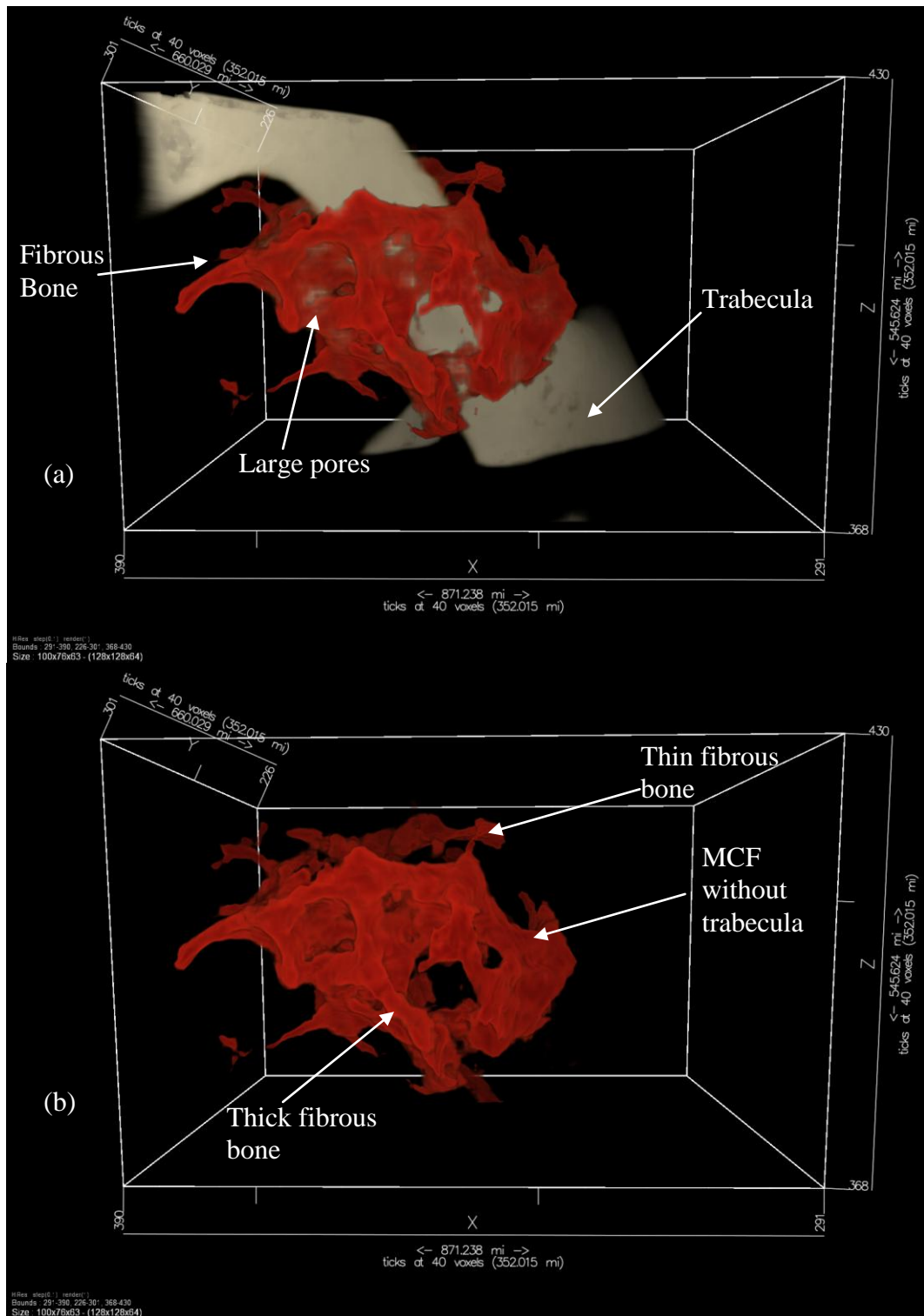


Figure 8.3: Rendered images of an MCF imaged at $8.8\mu\text{m}$ voxel size; with (a) and without (b) the trabeculae, bound by box measuring $871 \times 545 \times 660 \mu\text{m}$

8.2.3 Bone mineral concentration and Microcallus Formations

Figures 8.4 and 8.5 show contour maps superimposed onto the greyscale image relating to the distribution of mineral in the trabecular strut and surrounding microcallus. It is clearly evident that the trabecular strut (a) has a higher BMC than the MCF (b). It was also observed that the MCF decreased in BMC the further away it is from the trabecula. This was observed in both planes when analysing the MCF and trabecula (Figure 8.4 and 8.5).

By placing a line probe through the MCF, from point (a) to point (b) in Figure 8.5, it was possible to measure the BMC along that line. Figure 8.6 shows where the line was placed, resulting in the histogram in Figure 8.7.

From Figure 8.6 two distinguishable peaks were observed along the distance (a) to (b). By correlating Figure 8.7 with Figure 8.6, it was seen that the first peak (i) corresponded to the MCF, with the highest peak (ii) corresponding to the trabecular strut. This showed that the MCF lies between $0.6 - 0.8 \text{ cm}^{-1} \text{ LAC}$, whereas the trabecular strut is approximately $1.27 \text{ cm}^{-1} \text{ LAC}$.

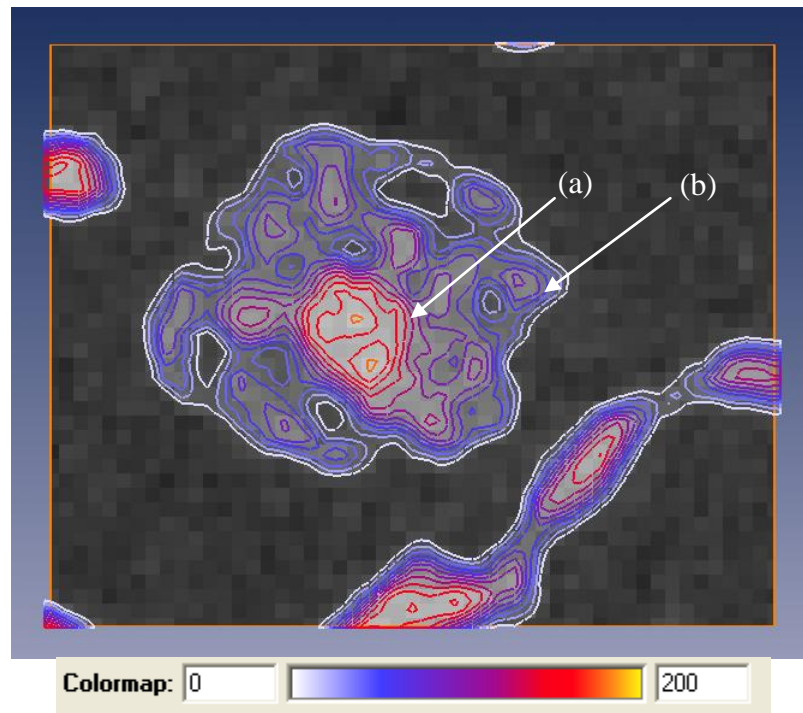


Figure 8.4: Axial mid-slice of a MCF removed from a major-load bearing region from specimen B6; the trabecula exhibiting a higher BMC than the surrounding MCF determined using superimposed contour maps of mineralisation from the greyscale values.

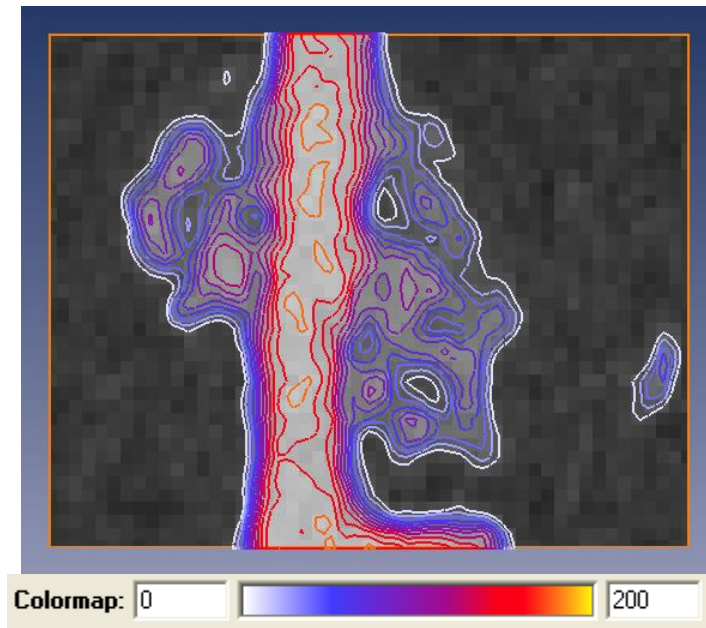


Figure 8.5: Coronal mid-slice of a MCF removed from a major-load bearing region from specimen B6; the trabecula exhibiting a higher BMC than the surrounding MCF determined using superimposed contour maps of mineralisation from the greyscale values.

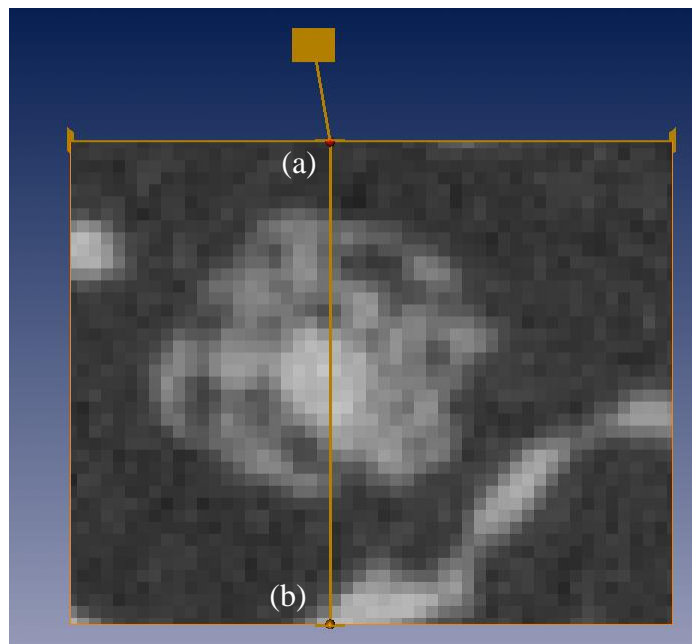


Figure 8.6: Location of line (measuring 1.1 mm) from (a) to (b); placed along the centre of the slice to measure LAC

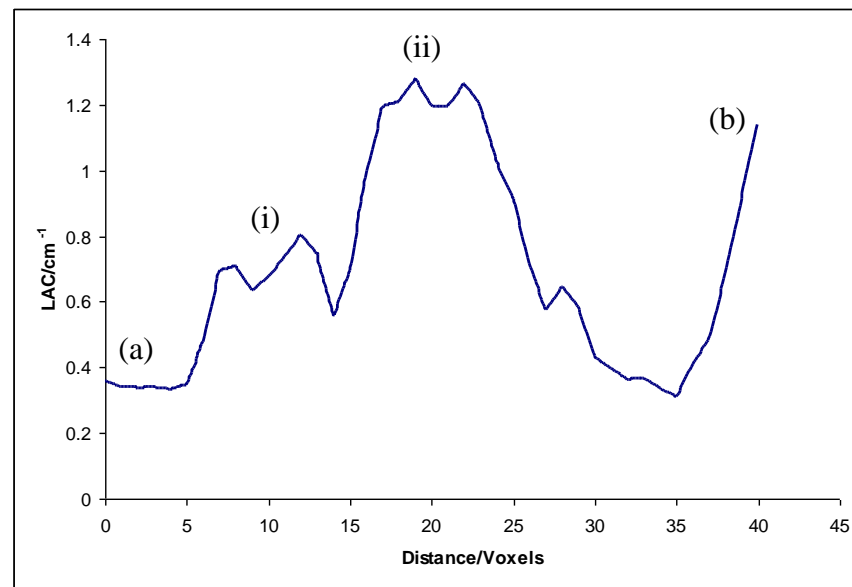


Figure 8.7: Histogram of the line probe showing LAC (as a measure of BMC). See Figure 8.6 for positions of (a) and (b).

8.2.4 Evaluation of Nano-structure of Microcallus Formation at 775nm

The MCF imaged at 8.8 μ m using XMT (Specimen B6 from major-load bearing region, Section 8.2.2), was further imaged at 775nm using XuM. The XuM data sets obtained were reconstructed (Figure 8.8) and rendered for morphological evaluation (Figure 8.9). At 775 nm voxel size various structural features were observed; cell space was clearly recognised along with the micro-crack that had penetrated the trabecular strut (Figure 8.8). Close to micro-crack several cell spaces were lighter in appearance and filled in comparison to the surrounding cell spaces.

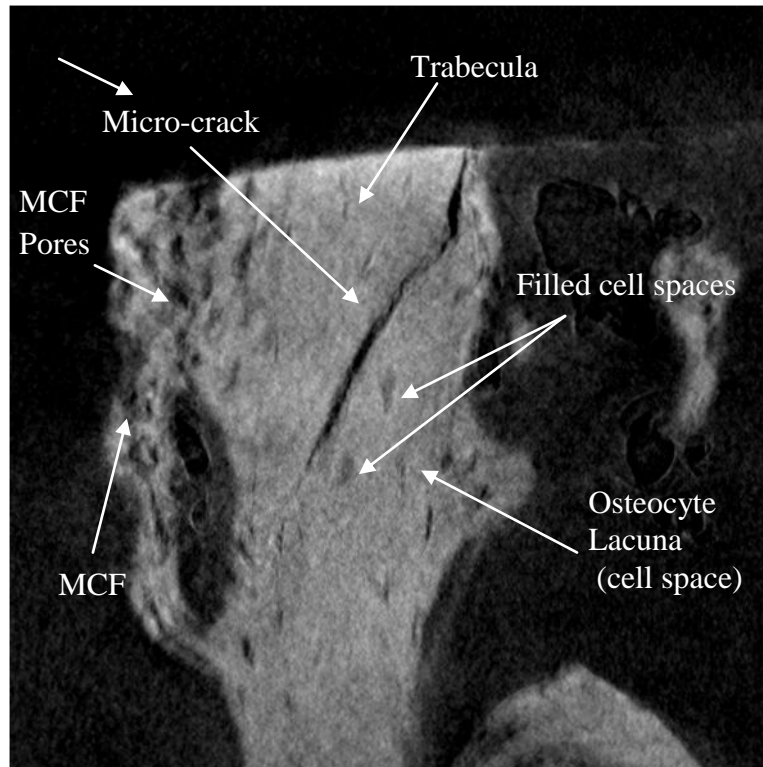


Figure 8.8: A sectional image through the trabecula encapsulated by a MCF, imaged at 775nm reconstructed voxel size, highlighting the micro-crack, which has propagated through the entire strut (Field width = 0.5 mm)

The data set obtained from XuM was rendered to provide a detailed 3D volumetric image, enabling 3D visualisation of structural features relating to the MCF and the trabeculae. The trabecula and MCF were observed (Figure 8.9) as two distinguishable features (Figure 8.9a). The micro-crack (shown with the white arrows) was determined close to the surface of the trabecula approximately a quarter of the way up the length of the strut (Figure 8.9b) and shown to propagate all the way to the top (Figures 8.9c and 8.9d). Further into the trabecula the micro-crack appeared to increase in diameter and propagate the entire length of the strut (Figure 8.9e) where some regions of the micro-crack appeared larger in size than others (Figure 8.9f). The micro-crack had formed along a shear plane (Figure 8.9g) and followed through across the diameter of the strut, with the MCF

forming around the trabecula and encapsulating the strut (Figures 8.9h and 8.9i). Osteocyte lacunae (cell spaces) were observed throughout the entire strut and the MCF exhibited a rough surface with fibrous bone organised with a large number of pores varying in size.

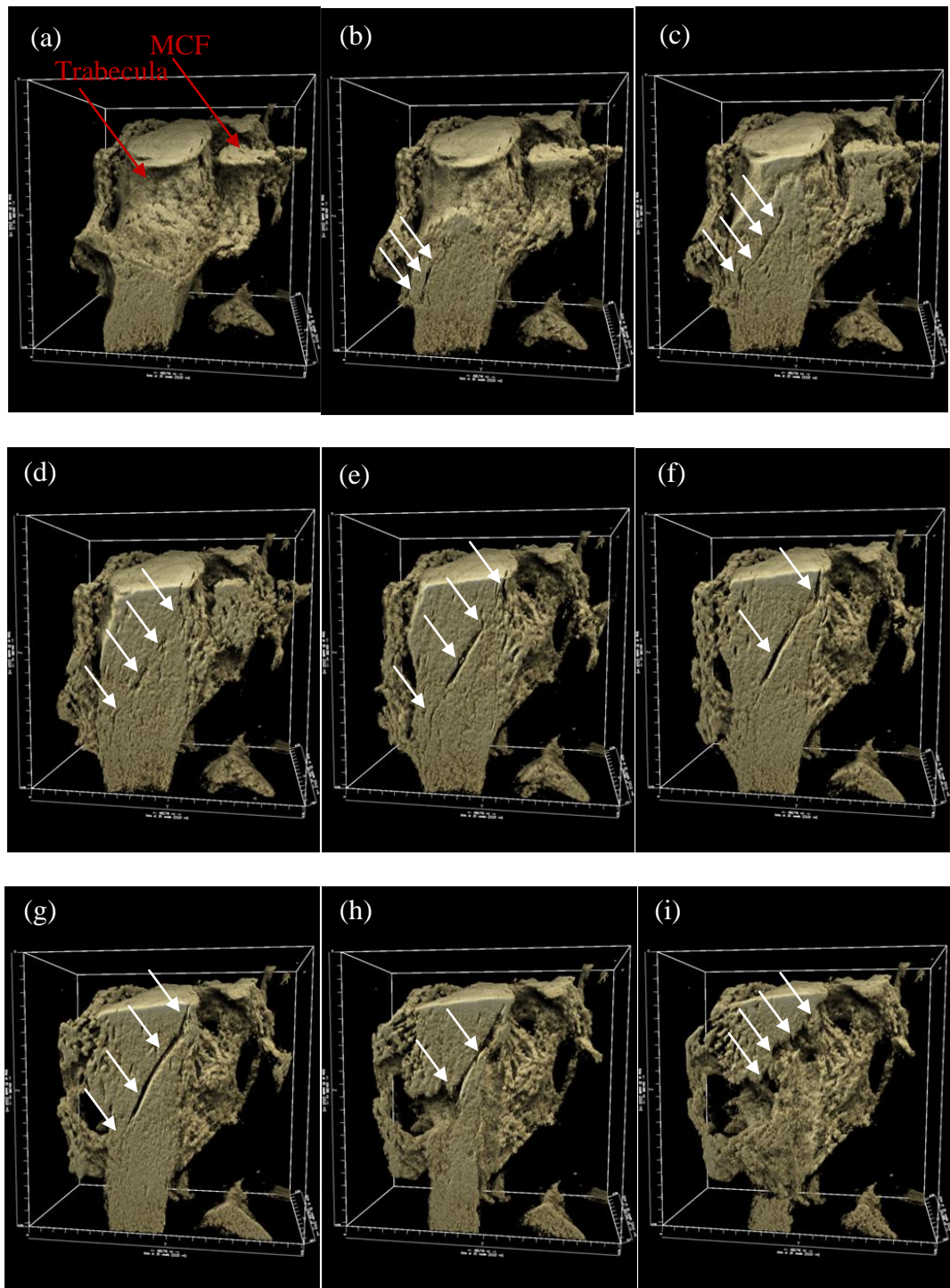


Figure 8.9: Micro-crack propogating through a trabecula, encapsulated in a microcallus formation, bound by box measuring $0.495 \times 0.490 \times 0.494 \text{ mm}^3$ (X,Y.Z)

Chapter 9 High resolution imaging of a trabecula using XuM

9.0 Introduction

Micro-cracks in ageing bone may accumulate in load bearing bones and may contribute to age-related increase in fracture risk. In trabecular bone, the understanding of micro-cracks is confounded by the complexities of trabecular architecture and their interactions with loading (Wachtel *et al.*, 1997). Thus in order to fully understand the effects and localisation of microdamage, it is necessary to develop a method to characterise microdamage such that architectural information is captured. Typically, microdamage labelling of bone is done through *en bloc* staining, followed by thin sectioning and assessment by optical microscopy (Burr and Hooser, 1995). While this method is considered to be the gold standard in bone microdamage labelling, there are clear disadvantages to this method: the irrecoverable destruction of the sample; the limited 2-dimensional visualisation of damage morphology; and the subjective and often laborious process of microdamage characterisation. The aim is investigate the 3D architecture of localised damage within a single trabecula post-fracture using XuM.

The objectives were:

- To determine the 3D structure of single trabeculae using XuM
- To correlate the structure of trabecula using 2D SEM and 3D XuM imaging techniques.

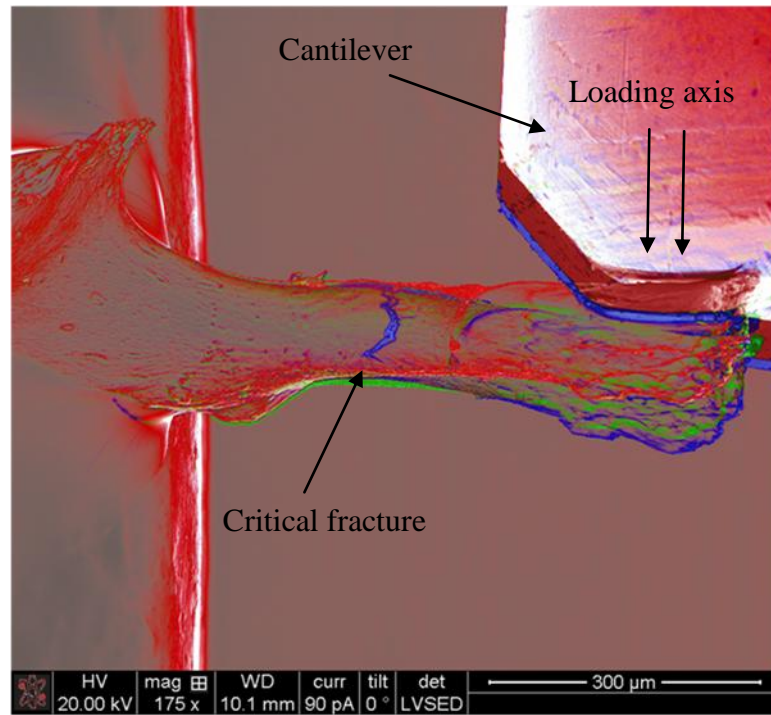
9.1 Materials and Method

A single rod-like trabecula was dissected from macerated slices of trabecular bone (Section 3.5.2), obtained from a femoral head of a patient who had undergone total hip arthroplasty (Section 3.5.1). The trabecula was dissected wet (using PBS) under a light microscope using a fine scalpel blade (Section 3.5.3). The excised trabecula was mounted on a SEM stub, placed in the SEM Quanta 3D FEG (FEI Company, Oregon, USA) chamber and subjected to cyclic compressive load (using a kleindiek manipulator) until critical fracture. It was then mounted and centred on a fine metal pin, and imaged using the XuM (Section 4.9). The XuM data sets were reconstructed and rendered for analysis.

9.2 Results

9.2.1 Loading of the single trabecula and micro-cracks

Images of pre-loading and post loading were superimposed to highlight the features contributing to fracture. From Figure 9.1, critical fracture was observed (in blue) and the pre-fracture state of the trabecula at the final load (in green). This showed the trabecula in bending with small microcracks appearing (Figure 9.2). A total of 4 parallel micro-cracks approximately 10 μ m were observed prior to critical fracture (Figure 9.2). The micro-cracks were located on the tensile surface, normal to the tensile stress. The length of the trabecula was measured as 675 μ m with a mean diameter of 101.6 μ m. The critical fracture was observed at a 20, 000 magnification (Figure 9.3) Here, the collagen fibres and bundles were observed, where collagen fibres exhibited bridging between the crack.



— Unloaded — Final Load — After fracture

Figure 9.1: SEM image highlighting the unloaded, final load and post-fracture condition of the trabecula, taken at 20 kV (scale bar = 300 μm).

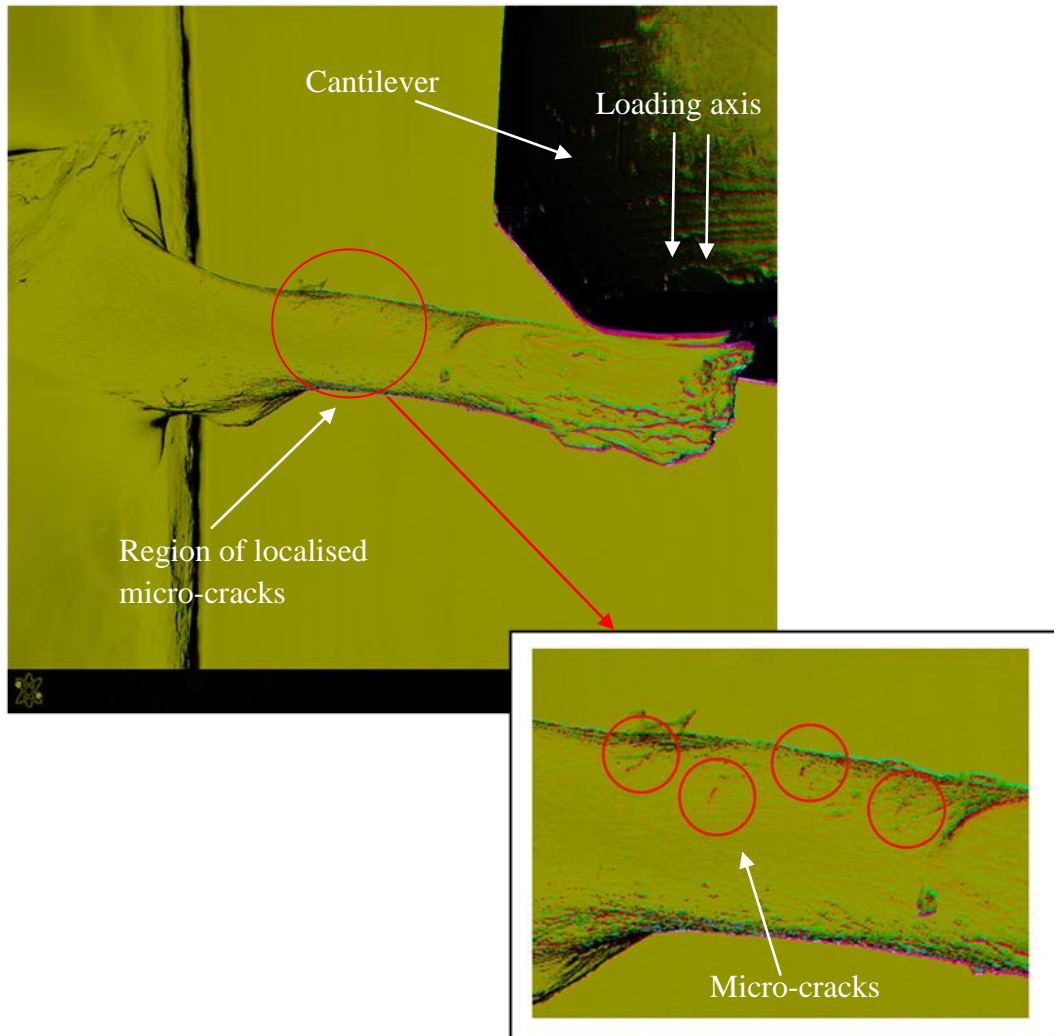


Figure 9.2: Final load image highlighting the micro-cracks on the tensile surface of the single trabecula

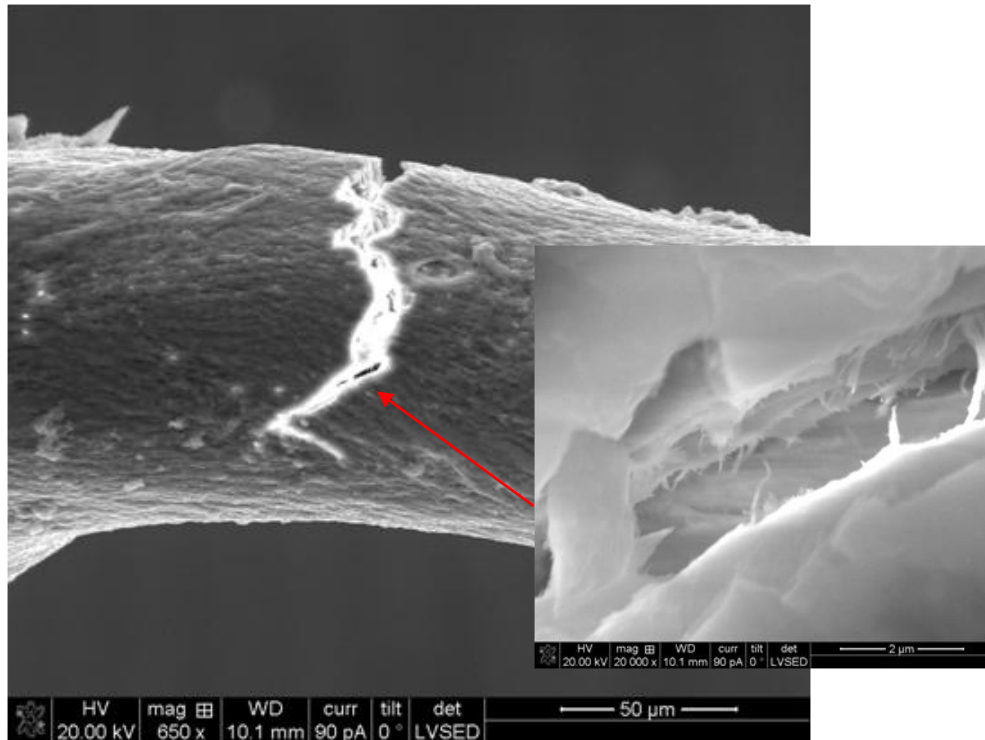


Figure 9.3: SEM image of the critical fracture with an inset image highlighting collagen fibre bridging, taken at 20kV, scale bar is 50 μm and in the enlarged image the scale bar is 2μm.

9.2.2 Qualitative Feature Detection of greyscale images

Images were reconstructed from XuM data sets. Typical features of trabeculae were observed with osteocyte lacunae, canaliculi and mineralised cell spaces. A crack close to the fractured surface was also observed (Figure 9.4). The secondary remodelling front with the presence of cell spaces within was also observed. Cell spaces also appeared to exhibit mineralised collagen bundles (Figure 9.5)

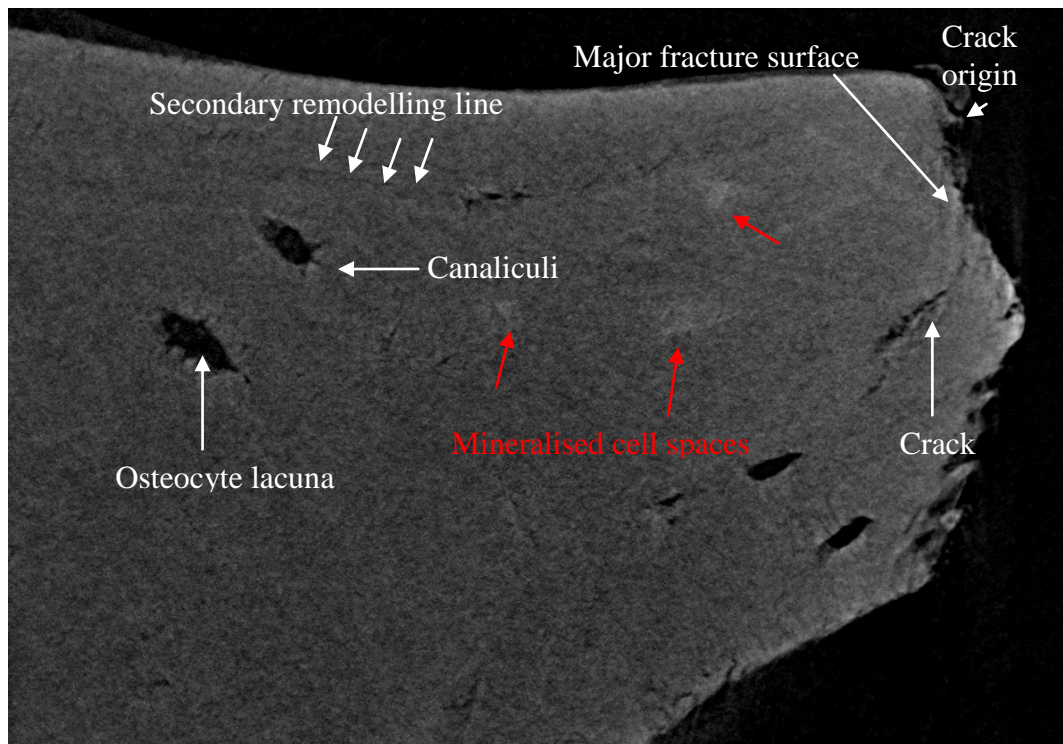


Figure 9.4: Greyscale image exhibiting typical features of a single trabecula with mineralised cell spaces (highlighted by red arrows). Field width = 0.24mm

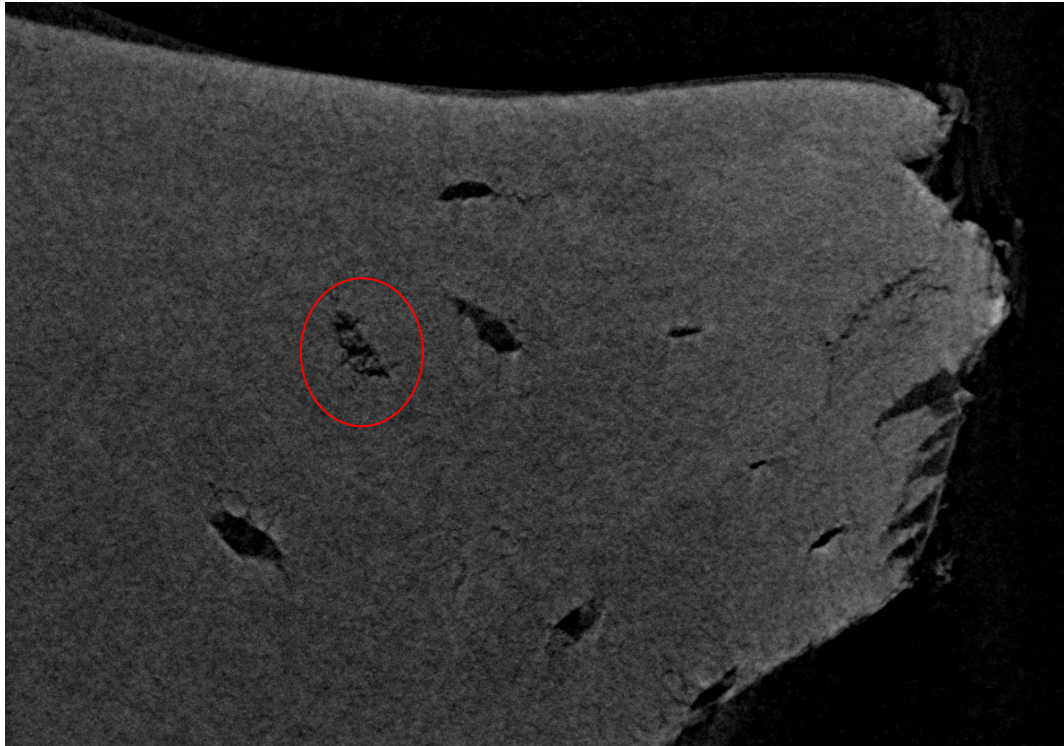


Figure 9.5: Greyscale XuM image of the single trabecula exhibiting internal structure. Field width = 0.24mm

9.2.3 Qualitative 3D analysis of a single trabecula

Cross-sectional images were taken of the rendered XuM data set of the trabecula (Figure 9.6). Osteocyte lacunae (b – highlighted in red) were distributed throughout the entire trabecula (c and d). The remodelling line incorporating the osteocyte lacunae was also observed, where the osteocyte lacunae appeared elongated and oval shaped (d). A higher number of cell spaces were present towards the centre of the trabecula (e) and were found away from the fractured site (f). Osteocyte lacunae observed with canaliculi (highlighted in white) (g). A higher number of osteocyte lacunae were also observed in the posterior region (h) in comparison to the anterior (a) region of the trabecula. The osteocyte lacunae and canaliculi were also observed within the trabecula (Figure 9.7), showing an absence of osteocyte lacunae close to the major fracture site.

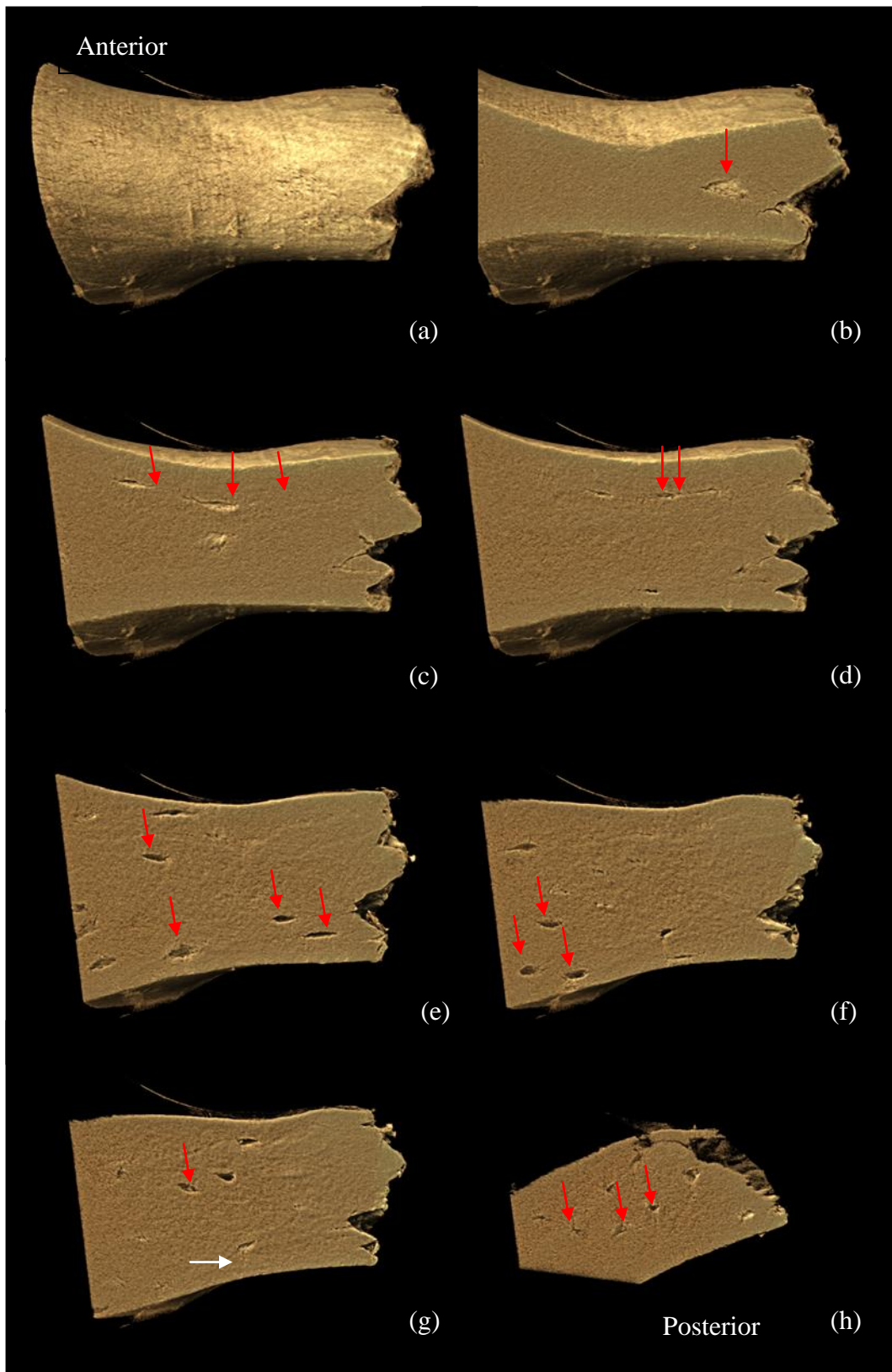


Figure 9.6: Cross sectional 3D images of the trabecula: anterior to posterior.

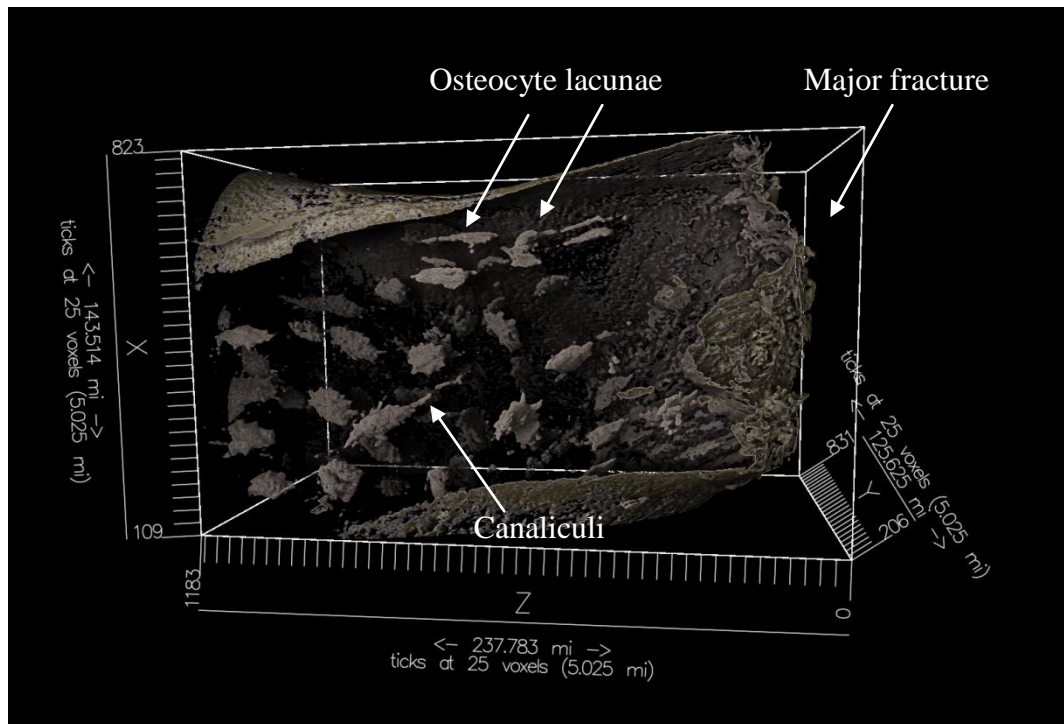


Figure 9.7: A rendered image showing the distribution of osteocyte lacunae within the trabecula (bound by box measuring 143.5, 125.6, 237.8 μm in the X, Y, Z), with very few present close to the major fracture site

Part IV General Discussion, Conclusions and Future Work

Chapter 10 General discussion, Conclusions and Future Work

10.1 Discussion

The aim of this study was to provide quantitative multi-scales information to ultimately aid interpretation of imaging data obtained from clinical 2D radiography of pathological and non-pathological trabecular bone.

10.1.1 Clinically Normal Femoral Head

Imaging techniques used to establish normal bone micro-architecture are well-established in 2D (Cowin, 2001). Most studies investigating normal bone have involved destructive techniques such as traditional histology, optical and electron microscopy (Boyd and Jones, 1996 and 2003b). The most widely-used clinical technique to investigate bone micro-architecture for the purpose of pathology is conventional 2D radiography. The methodological difficulty is that X-ray image acquisition conditions can cause intensity and contrast variations between images which make it difficult to evaluate bone structure or density accurately (Chappard *et al.*, 2005b). This results in a limitation in the understanding of the tissue as a whole.

Specimen Number and Limitations

One femoral head was used as a measure for normal healthy bone tissue from a population of six femoral heads which were identified as normal. Given this, only one femoral head was used (as a representative sample) due to time constraint, and therefore the number of femoral heads should be increased for any future work to establish an improved statistical analysis. The technique used to image an entire femoral head at a high resolution (for the purpose of this study greater than 30 microns voxel size) as the first of its kind and undoubtedly presented its own problems, in particular with the long period of scanning time where the filament would often burn out and therefore the scanning would have to be restarted, resulting in long scanning time and limiting the specimen number. It was also important to note the limitations presented during the analysis of the 3D data sets.

It is evident in Figure 5.10 that the BVF of the femoral head was not accurate at the superior and inferior regions. This was due to the inclusion of a high proportion of non-bone voxels. For the purpose of that analysis a cuboidal region of interest had to be used resulting in a high degree of inaccuracy in BVF. This limitation was presented by the software ImageJ and the plugin BoneJ, as spherical regions of interest could not be used, which would be more desirable in the future for such types of analyses.

Imaging Resolution

Microstructural parameters are known to depend strongly on the spatial resolution (Nägele *et al.*, 2004). The TDI XMT system successfully enabled imaging of an entire femoral head at a resolution of 26 μm reconstructed voxel size. Previously, Van Reitbergen *et al.*, (2003) have used commercial systems (Scanco, Bassersdorf, Switzerland) to image a whole femoral head but such systems restricted them to a much lower resolution (~80 μm voxel size).

Tb.Th has been reported on ranging from 120 – 290 μm (Müller and Ruegsegger, 1997; Nägele *et al.*, 2004; Nazarian *et al.*, 2006; Perilli *et al.*, 2007a; Tanck *et al.*, 2009) (Table 2.1), and from this study it was found to range between 137 – 224 μm . This showed that using 26 μm^3 reconstructed voxel size, features such as trabecular thickness, trabecular spacing and other bone quality parameters were successfully identified. It was observed that the partial volume effect may result in an overestimation of trabecular thickness. The overestimation was not quantified and requires further investigation.

Bone Mineral Concentration

TDI XMT carries the ability to detect subtle differences in the voxel grey-levels (Davis and Elliott, 2003). The LAC is a measure of the bone mineral concentration. The method for analysis is based on an assumed linear relationship with bone mineral and collagen. This relationship was used for the basis of relative measure of BMC and not for precise mineral concentration per voxel. The

localised BMC ranged from 0.9 - 1.114g cm⁻³ (approximately equating to 28 - 35 % mineralisation), with the mean BMC as 0.991 ± 0.132 gcm⁻³(for the entire head).

Partially-occupied voxels were not excluded from this result, resulting in an underestimation of BMC. No direct comparison can be made with other XMT BMC data since the TDI system is specifically designed to detect subtle greyscale differences in grey-level. But it has to be noted that the BMC reported is an average value of several thousand voxels in one virtual slice as a function of depth (including partially filled voxels), hence the consistent BMC observed throughout the head (Figure 5.9). One limitation (amongst the partial volume effect) in measuring BMC using this method is that there is a possibility of including microdamage; voids (including osteocyte lacunae) and the cortical shell surrounding the femoral head, resulting in a lower BMC. BMC measurements have shown differences at the nano-scale (Ferguson *et al.*, 2003), in particular between normal post-mortem and OA femoral subchondral bone with a mean BMC of 181 ± 31.0 and 158 ± 21.0 on the grey scale (on a range of 0 to 256) but this is due to the measure at a higher resolution (nano-scale). BMC was measured at a micron level scale for this study and so unable to detect the small changes in BMC, which occur at the nano-scale.

Bone Quality

Morphometric parameters were calculated from XMT data sets. Regional variations in bone quality were analysed according to load regions. Bone volume fraction can explain the variation in strength and stiffness in osteoporotic bone (Nazarian *et al.*, 2008), therefore the distribution of BVF throughout the femoral head was examined. Although the method used to establish this was restricted to using a cuboidal shape, and hence the superior and inferior regions were underestimated due to the inclusion of a high number of non-bone voxels, regions were cropped and used as a more accurate measure for BVF.

There were more trabeculae in the major loaded region that were thicker arranged closer in comparison to other loading regions and contained a higher amount of occupied bone volume (Figures 5.11, 5.12 and 5.13). From the SMI (Figure 5.14) the major loaded region exhibited a mixture of rod and plate-like structure with a large variation in connectivity density ($2.013\text{-}5.569\text{ mm}^{-3}$) (Table 5.3), with a median of 3.228mm^{-3} which is in agreement with Nägele *et al.*, (2004) for connectivity density in the normal proximal femoral head.

The microarchitecture in the non- and partially loaded region was similar in most cases except in relation to the SMI. The partially loaded region was arranged in a more rod-like manner whereas the non-loaded region contained a mixture of plate and rod-like structure. The trabeculae in both regions were thinner with lower BVF and larger Tb.Sp. Both regions showed a reasonable amount of overlap in the bone quality measures, with similar number of trabeculae and similar range for BMC (0.915 and 0.934 g cm^{-3} for partially and non-loaded, respectively) (Table 5.3). The BMC was lower in both these regions in comparison to the major-load bearing region, which may be due to the thinner trabeculae containing fewer voxels therefore including a higher proportion of partially filled voxels resulting in an underestimation of the BMC.

Generally, most studies report on bone quality from sections taken from femoral heads without any direct association to loading patterns. Instead age-related studies are more common. Established data on normal femoral heads in relation to bone quality is also less common due to the limited availability of normal tissue. Müller and Ruegsegger (1997) used XMT to investigate morphometric parameters of normal femoral heads and found BVF as 0.26, with Tb.Th as 0.12 mm and Tb.Sp as 0.36 mm. The BVF range for this study is between 0.086 – 0.328, and the value reported in their study lies within this range, but both that Tb.Th and Tb.Sp lay outside ranges reported in this study. This could be due to the fact that not all normal femoral heads are the same and the variation in microarchitecture is site specific as shown in this study, therefore direct comparisons of morphometric parameters require a very large sample size to draw any kind of trends. The partial

volume effect may also have resulted in an underestimation of the bone quality parameters. Furthermore, the number of regions cropped to assess for bone quality measurements could be increased so that the variation in the femoral head could be investigated further for a clearer understanding of the local variation within a normal femoral head.

The micro-architecture described in the bone quality measures can also be visualised in the rendered images of these regions (Figure 5.23). Figure 5.23 is in agreement with the SMI values reported in the results for this study. However, it should be noted that the non-loading region (Figure 5.23c) exhibited a high variation within the region which may have been due to an unclear definition of the load-bearing regions during cropping. In addition, the model based on load bearing by Brown and Shaw (1983) was produced from a contact stress distribution study and so the transfer of load towards the centre of the femoral head was assumption based.

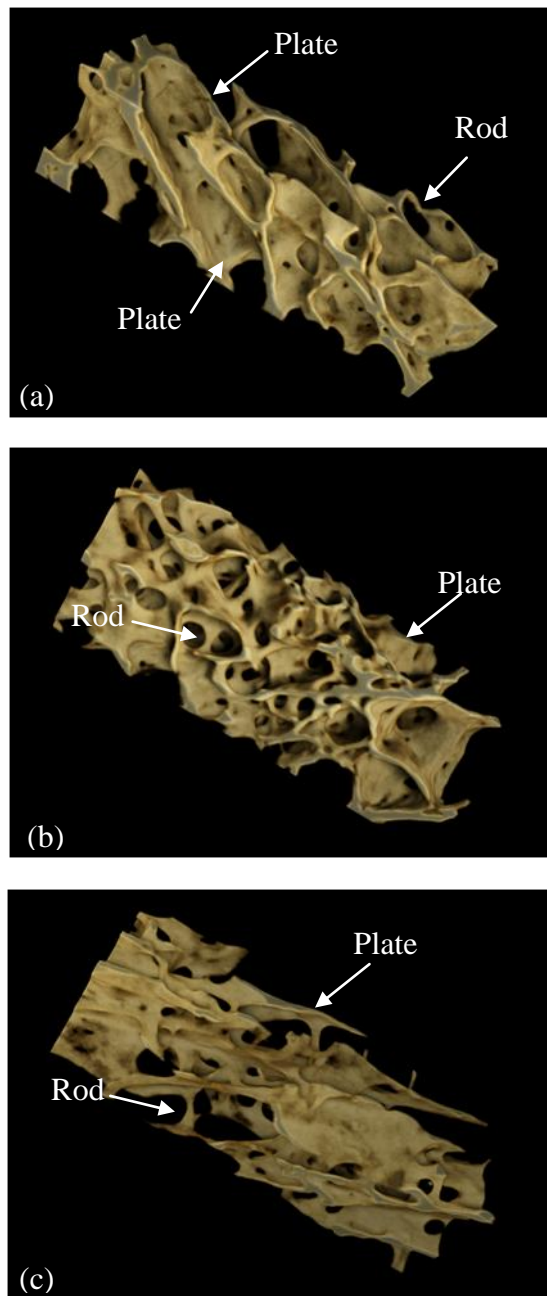


Figure 10.1: Rendered images of cropped regions, taken from (a) major-load, (b) partial-load and (c) non-load bearing regions of the normal femoral head.

Microdamage and Microcallus formations

Concentration of stress leads to damage accumulation and later fracture of the trabeculae (Banse *et al.*, 2005) and movement on the fracture site seems to trigger repair by microcallus formation. A total of 17 MCFs were determined in the normal femoral head. This is the first study to the author's knowledge where the 3D geometric distributions of MCFs are reported in an entire femoral head.

Cheng *et al.*, (1997), Boyde and Jones (1996) and Boyde (2003b) have studied the morphology of MCFs but in all studies the bone tissue inspected was either a biopsy or sectioned. The morphology described for determining MCFs in this thesis was in agreement with the studies carried out by Boyde and Jones (1996) and Boyde (2003b). The greyscale technique used to establish the MCFs was prone to human error, since they were located visually, therefore a systematic error of 5% was estimated. This technique was successful in determining early stage MCFs using the criteria outlined in this thesis, but MCFs which have a more smooth appearance and may be at the later stages of remodelling were rarely seen. Thus, a slight underestimation may have occurred, however the number of MCFs located is still valid using the criteria outlined.

From Figure 5.5, the majority of MCFs found in the femoral head appeared to have formed in the less-loaded region (between 4.8 and 0.69 MNm⁻² on the loading map) towards the posterior of the femoral head. This is where the trabeculae were found to be thinner, containing less occupied bone volume and fewer in number (Figures 5.11 and 5.13) and are most likely to be under resorption due to the low load transfer. It is generally understood that trabecular microfracture can occur in trabecular bone during normal physical activity (Fazzalari, 1993), hence the low number of MCFs found in this study.

From the results reported in this study, the MCFs appear to act as a repair mechanism in the clinically normal femoral head, mainly in the less loaded regions. This is shown in Figure 5.6, which shows only one MCF present in the major-loaded region, and the majority in the non-loaded region.

10.1.2 Pathological Femoral Heads

Specimen Number and Limitations

Three femoral heads, of which two were osteoarthritic and one osteoporotic, were successfully imaged using TDI XMT. Both pathologies were diagnosed by an experienced orthopaedic consultant pre-excision and therefore the femoral heads were representative of the bone diseases, which were confirmed using XMT in this study. Only three heads were imaged due to the difficulties in obtaining pathological tissue and scanning time as mentioned in Section 5.7. For further work a larger number of pathological femoral heads is required.

Imaging resolution

In this study the OA femoral heads were imaged at 25 and 26 μm and the osteoporotic at 25 μm voxel size. Using TDI XMT it was possible to identify microstructural features in relation to one another.

Factors attributing to OA and OP were identified from the reconstructed data sets. The results in the study were in agreement with the adapted Kellgren and Lawrence grading system for identifying OA using plain radiographs. The findings showed the presence of osteophyte formations, possible subchondral bone cysts (seen as spherical space), subchondral bone thickening, and regions of severe resorption, femoral head deformation and eburnated surfaces (Figure 6.5). These factors are often identified using XMT but not in a whole femoral head. In most cases sections are cut from entire femoral heads and imaged at high resolution (Müller and Ruegsegger, 1997). The close proximity of subchondral bone cysts was observed, and it was to be noted that they had formed under the thickened subchondral bone plate, which in turn was observed under eburnated surfaces (Figure 6.5). This may be due to a change in load transfer on the femoral heads where the surface of the femoral head results in worn away cartilage due to the presence of osteoarthritis.

The findings showed typical features of OP in the femoral head at 25 μm voxel size. The femoral neck fracture was distinguished along with a generally thinner trabecular structure with regions of resorption (Figure 6.3). The resolution used in this study proved to be successful in showing typical pathological features of the femoral heads but it should be noted that there were resolution limitations even at the 25 μm voxel size as the thinnest trabeculae were not detected, which was a limitation in investigating the entirety of trabecular thickness. Also, at this resolution the effect of partial voxels was more profound on the thinner trabeculae. Further studies are required on this effect for quantitative purposes.

Bone Mineral Concentration

A similar bone mineral concentration was observed in the OA femoral heads (B7; 1.134 ± 0.045 and B15; $1.15 \pm 0.052 \text{ g cm}^{-3}$). The OP femoral head exhibited a slightly higher BMC of $1.189 \pm 0.053 \text{ g cm}^{-3}$ (Figure 6.15). It was noted that the BMC was relatively similar throughout the femoral heads as indicated by the small deviations, therefore regional variations were investigated using cropped regions, and the findings showed that the OA femoral heads approximately ranged from 24 – 32% mineralisation in comparison to the OP head which ranged from 29 - 31%. When calculating BMC it was considered that voxels used in this project were either 25 or 26 μm for the whole femoral heads, therefore the BMC was an average measure of that voxel as discussed in Section 5.8. Ferguson *et al.*, (2003) have showed that degree of mineralisation varies vastly at a much higher hierarchical scale, therefore the voxel size used in this study is not sufficiently high enough to make an accurate measure of BMC for the purpose of investigating the relationship of BMC to bone quality in OP, OA or normal bone. These findings require further work at a higher resolution to establish an increased understanding relationship between BMC and different pathologies.

Bone quality and Osteoarthritis

In most cases of OA the change in load distribution in the femoral head leads to a change in the bone microarchitecture. The findings showed that bone quality of

the major-loaded regions exhibited similar behaviour in both cases of OA. The trabecular bone exhibited high occupied bone volume, thick trabeculae with small trabecular spacing, and high number of trabeculae (Figures 6.17, 6.18 and 6.19). The distinct difference was in the SMI, where specimen B15 in the major loaded-region showed a variation in the plate and rod-like structure (SMI 1.236), in contrast to B7 which exhibited a plate-like structure and was highly connected (8.606-15.342 mm⁻³).

From the results the bone quality of the partially loaded region was more closely associated with the non-loaded region (as observed in the case of the normal head Section 5.8). Partially loaded trabeculae occupied less bone volume than major-loaded trabeculae, and were similar in thickness but varied largely in trabecular spacing in both cases, and appeared more rod-like. Tb.N varied throughout each region.

The non-loaded region in B15 does not conform to the rest of the trend, containing the least amount of occupied bone volume, very few and thin trabeculae, exhibiting a higher variation of degree of anisotropy within the region. It is to be noted that this region shows the lowest bone volume and thinner and fewer trabeculae than the non-loaded region in OP. It is to be noted that femoral head B15 exhibited signs of extreme OA hence the reason for excising the entire femoral head.

From these findings it is seen that general trends cannot be drawn for bone quality in OA femoral heads based on such a small sample group. Bone quality deteriorates with the progression of the disease state. The variation in the microarchitecture may be as a result of several factors but in particular the load distribution, which in every case, dependent on the degree of the disease state, can be very individualistic.

Further clinical work is required in categorising the stage of the disease, and the Kellgren and Lawrence grading scale has been subject to debate since its use has

come into practice (Hart and Spector, 1995). Most importantly, a much larger sample group is required to further support the findings in this study.

Microdamage and Microcallus formations in the Osteoarthritic heads

MCFs were identified from the greyscale images. A total of 101 MCFs were found in specimen B7 and 132 in specimen B15. It was to be noted that only part of the femoral head was used for the XMT as it was obtained from total hip arthroplasty and the femoral head was excised above the healthy tissue therefore only approximately 2/3 of the head was used in this study. If the entire head was used (up to the femoral neck), more MCFs may have been determined. Taking this into consideration the number of MCFs found in both heads was similar.

In specimen B7 the MCFs were distributed mainly in the non-loading and partially-loaded regions, where 2 localised clusters of MCFs had formed. The MCFs in the major-loaded region were distributed throughout the region, with few close to the fovea. It was also noted that the MCFs were more prevalent toward the lateral region of the head. One large cluster had formed on the non- and partially-loaded boundary in the anterior region, and a smaller cluster in the non-loaded region. The inferior region exhibited no MCFs, which was due to the lack of bone tissue available for the XMT imaging.

Localised clusters were also observed in specimen B15 (OA) but in this case they were observed in the major-loaded and non-loaded regions. The larger cluster of the two was seen in the posterior and inferior non-loaded region, with isolated MCFs also present as seen by Todd *et al.*, (1972).

Vernon-Roberts and Pirie, (1973) found microfractures disposed along vertical pathways in a chain-like manner in vertebrae suggesting that microfractures occurred along the path of load transmission through the spine. This is not the case in this study where clusters have formed.

This may be due to the accumulation of large stress concentrations or change in loading patterns due to the pathological disease, but since this study is the first of its kind, further work is required to investigate this.

Since OA is a condition which affects the surface of the femoral heads and consequently the underlying subchondral bone (Sengupta *et al.*, 2006), microdamage is expected away from the centre of the head. Radially, the density of MCFs was greater away from the centre of the head in both cases. This suggests that microdamage is more prevalent away from the centre of the OA femoral heads.

Todd *et al.*, 1972 showed that, in femoral specimens taken from patients who had received oxytetracycline, MCFs fluoresced when illuminated by ultra-violet light, indicating new bone formation. They also found very isolated incidence of MCF whereas the results of this study mainly showed localised clusters. One reason for this may be that they are using sections taken from femoral heads, and that the technique limited them to only 2D surface analysis.

In OA it has been suggested that MCFs are a result of fatigue failure which occurs as a consequence of loss of cartilage on the femoral head surface (Todd *et al.*, 1972), and if this is the case the MCFs would be expected to form in regions of high loading or mechanical stress. This was not seen in this study; one obvious explanation is that the sclerosis seen close to the subchondral region under eburnated regions is a direct result of MCF formation, and here the thickened region may represent the final stages in remodelling of the MCF.

MCFs were found where the structure was rod-like but not always where less bone is present, as seen in the cluster in specimen B15 in the major loaded region. A very large cluster, however, was found where the occupied bone volume was very low, the trabeculae were thin, and where there were fewer trabeculae than other regions.

MCFs probably form as a result of the imbalance of load transfer as a result of the pathology in OA, possibly where the trabeculae become compromised, but further

work is required to gain the exact understanding of their role in microdamage and bone remodelling.

Bone Quality and Osteoporosis

OP is a result of an imbalance of bone remodelling. The bone matrix, mass and architecture are compromised, making the bone lighter and more porous (Marieb, 1998; Jee, 2001; WHO 2003). Clinically diagnosed with radiographs and DXA, only a 2D understanding is generally obtained of the disease. TDI XMT provided a 3-dimensional qualitative and quantitative understanding of the bone quality and micro-architecture of OP. The OP femoral head exhibited a fine structure, more rod-like in appearance and the surface showed the presence of articular cartilage.

Mosekilde *et al.*, (1987) have noted that horizontal trabeculae disappear with age leaving a predominance of vertical trabeculae which leads to domination of elastic buckling and bending forces instead of compressive forces. The thin rod-like structure (Figure 6.20) was observed in the findings of this study therefore the findings of Mosekilde *et al.*, (1987) may be true of the OP femoral head, and possibly related to the eventual neck fracture. Overall, the OP head exhibited significantly lower occupied bone volume than the OA femoral heads as seen in Figure 6.18. The inferior region also exhibited a higher BVF where the femoral neck fracture occurred, which was expected since this is where the trabecular bone structure collapsed and filled the void spaces.

BVF, Tb.Th and Tb.N in OP were closely related to that of the partial- and non-load bearing regions of the OA heads. Tb.Sp in the partial region exhibited a higher value (median 1.120 mm) than any other region in the other femoral heads.

Similarly in terms of connectivity density of the OP femoral head, when compared to partial- and non-loading regions of the OA head, it was relatively close. This suggests that possibly, some regions in the OA femoral head exhibit signs of OP based on bone quality measure.

The OP head exhibited a higher variation in anisotropy than the other femoral heads, which may have been due to a preferential destruction of cross-struts or plates leading to increased anisotropy but which requires further investigation.

Microdamage and Microcallus Formations in Osteoporosis

Fazzalari, (1993) suggested that the accumulation of MCFs compromised the trabecular structure leading to osteoporotic fracture, but Cheng *et al.*, (1997) found few MCFs in OP vertebral bodies suggesting otherwise. MCF prevalence has usually been underestimated with histological studies due to the fact that MCFs have often been overlooked or misinterpreted as trabecular thickening (Hahn *et al.*, 1995). MCFs had formed indiscriminately throughout the entire femoral head with no localised micro-damage. A total of 586 MCFs were determined. Radially, while the OP exhibited a normal distribution of MCFs throughout the head, they were less likely to be found towards the inferior region of the head. Since thinner trabeculae are more likely to fracture (Todd *et al.*, 1972), and the findings showed the OP head exhibited a very thin rod like structure, the high number of MCFs was reasonably expected. However, such a high number in contrast to the OA femoral heads and the nature of the geometric distribution was not expected. The findings showed a significant relationship between the number of microcallus formations found in the OP head, and the very thin, largely spaced, rod-like trabeculae.

10.1.3 Mechanical Properties of Trabecular Bone

It is known that OA alters the loading condition of the femoral head in the hip. The understanding between the mechanical properties of trabecular bone, its microarchitectural properties and the effect of loading conditions is unclear.

Mechanical Properties and Bone Quality

Bone quality parameters of the cylindrical specimens were generally similar to those of the cropped regions in Figures (Figures 6.17 – 6.28), as seen with the overlap in Figures 7.6 – 7.17. It was difficult to relate the bone quality measures in the cylinders to loading regions due to the small specimen size and uneven number of specimens per loading region. It was not possible during extraction of cylinders from the femoral head to remove the same number of specimens from each region. However, these findings show that the physical and virtual extraction of trabecular bone has no effect on the measure of bone quality.

No relationship between the load-bearing region and the compressive strength was observed. Instead, three distinct groups were observed in terms of compressive strength.

High Compressive Strength:

Partially-loaded Specimen B3 exhibited the highest compressive strength 14.94 ± 3.82 MPa occupying the highest bone volume (0.432 ± 0.089), with thick trabeculae (0.295 ± 0.051 mm) which spaced closely together (0.592 ± 0.054 mm), well-connected and plate-like in structure (SMI, 1.104 ± 0.499). This was only observed in one specimen therefore a larger sample size would be required for any future work to support this result.

Medium Compressive Strength:

Specimens B3 none, B5 major and B6 partial exhibited similar compressive strength. They were arranged in rods and plates (SMI, 1.259 – 1.703) with BVFs ranging from 0.231 to 0.363. They were all extracted from different load-bearing regions and different femoral heads suggesting that the compressive strength is not affected by the loading region.

Low Compressive Strength:

Specimens taken from the non-load bearing regions of femoral heads B5 and B6, and major-load bearing region of B6 exhibited the lowest compressive strength. The trabeculae exhibited a less connected ($6.030 - 9.405\text{mm}^{-3}$), rod-like (SMI, 1.65 – 2.498) thin structure (BVF, 0.173 – 0.274).

Degree of anisotropy, trabecular spacing and bone mineral concentration had no effect on the compressive strength. The results showed that trabecular bone with a high BVF and thicker and plate-like structure resulted in a higher compressive strength. This may be due to the fact that thin rod-like structures are more likely to fracture due to a high slenderness ratio, and therefore are more likely to buckle and fracture under compression (Gibson and Ashby, 1999).

Trabecular Failure using Image Analysis

In general, under compression the bone cylinders failed in shear as seen in Figure 7.18. All cylinders failed by 6% strain, with the majority (6 specimens) failing by 4% strain to failure. Nazarian *et al.*, 2008 reported that bone specimens which failed at the lower strains contained the minimum bone volume. No correlation was found between strain to failure and other bone parameters. To improve the understanding of mechanical properties in different loading regions and relate them to bone microarchitecture, a larger number of specimens are required.

On closer examination of the compressed bone cylinders, the results showed that on an individual trabeculae level the trabeculae collapsed in a buckling manner. The cellular structure of trabecular bone is made up of an interconnected network of rods and plates. A network of rods produces low-density, open cells, while one of plates gives higher-density virtually closed cells. The rod- or plate-like cell walls in low density bone have a higher slenderness ratio and fail by elastic buckling, both in wet and dry conditions. At higher densities the slenderness ratio is lower and buckling is more difficult; then it is found that wet specimens microcrack while dry ones fail in a brittle manner. Elastic buckling and shear

failure have also been suggested as modes of failure by Carter and Hayes, (1977) and Gibson and Ashby, (1999)

At strains of about 1% the stress-strain curve becomes non-linear as the trabeculae start to deform irreversibly (Gupta and Zioupos, 2008) and crack (Gibson and Ashby, 1999). Beyond the peak, the stress-strain curve falls gradually as the trabeculae progressively fail by tearing and fracturing, therefore it may be of more benefit to investigate failure at this level of strain to gain a better insight into the mechanical failure of trabeculae.

Specimen number and Limitations

With a limited number of specimens it was difficult to find any real conclusive relationships between the strength of trabecular bone and different loading regions in the femoral heads. Since each femoral head differs hugely within itself and from another femoral head (as discussed in Sections 5.8 and 6.8), a larger number of specimens are required. Errors in mechanical testing may have also contributed to the lack of any obvious relationship between compressive strength and loading regions. It has been reported that the length to diameter ratio of the machined specimen has a significant effect on strength and stiffness (Linde *et al.*, 1992). However, Keaveny *et al.*, (1994) observed that variance in trabecular bone strength was better explained by density when 2:1 length:diameter cylindrical specimens were used, and therefore this ratio was adopted in this study.

As mentioned in the literature, Ford and Keaveny (1996) suggested that axis misalignment during loading can also result in shear failure. Due to small specimen size, any small displacement would introduce artefacts in the testing technique (e.g. slippage or stress concentrations at loading or support points) resulting in a lower measured modulus than the true value. Since there were only six points used to derive the stress-strain curve, it has to be noted that a much greater number of points is required to interpret the mechanical variations between the points. Smaller increments of strain could be used to overcome this.

10.1.4 Multiscale Imaging of Microcallus Formations

The specimen examined in this study was taken from a cylinder removed from the major load bearing region of an osteoarthritic head (B6, Table 3.2). It has previously been observed that OA femoral heads contain microcallus formations (Chapter 6), in particular where the structure is compromised. This specimen, therefore, represented microcallus formations in osteoarthritic bone.

Morphology of Microcallus Formations

Most early studies investigating microcallus formations were limited to 2D understanding (Todd *et al.*, 1972; Vernon-Roberts and Pirie, 1973). The lack of systematic research into the phenomenon of MCFs may have been due to the few suitable preparation techniques available for the analysis of these structures (Hahn *et al.*, 1995). Since XMT does not require any preparation of specimens, the approach taken in this study proved successful in identifying MCFs. With the introduction of XMT, microcallus formations were studied recently in more detail in 3D (Müller and Ruegsegger, 1997). The true role of MCFs is still a topic for debate, but this study was the first to evaluate the morphology of MCFs at multiscale in 3D using XMT and XuM.

In this study MCFs were identified as porous, bulky nodular accretions. This was in agreement with studies carried out previously describing MCFs as globular formations (Banse *et al.*, 2005), nodular aggregates (Vernon-Roberts and Pirie, 1973) and nodular calluses (Blackburn *et al.*, 1992). Previous 3D studies of MCFs used low resolution imaging with sections or biopsies to evaluate the morphology (micron scale ~15 – 20µm voxel size) (Cheng *et al.*, 1997; Müller and Ruegsegger, 1997). They showed that MCFs had formed around trabeculae but did not provide any detailed description of the morphology of MCFs.

In this study only the very early stage MCFs were observed, which were characterised by Vernon-Roberts and Pirie (1973) as nodular aggregates, and by Fazzalari (1993) as actively woven bone bridging a microfracture with an open lattice. It was observed that the MCF had occupied much of the length of the

trabecula, which was also observed by a study of MCFs using SEM by Blackburn *et al.*, (1992).

Todd *et al.*, 1972 showed that, in femoral specimens taken from patients who had received oxytetracycline, MCFs fluoresced when illuminated by ultra-violet light, indicating new bone formation. This was obvious when MCFs were observed at a higher resolution (8.8 μ m voxel size) using XMT, where the MCF appeared as an unorganised, bulky, porous node. The fibrous, woven bone was heterogeneous in thickness (Figure 8.3) suggesting that it had been laid down quickly in an unorganised manner.

Blackburn *et al.*, (1992) found that the porous MCFs, of the nodular form, which were also observed in this study, were typically of the order of 0.5mm, but the results in this study showed a wide range of sizes, in three dimensions (Figures 8.1, 8.2 and 8.3). They observed and characterised the size of the MCF in 2D, thus were limited to measuring the size in one plane. This study enabled measurement of the MCF in 3D providing a more accurate result of the dimensions. The size of the MCF may provide an indication of the state of the micro-damage that has occurred in the trabecular strut, but requires further studies. It may also aid in understanding the whole process of microcallus formation.

Bone Mineral Concentration

Fazzalari (1993) has suggested that the mineralisation of fractured trabeculae should be measured to determine whether the trabeculae that are fractured are intrinsically flawed. MCFs have previously been characterised according to their development stage (Vernon-Roberts and Pirie, 1973) as mentioned in the literature. The MCF reported on in this pilot study was identified as early stage formation. When the MCF forms it is recognised as woven bone, therefore generally understood to be of a lower BMC. Although it is accepted that immature woven bone is less mineralised than mature bone, few studies have attempted to investigate the relationship of BMC between the trabeculae and the surrounding MCF in 3D. The results showed that the trabecular strut was approximately

double in BMC in comparison to the MCF. This may be true of the development stage of the MCF, in particular if it is in the very early stages of formation. This may not be true of the entire structure, however, since the method of analysis has some limitations. The BMC was measured along a line placed on the surface of a cross-section of the data, which is not a true representation of the entire 3D structure. This could be investigated further by increasing the sampling for measurement of BMC.

Microcracks and Microcallus Formations

XuM proved to be successful in highlighting the structural features resulting from microcallus formations. Greyscale imaging clearly showed the propagated crack, which appeared to be in the shear plane. Since shear damage in bone at micro-scale can be related to off-axis loading, it can be said that the trabecular bone failed in shear as the compressive load may not have aligned accurately with the principle trabecular orientation. The linear micro-crack was $>300\ \mu\text{m}$, which according to the work of Caler and Carter, (1989) and George and Vashishth (2005), relates to microdamage resulting from torsional loading.

The shear crack may be a result of both compression and torsional forces as presented by George and Vashishth (2005). Osteocyte lacunae were also observed, with a random distribution.

From the result it can be said that MCFs form where there are trabecular micro-fractures as observed in Figures 8.7 and 8.8. The findings suggest that MCFs appear as a repair mechanism for micro-fractures, thus providing an indication of microdamage as discussed in chapter 5. There was a clear interface between the trabecula and the surrounding MCF, also reported by Blackburn *et al.*, 1992, using SEM and the crack had propagated through the entire strut, in the shear plane, perpendicular to the surface (Figure 8.8).

With the rise in the hierarchical scale in resolution, the fibrous woven bone was seen as smooth fibres with a large number of pores present, but at the nano-scale,

the fibres also exhibited a porous structure within. The highly porous arrangement of the fibres may be indicative of the development stage of the MCF.

10.1.5 Trabecula Imaging at Nano-scale

This study was carried out as a pilot to explore the 3-dimensional nano-scale structure of trabeculae. No specimen preparation was required, therefore allowing other experimental tests pre- and post-XuM imaging. The SEM images and XuM images correlated well, with both sets of images shown in the results in the same orientation, and the same angle of the critical fracture.

The trabecula was fractured during a simple bending test, where the trabecula was loaded and unloaded cyclically till fracture. The critical fracture took place close to the loading tip but more interestingly four small parallel microcracks measuring approximately 10 μ m in length were observed away from the critical fracture just before the trabecula fractured. This qualitative test showed that there were a number of reasons explaining the location of the critical fracture. One very important point to note is that the shape of the loading tip, which may be wholly or partially responsible for the location of the fracture, since it can be seen from the results that the fracture took place close to the loading tip and the trabecula failed in simple bending. Therefore, it is essential to repeat this test with varied loading tips to investigate the stress distribution and concentrations caused.

Trabecula Structure

Structural exploration of the trabecula the region close to the small parallel microcracks showed no difference in the underlying structure and further work is required to investigate this phenomena.

Cross-bridging of collagen fibres was observed using SEM post-fracture (Figure 9.1). This can explain in part the way in which the fracture takes place. Several theories support that the hypothesis fracture travels along the weakest interface and that non-collagenous proteins, found between collagen bundles, have some

role to play in fracture mechanics at the nano-scale (Gupta and Zioupos, 2008). Since this was not the focus of this project, from these results it is not possible to confirm or falsify this theory, but further work is required to investigate this.

From the XuM results it was possible to determine structural features of the fractured trabecula. To the author's knowledge this is the first study showing the 3D structural features of a single trabecula at nano-scale using a desktop tomography system. Typical trabeculae features were observed at the nano-scale: osteocyte lacunae, canaliculi, (Figure 9.7) and the remodelling line. Interestingly, light regions of mineralised cell spaces were also observed. These mineralised cell spaces have been reported as a result of cell apoptosis (Boyde 2003b) and have formerly been known to be associated with microcracks in trabecular bone (Mori *et al.*, 1997; Vashishth *et al.*, 2000b).

Mori *et al.*, (1997) showed that an increase in microdamage resulted in a decrease in osteocyte lacunar density. It was observed that the number of osteocyte lacunae were lower close to the critical fracture, and therefore the theory suggested by Mori *et al.*, (1997) is reasonably supported by this work.

It was also observed that the mineralised cell spaces were close to the critical fracture, and so these possibly hypermineralised cell spaces could aid in stiffening the region of the trabeculae and hence the fracture occurred as a result of an increase in stiffness.

From the work of others mentioned in this discussion and the results in this study it can be suggested that osteocytes and their function in the cell spaces are closely linked to microdamage. It is difficult to say whether it is the microdamage which causes impairment of the osteocyte network or vice versa, and requires further work. It could be speculated that a minimum number of osteocytes are essential for an 'operational' network (Mori *et al.*, 1997).

Since the XuM is still developing technology, it is unable at present to provide any kind of quantitative data related to the LAC of the specimen.

10.2 General Overview

3D Imaging of Whole Femoral Heads using XMT (Macro/micro-scale)

This study was the first to successfully image whole femoral heads at high resolution using XMT as far as could be determined from an extensive literature review. Glycerol substitution was successfully introduced as an imaging medium by providing a stable environment for the imaging of the femoral heads. This was in agreement with *Giovani et al.*, (2006), where Glycerol-substitution was compared to cryopreservation. They used trabecular bone specimens, and placed them into 3 groups, cryopreserved, glycerol preserved and a control group. After preservation, the samples were subjected to histomorphological, cell feasibility and microbiological analyses resulting in no bacteria or fungi in samples, even after 1 year

This method enabled identification of clinically normal healthy bone showing no obvious signs of pathological features such as osteophytes, subchondral bone cysts, thickened subchondral bone plate and eburnated surfaces (Figure 5.2). This was in agreement with the assessment carried out using a plain radiograph. The micro-architecture in a normal head varies vastly from one loading region to another, as shown in a study by *Nazarian et al.*, (2007). They used cropped regions from cadaveric proximal femurs, and applied a mechanical compression test, followed by XMT. They measured similar morphometric parameters as outlined in Section 1.5. Their results were found to be in similar range to the results reported In Chapter 5, although their results were not related to loading conditions but different sites on the femoral heads. The results from Chapter 5 showed that the trabecular structure is generally well connected (3.114 mm^{-3}) (Table 5.3), with a less well-connected network in the less-loaded regions (2.611 mm^{-3}) and with no obvious loss of trabeculae (as often found in OP). There are a higher number of trabeculae arranged in a mixture of rods and plates in the major-load bearing region, which are thicker and spaced closer, and appear more mineralised than the other regions. Overall, factors such as anisotropy,

connectivity density and structure model index were independent of load-bearing regions.

Three-dimensional XMT of an entire femoral has provided an insight into the micro-architecture of a whole organ and the 3D structural nature of a normal head. Using this research technique it is possible to identify healthy tissue based on clinical diagnostic techniques such as the Kellgren and Lawrence grading scale. It is possible to use this technique to assess a normal femoral head as a baseline for comparison to other bone tissue, in particular pathological femoral heads.

Previously, various XMT studies have imaged pathological bone, and generally used biopsies or sections, therefore not resolving all the structural features related to the pathology in the entire bone organ as reported in the literature. In most cases only the bone quality is investigated. Chappard *et al.*, (2006) investigated the effect of monochromatic and polychromatic imaging on sections taken from eburnated and non-eburnated areas, thus limiting the understanding to the subchondral region of the OA femoral head. By imaging whole femoral heads at high resolution it has been possible to gain a much deeper understanding of the overall condition of the pathological tissue.

In this study, structural features were resolved and related to pathological conditions using greyscale and 3D image analysis. The OA femoral bone was indicative of the disease state, with the presence of osteophyte formation, possible bone cysts, subchondral bone sclerosis, eburnated regions, femoral head deformation and large areas of resorption. Conversely, the normal femoral head did not exhibit any of the features mentioned above in the OA femoral head. Structural features from the image analysis showed the OP femoral head contained large areas of resorption, and a rod-like poorly connected structure. These features are often observed in plain radiographs as described by Singh *et al.*, (1970) and Kellgren and Lawrence (1957), but this 2D approach imposes a limitation in the 3D understanding of the features attributing to the pathological

condition. The results from this study clearly contribute to a more global understanding of features in the femoral heads.

The OA femoral head exhibited similar bone quality to the normal head, with the exception of the major-load bearing regions and the non-load bearing in specimen B15. Bone quality in the major loading regions differed significantly from that in the same regions of the normal femoral head. Bone volume was much higher and trabeculae were thicker with a plate-like, closely-spaced (Figures 6.17, 6.18, 6.20 and 6.22), well-connected structure. In the major-load bearing region of specimen B15 a large cluster of microcallus formations was also observed (Figure 6.11), whereas, the non-load-bearing region of specimen B15 also contained a large cluster of microcallus formations but exhibited a thinner, rod-like, poorly-connected, less mineralised structure occupying less bone volume (Figures 6.17, 6.20, 6.22 and 6.28). The microarchitecture varied significantly within OA femoral heads, possibly due to the alterations in the remodelling mechanisms, as a result of the changes in stress distribution (Nazarian *et al.*, 2008). This suggests that a change in the load distribution of specimen B15 may have an effect on the formation of microcallus formations. It can be speculated that there is a ‘cut-off’ point on the stress placed on the bone structure, which when exceeded sets off microfracture resulting in the onset of microcallus formations. Further studies are required to test this hypothesis. It was noted that specimen B15 was a severe case of osteoarthritis, resulting in a largely deformed femoral head, as observed in Figure 6.16. From these studies it was not possible to find the factors responsible for the formations but a large insight into the nature of the bone structure surrounding microcallus formations was gained.

The results showed that BVF (also reported by Nazarian *et al.*, 2008) and SMI governed most other bone quality factors and compressive strength in the case of OA bone. SMI is an important structural feature which impacts on the mechanical properties of the trabeculae as reported by Chen *et al.*, (2008), suggesting that BVF and SMI could possibly be used to predict fracture or disease development stage.

The OP trabecular bone exhibited a similar microstructure to normal bone with the exception of the femoral head which exhibited a more rod-like, largely-spaced, poorly-connected structure (Table 6.2). The OP femoral head showed a largely compromised structure with 585 MCFs throughout. This homogenous MCF distribution was indicative of microdamage observed in OP trabecular bone and, unlike normal and OA bone, OP bone exhibited similar bone quality throughout the entire head with little localised variation. Since Connectivity density is important in the maintenance of bone strength (Mellish *et al.*, 1991), the high number of MCFs may be explained by the poorly-connected trabeculae in the OP head.

As the number of trabeculae decreased in the OP bone there was a corresponding decrease in connectivity density (Figure 6.26), possibly due to the loss of small interconnecting trabeculae with small diameter. As reported in the literature review, if new bone formation does not adequately restore the lost tissue, (i.e. microcallus formations) the narrowed trabeculae will become tapered, free-ended and unlikely ever to regain continuity, which was observed in this study (Figure 8.1).

Bone quality in OA and OP femoral heads used in this study varies significantly, since the two pathologies affect the microarchitecture in different ways. OA trabecular bone exhibits a mixture of rod- and plate-like structure whereas OP trabecular bone predominantly comprises a rod-like structure, and is overall less connected than the OA trabeculae. There are more trabeculae present in the major-loading region of OA femoral heads and these are generally thicker with less spacing, in comparison to OP bone.

Bone mineral concentration was measured and overall showed similar concentration throughout the heads, but on a more regional basis showed variations inter-loading in the OA femoral heads ($0.762 - 1.013 \text{ g cm}^{-3}$) in comparison to the OP femoral head ($0.923 - 0.989 \text{ g cm}^{-3}$). BMC in the OP femoral head was very similar inter-loading; Major- (0.985 g cm^{-3}), partial-

(0.956 g cm^{-3}) and non-load bearing (0.944 g cm^{-3}). Nazarian *et al.*, (2007) measured BMC from small cropped regions in the femoral head, and found a 42% variation. This may be due to the exclusion of partially filled voxels. Since they were not excluded in this study, it may explain the reason why the BMC was found to be so close in all the femoral heads. To successfully measure any effect of BMC on the pathology, further work is required.

3D Global and local morphometry is a useful method for a detailed and quantitative description of pathology-related changes in bone microstructure. The advantage of being able to image a whole femoral head at high resolution has successfully resolved features such as MCFs which are otherwise undetected or not possible to quantify due to limitations in clinical 3D low resolution imaging and 2D techniques. Small cropped specimens can only provide limited data for small localised bone volumes. Conversely, the larger specimens investigated in this study provided an average measure of BMC and an overview of structural properties of bone, which may not have reflected regional structural variations. The cropped regions in this study were virtually extracted and the boundaries between each region may not have been fully understood, although, this probably did not have a significant effect on the results, since several cubes were cropped from each region. This study showed that multiscale imaging is fundamental to the understanding of bone microarchitecture and prior to any further studies careful consideration is required in order to understand how best to interpret the data obtained from large XMT data sets. Furthermore, limitations such as partially occupied voxels resulted in an underestimation of bone mineral concentration. Any further work would require investigation into the effect of partially-occupied voxels on BMC.

Mechanical Findings of cylindrical samples using XMT (micro-scale)

From this study, it was not possible to relate the compressive strength to the loading regions of the OA bone. This may be due to the limited sample size, but it was observed that the specimen containing the highest occupied bone volume, with thick trabeculae, closely arranged in a plate-like well-connected structure,

resulted in a higher compressive strength (14.94 ± 3.82 MPa) (Table 7.1). Perilli *et al.*, (2007b) used cored cylinders from 37 OA femoral heads and subjected them to compression testing. Their results showed no significant differences in male and female ultimate strength, and found the mean compressive strength to be 14.8 ± 7.5 MPa for females, which is closely related to the value determined in this study, although a higher number of specimens is required to determine any real statistical understanding. The Tb.Th (0.295 ± 0.051 mm) was also found to be similar to that reported by Perilli *et al.*, (2007b) (0.257 ± 0.062 mm). No other morphometric parameters were in agreement with their study.

The failure behaviour of trabeculae was observed using rendered images, where trabeculae were found to fail in a buckling manner. These strut-like trabeculae probably failed in this manner due to their high slenderness ratio. This form of failure behaviour is seen as a 2D image in Figure 7.7 and can be seen in video 7 (Appendix V) for reference in 3D. This approach to determine the relationship between mechanical properties and load-bearing regions provides a better understanding, however due to the limited number of specimens, a reasonable statistical evaluation was not possible. Differences in compressive strength were observed in relation to bone volume fraction, structure model index, connectivity density and trabecular thickness.

Microcallus Morphology and Trabecular Microcracks using XMT (micro-scale)

Even though there is widespread occurrence of trabecular microfractures in trabecular bone, there is no clear insight into their physiological or pathological effects. Both XMT and XuM were used to determine the morphology of a microcallus formation. In this study, the MCF was characterised as a fine, highly-porous and fibrous structure, this was also observed by Boyde and Jones (1996). They used SEM to image MCFs and characterised their morphological appearance. The MCFs visually appeared to be similar when compared to 2D images obtained from SEM in Boyde and Jones (1996).

There were only 17 MCFs present in the clinically normal head showing that there is little evidence of microdamage present on a large scale, and the small amount of microdamage present is possibly a result of ageing and physical activity. In normal bone the microdamage (10 MCFs) is present in the regions where very little or no load is applied with few trabeculae (0.582 mm^{-1}) which are thinner (0.158 mm), more rod-like, spaced further apart (1.147 mm), less mineralised (0.934 g cm^{-3}), less connected and contain a low bone volume (11.5%). This study implies that there are factors, such as the presence of MCFs that indicate regions of damage in normal tissue which cannot be identified using current clinical techniques.

The results from this study also showed that a very large number of MCFs (586) were present in the OP head, with smaller numbers of localised clusters in OA femoral heads (101 and 132, in specimens B7 and B15, respectively). MCFs formed in the OP femoral head, where the trabecular structure was thin (0.163 – 0.212 mm), rod-like (SMI, 1.848 – 2.948), largely spaced (0.777 – 1.267 mm) and occupied low bone volume (BVF, 0.177 – 0.269). In the OA femoral heads, the localised clusters formed where the trabecular structure was less well-connected than a clinically normal head, and contained a rod-like structure. Although it is to be noted that in OA femoral heads the distribution in load varies significantly from one head to another, therefore it is not possible to draw a general trend between microdamage and loading pattern. To establish any ready conclusion, it is important to conduct further studies with a larger sample size. The number and distribution of MCFs has been reported in vertebral bodies, mainly due to their association with the compromised structure of OP bone. This study has shown the variation in MCFs between two pathological conditions and a normal femoral head in 3D successfully for the first time, therefore any direct comparison with literature has proven to be difficult.

The result in Section 8.2.3 showed that the trabecular strut (LAC of 1.27 cm^{-1}) exhibited a higher BMC in comparison to the MCF ($0.6 - 0.8 \text{ cm}^{-1}$). This may be due to the very early stages of formation. Since microcallus formations are woven

bone, and less mineralised, this result was expected. This result gives only an indication of the difference in BMC between the MCF and trabecula, as the measure is performed in 2-dimensions. Therefore, an increase in sampling during measurement is required. The findings showed that bone quality and microdamage vary largely between pathologies. Microcallus formations were determined as markers for microdamage and they showed that OP bone exhibits a higher level of microdamage throughout the femoral head. The OA femoral heads exhibit more localised microdamage. This is the first study, to the author's knowledge, to show this.

XuM Imaging of a Single Trabecula and Microcallus Formation (nano-scale)

This study is the first to image a microcallus formation at the nano-scale level in 3D. XuM successfully identified a microcrack penetrating the trabecula surrounded by a microcallus formation (Figure 8.9) and osteocyte lacunae and the highly porous fibres were observed at the nano-level in 3D. This study confirmed that microcallus formations do form where microcracks are present, but was unable to show if microcallus formations form in the absence of cracks or fracture. Furthermore, it could not be determined why microcallus formations form around some and not all fractured trabeculae. XuM was successful in highlighting the presence of a microcrack in the trabecula surrounded by the MCF. The microcrack propagated the entire length of the strut, with a varied width. The 775 nm voxel size enabled identification of typical structural features, such as osteocyte lacunae. It is seen in the results that MCFs are an important component of trabecular bone and play some form of role in micro-damage repair.

A single trabecula was imaged using the XuM post-fracture in the SEM chamber. Typical trabecular features were observed at nano-scale: osteocyte lacunae, canaliculi, and the remodelling line. In addition, regions possibly exhibiting mineralised cell spaces were also observed close to the major fracture. Boyde

(2003b) suggested that mineralised cell spaces may exist as a result of cell apoptosis and previous studies (Mori *et al.*, 1997; Vashishth *et al.*, 2000b) have shown cell apoptosis related to microcracks in trabecular bone. These findings suggest a relationship between the osteocyte lacunae network and fracture, but due to limitations in the sample size, no ready conclusions can be formed. Further, trabecular microfractures are influenced by many factors, some of which are correlated (Fazzalari, 1993); physical activity, age, bone viability and remodelling potential, trabecular bone volume, bone mineral content, bone fatigue properties and the direction of loading on the trabecular bone. These factors make it difficult to isolate or identify a unique pathway to the occurrence of trabecular microfracture and the resulting microcallus formation. With multiple paths to microfracture, any further studies to explore their physiological or pathological effect require careful consideration.

XuM provided a qualitative insight into the fracture mechanics of single trabeculae. The fractured regions were successfully correlated using SEM and XuM. XuM was successful in identifying typical features of trabeculae and those which may also be associated with or responsible for the failure of trabeculae. This pilot study highlights the possibility of a relationship between microcracks and cell death, but further work is required to determine any conclusive evidence of the relationship between microdamage and osteocyte lacunae apoptosis.

Summary

In summary, there were differences in bone microarchitecture between the normal, OA and OP femoral heads. There were also distinct differences in the number of MCFs, indicating a difference in microdamage occurrence and distribution. No ready conclusion could be made due to the low number of specimens when investigating mechanical properties of the different loading regions. From the studies in this project it can be suggested that the altered structure in patients with pathological diseases results from difference in bone adaptation mechanisms. This suggests that XMT can provide information on the structural integrity of pathological bone, and aid in differentiating diseases by their effects.

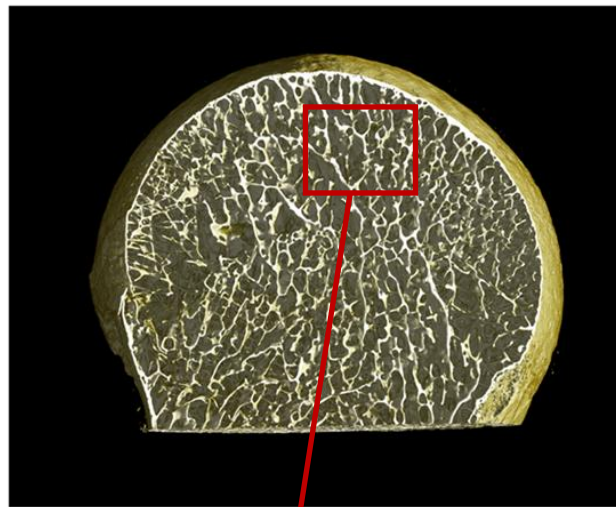
The greyscale analysis method developed to identify MCFs and structural features proved successful. MCFs were more prevalent in OP bone than in OA, with very few present in normal bone. MCFs formed around single trabeculae as well as around junctions of trabecular rods and plates, as seen in Figures 8.1 and 8.2. They varied in size and were found throughout OP bone, but in more localised regions in OA bone (discussed in Sections 10.1 and 10.2).

In the case of MCFs, whether they should be regarded as an indicator of poor architectural adaptation to prevailing stress or whether they are a sign of a physiological repair mechanism is difficult to conclude from this study. It is confirmed that MCFs play a significant role within the framework of physiological bone reorganisation. The development of fibrous bone shows that there is another mechanism for localised bone organisation within the basic multicellular unit (BMU) of remodelling. MCFs could represent an adaptive attempt to maintain bone strength through the redistribution of bone tissue.

Imaging whole femoral heads at the macro-scale provided an insight into the structural features contributing to the pathological condition of the bone. These features were successfully identified using XMT and XuM.

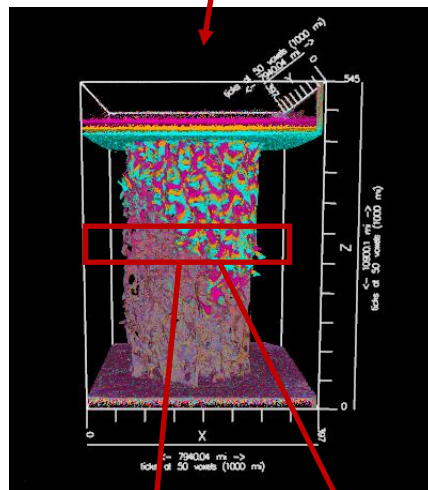
Using this multi-scaled information it was possible to relate the condition of the bone and the pathological condition of the bone at the multi-scale levels. The OA was identified using structural features at the macro-scale and clusters of MCF'S at the micro-scale. The OP was also identifiable at the macro-scale from the femoral neck fracture and the thin, less-connected structure, as well as from the micro-scale from the indiscriminate distribution and large number of MCFs. An increase in sample size would confirm if this can be used as a non-clinical method in identification of pathological diseases in trabecular bone in the future.

Each level of the scale has provided additional information in relation to the quality of the bone and the structural features contributing to the pathological condition as demonstrated in Figure 10.2. The structural features and MCF distribution at macro-level, the bone quality, trabecular failure and compressive strength at micro-level, and the MCF surrounding the micro-crack and the osteocyte lacunae distribution at the nano-level, all contribute to the pathology of the femoral head. This project has demonstrated the importance of multi-scale imaging by finding features and quantitative measures at different scales that indicate the condition of the bone, and successfully relating them to the pathology in all the studies presented.



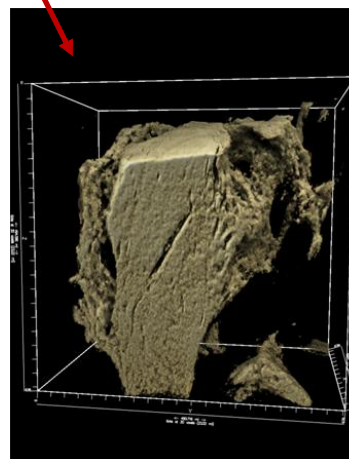
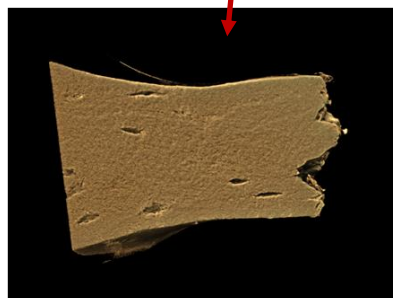
Macro-Scale

Whole femoral heads were imaged at 25-26 μ m voxel size. Subchondral cysts, subchondral bone thickening, osteophyte formations and bone quality were determined for OA femoral heads. Femoral neck fracture and bone quality were determined for the OP head. MCFs and their 3D distribution were determined for all femoral heads. Using the MCF distribution it was possible to distinguish between pathologies.



Micro-Scale

Cylindrical OA specimens were removed from load bearing regions and imaged at 15 μ m voxel size. Specimens were strained at 2% increments from 0-10%. Trabeculae were found to fail under buckling. Bone quality and compressive strength were determined for the cylinders.



Nano-Scale

A single trabecula and a MCF (extracted from an OA femoral head) were imaged using XuM at 200 and 775nm, respectively. The single trabecula was loaded to fracture and imaged to determine the structure. Osteocyte lacunae were identified and showed regions of high density way from the critical fracture. The morphology of MCF was determined. The MCF was identified as a porous bulky structure which had formed around a microcrack. The MCF and microcrack were present in the OA pathology.

Figure 10.2: Diagram showing the findings of the studies at different scales using XMT and XuM

TDI XMT has proved to be successful in providing a large amount of additional information on the bone quality, microdamage and mechanical variations within normal, OA and OP trabecular bone. This project has shown novel techniques for inspecting and determining microdamage in 3D, and in identifying structural features related to pathology.

Both XMT and XuM have provided a quantitative and qualitative insight into the structure of bone in different pathological states at a multiscale level. These findings may ultimately be used to focus clinical CT analyses and plain radiography analysis to specific trabecular regions, to further improve fracture prediction for specific fracture modalities and development stages of bone diseases.

10.3 Conclusions

Normal, OA and OP Bone Quality and Microarchitecture

- Whole head high resolution XMT imaging showed a difference in the bone quality and microarchitecture from one head to another and within.
- The highly loaded regions of the OA bone exhibited a significantly different bone quality to the normal head, occupying a much higher bone volume, exhibiting thick, plate-like, closely well connected trabecular structure.
- The OA femoral head exhibited more local variations in bone quality in comparison to the OP femoral head, showing that OA results in localised changes in bone microarchitecture whereas in OP the entire structure is compromised.
- Bone Mineral Concentration was similar at the micro-level for all the different femoral heads.

Microdamage and Microcallus Formations

- A distinct difference in the number of MCFs in the different pathological femoral heads was determined, with 17, 105 and 132, and 585 found in the normal, osteoarthritic and osteoporotic, respectively.
- The distribution showed isolated MCFs in normal heads, localised clusters in OA femoral head and an indiscriminately global distribution in the OP head.
- The type of pathology can be recognised using the number of microcallus formations found in the femoral heads.
- Microcallus formations were porous, nodular and bulky structures encapsulating trabeculae that had fractured, indicating that they could be used as a marker for damage.

Mechanical Failure of Trabecular Bone

- In OA trabecular bone, a high bone volume fraction, and thick plate-like trabeculae result in a higher compressive strength.
- At the micro-level using image analysis trabecular bone fails in shear.

Nano-scale Qualitative Fracture and Feature Evaluation

- At the single trabeculae level, fracture took place close to apoptotic cells where a low number of osteocyte lacunae are observed.

10.4 Future Work

Whole Femoral Heads

Further studies need to be carried out on the imaging of the whole femoral heads. The results in this project have shown the ability of the TDI XMT system to image large bone organs at high resolution. An increase in the number of specimens is essential in obtaining any conclusive trend to relate the prevalence of MCFs in pathological and non-pathological femoral heads. The current work carried out in this thesis demonstrated the capability in indentifying microdamage through MCFs with an additional understanding of the 3D distribution. Further work investigating the prevalence and distribution of other factors affecting or contributing to the pathology of bone should also be investigated. Studies investigating the subchondral bone cysts have been used to relate the onset of OA. Gaining an insight into the 3D relationship between cysts, eburnated areas on the surface of the femora head and the condition of the subchondral bone will deem beneficial in understanding the initiation process of OA.

Mechanical Study

In-vitro mechanical testing of cylindrical bone specimens in the XMT provided a huge insight into the failure mechanisms involved in compression of trabecular bone. This study requires a greater number of specimens, with a variation in the specimen size. This would ensure statistical stability in the results and also failure due to insufficient tissue could be eliminated. Furthermore, customising the XMT system to image in 'real time' would provide an extremely valuable understanding of the mechanical behaviour of bone in 3D.

FEA

Mechanical properties of a structure can also be determined using finite element analysis (FEA), which takes into account the geometric structure and material properties. Using XMT images to provide both three-dimensional geometric details and information about the material properties, a finite model can be generated. Though the use of FEA has been extensively examined, data used from XMT has either been of sectioned bone or very low resolution images of whole organs. The data obtained from TDI XMT will provide a whole new aspect on the geometric data available for FEA. Therefore future FEA studies on the mechanical loading of a whole femoral head using data obtained from TDI XMT imaging should be carried out.

Clinical Relevance

Three-dimensional imaging and quantification of bone mineral provide additional data about the quality and geometry of trabecular bone and microcallus formations. Quantitative imaging may be useful clinically for monitoring fracture-healing. It will not be possible to use XMT for clinical diagnosis due to the high dosage but in-vitro studies using XMT can provide additional information in interpreting conventional radiographs. Further correlative work should be carried out using data from XMT and comparing with radiographs to determine what, if any, additional information can be determined in aiding the understanding of bone diseases.

Part V References and Appendices

References

- AHMED, M. 2010. X-ray microtomography study of carious dentine and a comparison of its removal by three techniques. Ph. D. *Institute of Dentistry*. London, Queen Mary University of London.
- ASCENZI, A., BONUCCI, E., RIPAMONTI, A., ROVERI, N. 1978. X-ray-diffraction and electron-microscope study of osteons during calcification. *Calcified tissue Research*, 25, 133-143.
- AMERICAN SOCIETY FOR THE TESTING OF METALS. 2009. Annual book of ASTM standards. *Metal test methods and analytical procedures*. Philadelphia, ASTM.
- ARNOLD, J. S. 1980. Trabecular pattern and shapes in aging Osteoporosis. *Metabolic Bone Disease and Related Research*, 2, 297- 308.
- BACHUS, K. N., BLOEBAUM, R. D. 1992. Projection Effect Errors in Biomaterials and Bone Research. *Cells and Materials*, 2, 347-355.
- BANSE, X., DEVOGELAER, J. P., HOLMYARD, D., GRYNPAS, M. 2005. Vertebral cancellous bone turn-over: Microcallus and bridges in backscatter electron microscopy. *Micron*, 36, 710-714.
- BARON, R. 1999. Anatomy and ultrastructure of bone. In: MJ, F. (ed.) *Primer on the Metabolic Bone Diseases and Disorders of Mineral Metabolism*. 4th ed. Philadelphia: Lippincott Williams and Wilkins.
- BEAUPIED, H., DUPUIS, A., ARLETTAZ, A., BRUNET-IMBAULT, B., BONNET, N., JAFFRE, C., BENHAMOU, C. L., COURTEIX, D. 2006. The mode of bone conservation does not affect the architecture and the tensile properties of rat femurs. *Bio-Medical Materials and Engineering*, 16, 253-259.
- BEAUPRE, G. S., HAYES, W. C. 1985 Finite element analysis of a three-dimensional open-celled model for trabecular bone. *Journal of Biomechanical Engineering*, 107, 249 - 256.
- BEMBAY, A. K., BUSHBY, A. J., BOYDE, A., FERGUSON, V. L., OYEN, M. L. 2006. Hydration effects on the micro-mechanical properties of bone. *Journal of Materials Research*, 21, 1962-1968.

- BENHAMOU, C. L., LESPESSAILLES, E., JACQUET, G., HARBA, R., JENNANE, R., LOUSSOT, T., TOURLIERE, D., OHLEY, W. 1994. Fractal organization of trabecular bone images on calcaneus radiographs. *Journal of Bone and Mineral Research*, 9, 1909-1918.
- BENTOLILA, V., BOYCE, T. M., FYHRIE, D. P., DRUMB, R., SKERRY, T. M., SCHAFFLER, M. B. 1998. Intracortical remodeling in adult rat long bones after fatigue loading. *Bone*, 23, 275-281.
- BIRK, D., SILVER, F., TRELSTAD, R. 1991. Matrix assembly. In: HAY, E. D. (ed.) *In Cell Biology of Extracellular Matrix*. New York: Plenum.
- BLACKBURN, J., HODGSKINSON, R., CURREY, J. D., MASON, J. E. 1992. Mechanical Properties of Microcallus in Human Cancellous Bone. *Journal of Orthopaedic Research*, 10, 237 - 246.
- BLOEBAUM, R. D., BACHUS, K. N., BOYCE, T. M. 1990. Backscattered electron imaging: the role in calcified tissue and implant analysis. *Journal of Biomaterials Applied*, 5, 56 - 85.
- BOYDE, A. 1972. Scanning electron microscopic studies of bone. In: GH, B. (ed.) *The Biochemistry and Physiology of Bone*. 2nd ed. New York: Academic Press.
- BOYDE, A. 1973. Quantitative photogrammetric analysis and qualitative stereoscopic analysis of SEM images. *Journal of Microscopy*, 98, 452 - 471
- BOYDE, A. 1980. Electron microscopy of the mineralizing front. *Metabolic Bone Disease and Related Research*, 69 - 78.
- BOYDE, A. 1984. Methodology of calcified tissue specimen preparation for scanning electron microscopy. In Dickson, G. R. (ed.) *Methods of Calcified Tissue Preparation*. Amsterdam, Elsevier.
- BOYDE, A. 2003a. Improved digital SEM of cancellous bone: scanning direction of detection, through focus for in-focus and sample orientation. *Journal of Anatomy*, 202, 183-194.
- BOYDE, A. 2003b. The real response of bone to exercise. *Journal of Anatomy*, 203, 173-189.
- BOYDE, A., JONES, S. J. 1996. Scanning electron microscopy of bone: Instrument, specimen, and issues. *Microscopy Research and Technique*, 33, 92-120.

- BOYDE, A., JONES, S. J. 1998. Aspects of Anatomy and Development of Bone: the nm, μm and mm Hierarchy. *Advances in Organ Biology*, 3 - 44.
- BRITISH STANDARDS INSTITUTION, 2008. *BS 4443-17:2008. Methods of test for flexible cellular materials. Method 17. Determination of tear strength of flexible cellular material with an integral skin*. London: BSI.
- BROWN, T. D., FERGUSON, A. B. 1978. The development of a computational stress analysis of the femoral head. *Journal of Bone and Joint surgery*, 60A, 169-629
- BROWN, T. D., SHAW, D. T. 1983. In vitro contact stress distributions in the natural human hip. *Journal of Biomechanics*, 16, 373-384.
- BUCKLAND-WRIGHT, J. C., LYNCH, J. A., RYMER, J., FOGELMAN, I. 1994. Fractal signature analysis of macroradiographs measures trabecular organization in lumbar vertebrae of postmenopausal women. *Calcified Tissue International*, 54, 106-112.
- BULLOUGH, P. G. 1984. Osteoarthritis: pathogenesis and aetiology. *British Journal of Rheumatology*, 23, 166.
- BURATTINI, E. 1996. Synchrotron radiation. In: BURATTINI, E., BALERNA, A. (eds.) *Biomedical Applications of synchrotron radiation*. Bologna: The Italian Society of Physics.
- BURR, D. B., MARTIN, R. B., SCHAFFLER, M. B., RADIN, E. L. 1985. Bone remodeling in response to in vivo fatigue microdamage. *Journal of Biomechanics*, 18, 189-200.
- BURR, D. B., HOOSER, M. 1995. Alterations to the en bloc basic fuchsin staining protocol for the demonstration of microdamage produced in vivo. *Bone*, 17, 431-433.
- BURR, D. B., TURNER, C. H., NAICK, P., FORWOOD, M. R., AMBROSIUS, W., SAYEED HASAN, M., PIDAPARTI, R. 1998. Does microdamage accumulation affect the mechanical properties of bone? *Journal of Biomechanics*, 31, 337-345.
- BUSHBY, A. J., FERGUSON, V. L., BOYDE, A. (2004) Nanoindentation of bone: Comparison of specimens tested in liquid and embedded in polymethylmethacrylate. *Journal of Materials Research*, 19, 249-259.
- CALDWELL, C. B., WILLETT, K., CUNCINS, A. V., HEARN, T. C. 1995. Characterization of vertebral strength using digital radiographic analysis of bone-structure. *Medical Physics*, 22, 611-615.

- CALER, W. E., CARTER, D. R. 1989. Bone creep-fatigue damage accumulation. *Journal of Biomechanics*, 22, 625-635.
- CALIGIURI, P., GIGER, M. L., FAVUS, M. J., JIA, H., DOI, K., DIXON, L. B. 1993. Computerised radiographic analysis of osteoporosis – preliminary evaluation. *Radiology*, 186, 471-474.
- CAMERON, J. R., SKOFRONICK, J. G. 1978. *Medical Physics*, New York, John Wiley and Sons.
- CARTER, D. R., HAYES, W. C. 1977. The compressive behaviour of bone as a two-phase porous structure. *Journal of Bone and Joint Surgery*, 59A, 954 - 962
- CHAPPARD, C., BRUNET-IMBAULT, B., LEMINEUR, G., GIRAUDEAU, B., BASILLAIS, A., HARBA, R., BENHAMOU, C. L. 2005a. Anisotropy changes in post-menopausal osteoporosis: characterization by a new index applied to trabecular bone radiographic images. *Osteoporosis International*, 16, 1193-1202.
- CHAPPARD, D., GUGGENBUHL, P., LEGRAND, E., BASLE, M. F., AUDRAN, M. 2005b. Texture analysis of X-ray radiographs is correlated with bone histomorphometry. *Journal of Bone and Mineral Metabolism*, 23, 24-29.
- CHAPPARD, C., PEYRIN, F., BONNASSIE, A., LEMINEUR, G., BRUNET-IMBAULT, B., LESPESSAILLES, E., BENHAMOU, C. L. 2006. Subchondral bone micro-architectural alterations in osteoarthritis: a synchrotron micro-computed tomography study. *Osteoarthritis and Cartilage*, 14, 215-223.
- CHEN, H., SHOUMURA, S., EMURA, S., BUNAI, Y. 2008. Regional variations of vertebral trabecular bone microstructure with age and gender. *Osteoporosis International*, 19, 1473-1483.
- CHENG, X. G., NICHOLSON, P. H. F., LOWET, G., BOONEN, S., SUN, Y., RÜEGSEGGER, P., MÜLLER, R., DEQUEKER, J. 1997. Prevalence of Trabecular Microcallus Formation in the Vertebral Body and the Femoral Neck. *Calcified Tissue International*, 60, 479-484.
- CIARELLI, M. J., GOLDSTEIN, S. A., KUHN, J. L., CODY, D. D., BROWN, M. B. 1991. Evaluation of orthogonal mechanical-properties and density of human trabecular bone from the major metaphyseal regions with materials testing and computed-tomography. *Journal of Orthopaedic Research*, 9, 674-682.

- CICUTTINI, F. M., BAKER, J., HART, D. J., SPECTOR, T. D. 1996. Association of pain with radiological changes in different compartments and views of the knee joint. *Osteoarthritis and Cartilage*, 4, 143-147.
- COLLINS, D. H. 1949. Osteoarthritis. *The pathology of articular and spinal diseases*. London: Edward Arnold and Co.
- CORTET, B., MARCHANDISE, X. 2001. Bone microarchitecture and mechanical resistance. *Joint Bone Spine*, 68, 297-305.
- COWIN, S. C. 1989. *Bone Mechanics*, Boca Raton, CRC Press.
- COWIN, S. C. 2001. *Bone Mechanics Handbook*, Florida, CRC Press Boca Raton.
- COXON, J. P., OADES, G. M., COLSTON, K. W., KIRBY, R. S. 2004. Advances in the use of bisphosphonates in the prostate cancer setting. *Prostate Cancer Prostatic Dis*, 7, 99-104.
- CREMA, M. D., ROEMER, F. W., MARRA, M. D., NIU, J., LYNCH, J. A., FELSON, D. T., GUERMAZI, A. 2010. Contrast-enhanced MRI of subchondral cysts in patients with or at risk for knee osteoarthritis: The MOST study. *European Journal of Radiology*, 75, e92-e96.
- CULLINANE, D. A., EINHORN, T. A. 2002. Biomechanics of bone. In BILEZIKIAN, J. P., RAISZ, L. G., RODAN, G. A. (Eds.) *Principles of bone biology*. San Diego, Academic Press.
- CURREY, J. D. 1984. *The mechanical adaptations of bones*, Princeton, University Press.
- CURREY, J. D. 2002. *Bones: Structure and Mechanics*, New Jersey, Princeton University Press.
- CURREY, J. D. 2003. The many adaptations of bone. *Journal of Biomechanics*, 36, 1487-1495.
- DANIELSSON, L. G. 1964. Incidence and prognosis of coxarthrosis. *Acta Orthopaedica Scandanavia*, Suppl. 66.
- DAVIS, G. R. 1994. The effect of linear interpolation of the filtered projections on Image noise in X-ray computed tomography. *Journal of X-ray Science and Technology*, 4, 191-199.
- DAVIS, G. R., WONG, F. S. L. 1996. X-ray microtomography of bones and teeth. *Physiological Measurements*, 17, 121 - 146.

- DAVIS, G. R., ELLIOTT, J. C. 2003. High definition X-ray microtomography using a conventional impact X-ray source. *Journal of Physics IV France*, 104, 131 - 134.
- DAVIS, G.R. , JAIN, N., ELLIOTT, J. 2008. A modelling approach to beam hardening correction. *In: STUART, R. S., ed., 2008. SPIE, 70781E.*
- DAVIS, G. R., EVERSLED, A., ELLIOTT, J., MILLS, D. 2010. Quantitative x-ray microtomography with a conventional source. *In: STUART, R. S., ed. SPIE, 78040I.*
- DELIGIANNI, D. D., MISSIRLIS, Y. F., TANNER, K. E., BONFIELD, W. 1991. Mechanical behaviour of trabecular bone of the human femoral head in females. *Journal of Materials Science: Materials in Medicine*, 2, 168-175.
- DELMAS, P., TRACY, R., RIGGS, B., MANN, K. 1984. Identification of the noncollagenous proteins of bovine bone by two-dimensional gel electrophoresis. *Calcified Tissue International*, 36, 308-316.
- DIAB, T., CONDON, K. W., BURR, D. B., VASHISHTH, D. 2006. Age-related change in the damage morphology of human cortical bone and its role in bone fragility. *Bone*, 38, 427-431.
- DIAB, T., VASHISHTH, D. 2005. Effects of damage morphology on cortical bone fragility. *Bone*, 37, 96-102.
- DIAB, T., VASHISHTH, D. 2007. Morphology, localization and accumulation of in vivo microdamage in human cortical bone. *Bone*, 40, 612-618.
- DIEPPE, P., MAIR, F., ROGERS, J., LIM, K. 1998. Patterns of joint involvement in osteoarthritis: The evolutionary hypothesis. *Arthritis and Rheumatism*, 41, 329
- DOUBE, M., KLOSOWSKI, M. M., ARGANDA-CARRERAS, I., CORDELIÈRES, F. P., DOUGHERTY, R. P., JACKSON, J. S., SCHMID, B., HUTCHINSON, J. R., SHEFELBINE, S. J. 2010. BoneJ: Free and extensible bone image analysis in ImageJ. *Bone*, In Press, Corrected Proof.
- DOUGHERTY, R. P., KUNZELMANN, K.-H. 2007. Computing local thickness of 3D structures with ImageJ. *In: Microscopy, Microanalysis, 2007 Ft. Lauderdale, Florida. 5 - 9.*

- DOWKER, S. E., DAVIS, G. R., ELLIOTT, J. C. 1997. X-ray microtomography: nondestructive three-dimensional imaging for in vitro endodontic studies. *Surg Oral Med Oral Pathol Oral Radiol Endod*, 83, 510 - 516.
- EINHORN, T. A. 1996. The bone organ system: form and function. In: MARCUS, R., FELDMAN, D., KELSEY, J. (eds.) *Osteoporosis*. California: Academic Press.
- ELLIOTT, J. C., DOVER, S. D. (1982) X-ray microtomography. *Journal of Microscopy*, 126, 211 - 213.
- EVANS, F. G. 1973. Preservation Effects. In: THOMAS, C. C. (ed.) *Mechanical Properties of Bone*. Illinois USA: Springfield.
- FAULKNER, K. G., GLUER, C. C., MAJUMDAR, S., LANG, P., ENGELKE, K., GENANT, H. K. 1991. Noninvasive measurements of bone mass, structure, and strength – current methods and experimental techniques. *American Journal of Roentgenology*, 157, 1229-1237.
- FAULKNER, K. G., POCOCK, N. 2001. Future methods in the assessment of bone mass and structure. *Best Practice, Research Clinical Rheumatology*, 15, 359-383.
- FAZZALARI, N. L. 1993. Trabecular microfracture. *Calcified Tissue International*, 53, S143-S147.
- FAZZALARI, N. L., FORWOOD, M. R., MANTHEY, B. A., SMITH, K., KOLESIK, P. 1998a. Three-dimensional confocal images of microdamage in cancellous bone. *Bone*, 23, 373-378.
- FAZZALARI, N. L., FORWOOD, M. R., SMITH, K., MANTHEY, B. A., HERREEN, P. 1998b. Assessment of Cancellous Bone Quality in Severe Osteoarthritis: Bone Mineral Density, Mechanics, and Microdamage. *Bone*, 22, 381-388.
- FELDKAMP, L. A., DAVIS, L. C., KRESS, J. W. 1984. Practical Cone Beam Algorithm. *Journal of the Optical Society of America A-Optics Image Science and Vision*, 1, 612-619.
- FERGUSON, A. B. 1971. The pathology of degenerative arthritis of the hip and the use of osteotomy in its treatment. *Clinical Orthopaedics*, 77, 84 - 97.
- FERGUSON, V. L., BUSHBY, A. J., BOYDE, A. 2003. Nanomechanical properties and mineral concentration in articular calcified cartilage and subchondral bone. *Journal of Anatomy*, 203, 191-202.

- FORD, C. M., KEAVENY, T. M. 1996. The dependence of shear failure properties of trabecular bone on apparent density and trabecular orientation. *Journal of Biomechanics*, 29, 1309-1317.
- FRASCA, P., HARPER, R. A., KATZ, J. L. 1977. Collagen fiber orientations in human secondary osteons. *Acta Anatomica*, 98, 1-13.
- FROST, H. M. (1960) Presence of microscopic cracks *in vivo* bone. *Henry Ford Hospital Medical Bulletin*, 8, 25-35.
- FROST, H. M. 1995. Introduction to a New Skeletal Physiology. *Bone and Bones*. Pueblo: Parajo Group Inc.
- GALANTE, J., ROSTOKER, W., RAY, R. D. 1970. Physical properties of trabecular bone. *Calcified tissue Research*, 5, 236 - 246.
- GAO, D., WILKINS, S. W., PARRY, D. J., GUREYEV, T. E., MILLER, P. R., HANSEN, E. 2006. X-ray ultramicroscopy using integrated sample cells. *Opt. Express*, 14, 7889-7894.
- GEORGE, W. T., VASHISHTH, D. 2005. Damage mechanisms and failure modes of cortical bone under components of physiological loading. *Journal of Orthopaedic Research*, 23, 1047-1053.
- GERAETS, W. G. M., VAN DER STELT, P. F., NETELENBOS, C. J., ELDERS, P. J. M. (1990) A new method for automatic recognition of the radiographic trabecular pattern. *Journal of Bone and Mineral Research*, 5, 227-233.
- GERAETS, W. G. M., VAN DER STELT, P. F. 1991. Analysis of the radiographic trabecular pattern. *Pattern Recognition Letters*, 12, 575-581.
- GERAETS, W. G. M., VAN DER STELT, P. F., ELDERS, P. J. M. 1993. The radiographic trabecular bone pattern during. *Bone*, 14, 859-864.
- GERAETS, W. G. M., VAN DER STELT, P. F., LIPS, P., ELDERS, P. J. M., VAN GINKEL, F. C., BURGER, E. H. 1997. Orientation of the trabecular pattern of the distal radius around the menopause. *Journal of Biomechanics*, 30, 363-370.
- GERAETS, W. G. M., VAN DER STELT, P. F., LIPS, P., VAN GINKEL, F. C. 1998. The radiographic trabecular pattern of hips in patients with hip fractures and in elderly control subjects. *Bone*, 22, 165-173.
- GIBSON, L. J. 1985. The mechanical behaviour of cancellous bone. *Journal of Biomechanics*, 18, 317-328.

- GIBSON, L. J., ASHBY, M. F. 1997. *Cellular Solids: Structure and Properties*, Cambridge University Press, UK.
- GIBSON, L. J., ASHBY, M. F. 1999. *Cellular Solids - Structure and Properties*, Cambridge, Cambridge University Press.
- GIOVANI, A. M. M., CROCI, A. T., OLIVEIRA, C. R., FILIPPI, R. Z., SANTOS, L. A. U., MARAGANI, G. G., ALBHY, T. M. 2006. Comparative Study of Cryopreserved Bone Tissue and Tissue Preserved in a 98% Glycerol Solution. *Clinics*, 61, 565 - 570.
- GOLDSTEIN, S. A. 1987. The mechanical properties of trabecular bone: Dependence on anatomic location and function. *Journal of Biomechanics*, 20, 1055-1061.
- GOLDSTEIN, S. A., GOULET, R., MCCUBBREY, D., GRYNPAS, MONIERFAUGERE, BIEWENER. 1993. Measurement and significance of 3-dimensional architecture to the mechanical integrity of trabecular bone. *Calcified Tissue International*, 53, S127-S133.
- GREGG, E. W., KRISKA, A. M., SALAMONE, L. M., ROBERTS, M. M., ANDERSON, S. J., FERRELL, R. E., KULLER, L. H., CAULEY, J. A. 1997. The epidemiology of quantitative ultrasound: A review of the relationships with bone mass, osteoporosis and fracture risk. *Osteoporosis International*, 7, 89-99.
- GUPTA, H. S., ZIOUPOS, P. 2008. Fracture of bone tissue: The 'hows' and the 'whys'. *Medical Engineering, Physics*, 30, 1209-1226.
- GUYTON, A. C., HALL, J. E. 2001. *Textbook of Medical Physiology*, Philadelphia, Pennsylvania, W.B.Saunders Company.
- HAHN, M., VOGEL, M., AMLING, M., RITZEL, H., DELLING, G. 1995. Microcallus formations of the cancellous bone: a quantitative analysis of human spine. *Journal of Bone Mineral Research*, 10.
- HANS, D., UUML, RR, HEINER, M., CHRISTOPH, P., MARCUS, S., MARKUS, M., VOLKMAR, J. 2004. The cause of subchondral bone cysts in osteoarthritis. *Acta Orthopaedica Scandinavica*, 75, 554-558.
- HART, D. J., SPECTOR, T. D. 1995. The classification and assessment of osteoarthritis. *Baillière's Clinical Rheumatology*, 9, 407-432.
- HART, D. J., SPECTOR, T. D. 2003. Kellgren, Lawrence grade 1 osteophytes in the knee--doubtful or definite? *Osteoarthritis and Cartilage*, 11, 149-150.

- HASSENKAM, T., FANTNER, G. E., CUTRONI, J. A., WEAVER, J. C., MORSE, D. E., HANSMA, P. K. 2004. High-resolution AFM imaging of intact and fractured trabecular bone. *Bone*, 35, 4-10.
- HAYES, W. C., CARTER, D. R. 1976. Postyield Behaviour of Subchondral Trabecular Bone. *Journal of Biomedical Research Symposium*, 7, 537 - 544.
- HEO, S. H., IHSAN, A., CHO, S. O. 2007. Transmission-type microfocus x-ray tube using carbon nanotube field emitters. *Applied Physics Letters*, 90, 183109.
- HERNBORG, J., NILSSON, B. E. 1973. The relationship between osteophytes in the knee joint, osteoarthritis and ageing. *Acta Orthopaedica Scandinavica*, 44, 69 - 74.
- HILDEBRAND, T., RUEGSEGGER, P. 1997a. Quantification of bone microarchitecture with the structure model index. *Comput Methods Biomech Biomed Engin*, 1, 15 - 23.
- HILDEBRAND, T., RUEGSEGGER, P. 1997b. A new method for the model-independent assessment of thickness in 3D images. *Journal of Microscopy* 185, 67 - 75.
- HOBDELL, M. H., BOYDE, A. 1969. Microradiography and scanning electron microscopy of bone sections. *Zeitschrift Fur Zellforschung Und Mikroskopische Anatomie*, 94, 487.
- HOSOKAWA, A. 2010. Effect of porosity distribution in the propagation direction on ultrasound waves through cancellous bone. *Ultrasonics, Ferroelectrics and Frequency Control, IEEE Transactions on*, 57, 1320-1328.
- HOWARD, L. E., GUNDRUM, B., FAHEY, S., BOOTH, C. 2010. Nano-scale computed tomography inside a scanning electron microscope, using the gatan x-ray ultramicroscope: Getting the best out of your system *In Submission*.
- HOWELL, P. G. T., BOYDE, A. 2003. Volumes from which calcium and phosphorus X-rays arise in electron probe emission microanalysis of bone: Monte Carlo simulation. *Calcified Tissue International*, 72, 745-749.
- JACOBSON, J. A., GIRISH, G., JIANG, Y., SABB, B. J. 2008. Radiographic Evaluation of Arthritis: Degenerative Joint Disease and Variations. *Radiology*, 248, 737-747.

- JEE, W. S. S. 2001. Integrated Bone Tissue Physiology: Anatomy and Physiology. In: COWIN, S. C. (ed.) *Bone Mechanics Handbook*. New York: CRC Press.
- JENSEN, K. S., MOSEKILDE, L., MOSEKILDE, L. 1990. A model of vertebral Trabecular Bone Architecture and its Mechanical Properties. *Bone*, 11, 417 - 423.
- JONSON, R. 1993. Mass attenuation coefficients, quantities and units for use in bone mineral determinations. *Osteoporosis International*, 3, 103 - 106.
- KAK, A.C., SLANEY, M. 1998. Principles of Computerized Tomographic Imaging, IEEE Press, New York
- KAK, A.C., SLANEY, M. 2001. Principles of Computerized Tomographic Imaging, Society of Industrial and Applied Mathematics, 2001
- KALENDAR, W. A. 2000. *Computed Tomography: Fundamentals, System Technology, Image Quality and Applications*, Weinheim, Germany, Publics MCD Verlag.
- KANIS, J. A. 2002. Diagnosis of osteoporosis and assessment of fracture risk. *Lancet*, 359, 1929-1936.
- KANIS, J. A., JOHNELL, O., ODEN, A., DAWSON, A., DE LAET, C., JONSSON, B. 2001. Ten Year Probabilities of Osteoporotic Fractures According to BMD and Diagnostic Thresholds. *Osteoporosis International*, 12, 989-995.
- KAUFMAN, J. J., SIFFERT, R. S. 2001. Noninvasive Measurement of Bone Integrity. In: COWIN, S. C. (ed.) *Bone Mechanics Handbook*. 2nd ed.: CRC Press.
- KEAVENY, T. M., WACHTEL, E. F., GUO, X. E., HAYES, W. C. 1994. Mechanical behavior of damaged trabecular bone. *Journal of Biomechanics*, 27, 1309-1318.
- KELLGREN, J. H. 1983. Pain in Osteoarthritis. *Rheumatology*, 10, 108 - 109.
- KELLGREN, J. H., LAWERENCE, J. S. 1957. Radiological Assesment of Osteo-Arthrosis. *Annals of the Rheumatic Diseases*, 16, 494-502.
- KIM, H., AL-HASSANI, S. T. S. 2001. Plastic Collapse of Cellular Structures Comprised of Doubly Tapered Struts. *International Journal of Mechanical Sciences*, 43, 2453 - 2478

- KURUTZ, M., FORNET, B., VARGA, P. 2005. Age- and sex-related compressive strength and morphometry of lumbar vertebrae in osteoporosis. *In: The 3rd European Medical and biological Engineering Conference, 2005 Prague.*
- LANDELLS, J. W. 1953. The bone cysts of osteoarthritis. *Journal of Bone and Joint Surgery*, 35B, 643 - 649.
- LANDIS, W. J. 1995. The strength of a calcified tissue depends in part on the molecular structure and organization of its constituent mineral crystals in their organic matrix. *Bone*, 16, 533-544.
- LI, B., MARSHALL, D., ROE, M., ASPDEN, R. M. 1999. The electron microscope appearance of the subchondral bone plate in the human femoral head in osteoarthritis and osteoporosis. *Journal of Anatomy*, 195, 101-110.
- LIAN, J. B., STEIN, G. S., CANALIS, E. 1999. Bone formation: osteoblast lineage cells, growth factors, matrix proteins, and the mineralization process. *In: FAVUS, M. (ed.) Primer on the Metabolic Bone Diseases of Mineral Metabolism.* 4th ed. Philadelphia: Lippincott Williams, Wilkins.
- LIMAYE, A. 2006. Drishti - Volume Exploration and Presentation Tool. *VIS.* Baltimore.
- LINDE, F., HVID, I., MADSEN, F. 1992. The effect of specimen geometry on the mechanical behaviour of trabecular bone specimens. *Journal of Biomechanics*, 25, 359-368.
- LORENSEN, W. E. C., CLINE, H. E. 1987. Marching cubes: A high resolution 3D surface construction algorithm. *Proceedings of the 14th annual conference on Computer graphics and interactive techniques*, 163 -169.
- LOVERIDGE, N., POWER, J., REEVE, J., BOYDE, A. 2004. Bone mineralization density and femoral neck fragility. *Bone*, 35, 929-941.
- LUO, G., KINNEY, J. H., KAUFMAN, J. J., HAUPT, D., CHIABRERA, A., SIFFERT, R. S. 1999. Relationship between plain radiographic patterns and three-dimensional trabecular architecture in the human calcaneus. *Osteoporosis International*, 9, 339-345.
- MARCUS, R. 1994. Introduction: organizational and functional aspects of skeletal health. *In: KANIS, J. A. (ed.) Osteoporosis.* Oxford, England: Blackwell Science, Ltd.

- MARIEB, E. N. 1998. *Human Anatomy and Physiology*, Benjamin Cummings.
- MARTIN, R. B. 2003. Fatigue Microdamage as an Essential Element of Bone Mechanics and Biology. *Calcified Tissue International*, 73, 101-107.
- MAYO, S., DAVIS, T., GUREYEV, T., MILLER, P., PAGANIN, D., POGANY, A., STEVENSON, A., WILKINS, S. 2003. X-ray phase-contrast microscopy and microtomography. *Opt. Express*, 11, 2289-2302.
- MCCALDEN, R. W., MCGEOUGH, J. A., COURT-BROWN, C. M. 1997. Age-related changes in the compressive strength of cancellous bone. The relative importance of changes in density and trabecular architecture. *Journal of Bone and Joint Surgery America*, 79, 421-427.
- MCERLAIN, D. D., APPLETON, C. T. G., LITCHFIELD, R. B., PITELKA, V., HENRY, J. L., BERNIER, S. M., BEIER, F., HOLDSWORTH, D. W. 2008. Study of subchondral bone adaptations in a rodent surgical model of OA using in vivo micro-computed tomography. *Osteoarthritis and Cartilage*, 16, 458-469.
- MELLISH, R. W. E., FERGUSONPELL, M. W., COCHRAN, G. V. B., LINDSAY, R., DEMPSTER, D. W. 1991. A new manual method for assessing 2-dimensional cancellous bone-structure-comparison between iliac crest and lumbar vertebra. *Journal of Bone and Mineral Research*, 6, 689-696.
- MILGRAM, J. W. 1983. Morphological alterations of the subchondral bone in advanced degenerative arthritis. *Clinical Orthopaedics*, 173, 293 - 312.
- MORI, S., HARRUFF, R., AMBROSIUS, W., BURR, D. B. 1997. Trabecular bone volume and microdamage accumulation in the femoral heads of women with and without femoral neck fractures. *Bone*, 21, 521-526.
- MOSEKILDE, L. 1986. Normal vertebral body size and compressive strength - relations to age and to vertebral and iliac trabecular bone compressive strength. *Bone*, 7, 207-212.
- MOSEKILDE, L. 1988. Age-related-changes in vertebral trabecular bone architecture - assessed by a new method. *Bone*, 9, 247-250.
- MOSEKILDE, L. 1989. Sex differences in age-related loss of vertebral trabecular bone mass and structure--biomechanical consequences. *Bone*, 10, 425-432.

- MOSEKILDE, L. 1990. Consequences of the remodelling process for vertebral trabecular bone structure: a scanning electron microscopy study (uncoupling of unloaded structures). *Bone and Mineral*, 10, 13-35.
- MOSEKILDE, L. 1998. The effect of modelling and remodelling on human vertebral body architecture. *Technol Health Care*, 6, 287-97.
- MOSEKILDE, L. 2000. Age-related changes in bone mass, structure, and strength - effects of loading. *Zeitschrift für Rheumatologie*, 59, 11-19.
- MOSEKILDE, L., MOSEKILDE, L., DANIELSEN, C. C. 1987. Biomechanical Competence of Vertebral Trabecular Bone in Relation to Ash Density and Age in Normal Individuals. *Bone*, 8, 79 - 85
- MOSEKILDE, L., VIIDIK, A., MOSEKILDE, L. E. 1985. Correlation between the compressive strength of iliac and vertebral trabecular bone in normal individuals. *Bone*, 6, 291-295.
- MÜLLER, R., RUEGSEGGER, P. 1997. Micro-Tomographic Imaging for the Nondestructive Evaluation of Trabecular Bone Architecture. In: LOWET, G., RUEGSEGGER, P., WEINANS, H., MEUNIER, A. (eds.) *Bone Research in Biomechanics*. Amsterdam: IOS Press.
- MÜLLER, R., VAN CAMPENHOUT, H., VAN DAMME, B., VAN DER PERRE, G., DEQUEKER, J., HILDEBRAND, T., RUEGSEGGER, P. 1998. Morphometric analysis of human bone biopsies: A quantitative structural comparison of histological sections and micro-computed tomography. *Bone*, 23, 59-66.
- NÄGELE, E., KUHN, V., VOGT, H., LINK, T. M., MÜLLER, R., LOCHMULLER, E. M., ECKSTEIN, F. 2004. Technical considerations for microstructural analysis of human trabecular bone from specimens excised from various skeletal sites. *Calcified Tissue International*, 75, 15-22.
- NAZARIAN, A., STAUBER, M., ZURAKOWSKI, D., SNYDER, B. D., MÜLLER, R. 2006. The interaction of microstructure and volume fraction in predicting failure in cancellous bone. *Bone*, 39, 1196-1202.
- NAZARIAN, A., MÜLLER, J., ZURAKOWSKI, D., MÜLLER, R., SNYDER, B. D. 2007. Densitometric, morphometric and mechanical distributions in the human proximal femur. *Journal of Biomechanics*, 40, 2573-2579.
- NAZARIAN, A., VON STECHOW, D., ZURAKOWSKI, D., MÜLLER, R., SNYDER, B. D. 2008. Bone Volume Fraction Explains the Variation in

Strength and Stiffness of Cancellous Bone Affected by Metastatic Cancer and Osteoporosis. *Calcified Tissue International*, 83, 368-379.

NORMAN, T. L., WANG, Z. (1997) Microdamage of human cortical bone: Incidence and morphology in long bones. *Bone*, 20, 375-379.

ODGAARD, A. 1997. Three-dimensional methods for quantification of cancellous bone architecture. *Bone*, 20, 315 - 328.

ODGAARD, A. 2001. Quantification of cancellous bone architecture. In: COWIN, S. C. (ed.) *Bone Biomechanics Handbook*. Second Edition ed.: CRC Press.

ODGAARD, A., GUNDERSEN, H. J. G. 1993. Quantification of connectivity in cancellous bone, with special emphasis on 3-D reconstructions. *Bone*, 14, 173-182.

OGSTON, A. 1878. The growth and maintenance of the articular ends of adult bones. *Journal of Anatomy and Physiology*, 12, 503 - 517.

ONDROUCH, A. S. 1963. Cyst formation in osteoarthritis. *Journal of Bone and Joint Surgery*, 45B, 755 - 760.

PARFITT, A. M., MATHEWS, C. H. E., VILLANUEVA, A. R., KLEEREKOPER, M., FRAME, B., RAO, D. S. 1983. Relationships between surface, volume and thickness of iliac trabecular bone in aging and in osteoporosis – implications for the microanatomic and cellular mechanisms of bone loss. *Journal of Clinical Investigation*, 72, 1396-1409.

PARFITT, A. M., DREZNER, M. K., GLORIEUX, F. H., KANIS, J. A., MALLUCHE, J. A., MEUNIER, P. J., OTT, S. M., RECKER, R. R. 1987. Bone histomorphometry: standardization and nomenclature, symbols and units. Report of the ASBMR Histomorphometry Nomenclature Committee. *J Bone Miner Res*, 2, 595 - 610.

PERILLI, E., BARUFFALDI, F., VISENTIN, M., BORDINI, B., TRAINA, F., CAPELLO, A., VICECONTI, M. 2007a. MicroCT examination of human bone specimens: effects of polymethylmethacrylate embedding on structural parameters. *Journal of Microscopy*, 225, 192-200.

PERILLI, E., BALEANI, M., ÖHMAN, C., BARUFFALDI, F., VICECONTI, M. (2007b) Structural parameters and mechanical strength of cancellous bone in the femoral head in osteoarthritis do not depend on age. *Bone*, 41, 760-768.

- PETERLIK, H., ROSCHGER, P., KLAUSHOFER, K., FRATZL, P. 2005. From brittle to ductile fracture of bone. *Nature Materials*, 5, 52-55.
- PEYRIN, F., SALOME, M., NUZZO, S., CLOETENS, P., LAVAL-JEANTET, A. M., BARUCHEL, J. 2000. Perspectives in three-dimensional analysis of bone samples using synchrotron radiation microtomography. *Cellular and Molecular Biology*, 46, 1089-1102.
- PODGORSKAK, E. B. 2005. *Radiation Physics for medical physicist*, Tennessee, USA, Springer.
- POLKOWSKI, G., CLOHISY, J. C. 2010. Hip Biomechanics. *Sports Medicine and Arthroscopy Review*, 18, 56-62.
- POTHUAUD, L., VAN-RIETBERGEN, B., MOSEKILDE, L., BEUF, O., BENHAMOU, C. L., MAJUMDAR, S. 2002. Combination of topological parameters and bone volume fraction predicts the mechanical properties of trabecular bone *Journal of Biomechanics*, 35, 1091-1099.
- POUDERS, C., DE MAESENEER, M., VAN ROY, P., GIELEN, J., GOOSSENS, A., SHAHABPOUR, M. 2008. Prevalence and MRI-anatomic correlation of bone cysts in osteoarthritic knees. *American Journal of Roentgenology*, 190, 17-21.
- PUGH, J. W., ROSE, R. M., RADIN, E. L. 1973. A structural model for the mechanical behavior of trabecular bone. *Journal of Biomechanics*, 6, 657-670.
- REID, S. A., BOYDE, A. 1987. Changes in the mineral density distribution in human –bone with age – Image anlysis using backscattered electrons in the SEM . *Journal of Bone and Mineral Research*, 2, 13-22.
- REVELL, P. A. 1998. Bone Structure. In: HUGHES, S., MCCARTHY, I. (eds.) *Sciences Basic to Orthopaedics*. London: Saunders Co. Ltd.
- RHANEY, K., LAMB, D. W. 1955. The cysts of osteoarthritis of the hip. *Journal of Bone and Joint Surgery*, 37B, 663 - 675.
- ROBERTS, J. C. 1993. An overview of rendering from volume data - including surface and volume rendering. *Technical Report*. Canterbury, University of Kent.
- ROBLING, A. G., CASTILLO, A. B., TURNER, C. H. 2006. Biomechanical and Molecular Regulation of Bone Remodeling. *Annual Review of Biomedical Engineering*, 8, 455-498.

- ROCKOFF, S. D. 1967a. Quantitative microdensitometric x-ray analysis of vertebral trabecular bone. A preliminary report. *Radiology*, 88, 794-6.
- ROCKOFF, S. D. 1967b. Radiographic trabecular quantitation of human lumbar vertebrae in situ. I. Theory and method for study of osteoporosis. *Invest Radiol*, 2, 272-89.
- ROCKOFF, S. D., SCANDRET.J, ZACHER, R. 1971. Quantitation of relevant image information – automated radiographic bone trabecular characterization. *Radiology*, 101, 435.
- RUEGSEGGER, P., KOLLER, B., MÜLLER, R. 1996. A microtomographic system for the nondestructive evaluation of bone architecture. *Calcified Tissue International*, 58, 24-29.
- RUSS, J. C., DEHOFF, R. T. 2000. *Practical Stereology*, New York, Plenum Publishers.
- SAITO, T., TORIWAKI, J. 1994. New algorithms for euclidian distance transformation on an n-dimensional digitized picture with applications. *Pattern Recognition*, 27, 1551 - 1565.
- SALMON, P. L., SASOV, A. Y. 2007. *Application of nano-CT and high-resolution micro-CT to study bone quality and ultrastructure, scaffold biomaterials and vascular networks*, Berlin, Springer-Verlag Berlin.
- SCHAFFLER, M. B., CHOI, K., MILGROM, C. 1995. Aging and matrix microdamage accumulation in human compact bone. *Bone*, 17, 521-525.
- SCHENK, R. K., OLAH, A. J., HERRMANN, W. 1984. Preparation of calcified tissue for light microscopy. In: DICKSON, G. R. (ed.) *Methods of Calcified Tissue Preparation*. Amsterdam: Elsevier.
- SCHIPHOF, D., BOERS, M., BIERMA-ZEINSTR, S. M. A. 2008. Differences in descriptions of Kellgren and Lawrence grades of knee osteoarthritis. *Annals of the Rheumatic Diseases*, 67:, 1034-1036.
- SEDLIN, E. D. 1965. A Rheological Mode for Cortical Bone. *Acta Orthopaedica Scandinavica Supplement*, 83, 20 - 44.
- SEIBERT, J. A. 2004. X-Ray Imaging Physics for Nuclear Medicine Technologists. Part 1: Basic Principles of X-Ray Production. *J Nucl Med Technol*, 32, 139-147.
- SENGUPTA, M., ZHANG, Y. Q., NIU, J. B., GUERMAZI, A., GRIGORIAN, M., GALE, D., FELSON, D. T., HUNTER, D. J. 2006. High signal in

knee osteophytes is not associated with knee pain. *Osteoarthritis and Cartilage*, 14, 413-417.

SHARP, D. J. 1988. The subcondral bone of the normal and osteoarthritic head. Ph. D. *Department of Materials*. London, Queen Mary University of London.

SHARP, D. J., TANNER, K. E., BONFIELD, W. 1990. Measurement of the density of trabecular bone. *Journal of Biomechanics*, 23, 853-857.

SHEFELBINE, S. J., SIMON, U., CLAES, L., GOLD, A., GABET, Y., BAB, I., MÜLLER, R., AUGAT, P. 2005. Prediction of fracture callus mechanical properties using micro-CT images and voxel-based finite element analysis. *Bone*, 36, 480-488.

SHIER, D., BUTLER, D., LEWIS, R. 1996. *Hole's Human Anatomy, Physiology*, Dubuque, Iowa, Wm C Brown Publishers.

SINGH, M., NAGRATH, A. R., MAINI, P. S. 1970. Changes in trabecular bone pattern of upper end femur as an index of osteoporosis. *Journal of Bone and Joint Surgery-American Volume*, A 52, 457.

SOKOLOFF, L. 1969. *The biology of Degenerative Joint Disease*, Chicago and London, University of Chicago Press.

SPRAWLS, P. 1995. *Physical Principles of Medical Imaging*, Madison, Wisconsin, Aspen Publishers.

STAUBER, M., MÜLLER, R. 2006. Age-related changes in trabecular bone microstructures: Global and local morphometry. *Osteoporosis International*, 17, 616-626.

STAUBER, M., RAPILLARD, L., VAN LENTHE, G. H., ZYSSET, P., MÜLLER, R. 2006. Importance of individual rods and plates in the assessment of bone quality and their contribution to bone stiffness. *Journal of Bone and Mineral Research*, 21, 586-595.

STONE, J. L., BEAUPRE, G. S., HAYES, W. C. 1983. Multiaxial strength characteristics of trabecular bone. *Journal of Biomechanics*, 16, 743-747.

TANCK, E., BAKKER, A. D., KREGTING, S., CORNELISSEN, B., KLEIN-NULEND, J., VAN RIETBERGEN, B. 2009. Predictive value of femoral head heterogeneity for fracture risk. *Bone*, 44, 590-595.

- TANNER, K. E., SHARP, D. J., DOYLE, C., COOMBS, R. R. H., BONFIELD, W. 1988. *Implant Materials in Biofunction*, Amsterdam, Elsevier.
- TAYLOR, M., COTTON, J., ZIOUPOS, P. 2002. Finite Element Simulation of the Fatigue Behaviour of Cancellous Bone. *Meccanica*, 37, 419-429.
- TAYLOR, M., TANNER, K. E., FREEMAN, M. A. R., YETTRAM, A. L. 1995. Cancellous bone stresses surrounding the femoral component of a hip prosthesis: an elastic-plastic finite element analysis. *Medical Engineering, Physics*, 17, 544-550.
- TERMINE, J. D. 1993. Bone matrix proteins and mineralization process. In FAVUS, M. J. (Ed.) *Primer on the metabolic bone diseases and disorders of mineral metabolism, second edition*. Raven Press.
- TIMLIN, J. A., CARDEN, A., MORRIS, M. D., RAJACHAR, R. M., KOHN, D. H. 2000. Raman Spectroscopic Imaging Markers for Fatigue-Related Microdamage in Bovine Bone. *Analytical Chemistry*, 72, 2229-2236.
- TODD, R. C., FREEMAN, M. A. R., PIRIE, C. J. 1972. Isolated Trabecular Fatigue and Fractures in the Femoral Head. *J Bone Joint Surg Br*, 54-B, 723-728.
- TODOH, M., IHARA, M., MATSUMOTO, T., TANAKA, M. 2004. Relationship Between Mechanical Property of Cancellous Bone and Hardness of Trabeculae. *JSME International Journal*, 47, 1075 - 1078.
- TURNER, C. H., BURR, D. B. 2001. Experimental techniques for bone mechanics. In: COWIN, S. C. (ed.) *Bone Mechanics Handbook*. Second Edition ed.: CRC Press.
- VAN RIETBERGEN, B., HUISKES, R., ECKSTEIN, F., RUEGSEGGER, P. 2003. Trabecular bone tissue strains in the healthy and osteoporotic human femur. *Journal of Bone and Mineral Research*, 18, 1781-1788.
- VAN RIETBERGEN, B., WEINANS, H., HUISKES, R., ODGAARD, A. 1995. A new method to determine trabecular bone elastic properties and loading using micromechanical finite-element models. *Journal of Biomechanics*, 28, 69-81.
- VASHISHTH, D., KOONTZ, J., QIU, S. J., LUNDIN-CANNON, D., YENI, Y. N., SCHAFFLER, M. B., FYHRIE, D. P. 2000a. In vivo diffuse damage in human vertebral trabecular bone. *Bone*, 26, 147-152.

- VASHISHTH, D., VERBORGT, O., DIVINE, G., SCHAFFLER, M. B., FYHRIE, D. P. 2000b. Decline in osteocyte lacunar density in human cortical bone is associated with accumulation of microcracks with age. *Bone*, 26, 375-380.
- VASHISHTH, D. 2007. Hierarchy of bone microdamage at multiple length scales. *International Journal of Fatigue*, 29, 1024-1033.
- VERNON-ROBERTS, B., PIRIE, C. J. 1973. Healing trabecular microfractures in the bodies of lumbar vertebrae. *Ann Rheum Dis*, 32, 406-412.
- WACHTEL, E. F., KEAVENY, T. M. 1997. Dependence of trabecular damage on mechanical strain. *Journal of Orthopaedic Research*, 15, 781-787.
- WALDORFF, E. I., GOLDSTEIN, S. A., MCCREADIE, B. R. 2007. Age-dependent microdamage removal following mechanically induced microdamage in trabecular bone in vivo. *Bone*, 40, 425-432.
- WANG, X., MASSE, D. B., LENG, H., HESS, K. P., ROSS, R. D., ROEDER, R. K., NIEBUR, G. L. 2007. Detection of trabecular bone microdamage by micro-computed tomography. *Journal of Biomechanics*, 40, 3397-3403.
- WASSIF, H. 2007. Application of x-ray microtomography to studies of model dental caries systems. Ph.D. *Institute of Dentistry*. London, Queen Mary University of London.
- WENZEL, T. E., SCHAFFLER, M. B., FYHRIE, D. P. 1996. In vivo trabecular microcracks in human vertebral bone. *Bone*, 19, 89-95.
- WHITEHOUSE, W. J. 1974. The quantitative morphology of anisotropic trabecular bone. *Journal of Microscopy*, 153-168.
- WHITEHOUSE, W. J., DYSON, E. D., JACKSON, C. K. 1971. The scanning Electron Microscope in studies of trabecular bone from a human vertebral body. *Journal of Anatomy*, 108, 481-496.
- WONG, F. S. L. 1995. *Applications of X-ray Microtomography to the Study of Bones and Teeth*. PhD, Queen Mary University of London.
- WONG, F. S. L., ELLIOTT, J. C., DAVIS, G. R., ANDERSON, P. 2000. X-ray microtomographic study of mineral distribution in enamel of mandibular rat incisors. *Journal of Anatomy*, 196, 405 - 413.
- WOODS, C. G. 1972. *Diagnostic Orthopaedic Pathology*, Oxford, Blackwell Scientific Publications.

WORLD HEALTH ORGANISATION. 2003. *Pathogenesis of Osteoporosis and Related Fractures*. Geneva. World Health Organisation

WU, D., GAO, D., MAYO, S. C., GOTAMA, J., WAY, C. 2008. X-ray ultramicroscopy: A new method for observation and measurement of filler dispersion in thermoplastic composites. *Composites Science and Technology*, 68, 178-185.

ZANETTI, M., BRUDER, E., ROMERO, J., HODLER, J. 2000. Bone marrow edema pattern in osteoarthritic knees: Correlation between MR imaging and histologic findings. *Radiology*, 215, 835-840.

ZIOUPOS, P., CURREY, J. D., SEDMAN, A. J. 1994. An examination of the micromechanics of failure of bone and antler by acoustic emission tests and Laser Scanning Confocal Microscopy. *Medical Engineering, Physics*, 16, 203-212.

ZIV, V., WEINER, S. 1994. Bone crystal sizes: A comparison of Transmission and Electron Microscopic and X-Ray Diffraction Line Width Broadening Techniques. *Connective Tissue Research*, 30, 165-175.

ZOU, S., BEST, S., BONFIELD, W. 2007. Segmentation of X-Ray Microtomography Data of Porous Scaffold. *Key Engineering Materials*, pp330 - 332, pp911 - 914.

ZYSSET, K. P., GUO, X. E., HOFFLER, C. E., MOORE, K. E., GOLDSTEIN, S. A. 1999 Elastic modulus and hardness of cortical and trabecular bone lamellae measured by nanoindentation in the human femur. *Journal of biomechanics*, 32, 1005 -1012.

www.hesonline.nhs.uk/Ease/servlet/ContentServer?siteID=1937&categoryID=19

2

Appendices

Appendix I

Specimen	Osteophyte and Location	Bone cysts	Subchondral bone thickening	Sclerosis	Trabecular orientation	Femoral Head Geometry	Growth Plate	Additional Comments	Diagnosis
A1	None	None	No shadowing	No	Fine	Slightly Abnormal	Visible		Normal
A2	N/A	N/A	N/A	N/A	N/A	N/A	N/A	N/A	N/A
A3	None	None	No shadowing	No	Fine	Normal	Visible	Short femoral neck, porotic appearance of bone structure	Osteoporosis
A4	None	None	No shadowing	No	Fine	Normal	Visible		Normal
A5	Yes, Present at the head neck junction, superior and inferior	Yes	No shadowing	No	Fine	Abnormal	Visible	Beginning of OA, Cysts in the centre of the head	Osteoarthritis
A6	None	None	No shadowing	No	Fine	Normal	Visible		Normal
A7	Yes, new osteophyte embryo forming at the superior and inferior surface of the head/neck junction,	None	No shadowing	No	Fine	Slightly Abnormal	Visible	Early wear on the surface	Osteoarthritis
A8	Yes, Present at the superior and inferior surface of the head/neck junction	Yes	No shadowing	No	Fine	Slightly Abnormal	Visible	Reduced bone, Cysts present close to the Superior and inferior surface of the head/neck junction	Osteoarthritis

Part V References and Appendices

A9	None	yes	No shadowing	No	Fine	Slightly Abnormal	Visible	Early OA, Cysts present close to the inferior surface of the head/neck junction,	Osteoarthritis
A10	Yes, Present at the superior and inferior surface of the head/neck junction	None	No shadowing	No	Fine	Abnormal	Visible		Osteoarthritis
A11	None	None	No shadowing	No	Fine	Normal	Visible		Normal
A12	Yes, Present at the head neck junction, superior		No shadowing	No	Fine	Abnormal	Slightly Visible	Erosion at the superior surface close to head neck junction	Osteoarthritis
A13	Yes, Present at the superior surface of the head/neck junction	None	No shadowing	No	Fine	Slightly Abnormal	Visible		Osteoarthritis
A14	Yes, Present at the superior and inferior surface of the head/neck junction	None	No shadowing	No	Fine	Abnormal	Slightly Visible		Osteoarthritis
A15	None	None	No shadowing	No	Fine	Normal	Visible		Normal
A16	Yes, perioarticular osteophytes		No shadowing	No	Fine				Osteoarthritis
A17	None	None	No shadowing	No	Fine	Normal	Visible		Normal
A18	Yes, Present at the superior and inferior surface of the head/neck junction	None	No shadowing	No	Fine	Abnormal	Slightly Visible	Erosion at the surface	Osteoarthritis
A19	Yes, Present at the		No shadowing	No	Fine	Slightly	Visible		Osteoarthritis

	superior and inferior surface of the head/neck junction					Abnormal			
A20	None	None	No shadowing	No	Fine	Normal	Visible	Close to fracture	Severe Osteoporosis
A21	Yes, Specular Osteophytes present at the superior and inferior surface of the head/neck junction		No shadowing	No	Fine	Abnormal	Visible	Early OA	Osteoarthritis
A22	Yes, Present at superior and inferior surface of the head/neck junction	None	No shadowing	No	Fine	Slightly Abnormal	Slightly Visible	Severe OA	Osteoarthritis
A23	Yes, Present at the superior and inferior surface of the head/neck junction	None	Shadowing present around the surface edges	Subchondral Sclerosis	Poor	Severely Abnormal	Slightly Visible	Large Osteophyte formations	Severe Osteoarthritis
A24	None	None	No shadowing	No	Fine	Normal	Visible		Normal

Appendix II

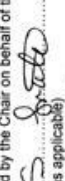
Code	Sex	Cause of death	Age	Date of death
QM14	M	IHD	90	17/03/06
QM15	F	Myeloma	75	21/03/06
QM16	F	Sub arachnoid haemorrhage	86	22/03/06
QM17	M	Bronchopneumonia 2ndry to COPD	89	25/03/06
QM18	F	Cerebrovascular Accident	86	29/03/06
QM20	F	Pneumonia/ chronic renal failure	89	05/05/06
QM22	M	COPD	81	18/05/06
QM24	F	Focal Invasive adenocarcinoma rectum	96	07/06/06
QM26	F	Breast cancer	91	04/09/06
QM28	M	Bladder cancer	91	23/11/06
QM29	M	Bronchopneumonia	91	05/01/07
QM30	M	Old age	91	11/01/07
QM31	F	MI	93	06/02/07
QM32	M	Bronchopneumonia	80	17/06/07

Appendix III

Ethical Permission

06/Q0604/1

Page 1

East London & The City HA Local Research Ethics Committee 2				
LIST OF SITES WITH A FAVOURABLE ETHICAL OPINION				
For all studies requiring site-specific assessment, this form is issued by the main REC to the Chief Investigator and sponsor with the favourable opinion letter and following subsequent notifications from site assessors. For issue 2 onwards, all sites with a favourable opinion are listed, adding the new sites approved.				
REC reference number:	Issue number:	Date of issue:		
06/Q0604/1	1	08 February 2006		
Chief Investigator:	Professor K. Elizabeth Tanner			
Full title of study:	Fracture and Fatigue of Bones and the effect of Pathology, Mineralisation of Cancellous Bone and Failure of Individual Trabeculae			
This study was given a favourable ethical opinion by East London & The City HA Local Research Ethics Committee 2 on 08 February 2006. The favourable opinion is extended to each of the sites listed below. The research may commence at each NHS site when management approval from the relevant NHS care organisation has been confirmed.				
Principal Investigator	Post	Research site	Site assessor	Notes ⁽¹⁾
Prof K. Elizabeth Tanner	Professor of Biomedical Materials	Queen Mary University of London	East London & The City HA Local Research Ethics Committee 2	08/02/2006
Approved by the Chair on behalf of the REC:				
 (delete as applicable) (Signature of Chair/Administrator)				
..... Sara J. Tate (Name)				

(1) The notes column may be used by the main REC to record the early closure or withdrawal of a site (where notified by the Chief Investigator or sponsor), the suspension of termination of the favourable opinion for an individual site, or any other relevant development. The date should be recorded.

Appendix IV

Publications and Conference abstracts

Safir F and Tanner K.E. Use of Problem-based Learning in Biomaterials Education in IFMBE Proceedings, Vol. 11. Prague: IFMBE, 2005. ISSN 1727-1983. Editors: Jiri Hozman, Peter Kneppo (Proceedings of the 3rd European Medical & Biological Engineering Conference - EMBEC'05. Prague, Czech Republic, 20-25.11.2005) pp. 4642-4645

Ahmed F. Bushby A.J. Davis G.R. X-ray Microtomography of Trabecular Bone Using Time-delay Integration. Rank Symposium on High Resolution X-ray Imaging, Lake District, October 2010 (Rank prize awarded for best paper)

Ahmed F. Kosoric J. Barber A.H. and Anderson P. Measuring the interaction between statherin-like peptide and hydroxyapatite using liquid cell atomic force microscopy. ORCA, Montpellier, July 2010

Ahmed F. Bushby A.J. and Gupta H.S. Compressive Failure of Human Trabecular Bone Studied by X-ray Microtomography. MRS, San Francisco, Spring 2009

Tang K. **Ahmed F.** Davis G. Mohsin S. 2009 Visualization of Blood Vessels using High Definition X-ray Microtomography. *Calcified Tissue International*. 85(2): 65

Ahmed F. Bushby A.J. and Davis G.R. Microcallus Distribution in an Osteoarthritic Femoral Head Using X-Ray Micro-CT. *ES of Biomechanics*, Lucerne, July 2008

Davis G R. **Ahmed F** and Boyde A. X-ray Microtomography and Scanning Electron Microscopy in Study of Loss of Articular Calcified Cartilage and Subchondral Bone in Human Femoral Head. *BSMB*, York, April 2008

Ahmed F. Tanner K.E. and Davis G.R. Measurement of Bone Mineral Concentration Using Micro-computed Tomography. ES of Biomaterials, Brighton, 2007

Green M. **Ahmed F.** Vanezis P. and Tanner K.E. Analysis of Bone Injury as a Cause of Knife Stabbing UKSB, 2007

Publications in preparation

Ahmed F. Davis G.R. Bushby A. J and Boyde A., *3D Distribution of Microcallus Patches in Relation to Load Bearing Areas of an Osteoarthritic Femoral Head*

Ahmed F. Howard L. Davis G.R. and Bushby A. J., Ultra-microtomography of microcallus in human femoral head

Ahmed F. Howard L. Bushby A. J. Davis G.R. and Boyde A., *Correlative 3D imaging from millimeters to nanometers in human bone*

Appendix V

Video 1

Video 2

Video 3 (Specimen B7)

Video 4 (Specimen B14)

Video 5 (Specimen B7)

Video 6 (Specimen B14)

Video 7